Muon Correlated Background at The Sudbury Neutrino Observatory

by

Q. Rushdy Ahmad

B.A., Bates College, 1991

M.S., Brown University, 1993

Thesis

Submitted in partial fulfillment of the Degree of Doctor of
Philosophy in the Department of
Physics at Brown University

Providence, Rhode Island

May 2002

This dissertation by Q. Rushdy Ahmad
is accepted in its present form by the Department of
Physics as satisfying the
dissertation requirements for the degree of Doctor of Philosophy

Date____________ ________________________
Prof. D. Cutts, Chair

Recommended to the Graduate Council

Date____________ ________________________
Prof. R. Lanou, Reader

Date____________ ________________________
Prof. R. Brandenberger, Reader

Date____________ ________________________
Prof. G. Tucker, Reader

Date____________ ________________________
Prof. J. Wilkerson, Reader

Approved by the Graduate Council

Date____________ ________________________
Peder J. Estrup
Dean of the Graduate School and Research

To my loving parents

Preface

The Sudbury Neutrino Observatory (SNO) is a real time solar neutrino experiment. The detector utilizes 1,000 metric tons of heavy water to study the fundamental properties of neutrinos. The SNO detector has been designed to measure the flux and energy spectrum of electron-type solar neutrinos in addition to measuring the total flux of all active flavors of solar neutrinos. A measurement of a distortion in the energy spectrum or a measurement of a reduction in the electron-type neutrino flux with respect to the total solar neutrino flux would provide strong evidence for neutrino mass, which is an indication of physics beyond the Standard Model of fundamental particle interactions.

A brief introduction and history of Neutrino Physics will be presented in Chapter 1. In Chapter 2 the Solar Neutrino Problem (SNP), the Standard Solar Model (SSM), past and present solar neutrino experiments and possible solutions to the SNP will be discussed. A general description of the Sudbury Neutrino Observatory will be given in Chapter 3.

A primary component of the SNO detector is the electronics and data acquisition [DAQ] system. The author has been intricately involved in the design and implementation of the Data Acquisition system and a detailed discussion of the system will be presented in Chapter 4.

The SNO detector has a rock overburden of 6,150 meter water equivalent. Even though this provides a very good shield to cosmic muons, enough of them penetrate the detector to produce secondary particles, in particular neutrons. These neutrons contribute to the background signal of the detector. A study of through-going muons and neutron production due to muon spallation in the SNO detector will be presented in Chapters 5 and 6. In Chapter 7 the conclusion to the dissertation will be provided.

Acknowledgements

I believe that my life and career have been shaped by the varied influences of nature and nurture. Over the course of time I have been fortunate to have had individuals guide me through the process of learning the values and practices that make one successful in any given endeavor. Like other important landmarks in my life, the successful completion of this dissertation would not have been possible without the help and guidance of a number of soulful and insightful individuals. I believe that the appropriate gesture of thanking the people who have helped me achieve this goal is to salute them all without attempting to mention each one of them by name. In this measure I avoid the gross error of failing to thank someone who requires my sincere gratitude.

I, therefore, thank and applaud you for the support and guidance that you have provided me over the years and I happily look forward to many more years of our journey together through space and time.

I am now compelled to violate the above directive. This dissertation would be incomplete if I were to not acknowledge in public the support, encouragement and guidance that I have received from my thesis advisors, Professor John F. Wilkerson and Professor Robert Lanou.

I must gratefully thank my parents and my mother and father in-law for their unconditional love, support and encouragement. Whenever I thought that I might be at the end of my ropes they provided the helping hand that enabled me to hang tight and proceed with renewed vigor and purpose. I am extremely lucky to have them as my guide.

Finally, I must show my utmost gratitude to my loving wife, Farzin, for her constant support, caring and understanding. Not enough words can ever vouch for my deepest of appreciations for such a beautiful and gifted soul.

Contents

List of Figures

List of Tables

Chapter 1

Neutrino Physics

1.1 The Standard Model and the Neutrino

1.1.1 Introduction

One of the great scientific achievements of the 20th century has been the formulation of the Standard Model of fundamental interactions of elementary particles. Since its inception, many experiments have been carried out to test the theory. The accuracy with which the results of these experiments have matched the prediction of the model is nothing short of remarkable. Although the Standard Model is a fairly accurate description of nature at its fundamental level, it is nevertheless an incomplete model. For example, the model doesn't include one of the key forces of nature: gravity. Furthermore, the properties of the neutrino, which is one of the key elements in the model, are not very well understood. Given that the model is incomplete, people have attempted to formulate other all encompassing theories of nature with varying degrees of success. Recently, the need for physics beyond the Standard Model has been underscored by the experimental evidence of neutrino oscillation. In subsequent chapters, the details of neutrino oscillations, its ramifications, and the role that the Sudbury Neutrino Observatory

(SNO) will play in elucidating this area of research will be discussed. But first, for completeness, a brief overview of the primary facets of the Standard Model will be given.

1.1.2 A Brief Overview

Three generations of quarks and leptons, including their respective antiparticles, are the primary building blocks of matter in the Standard Model. Based on current experimental limits, these particles are effectively point-like and possess no inherent structure. There are also three basic non-gravitational forces : strong, weak and electromagnetic. These forces are mediated or carried by various gauge bosons (particles with integer spin) : eight gluons, which carry the strong force; the $W^{\pm}$ and Z^0, which carry the weak force; the photon, which carries the electromagnetic force. These carriers are referred to as "gauge bosons" because the form of interaction that they mediate is determined by a symmetry principle called gauge invariance. The familiar photon, the carrier of the electromagnetic force, is massless and has an infinite interaction range similar to the carrier of gravity. The carriers of the weak force, the gauge bosons $W^{\pm}$ and Z^0, were discovered after an extensive search. Their masses have been measured to be 80.22 GeV/c^2 and 91.187 GeV/c^2 respectively [9], and until the recent discovery of the top quark, these were the heaviest elementary particles. The evidence for gluons, the carriers of the strong force, is indirect since gluons are not observed to exist freely in nature. According to the model, the gluons are massless and are confined within hadrons. In Table 1.1 [10] a list of the fundamental forces of nature is presented along with the carriers, the ranges and the relative strengths of the forces.

After all the counting is done, one finds in the Standard Model a total of at least 61 elementary particles (antiparticles included): 12 leptons; 36 quarks, since the quarks come in three colors; 12 gauge bosons and at least 1 Higgs particle. According to the Standard Model, it is the coupling of the particles to the Higgs

Interaction	Field Quantum	Range (m)	Relative Strength
Strong	Gluon	10^{-15}	1
Weak	$W\pm$, Z^0	10^{-18}	10^{-5}
Electromagnetic	Photon	∞	$\alpha = \frac{1}{137}$
Gravity	Graviton	∞	10^{-38}

Table 1.1: The Fundamental Interactions

that is responsible for giving mass to the particles. The fermions (particles with half integer spin) consisting of electrons (e), muons (μ), taus (τ) and neutrinos (ν_e, ν_μ, ν_τ) and their antiparticles are collectively called leptons. The six quarks, up (u), down (d), charm (c), strange (s), top (t), and bottom (b), are also fermions. Like gluons, the quarks cannot exist freely and strong theoretical arguments and experimental evidence imply that quarks must remain confined within hadrons. However all six quarks have been indirectly observed. In Table 1.2 [9] a list of the quarks and leptons is presented along with their charges and masses. Since free quarks do not exist, their masses cannot be measured directly. The quark masses listed in Table 1.2 are estimates based on experimental and theoretical arguments.

The particles divide into three generations or families. Within each family there are two flavors and the table consists of six flavors of lepton and six flavors of quarks. Recent experimental evidence from the Z^0 decay shows [9] that there are only three generations ($N_\nu \sim 3$) of neutrinos. As can be seen from the table, the neutrinos are massless, electrically neutral particles. However, the masses of the different flavors of the neutrino have been denoted with a question mark. This has been done because the Standard Model, in its present incarnation, accommodates

Generation	Family	Charge (e)	Mass (MeV/c^2)	Flavor	Charge (e)	Mass (MeV/c^2)
First	ν_e	0	0?	u	$\frac{2}{3}$	1.5 to 5
	e	-1	0.511	d	-$\frac{1}{3}$	3 to 9
Second	ν_μ	0	0?	c	$\frac{2}{3}$	1100 to 1400
	μ	-1	105.7	s	-$\frac{1}{3}$	60 to 170
Third	ν_τ	0	0?	t	$\frac{2}{3}$	173800 ± 5200
	τ	-1	1777.1	b	-$\frac{1}{3}$	4100 to 4400

Table 1.2: Leptons and Quarks

only massless neutrinos.

The law of parity conservation was presumed for quite some time to be one of the fundamental laws of physics. Simply stated, a phenomenon observed in the reflection of a mirror obeys the same physical laws as the identical phenomenon observed directly, without a mirror. This law had been extensively studied for gravitational and electromagnetic interactions and it always appeared to hold true for these cases. Until 1956 it was assumed that the law of parity conservation also held true for weak interactions. T.D.Lee and C.N.Yang challenged the idea of parity conservation in weak interactions in a paper in 1956 and pointed out that there was no experimental evidence proving that fact [11]. Taking up the challenge posed by Lee and Yang, Wu et.al.[12] that same year demonstrated in a ^{60}Co β-decay experiment that the weak force with respect to neutrinos did not conserve parity, i.e. the symmetry between left and right was violated. The physics world was rocked and shocked by the discovery that the weak interaction makes such a distinction. An eventual consequence of this result was the formulation of the Standard Model theory of the two-component massless neutrino by Lee and Yang in 1957 [13]. In this model the neutrino is always left-handed and the antineutrino is always right-handed. However, it was soon shown that the weak force violated parity irrespective of the mass of the leptons. Therefore, the neutrinos need not be massless particles. There have been many experimental searches for the neutrino mass over the past decades, and to this date neutrino mass determination remains a hot topic of fundamental research in physics.

Evidence of neutrino mass has been explored through experiments on neutrinos created astrophysically, in the earth's atmosphere, by accelerators, by reactors, and by nuclear decays. Most direct measurements of the neutrino masses come from kinematical studies of the particles produced in the reactions $^3H \rightarrow {}^3He\ e^-\,\nu_e$, $\pi \rightarrow \mu\nu_\mu$ and $\tau \rightarrow n\,\pi\,\nu_\tau$. The Current mass limits are $m_{\nu_e} < 3$ eV, $m_{\nu_\mu} < 170$ keV (90% CL), and $m_{\nu_\tau} < 18.2$ MeV (95% CL) [9]. Neutrino mass does not only affect the structure of the Standard Model. For example, a neutrino mass of only a few electron-volts would affect cosmology and the evolution of the universe. Furthermore, the issue of whether the neutrino is its own antiparticle, as suggested by E.Majorana in 1937 [14], still remains unresolved. With the success of the two component theory of the neutrino, interest in Majorana neutrinos subsided after 1957. However, with the emergence of the grand unified theories in the late 1970s, theorists began predicting the existence of Majorana neutrinos with small masses. According to Dirac's theory there are four possible neutrino states - particle and antiparticle, each with right or left-handedness. On the other hand, Majorana's theory leads to only two states, a right-handed or left-handed version of a single particle. If the neutrino has no mass, then it would be impossible to tell whether a neutrino is of the Dirac type or of the Majorana type. Both theories in this case would give the same experimental results. However, if the neutrino is even slightly massive and is its own antiparticle then the observation of a process known as neutrinoless double beta decay could reveal the Majorana identity of the neutrino.

Neutrinos and all other elementary particles in the Standard Model are governed by two fundamental gauge theories that describe all known interactions. These gauge theories are quantum mechanical theories for which the Lagrangian of the interaction is invariant under a local gauge transformation. The theory describing the strong interaction is known as QCD or quantum chromodynamics, where the local gauge group is $SU(3)_c$(color). Electroweak theory, which combines the electromagnetic and weak forces into a single theory uses the gauge groups $SU(2)_L$ (weak isospin, L denotes that the theory only involves left handed fermions or right handed antifermions) x $U(1)_{em}$(weak hypercharge). It is interesting to note that in 1879 James Clerk Maxwell formulated a unified theory of electricity and magnetism; and exactly one hundred years later Sheldon Glashow, Abdus Salam, and Steven Weinberg received the Nobel Prize for unifying the weak and electromagnetic forces. A crucial prediction of the electroweak theory was the existence of the $W^{\pm}$ and Z^0 gauge bosons and they were indeed discovered at the predicted masses. As of this writing no one has yet been able to combine QCD and the electroweak theory. One hopes that this time the wait will not be as long.

1.1.3 Conclusion

The Standard Model has done a very good job of explaining most of the experimental results regarding fundamental particle interactions. However, there is currently strong experimental indication of physics reaching beyond the influence of this very successful theory. The evidence is manifested in the form of neutrino oscillations, which demands the incorporation of massive neutrinos into the Standard Model. As seen earlier in Table 1.2, neutrinos in the Standard Model are assumed to be massless fermions. Therefore, massive neutrinos would definitely require the revision of the present day model. Even without incontrovertible experimental evidence for neutrino mass, many people believe that the neutrinos are in fact massive particles. In the Standard Model particles attain mass by coupling to the Higgs boson, and there is no sound reason why the neutrinos, like all other leptons, shouldn't also couple to the Higgs. Furthermore, from the standpoint of the grand unified theories (GUTs), which attempt to unify the electromagnetic, weak, and strong interactions, it is more natural for the neutrinos to be massive than to be massless. In these schemes the neutrinos become equal partners of the leptons and the quarks, which are all massive. Even though this is not proof of neutrino mass, to claim that they are so different from their partners would be a strong and highly exceptional claim. If however the neutrinos are massive then it would be natural for the different flavors of neutrinos to mix in a manner analogous to the quark sector. Such mixing would make it possible for one type of neutrino to transform into another type of neutrino during travel through space. This explanation is one of the leading hypotheses that accounts for recent experimental data regarding neutrino detection from the sun and from the earth's atmosphere. If the Sudbury Neutrino Observatory (SNO), which is studying solar neutrinos, is successful at confirming the neutrino oscillation hypothesis then one would have definitive proof of physics beyond the Standard Model. In order to fully appreciate the resounding implications of such a finding it would be worthwhile to briefly review the history pertaining to the discovery of the neutrino. That is the subject matter of the next section.

1.2 Neutrino Geneology

1.2.1 Introduction

The history of science is replete with examples of scientific revolutions brought about by the inadequacy of a paradigm to successfully lead the efforts in exploring and understanding an aspect of nature which the paradigm itself was designed to address. Eventually the shortcomings of an ineffectual and problematic paradigm are overcome by the construction and espousal of a new paradigm. Scientists, guided by this new paradigm, attempt to look in places where they have not looked before and adopt new tools and devise novel experiments to aid them in their quest to expand the boundaries of knowledge. The birth of the concept of the neutrino and the ensuing events leading to its triumphant discovery are prime examples of the revolutionary scientific processes that enhance our understanding of the inner workings of nature. The path to the discovery of the neutrino began with the emergence of an anomalous observation, an accounting of which necessitated a revolutionary shift in a paradigm that demanded the existence of the neutrino. The validation and general acceptance of this new paradigm was made possible only through the unequivocal proof of the existence of the neutrino by direct observation. This event marked the dawn of a new era for experimental neutrino physics. In what follows, a qualitative historical account of the events leading to and culminating in the discovery of the neutrino will be presented. The purpose of this endeavor is to provide an understanding of one of the many ground-breaking scientific events that have been responsible for paving the way for present and future neutrino experiments. The neutrino hypothesis, the discovery of the neutrino, the idea of neutrino oscillations, and the observation of an anomalous reduction in the solar neutrino flux are events that have been witness to the hard work and dedication of numerous scientists around the world. Needless to say, the Sudbury Neutrino Observatory owes its existence to these past achievements in theoretical and experimental neutrino physics.

1.2.2 The Neutrino Hypothesis

The process of radioactive decay involves the transmutation of a nucleus in which the radioactive nucleus not only emits alpha, beta or gamma radiation but also converts mass into energy as it goes from a higher to a lower energy state. According to the fundamental law of conservation of energy, the total energy before and after the process is required to remain constant. In the scenario where a nucleus at rest undergoes radioactive decay into two bodies, a final nucleus and an electron, conservation of momentum dictates that the nucleus and the electron in the final state separate in opposite directions with equal momentum. A direct consequence of this and the conservation of energy is that the electron in this decay mode, known as nuclear beta decay, is emitted with a constant amount of energy.

During the early decades of this century, scientists investigating the recently discovered phenomenon of nuclear beta decay observed an anomalous behavior in which the energy of the emitted electron did not seem to obey the laws of conservation of energy and momentum. In 1914 James Chadwick convincingly demonstrated that the electron emitted in beta decay did not possess a singular value for its energy but instead exhibited a continuous spectrum of energies. A good historical description of Chadwick's discovery can be found in the book by Christine Sutton titled "Space Neutrino"[15]. Further experiments carried out by other scientists confirmed this anomaly where it appeared that the laws of conservation of energy and momentum were being violated. The eminent physicist Niels Bohr in 1930 noted that evidence "either empirical or theoretical" didn't exist to support the conservation of energy in this case. He was even willing to abandon this fundamental law in the domain of nuclear physics.

In the year 1930 Wolfgang Pauli, in an attempt to preserve the conservation laws, came up with a solution to explain the anomalous observations in nuclear beta decay experiments. Pauli's hypothesis, which he himself considered to be a "desperate way out"[16], proclaimed the existence of the neutrino[1], an electrically neutral, spin-$\frac{1}{2}$ particle which is emitted simultaneously with the electron in the beta decay of a neutron. According to Pauli's prescribed solution the nucleus

---

[1] Pauli originally called it the "neutron" which meant the "neutral one". This was done before Chadwick discovered the neutron in 1932. Later Fermi renamed it to be the neutrino which in Italian means the "little neutral one".

undergoing β-decay produces three bodies in the final state and as a result the constant energy that is expected for the emitted electron is now shared by the electron and the hypothesized neutrino. The neutrino hypothesis, thus, enabled one to account for the apparent non-conservation of energy and momentum in the β-decay of a neutron.

Shortly thereafter in 1934, long before the neutrino was detected in an experiment, Enrico Fermi convincingly validated the existence of the neutrino by his successful quantitative theory of β-decay [17]. Fermi's formulation of a field theory for β-decay was able to explain all the observed properties of such a radioactive decay mechanism. The theory assumed that the β-decay of a nucleus took place as a result of the β-decay of one of the nucleons that made up the nucleus. Fermi described β-decay in analogy to Dirac's model of electromagnetic interaction, where two charged particles interact via the exchange of a virtual photon that is produced and then absorbed by the electromagnetic currents associated with the particles. Fermi formulated the weak interaction in terms of the product of weak currents, one connecting the initial and final nucleon and the other connecting the final state electron/positron and Pauli's neutrino. Unlike electromagnetism where the virtual photon connects the two currents at distinct points in space-time, the weak interaction theory of Fermi connected the currents at the same space-time point. The underlying assumption is that the weak interaction is very short ranged. The weak Hamiltonian can be written as follows:

$$H_w = \frac{G_F}{\sqrt{2}} \psi_p^\dagger j_\mu \psi_n \psi_e^\dagger j^\mu \psi_\nu \tag{1.1}$$

where, G_F is the Fermi constant that determines the overall coupling strength of the interaction. As written above, one of the weak currents is associated with the conversion of a neutron into a proton, and the other weak current is associated with the production out of the vacuum of an electron and antineutrino. Fermi's theory predicted the decay of the neutron, which was later verified. Furthermore, it not only correctly predicted the dependence of the radioactive nucleus lifetime on the energy released in the decay but it also predicted the proper shape of the energy spectrum of the emitted electrons. The excellent fit to the experimentally measured electron spectrum in β-decay was an important confirmation of Fermi's theory, and thus provided compelling evidence for the existence of the neutrino. However, it was generally accepted that the proof of its existence required an observation of a neutrino inverting a β-decay or interacting with matter at a remote point. This was not an easy task since a sophisticated and a very low background experiment would be needed to make such an observation. Therefore, physicists during the early days of the search for the neutrino labeled it "elusive". Given that experimental physicists seeking to detect the neutrino were being repeatedly frustrated by its "elusive" nature, it is not hard to understand Pauli's self-inflicted blame evident in his statement[18],

> "I have done a terrible thing. I have postulated a particle that cannot be detected."

1.2.3 The Discovery

Introduction

In the summer of 1951, scientists at the Los Alamos National Laboratory, under the direction of Fred Reines and Clyde Cowan, began work on a very bold and novel project to detect neutrinos. This was the first neutrino physics experiment and because the neutrino had managed to remain hidden for more than two decades since Pauli's claim of its existence, it was aptly called "Project Poltergeist". A very good historical description of the discovery of the neutrino can be found in [19], from which has been drawn the material in this section. Physicists at the time believed, in general, that the existence of the neutrino had been demonstrated indirectly and were under the impression that the particle could not be directly observed. Pauli's neutrino hypothesis and Fermi's theory of beta decay provided the framework within which the neutrino played a key role in explaining the apparent lack of energy and momentum conservation in nuclear beta decay, and it was therefore very likely that it existed in nature. Reines and Cowan knew that strong indirect evidence for the neutrino could not stand alone and that a direct observation of the particle was necessary for the proof of its existence.

The task of detecting neutrinos via neutrino induced interaction was deemed very difficult to say the least. The probability of a neutrino colliding with matter was reduced enormously because the weak force which governs neutrino interaction has a very short range. It was estimated that in order to guarantee a collision between a neutrino and matter, one would require a target of lead one light-year thick. However if one were to use a very large number of neutrinos, then the required thickness, i.e. the number of target elements, to ensure a collision once in a while could be reduced accordingly. Reines and Cowan were very much aware of this and knew of a mechanism to produce copious amounts of neutrinos.

The Bomb

The audacious experiment that Reines and Cowan designed to directly observe neutrinos involved the utilization of a 20-kiloton nuclear fission bomb at the Nevada Test Site. Calculations had shown that this nuclear explosion might be able to produce an intense pulse of neutrinos which would rise above the background and provide a measurable signal. This was definitely a much more sensitive neutrino detection experiment than had previously been thought of. After deciding on the source of neutrinos they needed to choose a neutrino induced interaction so that they might construct a detector in order to facilitate such a reaction. They turned to Fermi's theory of β-decay which predicts that the antineutrino, the antiparticle of the neutrino, will occasionally interact with a proton in a nucleus via the weak force to turn it into a neutron. In this process the antineutrino transforms itself into a positron and charge is conserved before and after the reaction:

$$\overline{\nu}_e + N(n,p) \rightarrow N(n+1,p-1) + e^+ \tag{1.2}$$

where $\overline{\nu}_e$ and e^+ are an electron antineutrino and a positron and n and p are the number of neutrons and protons in the nucleus denoted by N. If the nucleus is that of a hydrogen, in other words if the target is a proton, then the above reaction will produce a neutron and a positron:

$$\overline{\nu}_e + p \rightarrow n + e^+ \tag{1.3}$$

where n and p are a neutron and a proton respectively. It was this interaction, where an $\overline{\nu}_e$ impinged upon a target proton to produce a neutron and a positron, that Reines and Cowan decided to employ in their experiment. With the idea of a feasible neutrino source and a reaction at hand they now had to design and build a viable, robust and large enough detector which would contain a sufficient number of target protons that would interact with neutrinos to produce a signal. The detector that they decided to build was a very large liquid scinitillation device, which they nicknamed 'El Monstro'[19]. In the experiment $\overline{\nu}_e$s from the fireball of the nuclear explosion would strike 'El Monstro' which was suspended in a hole dug below ground at a distance of about 40 meters from the impact point of the detonation.

The Hanford Experiment

The very extraordinary plan to detect the neutrino via the explosion of a nuclear bomb was granted approval by Norris Bradbury, the Laboratory Director at that time. This by itself was a testament to the tenacious persistence and ingenuity of idea of Reines and Cowan. However, they were not merely satisfied with the prospect of being able to conduct such a novel and challenging experiment; they were constantly looking for ways to improve their chances of detecting the neutrino. During the fall of 1952 when they got a suggestion about using a nuclear fission reactor instead of a bomb, they did not hesitate to give the idea some serious consideration even though other prominent physicists believed that the bomb was a much more suitable candidate than the reactor. It was argued that the bomb would be able to provide a neutrino flux that would be many orders of magnitude larger than that provided by the most powerful reactor available at the time. Furthermore, the background noise was deemed to be roughly the same for both cases. Unless the background events at the reactor could be further reduced by an appreciable amount, the nuclear explosion method with its intense source of a very large neutrino flux looked to be the best available approach. It should also be noted that in 1946 Bruno Pontecorvo, a prominent Italian physicist residing in Canada, had independently developed the idea of using a reactor as a neutrino source [20]. Unfortunatley, he was unable to pursue this idea when he moved to the former Soviet Union shortly thereafter.

Even though all the arguments seemed in favor of the bomb, Reines and Cowan gave serious thought to the idea of using a reactor to detect the neutrino, and in the process they eventually realized how to achieve a significant reduction in the background noise at a reactor. The mechanism involved the detection of both products of the inverse beta decay of Eq. (1.3). In this method the signature of the neutrino event would be the prompt detection of the positron coupled with a delayed detection of the neutron. This delayed coincidence between the positron and the neutron could be used to suppress the background, thus making the reactor a much more attractive and viable source of neutrinos than the bomb. Upon this realization they immediately stopped the preparation for the bomb measurement and began in earnest to develop the plans for building a detector that would be appropriate for a neutrino detection experiment utilizing the services of the nuclear reactor at Hanford, Washington. This reactor, the latest and largest in the country, was able to produce an antineutrino flux unparalleled by any other reactor at the time and that was exactly what Reines and Cowan wanted.

The basic idea behind the experiment was to detect both the positron and the neutron produced in the inverse beta decay reaction. In this reaction the positron very quickly comes to rest by ionization loss and annihilates with an electron to produce two γ-rays, which in turn create fast electrons via the Compton effect. These fast electrons eventually produce flashes of visible light in the scintillator, which is detected by photomultiplier tubes (PMTs) and then recorded by the detector electronics. The time scale involved in this process of producing the scintillation light is of the order 10^{-9} s, and the positron therefore generates a so-called prompt pulse. On the other hand, the neutron after it is produced thermalizes through the successive elastic collisions with the protons in the detector. The moderated neutron is then radiatively captured by cadmium nucleus with the release of about 9 MeV energy in the form of γ-rays. The γ-rays from the neutron capture on cadmium also produce a flash of light in the scintillator. The time difference between the flash of light from the electron-positron annihilation and that from the neutron capture on cadmium is a few microseconds. This delayed coincidence was used to discriminate the neutrino induced events from the background events.

The detector was operational for several months, during which the research team attempted their best to enhance the signal to noise ratio. In the end, after a thorough analysis of the acquired data they found a reactor-associated delayed coincidence rate of (0.41 ± 0.20) counts/min [21]. However the delayed-coincidence background, with or without the reactor being on, was measured to be around 5 counts/min. Therefore, in spite of a positive signal for neutrino events, the signal count rate was many times lower than the background rate and this is what Reines and Cowan tried very hard to understand and resolve. Even though they were unable to reduce this background any further, by placing the detector underground they were able to verify that cosmic rays were the cause for the background delayed-coincidence rates. This knowledge and understanding of the source of the background would aid them and others significantly in future neutrino experiments.

The Hanford experiment, therefore, produced a moderately strong case for the existence of the neutrino by providing some evidence for neutrino induced events. However, since the researchers were unable to sufficiently reduce the number of background signals generated by cosmic rays, the experiment failed to prove definitively that neutrinos really existed. Cowan summarized the results of the Hanford experiment in the following way:

> “We did record neutrino-like signals but the cosmic rays with their neutron secondaries in our shields were 10 times more abundant than were the neutrino signals. We felt we had the neutrino by the coattails, but our evidence would not stand up in court.”

The Savannah River Experiment

The encouraging results at Hanford gave Reines and Cowan the necessary motivation and insight to design and construct a new detector that would be able to discriminate more selectively against reactor-independent and reactor-associated backgrounds. Given their experience at Hanford, one of their prime objectives was to build a detector with the capability of significantly reducing the number of cosmic ray induced background events from their data set. This required a sophisticated and robust design of the detector, electronics and shielding.

In this experiment, as in the Hanford experiment, the reactor would generate the large flux of anti-neutrinos which would then impinge upon the target protons in the detector to initiate the inverse beta decay reaction. The delayed coincidence between the prompt pulses produced by positron annihilation and those produced by the neutron capture on cadmium would provide the signature for a neutrino event. In order to shield the detector from reactor produced neutrons, 11 meters of concrete was placed between the detector and the reactor center. Furthermore, 12 meters of overburden provided the detector with adequate protection from unwanted neutrons, charged particles, and gamma rays produced by cosmic rays.

The construction of this improved neutrino detector was completed in 1955 and was subsequently taken to a newly built powerful, approximately 700 megawatts, fission reactor at the Savannah River Plant in South Carolina. In 1956, three years after the tentative observation of the neutrino at the Hanford reactor and more than thirty years after Pauli's initial neutrino hypothesis, Reines and Cowan brought an end to the search for the neutrino in a very convincing manner at the Savannah River Plant reactor. Pauli after hearing about the discovery of the neutrino wrote [2] to Reines and Cowan[22],

> "Everything comes to him who knows how to wait."

The discovery of the neutrino finally put a stamp of approval on the new field of neutrino physics, and brought about the need to carry on further neutrino experiments so as to study and understand the properties of the newly found elementary particle. Reines and Cowan had already demonstrated the difficulties involved in performing a sensitive neutrino experiment but that did not deter people from initiating further research in the field. It is worth mentioning that Reines did not just stop with the discovery of the neutrino. He went on to personally conduct and also inspire others in designing and implementing various experiments to meticulously study the properties of the neutrino. Reines was one of the pioneers of the field of neutrino astronomy and he has definitely left his mark on experimental solar neutrino physics. Following his lead, people have embarked on sophisticated theoretical and experimental studies of the properties of neutrinos. However, as we have seen earlier, the Standard Model doesn't provide a complete description of the neutrino. An anomalous observation of a less than predicted solar neutrino flux, as measured by the first solar neutrino experiment more than 30 years ago,

---

[2] The message was sent to Reines and Cowan in 1956, but they didn't receive it at that time. Later in 1986 C.P. Enz, a student of Pauli's, sent it to Reines.

raised serious concern about the validity of the Standard Model assumption that neutrinos are massless particles. Many experiments since then have addressed the problem but the mystery still remains unresolved.

1.2.4 Conclusion

The purpose of the last three sections was to point out some of the key events that have led to the discovery of the neutrino with the goal of showing that they are very good examples of the necessary scientific processes that define and direct fundamental research. The realization of a crisis, the espousal of a revised or a completely new theory to explain the anomalous phenomena, the subsequent experiments to ratify this proposed theory, and all the hard work and careful attention to detail that goes into making sure that the experiment is sensitive to the sought after signal by reducing the background internal and external to the experiment, are the crucial stepping stones of a successful scientific endeavor. The reason I am belaboring this point is to make clear what I have learned during my tenure as a scientist working on the Sudbury Neutrino Observatory. In order to be a contributing member of the experiment, it was necessary for me to have a clear understanding of the motivation behind the experiment and to develop a deep appreciation for the hard work and dedication that is required to ensure that the experiment will yield satisfactory if not ground-breaking results. We have seen how a study of the history of the discovery of the neutrino illustrates the salient features of a successful experiment. I have used this as a guide to provide the outline of this dissertation, and hopefully that will become clear as I progress through the coming chapters. In the following chapter, description of the solar neutrino problem and the motivation behind past and present solar neutrino experiments will be presented.

Chapter 2

The Solar Neutrino Problem

2.1 Introduction

The sun is not only the primary source of energy responsible for the sustenance of life on this planet, but also the best source from which one can learn, with great precision, about the dynamics of stellar function and evolution. Most of the radiant energy of the sun, and hence stars, is derived from nuclear reactions. In addition to γ-rays or photons, the reactions in the sun produce a large number of neutrinos. Most of the reactions take place deep within the sun and the γ-rays lose almost all of the information about the solar interior as they traverse the sun. It takes about $1 \sim 2\text{x}10^4$ years for the photons generated in the core of the sun to reach the solar surface. As a result one cannot directly investigate the properties of the solar core by performing terrestrial optical measurements of the sun. Unlike photons, neutrinos have a very small interaction cross section (typically $10^{-48} m^2$) and most emerge from the solar core unscathed by collision (neutrinos escape from the sun in about 2 seconds). The resulting neutrino flux and energy spectrum can therefore provide an accurate and robust description of the conditions of the solar interior. It is evident that a detailed study of solar neutrinos provides a unique probe of the sun's innermost regions and of the nuclear reactions that fuel them. It was for this primary reason that the field of neutrino astronomy was launched. In order to understand the sun with respect to neutrinos, detailed theoretical and experimental studies had to be performed to provide precise predictions about the solar neutrino flux and energy spectrum. The result of all these studies is the successful implementation of a detailed theory of the sun known as the Standard Solar Model (SSM). Based on this model one can predict, among other things, the total number of solar neutrinos that should be detected by a terrestrial solar neutrino experiment. To date, six different experiments have made such measurements and all of them observe an appreciable reduction of the solar neutrino flux with respect to theoretical predictions. This discrepancy or anomaly is generally referred to as the Solar Neutrino Problem (SNP). Similar to the case of the anomalous observation regarding nuclear beta decay which challenged the prevailing views of elementary particles, the solar neutrino anomaly, due to the precision of the experimental measurements, has been able to challenge existing views of the sun and neutrino properties. In the next section, I will present a description of the Standard Solar Model and show why people strongly believe that the model of the sun is fairly accurate and therefore a solution to the solar neutrino problem will most probably require the invocation of new physics.

2.2 The Standard Solar Model

2.2.1 Introduction

“How does the sun shine?” This question about the source and mechanism of solar energy had puzzled people for quite some time. It was hypothesized that gravitational and chemical energy was responsible for ensuring the continuous generation of solar energy. Based on this assumption, the time scale that the gravitational energy can provide the necessary mechanism for solar power is $\sim GM_\odot/R_\odot L_\odot$

$\sim 10^7$ years. Here, G, $M_\odot$, $R_\odot$ and $L_\odot$ are the gravitational constant, the solar mass, the solar radius and solar luminosity respectively. Chemical energy can provide the energy for an even shorter period of time, roughly 10^4 years. However, terrestrial evidence suggested that the age of the sun was much greater than that allowed by gravitational and chemical energy. This evidence was supported by the finding that the oldest rocks were molded about 3.8x10^9 years ago, and that meteoritic ages are of order 4.5x10^9 years. Therefore it wasn't possible for gravitational and chemical energy to fuel the solar furnace. The discovery of radiation and the development of quantum mechanics finally demonstrated that nuclear fusion is the only mechanism that could keep the sun shining for such a long time.

The *standard solar model* (SSM), in its current form, is the result of more than seventy-five years of detailed and rigorous scientific investigations of the sun. The process began in earnest with Sir Arthur Eddington who, in the 1920s, first proposed nuclear reactions to be the primary energy source of the sun. Then in the late 1930s Gamow, Weizsäcker, Bethe, Critchfield [23][24] and others developed the proton-proton (pp) and carbon-nitrogen-oxygen (CNO) thermonuclear fusion reaction cycles that power the sun and produce not only heat and light, but also vast numbers of neutrinos. Any theory in the physical sciences has to be validated by rigorous experiments which test the predictive power of the proposed theory or model. However testing the details of the solar models is difficult since the solar luminosity and emission spectrum depend mainly on solar mass, radiation optics, and solar surface physics. Due to turbulent convective motions and differential rotations, the outer layers of the sun are quite complex, however, a simple equation of state in quasi-static equilibrium can be used to accurately predict the dynamics of the solar inner core. We have seen that optical measurements cannot probe the solar interior. Therefore, an investigation of the inner core requires probing techniques such as helioseismology and detection of solar neutrinos. With these methods one has a way to test the standard solar model and figure out to what degree of accuracy the model determines the inner workings of the sun. Furthermore, different methods of testing techniques also provide valuable cross-checks which are necessary to build confidence in the model.

In the following two sections the background needed for developing the standard solar model will be presented. In particular, the various approximations and input parameters that are utilized in the model will be discussed and then an outline for the calculational procedure that the model employs to predict the various solar neutrino fluxes will be presented. The principle uncertainties in the predictions will also be discussed.

2.2.2 Definition, Approximations and Input Parameters

Definition

The SSM has been developed to perform detailed numerical simulations of the sun in which the only constraint is that the observable properties of the sun be reproduced by the model. The model uses "standard model" physics, the best nuclear cross sections, measured solar observables, and a set of realistic initial conditions which is used to iterate the equation of state from an initial primordial composition to the present age. The set of numbers describing the input parameters that have been used to generate the solar models have varied with time and as a result the solar neutrino flux predictions of these models have also fluctuated with time. There are several recent SSMs that have been developed by a number of authors, Turck Chièz and Lopez (1993) [25], Castellani et al.(1994) [26], Kovetz and Shaviv (1994) [27], Christensen-Dalsgaard (1994) [28], and Shi et al. (1994) [29]. In this work, I have opted to use the BP98 standard solar model, developed by Bahcall and Pinsonneault [3], as a theoretical reference for the calculated neutrino flux and energy spectrum. It has been shown that when the different solar models use the same input parameters, the solar neutrino fluxes calculated by these models are consistent to within $\sim 2\%$ [1].

Approximations

In order to construct the solar models one has to make certain approximations or assumptions. The primary equations that describe the sun are based on these assumptions and when these equations are solved numerically one can determine the evolution and inner structure of the sun. The principal approximations that are utilized in the models are given below:

- The sun is assumed to be a spherically symmetric entity with no significant rotation. Pulsation and pressure due to magnetic fields is assumed to be negligible. There is also no mass loss or accretion during the lifetime of the sun.

- The primary energy source of the radiated photons and neutrinos is nuclear fusion which includes the *pp* and *CNO* cycle reactions. However, small effects of contraction and expansion are included in the model.

- It is assumed that the primordial solar interior is chemically homogeneous and that the chemical composition of the sun is modified only by nuclear reactions. There have been recent modifications to solar models in which diffusion of heavy elements was also included. These modifications are included in the BP98 model. However, it has been found that the changes to the calculated neutrino flux due to these modifications is minimal.

- The sun is assumed to be in hydrostatic equilibrium, i.e. the radiative and thermal pressures are exactly balanced by gravity [1]:

$$\frac{\partial P(r)}{\partial r} = -\frac{GM(r)\rho(r)}{r^2} \tag{2.1}$$

where, P(r) and $\rho(r)$ are the pressure and density at solar radius r respectively, and M(r) is the solar mass within this radius. This is regarded as an excellent approximation since a slight departure from it would cause the sun to contract or expand in less than an hour.

- The energy transport within the sun is accomplished by electromagnetic radiation or by convection and the rates of these processes determine the temperature gradient at a given radius. The equation governing the energy transport mechanism below the convective zone is[1]:

$$L_r = -4\pi r^2 \frac{ac}{3}\frac{1}{\kappa\rho}\frac{\partial T^4}{\partial r} \tag{2.2}$$

where, L_r is the energy through a sphere of radius r per unit time and temperature T. The total opacity κ is the combination of the radiative and conductive opacities: $\kappa^{-1} = \kappa^{-1}{}_{rad} + \kappa^{-1}{}_{cond.}$. The radiative opacity is dominant in the solar interior. The Stefan-Boltzmann constant a is given by: $\frac{8\pi^5 k^4}{15c^3h^3}$ [1]. Additional transport due to acoustic or gravity waves is assumed to be negligible.

Input Parameters

The essential input parameters used in the numerical calculation phase of the standard solar model are: nuclear parameters, solar luminosity, solar age, equation of state, elemental abundance, and radiative opacity.

- **Chemical Abundance.** The solar neutrino flux is strongly correlated with the effective temperature-density profile of the sun. This in turn is affected by the solar radiative opacity which depends on the chemical abundance of the elements in the sun. It is therefore essential for solar models to have as input an accurate description of the elemental abundance. One of the crucial input parameters in the solar model is the initial ratio by mass of isotopes heavier than helium relative to hydrogen, $\frac{Z}{X}$, which is taken to be 0.0245 in BP98. The typical systematic uncertainty of $\frac{Z}{X}$ is about 6.1%(1 σ) [1].

- **Radiative Opacity.** The solar neutrino flux is strongly dependent on the solar radiative opacity. As a result the adopted opacity in the solar model represents an important source of uncertainty for solar neutrino flux calculations. The calculated radiative opacity depends on the chemical composition and the modeling of complex atomic processes in the sun. Two different opacity codes (Los Alamos and Livermore) have been used for solar neutrino flux comparison and it has been found that the results agree to better than 16% for all sources of solar neutrinos.

- **Solar Luminosity and Age.** These measured values are determined by careful experiments. Measurements of the solar luminosity agree with each other at the one percent level [1]. The solar age is derived from the accurately determined age of the meteorites. The time interval between the formation of the meteorites and the formation of the sun, although uncertain, is expected to be small on the time scale of interest. As long as the true solar age is in the currently estimated range, a precise value for the solar age is unimportant for solar neutrino calculations.

Parameter	Value
Age	(4.52 ± 0.04) x 10^9 yr
Mass ($M_\odot$)	(1.9891 ± 0.0004) x 10^{33} g
Radius ($R_\odot$)	(6.9599 ± 0.0002) x 10^{10} cm
Oblateness	$\leq$ 2 x 10^{-5}
Luminosity ($L_\odot$)	(3.846 ± 0.004) x 10^{33} ergs s^-1

Table 2.1: Observed Solar Parameters [1]

- **Equation of State.** The equation of state of the sun describes the relation between pressure and density. Therefore it must include the effects of radiation pressure and electron degeneracy and screening interactions. These effects can be simply incorporated into the stellar interior model without undue complications. The uncertainties that are ignored do not significantly affect the computed solar structure or the neutrino fluxes. In fact, the neutrino fluxes calculated by various authors using different equations of state exhibit a difference less than 1.5% [1].

2.2.3 SSM Calculation, Neutrino Flux & Uncertainties

SSM Calculation

A successful standard solar model is the end product of a sequence of calculations which are based on the approximations and input parameters that have been described in the above sections. The starting point of the model is a main sequence star with a homogeneous composition which burns hydrogen deep in its interior and provides the radiated luminosity and thermal pressure to support the star against gravitational contraction. The solar model calculation begins by guessing an initial set of parameters. Equations for hydrostatic equilibrium and an equation for an ideal gas under thermal and radiative pressure, in addition to expressions for radiative opacity and nuclear fusion energy, form a set of simultaneous differential equations. The calculation then proceeds by iterating the solutions of these equations in discrete time steps until the present day age of the sun is achieved. At the end of a single iteration the predicted characteristics of the present day sun are compared to the observed solar parameters listed in Table 2.1. This whole procedure is iterated , by adjusting any or all of the starting input parameters, until a satisfactory convergence to the present day observed solar parameters is achieved. The model also determines other solar characteristics, such as the surface temperature and pressure mode oscillation speeds, which are then compared to measured values. These independent cross-checks are valuable for building confidence in the solar model. Upon completion the model also generates a set of predicted values for other solar parameters, in particular it provides predictions for the solar neutrino flux.

Neutrino Flux, Spectrum & Uncertainties

The origin of the energy and neutrinos in main sequence stars like the sun is given by the following nuclear reaction:

$$4p \rightarrow {}^4He + 2e^+ + 2\nu_e + 26.73MeV \tag{2.3}$$

Therefore, the radiant energy and the neutrinos come from fusing four protons into a helium (${}^4He$) nucleus. However, the actual process takes place in several distinct steps, as direct conversion of four protons into ${}^4He$, a four-body reaction, is extremely unlikely. There are eight principal nuclear reactions or decays that produce solar neutrinos; six of the eight nuclear sources produce neutrinos with continuous energy spectra and the other two (pep and ${}^7Be$) produce neutrino lines as shown in Figure 2.1 [3]. These set of reactions are called the proton-proton

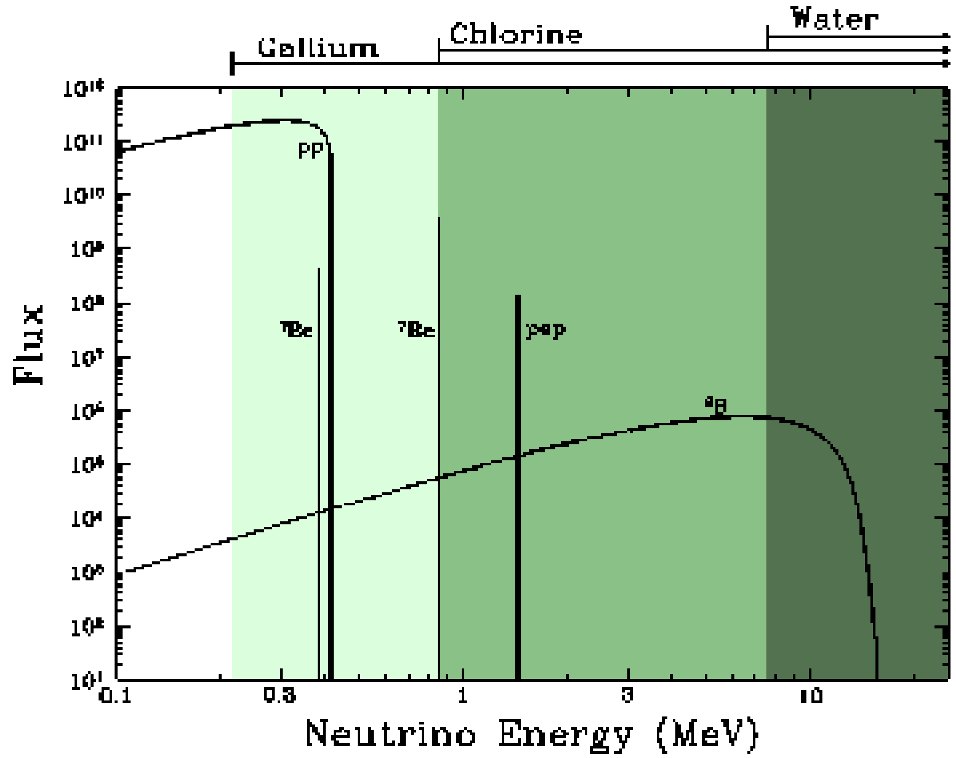

Figure 2.1: Energy spectrum of solar neutrinos [BP98].

or *pp* chain and this is shown in Figure 2.2. The neutrinos from each reaction in this chain are called *pp*, *pep*, ^7Be, ^8B and *hep* neutrinos respectively. The neutrinos from the *pp* reaction initiate the chain and supply nearly all of the solar luminosity. However, the *pp* neutrinos have low energies and, as a result, are much harder to detect in solar neutrino experiments. Although not as abundant as the *pp* neutrinos, the easiest neutrinos to detect are the relatively high energy neutrinos from the *hep* and ^8B reactions. As will be discussed later, given the operational threshold, the Sudbury Neutrino Observatory (SNO) is sensitive only to these types of high energy neutrinos. The end-point energies for the *pp*, ^8B, and *hep* reactions are given in Table 2.2. One of the features of the hydrogen burning phase is that it depends on the most feeble of nuclear processes, namely the weak interaction. The first step in the chain is a reaction similar to β-decay.

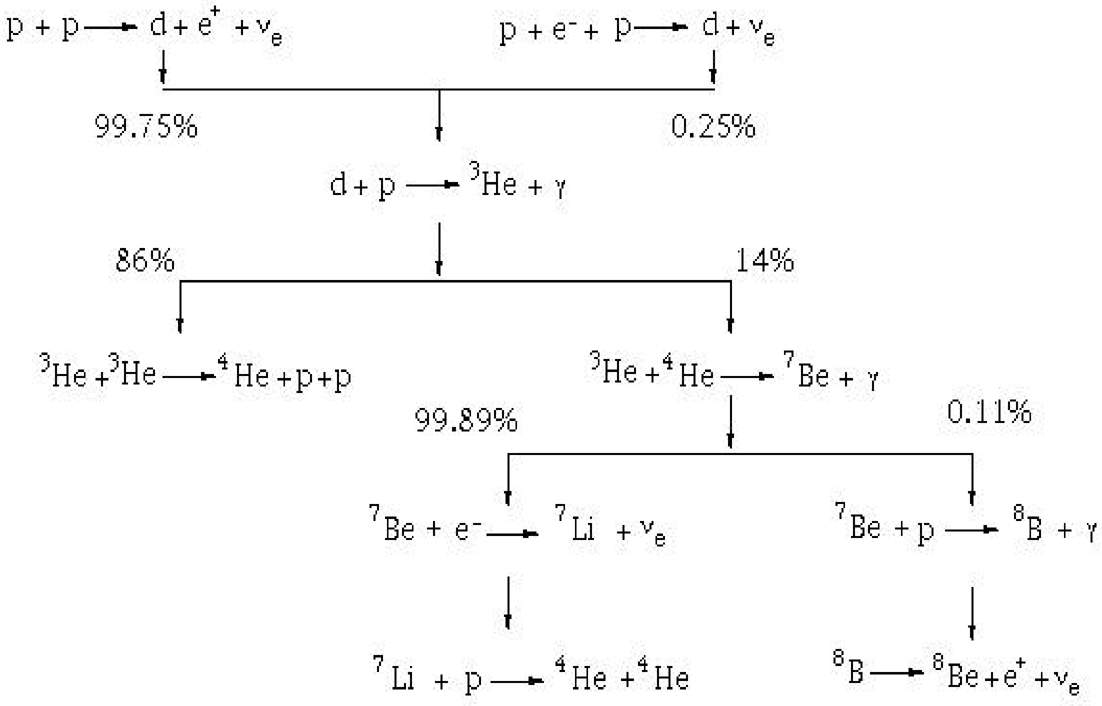

Figure 2.2: The *pp*-chain Solar Fusion Cycle [1].

Label	Reaction	$E_{max}(\nu_e)$ MeV
pp	p + p $\rightarrow$ d + $e^+ + \nu_e$	0.420
^8B	$^8B \rightarrow {}^8Be^* + e^+ + \nu_e$	14.9
hep	p + $^3He \rightarrow {}^4He + e^+ + \nu_e$	18.773

Table 2.2: End-point Energy (MeV) of neutrinos in *pp*-chain [1].

A proton transforms into a neutron, which is close to another proton, and the resulting neutron and proton bind together to form a deuteron. In the process an electron neutrino with an average energy of 0.26 MeV is also produced. But, in order to form a deuteron, the initial two protons need to come close together.To achieve this the two protons must overcome the inherent Coulomb barrier. This happens only through the quantum process known as "*tunneling*", since the thermal energies of the protons in the solar interior aren't sufficient to overcome the electrical repulsion.

All solar models predict the *pp* chain to be the dominant mode in which 98% of the solar energy is produced. The *CNO*-cycle, first studied by H. A. Bethe in the 1930s [30], produces the remaining energy and is given by the following set of six reactions:

$$\boxed{\begin{array}{ccccccccc}
{}^{12}C & + & p & \rightarrow & {}^{13}N & + & \gamma & & \\
 & & {}^{13}N & \rightarrow & {}^{13}C & + & e^{+} & + & \nu_e \\
{}^{13}C & + & p & \rightarrow & {}^{14}N & + & \gamma & & \\
{}^{14}N & + & p & \rightarrow & {}^{15}O & + & \gamma & & \\
 & & {}^{15}O & \rightarrow & {}^{15}N & + & e^{+} & + & \nu_e \\
{}^{15}N & + & p & \rightarrow & {}^{12}C & + & {}^{4}He & &
\end{array}}$$

As can be seen, the final result again consists of four protons being converted into ${}^{4}He$ together with two positrons and two electron neutrinos, the same final result that is achieved via the *pp*-chain. In this case, however, ${}^{12}C$ is used as the catalyst.

In the solar models, the rate of these nuclear reactions determine the neutrino fluxes. The results, as calculated by the BP98 SSM, are given in Table 2.3 [3]. From this table it can be seen that the uncertainty in the *pp* neutrino

Source	Flux (10^{10} $cm^{-2}s^{-1}$)
pp	$5.94(1.00^{+0.01}_{-0.01})$
pep	1.39 x $10^{-2}(1.00^{+0.01}_{-0.01})$
hep	2.10 x 10^{-7}
^{7}Be	4.80 x $10^{-1}(1.00^{+0.09}_{-0.09})$
^{8}B	5.15 x $10^{-4}(1.00^{+0.19}_{-0.14})$
^{13}N	6.05 x $10^{-2}(1.00^{+0.19}_{-0.13})$
^{15}O	5.32 x $10^{-2}(1.00^{+0.22}_{-0.15})$
^{17}F	6.33 x $10^{-4}(1.00^{+0.12}_{-0.11})$

Table 2.3: The BP98 Solar Neutrino Fluxes (1σ uncertainties).

Source of Uncertainty	Fractional Uncertainty
pp cross section	0.040
^{3}He-^{3}He cross section	0.021
^{3}He-^{4}He cross section	0.075
^{7}Be + p cross section	0.105
Primordial Z/X	0.042
Opacity	0.052
Luminosity	0.028
Solar Age	0.006
Diffusion	0.040

Table 2.4: Contributions to fractional uncertainty in ^{8}B ν flux (BP98).

flux is very small (±1%) due to the stringent luminosity constraint (as mentioned earlier the *pp* reaction provides almost all of the solar luminosity, which is determined very accurately). The largest uncertainty in the *pp*-chain is associated with the ^{8}B neutrinos ($^{+0.19}_{-0.14}\%$). The main sources of the uncertainty in the ^{8}B neutrino flux comes from the uncertainties in the following parameters: $^{7}Be(\mathrm{p},\gamma)^{8}B$ cross section (10.5%), ^{3}He-^{4}He cross section (7.5%), opacity (5.2%), the ratio of heavy element abundance relative to hydrogen (Z/X) (4.2%), and element diffusion (4.0%) [3]. A list of these uncertainties for the BP98 solar model is provided in Table 2.4. The dependence of the ^{8}B neutrino flux ($\phi(^{8}B)$) on two of these parameters is expressed as follows:

$$\phi(^{8}B) \propto S_{17}^{1.0}(Z/X)^{-0.08} \tag{2.4}$$

where, S_{17} is the cross section for the $^{7}Be(\mathrm{p},\gamma)^{8}B$ reaction. The ^{8}B neutrino flux is directly proportional to S_{17}. Therefore, a precise measurement of this cross section is crucial in order to reduce the uncertainty in the prediction of the neutrino flux. If the 1σ uncertainty in the cross section can be reduced by a factor of two to 5%, then it will no longer remain the limiting uncertainty in predicting the ^{8}B neutrino flux. However it is almost impossible to measure the ^{7}Be+p cross section at the temperature of the solar core (10^{7} K), since at these low energies (10^{7} K $\sim$ 1 keV) the reaction event rate is too low. Currently the only reasonable way to derive this cross section is to measure it at energies around $\sim$ 100 keV and then extrapolate down to the solar temperature. Recently a workshop [31] devoted to determining the best estimates and the uncertainties of this and other solar nuclear reaction cross sections recommended adoption of the measured value of the ^{7}Be+p cross section by Fillipone et al. [32]. The BP98 model uses this value of the cross section to calculate the ^{8}B neutrino flux.

A solution to the solar neutrino problem can be achieved by a precise measurement of the ^{8}B neutrino energy spectrum. The ^{8}B neutrinos are generated in the β-decay reaction given in Figure 2.3. The dominant decay mode for ^{8}B is to

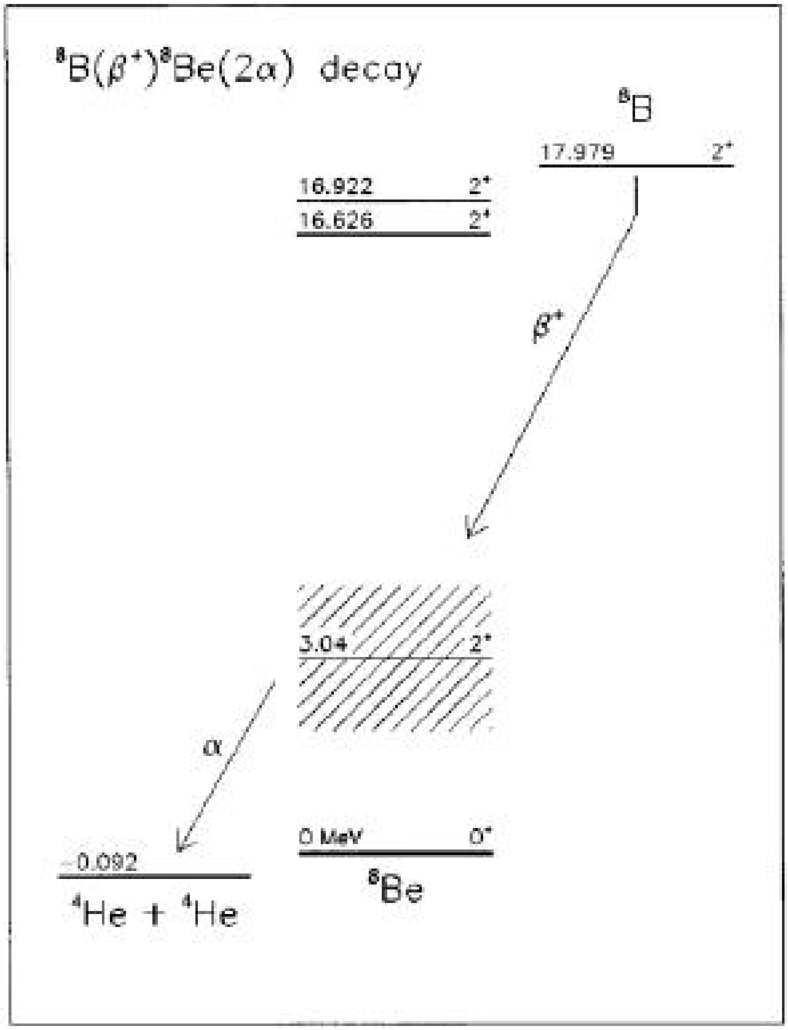

Figure 2.3: Energy levels in the ^8B decay chain [2].

go to the 2^+ first excited state at 3.040 MeV, which then decays to two alpha particles. Since this is a broad state with a width of 1.50 MeV, it affects the β-decay spectrum. There have been several measurements of the energy spectrum of these decay alpha particles and a review of the data is given in [2]. The authors in that study have calculated the ^8B neutrino energy spectrum, $\lambda(E_\nu)$, and have assigned an uncertainty in the shape caused by uncertainties in the alpha spectrum. The result is shown in Figure 2.4 with additional curves, λ^+ and λ^-, at $\pm 3\sigma$ error. In this work the ^8B neutrino energy spectrum as calculated in Ref.[2] has been used.

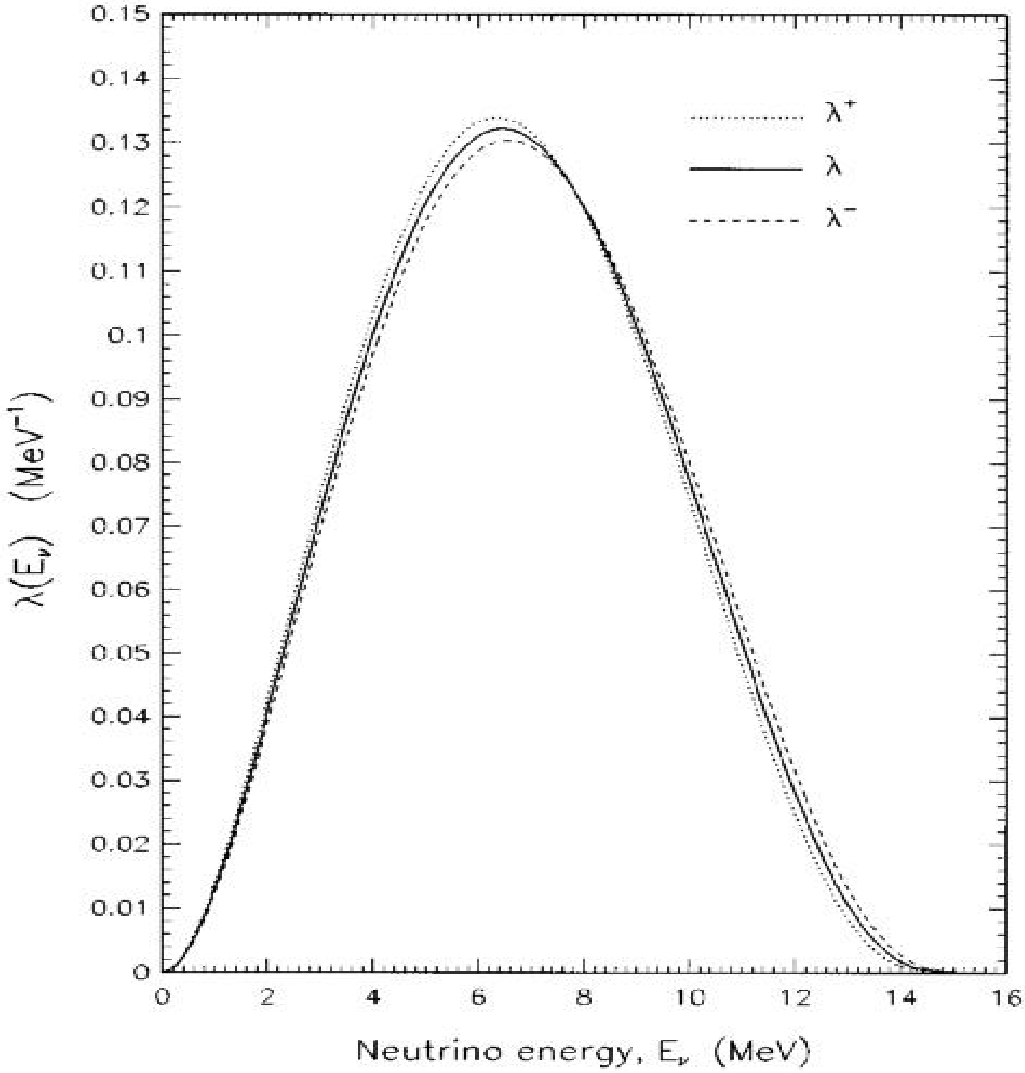

Figure 2.4: The ${}^{8}B$ neutrino spectrum [2].

The SSM predicted value of the *hep* neutrino flux is currently a controversial number. The Sudbury Neutrino Observatory is sensitive to the *hep* neutrinos in addition to the ${}^{8}B$ neutrinos. These neutrinos have a much higher end-point energy (Table 2.2), however, the flux is reduced by three orders of magnitude with respect to the ${}^{8}B$ neutrino flux. Recently, the SuperKamiokande solar neutrino experiment has measured an excess number of counts in the high energy region of the neutrino spectrum. This has raised considerable doubts about the SSM prediction of the *hep* neutrino flux. It is possible that the SSM has underestimated this flux by a large factor, as recent results from SuperKamiokande suggest a value almost as large as 5 to be the enhancement factor (4.3 times the BP2000 prediction[33]). The uncertainty in the SSM *hep* neutrino flux arises from a large uncertainty in the cross section of the underlying nuclear reaction. Since *hep* neutrinos are on a small branch of the *pp*-chain, the rate of the reaction can be elevated by a large factor without affecting the rates of the other reactions. SNO should be able to make important contributions to settling the issue of the *hep* neutrino flux.

Given that there are all these uncertainties associated with the various solar neutrino fluxes, it is important to point out that these uncertainties do not affect the resulting neutrino energy spectra. Since the shapes are solely determined by nuclear physics (doppler broadening of the neutrino energies is negligible at solar energies), they are a key ingredient in solving the solar neutrino problem. Changes to the astrophysical parameters are unlikely to bring about any appreciable change in the neutrino energy spectrum, so a spectrum distortion would be an indication of new physics beyond the standard model.

2.2.4 Helioseismology : Validating the SSM

Over the last thirty years the *standard solar model* has been continuously refined and improved in order to provide an accurate description of the sun. The solution to the solar neutrino problem is dependent on accurate predictions provided by this model. Could the solar model calculations be wrong by an amount that would explain the discrepancies between predictions and measurements of the solar neutrino flux? Most probably not, since recent results from helioseismology very strongly indicate that the solar model predictions are indeed very accurate.

Helioseismology provides information about the interior composition of the sun by analyzing pressure oscillations on the solar surface. The sun is an oscillating star and its motion can be determined by Doppler shifts in spectral lines that are

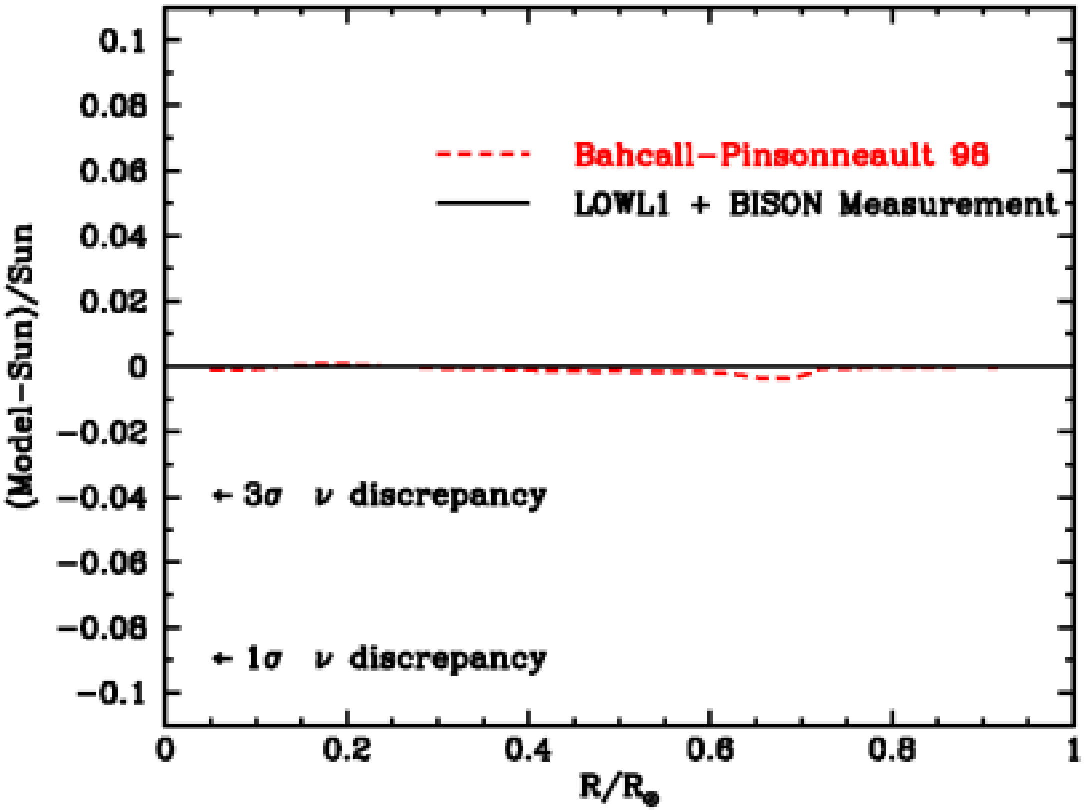

Figure 2.5: Solar sound speed measurements [3].

formed in the solar atmosphere. These oscillations can be divided into two classes: sound waves or p-modes and gravity waves or g-modes. Recent helioseismological measurements are based on the p-modes since the g-modes are much more difficult to measure. These measurements of the sound waves in the sun provide information about the sound speed as a function of solar radius which can then be compared to the predictions of the solar model. There have been a number of precise helioseismological measurements in the past few years and all of them are in very good agreement with the predictions. The fractional differences between the most accurate sound speed measurements and sound speeds calculated with the BP98 model is shown in Figure 2.5 [3]. The RMS fractional difference between the calculated and the measured sound speeds is 1.1×10^{-3} for the entire region over which the sound speeds were measured, $0.05R_{\odot} < R_{\odot} < 0.95\mathrm{R}\odot$ (where, $R_{\odot}$ is the solar radius). In addition, helioseismology determines two other solar parameters: the depth of the solar convective zone and the present day surface abundance by mass of helium. The measured values of these parameters are also in good agreement with the BP98 model. Therefore, these independent tests, which are in good agreement with the predictions of the solar model, provide confidence in the solar model prediction of the neutrino fluxes.

In addition to the excellent agreement between the helioseismological measurements and the predictions of the BP98 model of the solar sound speeds it is important to mention that over the last few decades a fair number of solar models have been constructed by various authors and almost all of these models are in good agreement with each other with regards to the solar neutrino flux predictions. In Ref.[4] it is shown that all of the 19 standard solar model calculations published between the years 1988 and 1998 predict values for neutrino fluxes that are consistent with each other. Figure 2.6 plots the predictions of 19 solar models in the plane defined by the ^{7}Be and ^{8}B neutrino fluxes. The abbreviations that are used in this figure can be found in the bibliography of Ref.[4]. The fluxes have been normalized to the predictions of the BP98 solar model. The rectangular error

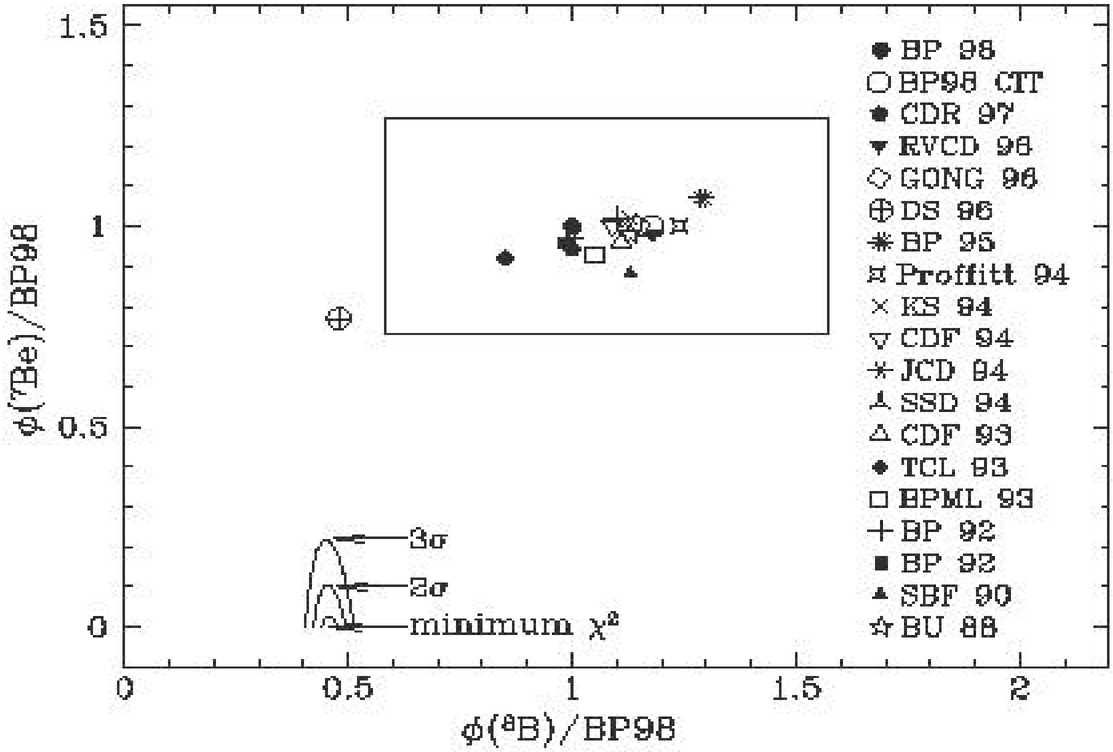

Figure 2.6: Standard solar model predictions [4].

box defines the 3σ error range of the BP98 fluxes. As can be seen from the figure, all of the solar model results from the different groups fall within this rectangular box. The only exception is the Dar-Shaviv model whose results have not been reproduced by other groups. The good agreement between the predictions of the different models underscores the robustness and reliability of the predictions since the calculations employed by the models use different computer codes and involve a variety of choices for the nuclear parameters, the equation of state, the initial heavy element abundance, and the stellar radiative opacity.

2.2.5 Conclusion

The goal of the last four sections was to present a concise but cogent description of the *standard solar model*. The material presented provides the background needed for understanding the solar neutrino problem and it helps elucidate the motivation behind performing solar neutrino experiments. It has also been shown that the *standard solar model* stands on firm ground as a valid model of the sun and therefore an astrophysical solution to the solar neutrino problem is unlikely (this topic will be discussed in latter sections). In the following sections descriptions of past solar neutrino experiments that were responsible for identifying the solar neutrino problem will be presented, and it will be shown how they attempted to help resolve it. With an understanding of past experiments, the driving force behind the Sudbury Neutrino Observatory will become evident.

2.3 Solar Neutrino Experiments

2.3.1 Introduction

Armed with a viable mechanism for solar energy production and with a knowledge of the measured solar luminosity, one could use a simple back of the envelope calculation to show that each second roughly 7x10^{28} neutrinos should pass through the surface of the earth. This is equivalent to a neutrino flux of $\sim$ 6x10^{10} cm^{-2} s^{-1} or 25 watts per m^2. Therefore it is clearly apparent that the sun could be used as an immense source of neutrinos and that a measurement of these neutrinos would demonstrate, among other things, the validity of the solar energy production mechanism. Furthermore, since neutrinos interact with other particles solely via the weak process, a study of the solar neutrinos would also be a probe of the weak interaction process of the standard model. Following some ideas of B. Pontecorvo(1946) and L. W. Alvarez(1949), Raymond Davis Jr. developed a radiochemical technique to detect neutrinos from the sun and in 1955 he published his first findings about solar neutrinos[34]. Although he wasn't able to directly observe solar neutrinos at that time he was nevertheless able to place an upper limit (10^{14} cm^{-2} s^{-1}) on the number of detectable solar neutrinos in his experiment. Since then there have been six solar neutrino experiments that have made measurements of the solar neutrino flux : four radiochemical experiments (Homestake, GALLEX, SAGE, and GNO) and two water $\check{C}$erenkov experiments (Kamiokande, SuperKamiokande). In what follows, an overview of these experiments with the goal of providing the historical background and motivation for the Sudbury Neutrino Observatory will be presented.

2.3.2 The Chlorine Experiment

In the 1960s Raymond Davis Jr. persisted with the idea of building a solar neutrino detector and finally in 1967, after many ups and downs, he began an experiment capable of detecting solar neutrinos almost continuously. The ^{37}Cl detector built by Davis and his collaborators at the 4850 ft level of the Homestake Gold mine near Lead, South Dakota, was the first experiment that had the requisite sensitivity to detect solar neutrinos [35]. Until 1988, this was the only experiment to claim that it had detected solar neutrinos. However, its results regarding the solar neutrino flux were responsible for starting the controversy known as the *solar neutrino problem* (SNP). The experiment measured a solar neutrino flux that was appreciably less than that predicted by the SSM.

The ^{37}Cl detector is a 6m diameter, 380000-liter tank containing 615 tons of perchloroethylene (C_2Cl_4). The detector was built deep underground, a feature common to all solar neutrino experiments, in order to reduce the background due to cosmic ray muons whose cascade products eventually produce ^{37}Ar via a (p,n) reaction on ^{37}Cl. The reaction employed in this experiment:

$$\nu_e + {}^{37}Cl \rightarrow e^- + {}^{37}Ar \tag{2.5}$$

proceeds via an absorption of a neutrino by a chlorine-37 atom and through this inverse β-decay reaction an electron and an argon-37 atom is produced. Due to the 814 KeV threshold, this reaction is sensitive mainly to the ^{8}B and ^{7}Be solar neutrinos. The ^{37}Ar atom is radioactive with a half-life of 35 days and it converts back to a ^{37}Cl atom by capturing an atomic shell electron. The signature of this reaction is the emission of an Auger electron which can be detected in low background proportional gas counters. In the experiment, every 1 to 3 months the ^{37}Ar atoms are flushed from the volume of the detector by helium bubblers and then counted by detecting the Auger electrons.

The ^{37}Cl detector has been in nearly continuous operation for 26 years with a break in 1985 due to failures in two of the gas pumps. The data for 108 runs from 1970 to 1995 is shown in Table 2.5 and the flux has an overall average of [36, 37, 38]:

$$\langle \phi_{\nu_e} \sigma \rangle_{Cl} = 2.56 \pm 0.16 (stat) \pm 0.14 (sys) \ SNU \tag{2.6}$$

where, $\langle \phi_{\nu_e} \sigma \rangle_{exp.}$ stands for the average experimental capture rate (flux times reaction cross section) and SNU (solar neutrino unit) is one capture per 10^{36} atoms per second. The BP98 solar model prediction of the total neutrino flux for

Neutrino Source	Cl (SNU)	Ga (SNU)
pp	0.00	69.6
pep	0.20	2.8
hep	0.00	0.0
^{7}Be	1.15	34.4
^{8}B	5.90	12.4
^{13}N	0.10	3.7
^{15}O	0.40	6.0
^{17}F	0.00	0.1
Total	$7.7^{+1.2}_{-1.0}$	129^{+8}_{-6}

Table 2.5: BP98 Solar Neutrino Capture Rates for Chlorine and Gallium Detectors

this experiment is:

$$\langle \phi_{\nu_e} \sigma \rangle_{theory} = 7.7 \pm 1.2 \ SNU \tag{2.7}$$

The BP98 predicted capture rates for the different neutrino flux components are given in Table 2.5. As can be seen, the experimental value of the total neutrino flux is much lower than the predicted value and doesn't overlap with the prediction even if the uncertainties are taken to their extreme values. For almost twenty years it was the only experiment to have made the claim that either we don't understand the sun properly, i.e. the solar model might be wrong, or that we don't yet understand the properties of the neutrino, since something might be happening to them on their way to earth so as to account for the discrepancy. However, in 1989 a second neutrino experiment, Kamiokande II [7], not only gave support to the ^{37}Cl results but also demonstrated definitively that the detected neutrinos come from the sun and that nuclear fusion is indeed the source of solar energy.

2.3.3 The Kamiokande Experiments

The Kamiokande water Čerenkov detector was initially constructed to search for the possible decay of the proton, and hence the name Kamiokande, which stands for Kamioka *nucleon decay experiment*. In 1984, the collaboration decided to modify and improve the detector to make it sensitive to solar neutrinos and with this enhancement the detector was called Kamiokande II. The upgrade included improvements to the electronics, enhancement of the water purification system in order to remove uranium and radium elements and the addition of an inert cover gas system.

The Kamiokande II detector was situated 1,000m (2,700m water equivalent) under the Japanese Alps in the Mitsui Mining and Smelting Company zinc mine near Kamioka, 300 kilometers west of Tokyo. It consisted of a cylindrical tank containing 2,140 tons of water, viewed by 948 20-inch photomultiplier tubes (PMTs) which provided approximately 20% coverage of the entire inner surface of the tank. The detector was situated underground, like all solar neutrino experiments, in order to shield itself from cosmic ray muons. Furthermore, only the inner 680 tons of water were used as the fiducial volume for solar neutrino detection while the surrounding water, or anticounter, provided shielding against cosmic muons and against gammas and neutrons from the surrounding environment. This 4π solid angle anticounter was also a water Čerenkov detector which had a mean thickness of 1.5 meters and was viewed by an additional 123 photomultipliers. Some of the important characteristics of the detector [7] are given in Table 2.6.

The reaction employed in the detector is the elastic-scattering interaction be-

Location	Kamioka, Japan
Depth	1 km (2700 MWE)
Fiducial Volume	680 tons
Trigger Efficiency	50% at 5.2 MeV 90% at 7.5 MeV
Energy Resolution	$19/(T_e/10 \text{ MeV})\%$
Vertex Resolution	1.5m at 10 MeV
Angular Resolution	28° at 10 MeV

Table 2.6: Important Characteristics of the Kamiokande II Detector [7]

tween the incoming neutrino and the target electrons in the water:

$$\nu_x + e^- \rightarrow \nu_x + e^- \ \ (x = e, \mu, \tau) \tag{2.8}$$

The scattered electron emits Čerenkov photons and these are detected by the photomultiplier tubes that surround the fiducial volume. The main advantage of using a water Čerenkov detector is that it provides real time energy and directional information about the incoming neutrinos. The angular distribution of the scattered electrons is forward peaked with respect to the sun and is in the same direction as the neutrinos. In fact, it was this measurement which showed that the detected neutrinos had their origin within the sun. Furthermore, an accurate measurement of the energy distribution of the scattered electrons can be used to determine the energy spectrum of the solar neutrinos. As will be shown later, one can use this information to distinguish between competing solutions to the solar neutrino problem.

One of the main disadvantages of a water Čerenkov detector is that, unlike radiochemical detectors, any charged particle with velocities greater than the speed of light in water is able to generate Čerenkov radiation. For example, energetic electrons can arise from the β-decay of radioactive nuclei and form the interactions of γ-rays and neutrons due to radioactive materials. Therefore, the operating threshold in water Čerenkov detectors has to be set fairly high in order to eliminate false signals from these types of radioactive backgrounds. The threshold for the Kamiokande II experiment was initially set at 9.3 MeV and then it was later reduced to 7.5 MeV. Therefore, the detector was only sensitive to the ^{8}B and *hep* solar neutrinos.

The Kamiokande II detector was upgraded (Kamiokande III) in 1990, with new electronics, PMT reflectors to increase the coverage, and improvements to the water purification system to further reduce radioactive backgrounds. Until the detector was decommissioned in 1995, it had achieved a total live time of 2,079 days and the final analysis had produced a sample of 6,368 events in the energy range 7 - 20 MeV. Upon a maximum likelihood analysis of this data sample, where the data is fit to the theoretical angular distribution (folded with the proper energy and angular resolution of the detector), the collaboration reported a value of 597^{+41}_{-40} events above background, whereas the BP98 solar model predicts a value of 1121^{+13}_{-157}. The measured solar neutrino flux, comprising of mostly ^{8}B neutrinos, and the ratio between the measured flux and the BP98 predicted ^{8}B neutrino flux is:

$$\phi_{Kam} = 2.80{\pm}0.19(stat.){\pm}0.33(sys.){\times}10^6\,cm^{-2}s^{-1} \tag{2.9}$$

$$\frac{\phi_{Kam}}{SSM_{BP98}} = 0.533{\pm}0.088(theory){\pm}0.036(stat.){\pm}0.063(sys.) \tag{2.10}$$

This result [39] supports the findings of the ^{37}Cl experiment and underscores the claim that there is a deficit in at least one of the measured solar neutrino fluxes. The experiment also measured the recoil energy spectrum of the scattered electrons. A spectral distortion would be an indication of neutrino flavor oscillation.

Super-Kamiokande

The Super-Kamiokande experiment employs a cylindrical water Čerenkov detector that contains 50 kilotons of purified water within a stainless steel tank. The cylinder has a diameter of 39m and is 41m high. The detector has been optically divided into an inner detector (ID) and an outer detector (OD). The OD serves as a cosmic-ray veto counter and also passively shields the ID from gamma activity from the surrounding rock. A total of 11,146 inward-facing 50cm-diameter photomultiplier tubes (PMTs) cover 40% of the light barrier between ID and OD. These PMTs are uniformly distributed on a 0.707m square grid, enclosing 32 kilotons of water in a volume of 36.2m height and 33.8m diameter. The fiducial volume for solar neutrino detection begins 2 meters inside the ID, and contains 22.5 kilotons of water. A total of 1,885 outward-facing 20cm-diameter PMTs are used to view the OD. Similar to past Kamiokande experiments, the 2,700m water equivalent rock overburdern provides shielding from cosmic ray muons. Detailed description of the Super-Kamiokande detector can be found in reference [40].

The Super-Kamiokande experiment, with its immense target volume and improved detector sensitivity, has been operational since April of 1996. The larger volume and lower operational threshold guarantees a much higher event rate than past Kamiokande experiments. Therefore, within a short period of time Super-Kamiokande has been capable of providing a much more accurate determination of the solar neutrino energy spectrum. Recently the collaboration has performed a sophisticated energy calibration of the detector with an electron LINAC (linear accelerator) providing energy calibration with an accuracy better than 1% [41].

Like its predecessor, the Super-Kamiokande detector is sensitive only to the ^8B and *hep* solar neutrinos, which it detects via the elastic neutrino-electron scattering reaction (Eq. 2.8) in water. However, in this detector the operational threshold is 5.5 MeV, lower than the 7.5 MeV in Kamiokande III. Since the experiment records the production time, location (vertex), direction and energy of an event, one can study the day-night and seasonal variation of the solar neutrino energy spectrum. Furthermore, the reconstruction of the recoil electron energy provides a lower bound on the incoming neutrino energy and therefore one can also look for spectral distortions of the solar neutrino flux. Super-Kamiokande has measured the electron recoil spectrum [42] and the day-night variation [43] above a threshold of 6.5 MeV using the Low Energy (LE) analysis method. Below a threshold of 6.5 MeV the background of this analysis method increases rapidly with decreasing energy. Therefore, a Super Low Energy (SLE) analysis was implemented to reject these backgrounds more efficiently. Currently the SLE analysis threshold is at 5.5 MeV and the plan is to reduce it further. Both analysis methods are combined to study the solar neutrino energy spectrum. Preliminary results of 708 days of data taking give $9397^{+154}_{-144}(\text{stat.})^{+263}_{-254}(\text{sys.})$ signal events above a threshold of 6.5 MeV [5]. This corresponds to the following measured total ^8B neutrino flux and the ratio between the measured and expected BP98 ^8B neutrino flux:

$$\phi_{SK} = 2.44 \pm 0.04(stat.) \pm 0.07(sys.) \times 10^6\, cm^{-2} s^{-1} \tag{2.11}$$

$$\frac{\phi_{SK}}{SSM_{BP98}} = 0.471^{+0.088}_{-0.007}(stat.)^{+0.013}_{-0.013}(sys.) \tag{2.12}$$

Figure 2.7 shows the detected flux of solar neutrinos as a function of the angle between the scattered electron relative to the direction of the sun. Similar to the Kamiokande II and III experiments the distribution peaks away from the direction of the sun and this “solar peak” above the background is used to measure the solar ^8B neutrino flux and spectrum. The measured neutrino energy spectrum normalized by the BP98 SSM expectation is shown in Figure 2.8. One notices a deviation from a flat normalized spectrum at the high energy end of the spectrum. As mentioned earlier, an increase in the *hep* flux by a factor as large as twenty times the SSM *hep* flux can explain this deviation. This can be justified because the SSM *hep* flux normalization is quite uncertain. However, given the low statistics in this energy region it is still too early to make firm conclusions

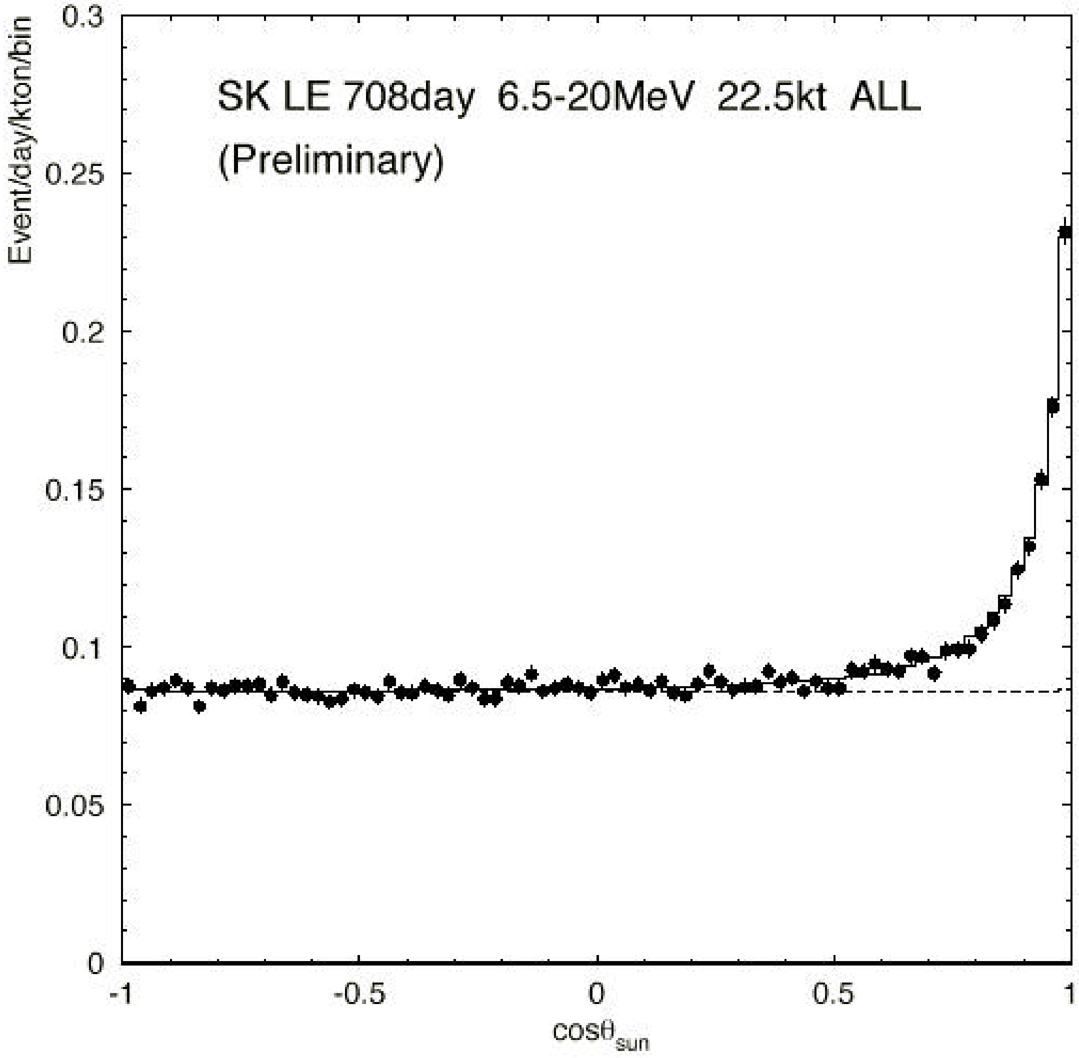

Figure 2.7: Super-Kamiokande angular distribution of events[5].

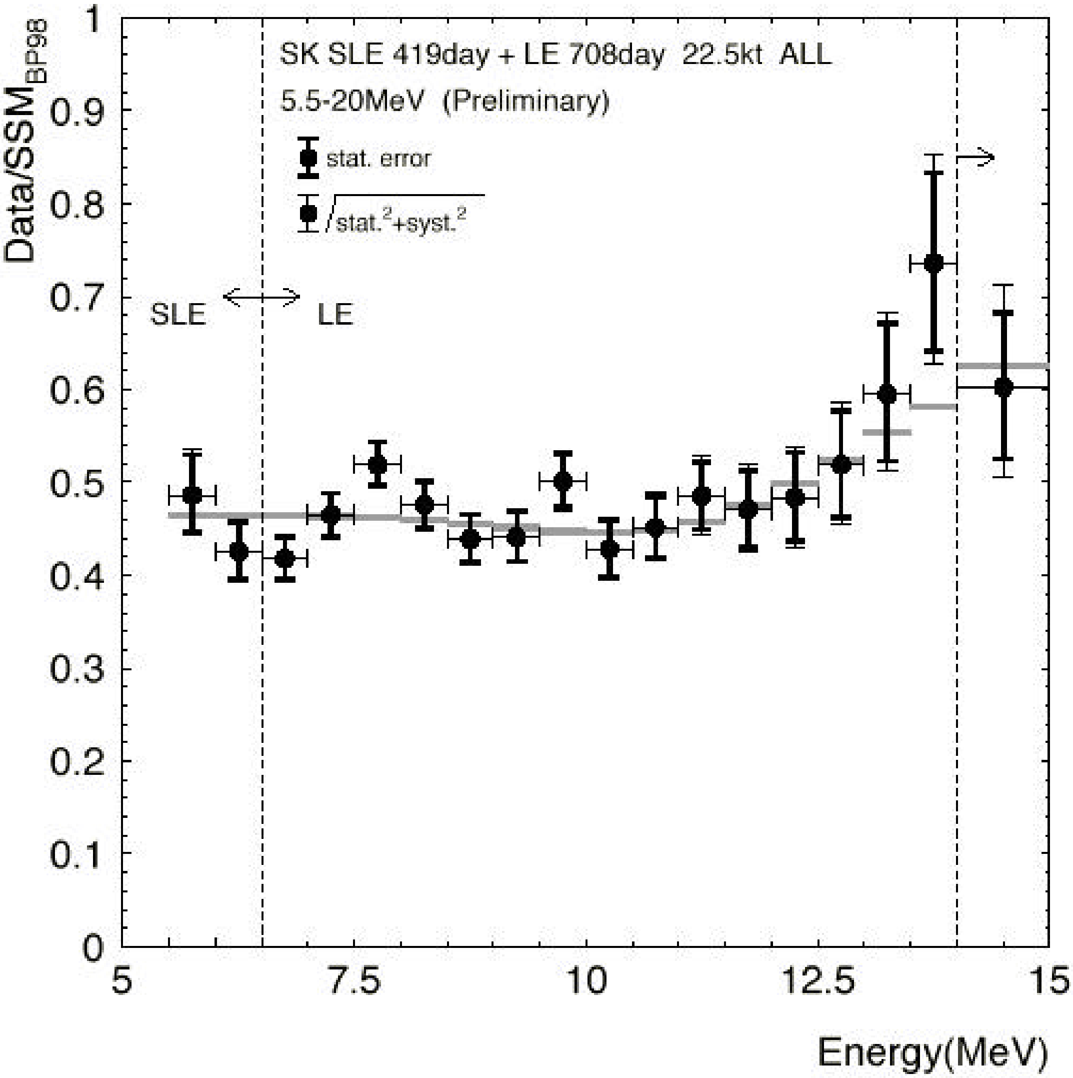

Figure 2.8: Super-Kamiokande energy distribution of events[5].

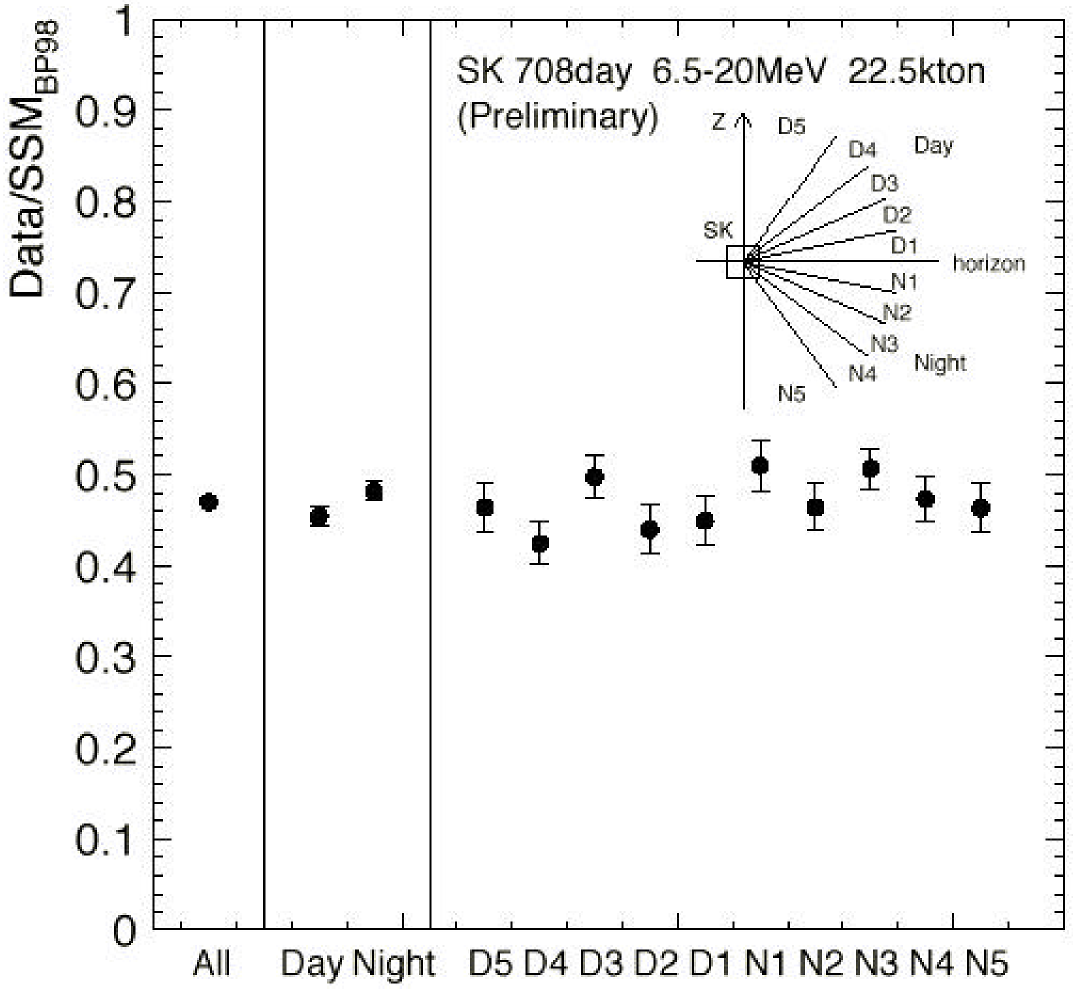

Figure 2.9: Super-Kamiokande day-night data[5].

about the anomaly.

In addition to measuring the solar neutrino energy spectrum they have also measured the day-night and seasonal variation of the data. Figures 2.9 and 2.10 show the Super-Kamiokande day-night and seasonal variation data. So far there is no significant indication of flux normalization independent signatures (day-night and seasonal variation). With more data and improved understanding of the detector behavior one hopes that within a few more years the Super-Kamiokande experiment will be able to provide an answer to the solar neutrino problem.

Most recently, in March 2001, Super-Kamiokande has published results from

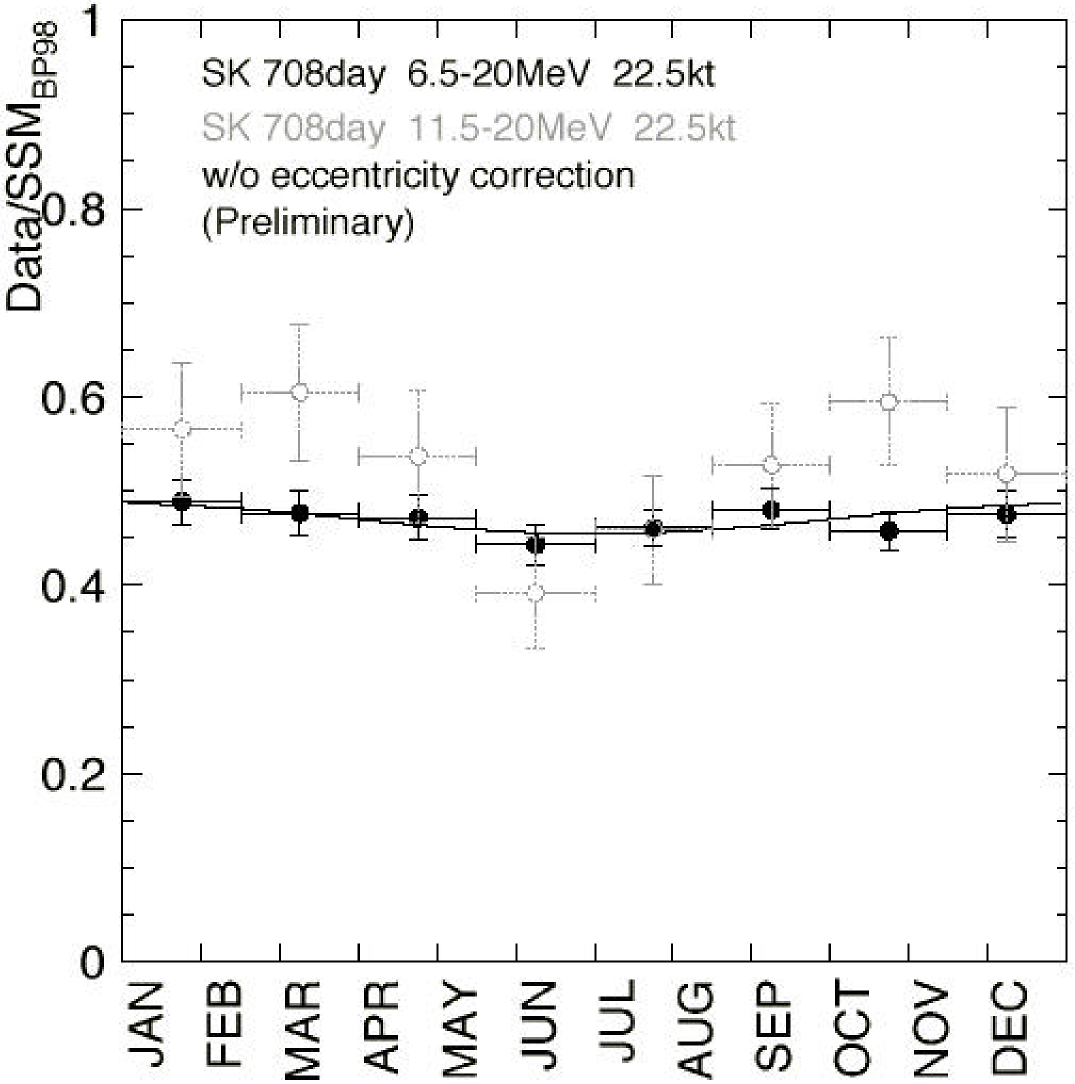

Figure 2.10: Super-Kamiokande seasonal data[5].

1258 days of detector operation[33]. They have lowered the analysis energy threshold to 5.0 MeV and have reduced systematic errors by refinements in data analysis and extensive detector calibrations. The measured ^{8}B flux is $45.1 \pm 0.5(\text{stat.})^{+1.6}_{-1.4}(\text{sys.})\%$ of the BP2000 prediction. The corresponding ^{8}B flux is:

$$\phi_{SK} = 2.32{\pm}0.03(stat.)^{+0.08}_{-0.07}(sys.){\times}10^6\, cm^{-2}s^{-1} \tag{2.13}$$

They found no statistically significant energy spectrum distortion and the day-night flux difference of 3.3% of the average flux is 1.3σ from zero. The expected 7% annual variation of the flux due to the eccentricity of the Earth's orbit is found in the seasonal dependence of the measured flux. Furthermore, they have been able to place a stringent limit on the hep neutrino flux, which has been found to be less than or equal to 4.3 times the predicted value of BP2000.

2.3.4 The Gallium Experiments

According to the SSM the *pp* neutrinos are the most abundant and have a very low end point energy of 0.42 MeV. Because of their relatively high operational thresholds the ^{37}Cl, Kamiokande and SuperKamiokande experiments are not capable of detecting the *pp* neutrinos. As early as 1965, when Davis was constructing his ^{37}Cl detector, Vladimir Kuzmin suggested an alternative radiochemical technique to detect neutrinos [44]. His proposal involved the use of ^{71}Ga instead of ^{37}Cl as the target element. The great advantage was that ^{71}Ga could capture neutrinos with energies as low as 0.23 MeV. Therefore, it would be sensitive to the neutrinos that are emitted in the basic *pp* interactions that start the nuclear fusion process in the sun. At that time the procurement of a large quantity of ^{71}Ga for a detector was not feasible. However, the semiconductor revolution of the 1970s soon made such a possibility a viable option and researchers started considering the design and implementation of a gallium solar neutrino detector.

Two ^{71}Ga radiochemical experiments, GALLEX [45, 46] and SAGE [47, 48], have been specifically constructed to detect and measure the flux of the *pp* neutrinos. Both these experiments use the following inverse β-decay reaction to detect neutrinos:

$$\nu_e + {}^{71}Ga \rightarrow e^- + {}^{71}Ge \;\; (E_{th} = 0.2332\,MeV) \tag{2.14}$$

The low threshold energy (E_{th} = 0.2332 MeV) allows for the detection of neutrino from all branches of the *pp* and *CNO* nuclear fusion chain. The detector is therefore sensitive to the dominant low energy *pp* neutrinos which contribute 54% to the expected event rate. The other main contributions are from ^{7}Be and ^{8}B neutrinos (26% and 11%). Many of the techniques used by these two experiments are similar to those used by Davis et al. in the ^{37}Cl experiment. Gallium, a metal, can be found in nature in two forms: ^{69}Ga and ^{71}Ga. It is ^{71}Ga, which forms 40% of natural gallium, that is useful in detecting neutrinos. The capture of a neutrino by a ^{71}Ga nucleus produces ^{71}Ge (germanium-71) which has a half-life of 11 days and reverts back to ^{71}Ga by emitting X-rays and Auger electrons from K and L shell electron capture. The BP98 solar model prediction of capture rates for the different sources of solar neutrinos in gallium detectors are given in Table 2.5.

The GALLEX experiment was located in an underground facility in the Gran Sasso Laboratory in Italy. The rock overburden provides 3,500m of water equivalent shielding from cosmic ray muons. The detector utilized 30 tons of gallium in a $GaCl_2$:HCl solution, which for a solar neutrino run is typically exposed to solar neutrinos for three to four weeks. At the end of this period the neutrino produced ^{71}Ge in the form of $GeCl_4$ is extracted from the target in a gas stream and converted to GeH_4. Subsequently in the counting period the decay of ^{71}Ge to ^{71}Ga is observed. Data taking started in May 1991 and counting lasted till June 19, 1997. The combined results of the published 65 solar neutrino runs performed during a period of six years is[49]:

$$\langle \phi_{\nu_e} \sigma \rangle_{Gallex} = 78{\pm}8 \; SNU \tag{2.15}$$

The data taking period comprised of 1594 net days of exposure. As compared to the BP98 solar model prediction (129 SNUs) one sees that there is a definite reduction in the measured solar neutrino flux.

The SAGE experiment is located at the Baksan Neutrino Observatory in Russia's Caucasus mountains and is at a depth of 4,715 meters water equivalent. The detector utilizes 55 tons of pure Gallium metal for neutrino detection. The advantage of using a metal target is that it is less sensitive to the backgrounds induced by radioactive impurities because of its appreciably larger density, smaller volume and absence of free protons. A detailed and informative discussion of the SAGE experimental procedures, including chemical extraction, low background counting of ^{71}Ge, data analysis methods, and systematic effects, can be found in [48]. The combined results of the 88 separate counting data sets are:

$$\langle \phi_{\nu_e} \sigma \rangle_{SAGE} = 67.2^{+7.2+3.5}_{-7.0-3.0}\ SNU \tag{2.16}$$

The main contributions to the systematic uncertainty come from the Ge extraction efficiency and the ^{71}Ge counting efficiency. The result of 67.2 SNU is approximately 7σ lower than the BP98 SSM prediction.

Both GALLEX and SAGE have measured reduced solar neutrinos and the question obviously arises about the reliability of the two detectors. The two experiments have tested the robustness of the detectors by performing meticulous neutrino source experiments. Both detectors have been tested with strong ^{51}Cr neutrino sources to examine the overall values of ^{71}Ge extraction efficiency and the neutrino interaction cross section. The man-made ^{51}Cr source is produced in a reactor by neutron irradiation of ^{50}Cr. The ^{51}Cr atoms then decay, with a half life of 27.71 days, via electron capture producing ^{51}V and neutrinos:

$$^{51}Cr + e^- \rightarrow {}^{51}V + \nu_e \tag{2.17}$$

During the calibration procedure the target element is exposed to these neutrinos.

The source experiments yield the ratio (R) of the expected neutrino event rate

Experiment	Data	Ref.	Theory	Units
Homestake	2.56±0.16±0.15	[36]	$7.7^{+1.2}_{-1.0}$	SNU
Kamiokande	2.80±0.19±+0.33	[39]	$5.15^{+0.98}_{-0.72}$	$10^6 cm^{-2} s^{-1}$
SAGE	$67.2^{+7.2+3.5}_{-7.0-3.0}$	[52]	129^{+8}_{-6}	SNU
GALLEX	78±8	[46]	129^{+8}_{-6}	SNU
Super-Kamiokande	2.44±0.04±+0.07	[5]	$5.15^{+0.98}_{-0.72}$	$10^6 cm^{-2} s^{-1}$

Table 2.7: Observed solar neutrino event rates

to the measured event rate. The results are:

$$GALLEX: \; R = 0.92 \pm 0.08 \, (1\sigma \, stat. \, and \, sys.) \, [50] \tag{2.18}$$

$$SAGE: \; R = 0.95 \pm 0.11 + 0.05/-0.08 \, (1\sigma \, stat. \, and \, sys.) \, [51] \tag{2.19}$$

Given the very good agreement between the expected and measured rates there is good confidence in the results reported by both the GALLEX and SAGE experiments.

The Gallium Neutrino Observatory (GNO) succeeded the GALLEX experiment at the Gran Sasso Underground Laboratory (LNGS). The end of the GALLEX measurements in early 1997 was followed by a break until early 1998. During this break a major overhaul and modernization of the GALLEX experimental set-up took place. In early 1998 solar neutrino observations resumed with the new experiment GNO[49].

2.4 The Missing Solar Neutrino Puzzle

The discrepancies between the observed solar neutrino flux and that predicted by the *standard solar model* constitutes the solar neutrino problem. As can be seen from Table 2.7 the discrepancy cannot be explained by resorting to mere statistical fluctuations of the data. The chlorine and gallium experiments integrate over energy and cannot provide spectral information for the observed neutrino flux. The spectral sensitivity of the Kamiokande detectors is weak and an accurate determination of the neutrino spectrum requires high statistics and very good understanding of the detector systematics. However, taken together the experiments demonstrate not only a suppression of the expected neutrino flux but they also reveal a distortion of the solar neutrino spectrum. Many rigorous studies have been performed where one has combined the various experimental results with the assumption that the neutrino spectra are not being distorted by oscillations or other new physics and have found in general the following pattern of solar neutrino fluxes [53]:

$$\begin{aligned}
\phi(pp) &\sim 0.9 \times \phi^{SSM}(pp) && (2.20)\\
\phi(^8B) &\sim 0.4 \times \phi^{SSM}(^8B) && (2.21)\\
\phi(^7Be) &\sim 0 && (2.22)
\end{aligned}$$

In fact, the best value for $\phi(^7Be)$ turns out to be negative (at 2 to 3σ) in unconstrained fitting algorithms. Therefore, from these analyses one finds not only a significant suppression of the ^{8}B neutrino flux but also a near complete suppression of the ^{7}Be neutrino flux. Initially the results of the ^{37}Cl experiment demonstrated a deficit in the observed flux, which is primarily comprised of ^{8}B and ^{7}Be neutrinos. But now with five different experiments sampling different parts of the solar neutrino spectrum we have a much more rigorous manifestation of the solar neutrino problem.

2.5 Possible Solutions to the SNP

2.5.1 Introduction

The solar neutrino problem has persisted for more than three decades. During this period of time, people have attempted to formulate ingenious and novel ways of solving the problem. One line of attack was to cast doubt on the results. A single experiment, no matter how accurate and precise in its measurements, cannot bring about a fundamental shift in a prevailing paradigm if its results cannot be independently verified by another experiment. The ^{37}Cl experiment was the first to report the anomaly and for two decades it stood on its own, all the while, withstanding the careful scrutiny of the scientific world. The experiment raised important questions about our understanding of the sun and of the properties of the neutrino, and it provided the impetus to carry out research investigating these questions. However, the ^{37}Cl result on its own, though necessary, wasn't sufficient to start a serious revolution. Then in the late '80s and early '90s the Kamiokande and Gallium experiments confirmed the ^{37}Cl solar neutrino results. Recently the Super-Kamiokande experiment has also corroborated the results of the past solar neutrino experiments. With these independent measurements, the proposition that there is a solar neutrino problem no longer rested on the results of a single experiment. Even though it is possible for all these experiments to be in error, it is highly unlikely. Various solutions to the solar neutrino problem have been advocated since the initial results of the ^{37}Cl experiment. The complexity and breadth of the solutions have evolved over time as additional experiments started reporting their results. The solutions primarily fall into two categories: astrophysical or particle physics solutions. Astrophysical solutions typically involve non-standard solar models which generally modify the solar temperature profile in an attempt to fit the solar neutrino data or they deal with large systematic errors in the input parameters to the standared solar models. Particle physics solutions involve the incorporation of extended properties of the neutrino, in particular they postulate that neutrinos have mass and/or they have a magnetic moment. Since the solar neutrino energy spectra are determined by the weak interaction physics of β-decay, they are not affected by any particular solar model. Therefore any spectral distortion would be evidence for new physics.

2.5.2 Astrophysical Solution

The recognition of the solar neutrino problem has prompted physicists to propose speculative solutions to the problem in the form of nonstandard solar models. Nearly all of these solutions alter the standard solar model in such a way so as to reduce the calculated flux of ^{8}B and ^{7}Be neutrinos. In order to achieve this, all of these proposed nonstandard solar models change some solar parameter or some physical relation from something that is generally accepted to something that is generally regarded as unlikely or in some cases impossible. Examples of these include the low central temperature (T_C), low opacity, low Z, large S_{11}, large S_{33}, small S_{34}, small S_{17}, and weakly interacting massive particle (WIMP) models[1].

Most of these models attempt to explain the observed solar neutrino deficit by invoking non-standard input parameters or nonstandard mechanisms to decrease the solar core temperature, since lower temperature makes the penetration of the Coulomb barrier in the p-p chain fusion reactions more difficult which results in a decrease in the reaction rates and solar neutrino fluxes. Low Z or low opacity models smooth the temperature distribution inside the sun; strong magnetic field or rapid rotation models change the equation of hydrostatic equilibrium; WIMP models use new types of exotic particles to remove energy from the center of the sun. Although these models are able to achieve lower central temperature, almost all of them predict a greater reduction in the ^{8}B neutrino flux than the

---

[1] S_{11}, S_{33}, S_{34}, and S_{17} are the S factors proportional to the cross sections for $p + p \rightarrow {}^2H + e^+ + \nu_e$, ${}^3He + {}^3He \rightarrow {}^4He + 2p$, ${}^3He + {}^4He \rightarrow {}^7Be + \gamma$, and $p + {}^7Be \rightarrow {}^8B + \gamma$, respectively.

^{7}Be neutrino flux. As described earlier, the solar neutrino problem is not only the energy dependent suppression of the ^{8}B neutrino flux but it also involves the almost complete suppression of the ^{7}Be neutrino flux. Bahcall and Ulrich [54] have determined the approximate correlation between solar core temperature, T_C, and neutrino flux by calculating 1000 solar models with the input parameters randomly varied over their uncertainty ranges. They have found the following relation:

$$\phi(pp) \sim T_c^{-1.2}, \ \phi(^7Be) \sim T_c^8, \ \phi(^8B) \sim T_c^{18} \tag{2.23}$$

If the solar neutrino production region as a function of solar radius is plotted it can be seen that the solar model with the highest central temperature has the highest ^{8}B neutrino flux. However, the temperature falls more rapidly with the solar radius for a higher T_C. As a result, the ^{7}Be neutrino flux is increased less and the flux of *pp* neutrinos, which are produced further out, is reduced. Therefore, a nonstandard solar model intended to properly explain the solar neutrino deficit would require a ingenious custom tailored inversion of the solar temperature profile. The models suggested for this purpose include out of equilibrium ^{3}He mixing or filament ^{3}He mixing [55]. But all of these models are severely constrained by helioseismological data and in most cases they are unable to corroborate the helioseismological findings. In conclusion, this demonstrates the incompatibility between nonstandard solar models and solar neutrino data.

There have been numerous studies by different authors which have used a model independent analysis approach to look at the existing solar neutrino data. These studies have demonstrated that the solar neutrino problem is essentially independent of any details of the standard solar models. These model independent analyses [56, 57, 58, 59] have shown that the ^{7}Be neutrinos must be strongly depleted compared to the SSM prediction. One then concludes from these analyses that the solar neutrino problem cannot be explained by astrophysical mechanisms utilizing nonstandard solar models.

In addition to searching for astrophysical solutions, people have attempted to solve the problem by proposing various neutrino properties that go beyond the standard model description of the neutrino. For example, if neutrinos decay then this would lead to a deficit in the observed rate [60]. However, this mechanism requires the inclusion of new particles and/or new interactions that has been ruled out by the data from the supernova of 1987 (designated SN1987a). If neutrinos have a large magnetic moment, then the left-handed neutrinos produced in the solar core could be flipped into right-handed neutrinos by the solar magnetic field and thus go undetected in terrestrial experiments. But this mechanism requires a neutrino magnetic moment which is much larger than the value predicted by conventional models and it also needs a large solar magnetic field. Furthermore, the spin flip in the sun should yield a rate correlation with solar magnetic phenomena (sunspots or solar euqatorial variation) and this is not supported by data [61]. There have also been other novel proposals to explain the solar neutrino problem but the most compelling has to do with the proposition that the neutrino is massive. That is the subject matter of the next section.

2.5.3 Particle Physics Solution

A search for a plausible particle physics solution to the solar neutrino problem involves the extension of the properties of the neutrino that go beyond its standard model description. If neutrinos, contrary to the standard model view, are massive particles then the flavor expectation value (the probability of observing a particular neutrino flavor state) could oscillate if the flavor states are an admixture of the propagated mass eigenstates. A direct consequence of this quantum mechanical process involves the electron neutrinos produced in the solar core possibly oscillating into muon, tau or sterile neutrinos on their travel to earth. Since the solar neutrino experiments described earlier are primarily sensitive to electron neutrinos, this mechanism could be used to explain the reduction in the measured solar neutrino flux.

The idea of neutrino oscillations was first put forward by Bruno Pontecorvo in 1957, soon after parity violation in β-decay was discovered by Wu et. al. [12] and the theory of the two-component massless neutrino was proposed by Landau [62], Lee and Yang [13], and Salam [63]. Pontecorvo in his paper [64] mentioned the possibility of neutrino $\leftrightarrow$ antineutrino transitions in vacuum analogous to the, then recently, observed phenomenon of the $K^\circ \leftrightarrow \overline{K^\circ}$ oscillations, which resulted because the quark mass states are admixtures of the weak states. Pontecorvo had noted that if the neutrino had mass and if the total lepton number was not conserved, then it could oscillate between particle and antiparticle. At that time only one type of neutrino was known and (for many years later) the neutrino was generally believed to be a massless particle. Pontecorvo's idea of neutrino oscillations wasn't seriously pursued since the two component massless neutrino theory had gained wide acceptance by successfully explaining parity violation in β-decay. The idea of vacuum oscillations between two distinct flavors of neutrino came into being after the discovery of the muon type neutrino (ν_μ) by Lederman, Steinberger and Schwartz in 1963, which showed that there are two distinct flavors of neutrino, the ν_e and the ν_μ [65]. Soon there after, Pontecorvo in a paper [66] in 1967 discussed the possibilities of two flavor neutrino oscillations and for the first time put forth the idea of solar neutrino oscillations. Even before the first results of Davis' ^{37}Cl experiment were published, Pontecorvo had pointed out neutrino oscillations could result in an observed flux of solar neutrinos half the expected flux. Interestingly, he had anticipated the solar neutrino problem. The possibility of neutrino oscillations requires mixing across the lepton families as well as nonzero neutrino masses. In the early seventies, after the Cabibbo-GIM quark mixing was established, the main arguments for neutrino mixing were based on quark-lepton analogy. Given that the theory of massless strictly two-component neutrinos still prevailed, the idea of neutrino mixing and neutrino oscillations wasn't pursued in earnest. However, the situation changed dramatically after the appearance of Grand Unification models and of the sea-saw mechanism [67, 68, 69] that connect the smallness of neutrino masses with the violation of the lepton numbers at very large scale. In the Grand Unification models it is natural and plausible for neutrinos to have mass and, therefore, neutrino oscillations become a possibility.

Currently the most plausible explanation of the solar neutrino puzzle lies in the oscillation of electron neutrinos into other types of neutrinos. Even if neutrino oscillations in vacuum isn't able to account for the measured deficit one can still use neutrino oscillations to explain the shortfall via the MSW effect. Named after Mikheyev, Smirnov, and Wolfenstein, the MSW effect provides the mechanism in which electron neutrinos, through their interaction with electrons in solar matter, can oscillate as they travel from the solar core to the surface. In the next section the formalism for neutrino oscillations in vacuum will be discussed. This will then provide the background needed to better understand the MSW effect which will be described in the subsequent section.

Vacuum Oscillations

The phenomenon of neutrino oscillations is based on the premise that neutrinos have a nonzero mass. In the case of massive neutrinos, it is possible for the weak interaction eigenstates (the flavor states that couple to the charged leptons) to not be identical to the mass eigenstates (the propagation eigenstates that diagonalize the free Hamiltonian). But instead they are coherent, linear superpositions of the mass eigenstates. By "coherent" one means that the phases of two or more of the mass states are correlated, so that the relative phase between the states leads to an interference term during the calculation of the oscillation probabilities. Neutrino oscillation is a pure quantum mechanical effect and can be understood by considering what happens when a neutrino of definite initial flavor is traveling from one destination to another. Since the neutrino is a superposition of mass eigenstates, the lighter mass states will travel faster than the heavier ones and get ahead of the latter. Therefore, the various mass components get out of phase with one another and depending on the time of the final measurement they might not add up to form the initial flavor state. So, during travel the original electroweak interaction eigenstate of the neutrino has a probability of being detected as a different electroweak interaction eigenstate. (It is assumed here that all mass eigenstates have the same momentum and it has been shown in reference [70] that the final results are not altered if this assumption is not made.)

Vacuum oscillations can be formalized by considering, for simplicity, only two of the three flavors of neutrinos: ν_e and ν_x, where $\nu_x = \nu_\mu$ or ν_τ. This is similar to that for three flavors, where the formulation is more involved and complicated. However, the two flavor oscillation treatment is generally justified, since the neutrino masses are expected to be hierarchical in order to explain both the solar neutrino and the atmospheric neutrino data [71]. We can express the flavor eigenstates as a superposition of the mass eigenstates in the following manner:

$$\begin{pmatrix} |\nu_e\rangle \\ |\nu_\mu\rangle \end{pmatrix} = \begin{pmatrix} cos\theta & sin\theta \\ -sin\theta & cos\theta \end{pmatrix} \begin{pmatrix} |\nu_1\rangle \\ |\nu_2\rangle \end{pmatrix} \equiv U \begin{pmatrix} |\nu_1\rangle \\ |\nu_2\rangle \end{pmatrix} \tag{2.24}$$

where $|\nu_e\rangle$ and $|\nu_\mu\rangle$ are wave functions for the neutrino electroweak interaction eigenstates, $|\nu_1\rangle$ and $|\nu_2\rangle$ are wave functions for the neutrino mass eigenstates, and θ is the vacuum mixing angle. If θ is small, then ν_e consists primarily of the state $|\nu_1\rangle$ and has only a small admixture of $|\nu_2\rangle$, whereas ν_x would be dominated by $|\nu_2\rangle$ and would have only a small amount of $|\nu_1\rangle$. The two-dimensional orthogonal rotation matrix U, characterized by θ, is used to convert between the mass and electroweak interaction states. Now, the evolution of the neutrino mass eigenstates from a time t=0 to a later time t is given by:

$$|\nu_i(t)\rangle = e^{-iE_i t} |\nu_i(0)\rangle \tag{2.25}$$

where, E_i is the energy of the ith neutrino mass eigenstate. For generality we are now using i, j to denote the mass eigenstates *1* or *2*. We are also working in natural units with $\hbar$ = c = 1. For relativistic neutrinos we can approximate E_i by:

$$E_i = \sqrt{p^2 + m_i^2} \simeq p + \frac{m_i^2}{2p} \simeq E + \frac{m_i^2}{2E} \tag{2.26}$$

where, m_i is the mass of the ith mass eigenstate and E ≅ p. As mentioned earlier, we assume that each mass eigenstate has the same momentum p, which is much greater than the masses m_i. Because $m_1 \neq m_2$, and hence $E_1 \neq E_2$, the relative phase between $|\nu_1\rangle$ and $|\nu_2\rangle$ will change as the flavor eigenstate evolves with time. Now, using the above equation we get the following relationship:

$$E_2 - E_1 = \frac{{m_2}^2 - {m_1}^2}{2E} \equiv \pm\frac{\Delta m^2}{2E} \tag{2.27}$$

Here, the positive definite quantity Δm^2 is defined as:

$$\Delta m^2 \equiv |{m_1}^2 - {m_2}^2| \tag{2.28}$$

The plus sign in Eq.(2.27) applies if $m_2 > m_1$ and the minus sign applies if $m_1 > m_2$. Let us now write the time evolution of Eq.(2.19) in the following way:

$$|\nu_a(t)\rangle = \sum_i U_{ai}|\nu_i(t)\rangle \tag{2.29}$$

Again, for generality, we are using a, b to denote the flavor states e or x. After substituting Eq.(2.25) in Eq.(2.24) we get:

$$\begin{aligned} |\nu_a(t)\rangle &= \sum_i U_{ai} e^{-iE_it}|\nu_i(0)\rangle && (2.30)\\ &= \sum_i\sum_b U_{ai}U_{ib}^{-1} e^{-iE_it}|\nu_b(0)\rangle && (2.31)\end{aligned}$$

The probability that the neutrino flavor remains unchanged after propagating through vacuum for a period of time t is the square of the amplitude $|\langle\nu_a|\nu_a(t)\rangle|^2$. The amplitude is given by:

$$\begin{aligned} \langle\nu_a|\nu_a(t)\rangle &= \sum_i\sum_b U_{ai}U_{ib}^{-1} e^{-iE_it}|\langle\nu_a|\nu_b(0)\rangle && (2.32)\\ &= \sum_i\sum_b U_{ai}U_{ib}^{-1} e^{-iE_it}\delta_{ab} && (2.33)\\ &= \sum_i U_{ai}U_{ia}^{-1} e^{-iE_it} && (2.34)\end{aligned}$$

Therefore, the probability that the neutrino doesn't change flavor while traveling through vacuum is:

$$\begin{aligned} P_V(a \to a, t) &= |\,\langle\nu_a|\nu_a(t)\rangle\,|^2 && (2.35)\\ &= \sum_i\sum_j U_{ai}^{*}U_{ia}^{-1*}U_{aj}U_{ja}^{-1} e^{-i(E_i-E_j)t} && (2.36)\end{aligned}$$

Finally, from Eq.(2.35) we get the following:

$$P_V(a \rightarrow a, t) = 1\ -\ sin^2 2\theta sin^2 \frac{\Delta m^2}{4E} t \tag{2.37}$$

where, we have used Eq.(2.26) and, without loss of generality, we have assumed $m_2 > m_1$. Here m_1 and m_2 are rest masses of the states ν_1 and ν_2. Therefore, the probability that an electron neutrino generated at t=0 remains an electron neutrino after traveling a distance L in time t is given by:

$$P_V(\nu_e \rightarrow \nu_e, L) = 1\ -\ sin^2 2\theta sin^2 \frac{\pi L}{L_V} \tag{2.38}$$

where,

$$L_V = \frac{4\pi E}{\Delta m^2} = 2.48\Big(\frac{E}{MeV}\Big)\Big(\frac{eV^2}{\Delta m^2}\Big)\ meters \tag{2.39}$$

is called the vacuum oscillation length and Δm^2 is measured in electron volts squared, L is in meters, and E is in million electron volts. Since the neutrinos are relativistic we have replaced t in Eq.(2.36) by L/c = L (in natural unit c = 1). From the conservation of probability we can get the probability, $P_V(\nu_e \rightarrow \nu_x, L)$, that a ν_e will transform into a ν_x:

$$P_V(\nu_e \rightarrow \nu_x, L) = sin^2 2\theta sin^2 \frac{\pi L}{L_V} \tag{2.40}$$

The quantities Δm^2 and $sin^2 2\theta$ are typically considered and treated as free parameters to be determined by the analysis of the data from neutrino oscillation experiments. Form Eq.(2.37) and Eq.(2.39) we see that the transition probability depends on two factors: on L_V, which exhibits oscillatory dependence on the distance traveled by the neutrinos and the neutrino energy, and on $sin^2 2\theta$ which determines the amplitude of the oscillation. In order for the $\nu_e \rightarrow \nu_x$ oscillation probability to be large, $P_V(\nu_e \rightarrow \nu_x, L) \cong 1$, two conditions need to be met: the neutrino mixing in vacuum needs to be large, $sin^2 2\theta \cong 1$, and the oscillation length, L_V, in vacuum has to be of the order or smaller than the distance traveled by the neutrinos, L: $L_V \leq \pi L$. If the second condition is not satisfied, i.e. if $L_V \gg \pi L$, the oscillations do not have enough time to develop on the way from the source to the detector as the source-detector distance L is too short, and we get $P_V(\nu_e \rightarrow \nu_x, L) \cong 0$.

In general, a neutrino oscillation experiment is specified by the average energy of the neutrinos being studied, $\overline{E}$, and by the distance between the neutrino source and neutrino detector. The requirement $L_V \leq \pi L$ determines the minimal value of the parameter Δm^2 to which the experiment is sensitive to: $min(\Delta m^2) \sim \frac{2\overline{E}}{L}$. Typically neutrino oscillation experiments can probe fairly small values of Δm^2 because of the interference nature of neutrino oscillations. In particular, given the large distance between the sun and the earth, $L = 1.4966 \times 10^{11} m$, and the relatively low energies of the neutrinos, $\overline{E} \sim 1 MeV$, the solar neutrino experiments are very sensitive to the Δm^2 parameter and can probe values as small as $\sim 10^{-12}\ eV^2$. This is many orders of magnitude smaller than the values probed by other, terrestrial, neutrino oscillation experiments.

As mentioned earlier, one can apply the mechanism of neutrino oscillations in vacuum to help solve the solar neutrino problem. We have seen that if $L_V \gg \pi L$ then there won't be any reduction in the incoming neutrino flux. However, if $L_V \ll \pi L$, then the probability is averaged over time so that $P_V(\nu_e \rightarrow \nu_e, L) = 1 - \frac{1}{2} sin^2 2\theta$ [72]. If we now consider the case of maximal mixing, i.e. $sin^2 2\theta = 1$, the probability reduces to 0.5 and this should be observed uniformly in all solar neutrino experiments. However, we have seen that the ^{37}Cl experiment reports a value much smaller than 0.5 and the probability obtained by other experiments is not uniform. Therefore it is difficult to solve the solar neutrino problem in this manner. One can fine tune the vacuum oscillation parameters to fit the results of the solar neutrino experiments. The parameter ranges are calculated to be $sin^2 2\theta > 0.7$ and $\Delta m^2 \sim 10^{-12}(eV^2)$, which implies that the oscillation length is of the order of the distance from the sun to the earth. In the literature this is generally referred to as the "just-so" oscillation scenario [73]. It should be pointed out that there is nothing obviously spectacular about this coincidence since any solution to the solar neutrino problem will require parameters which have been "just-so" tuned so as to explain the data. Given particular values for the parameters Δm^2 and $sin^2 2\theta$, the mechanism of neutrino vacuum oscillations can provide an explanation for the neutrino flux deficit and the distortion of the neutrino energy spectrum. However, the definitive signature of vacuum oscillations is the measurement of a seasonal variation of the solar neutrino flux. The oscillation probability will vary as the distance between the earth and the sun varies over the course of a year and this variation should be observed as a variation in the measured flux by all solar neutrino experiments. Currently none of the experiments have measured a significant seasonal solar neutrino flux variation other than measuring the expected seasonal variation due to the earth's orbital eccentricity.

Matter Enhanced Oscillations : The MSW Effect

In 1986, based on the initial work of Lincoln Wolfenstein [74], S.P.Mikheyev and Alexei Smirnov [75, 76] recognized and demonstrated the effect of solar matter on neutrino oscillation probabilities. Named after Mikheyev, Smirnov, and Wolfenstein the MSW effect is an application of quantum mechanics that explains how neutrino oscillations can be enhanced by the medium through which the neutrinos travel. At the right density of matter and if neutrinos have mass, a neutrino of a particular flavor within a certain energy range can transform into a neutrino of a different flavor even though its intrinsic vacuum oscillation probability for doing so may be very small. Similar to vacuum oscillations, the formulation of the MSW effect can be understood by considering only two flavors of neutrinos.

Only the electron neutrinos interact with electrons via the weak charged current, hence in a dense medium the electron neutrinos have a larger cross section for electron scattering than do muon or tau neutrinos. As a result, the electron component of a neutrino mass eigenstate of mixed flavor will gain an additional phase shift which affects the oscillation probability. The equation of motion of the neutrino flavor eigenstates in matter is given as follows:

$$i\frac{d}{dt}\begin{pmatrix}|\nu_e(t)\rangle\\|\nu_\mu(t)\rangle\end{pmatrix}=\left\{U\begin{pmatrix}E_1&0\\0&E_2\end{pmatrix}U^{-1}+\begin{pmatrix}V_C+V_N&0\\0&V_N\end{pmatrix}\right\}\begin{pmatrix}|\nu_e(t)\rangle\\|\nu_\mu(t)\rangle\end{pmatrix}\qquad(2.41)$$

where, V_C and V_N are the effective potential for the neutral and charged current interactions respectively. The diagonal component, V_N, can be absorbed into a common phase factor, $e^{-i\int V_N dt}$. The effective charged current potential, V_C, is given by:

$$V_C=\sqrt{2}G_FN_e\qquad(2.42)$$

where, G_F is the Fermi coupling constant and N_e is the electron density of the matter through which the neutrino is traveling. After some algebra we can write Eq.(2.41) as follows:

$$i\frac{d}{dt}\begin{pmatrix}|\nu_e(t)\rangle\\|\nu_\mu(t)\rangle\end{pmatrix}=\frac{1}{2E}\left\{\frac{1}{2}(m_1^2+m_2^2+A)I+\frac{\Delta m^2}{2}\begin{pmatrix}-sin2\theta+\beta&sin2\theta\\sin2\theta&sin2\theta-\beta\end{pmatrix}\right\}\begin{pmatrix}|\nu_e(t)\rangle\\|\nu_\mu(t)\rangle\end{pmatrix}\qquad(2.43)$$

where, $A=2\sqrt{2}G_FN_eE$, $\beta=A/\Delta m^2$, and I is the 2×2 identity matrix. The eigenvalues of the matrix, m_{1m}^2 and m_{2m}^2, can be regarded as effective masses of the two mass eigenstates in matter. These eigenvalues are given by:

$$m_{im}^2=\frac{m_1^2+m_2^2+A}{2}\pm\frac{1}{2}\sqrt{(\Delta m^2cos2\theta-A)^2+\Delta m^4sin^22\theta}\qquad(i=1,2)\quad(2.44)$$

and the eigenstate in matter is:

$$\begin{pmatrix}|\nu_{1m}\rangle\\|\nu_{2m}\rangle\end{pmatrix}=\begin{pmatrix}cos\theta_m&-sin\theta_m\\sin\theta_m&cos\theta_m\end{pmatrix}\begin{pmatrix}|\nu_e\rangle\\|\nu_x\rangle\end{pmatrix}\qquad(2.45)$$

where, θ_m is the effective mixing angle in matter and from matrix unitarity we get:

$$tan2\theta_m=\frac{tan2\theta}{1-\frac{L_V}{L_ecos2\theta}}\qquad(2.46)$$

where, $L_e=\sqrt{2}/GN_e$ and $L_V=4\pi E/\Delta m^2$. Therefore, if the following condition is satisfied, then the mixing angle in matter becomes maximal ($\theta_m=\pi/4$) even if the vacuum mixing angle is small:

$$L_V=L_ecos2\theta\qquad\text{or}\qquad\beta=2\sqrt{2}G_FN_eE/\Delta m^2=cos2\theta\qquad(2.47)$$

This is called the MSW "resonance condition". When this matching occurs, a neutrino of a particular flavor will have a high probability of transforming into a neutrino of a different flavor, even if its intrinsic vacuum oscillation probability for doing so might be very small. The electron density, $N_{e,res}$, at which the resonant condition is satisfied is given by:

$$N_{e,res} = \Delta m^2 cos2\theta / 2\sqrt{2} G_F E \tag{2.48}$$

As in the vacuum oscillation case we can define an oscillation length, L_m, for the MSW effect:

$$L_m = \frac{L_V}{\sqrt{(\beta - cos2\theta)^2 + sin^2 2\theta}} \tag{2.49}$$

The survival probability is given by:

$$P_M(\nu_e \rightarrow \nu_e, t) = 1 - sin^2 2\theta_m sin^2 \left(\frac{\pi t}{L_m} \right) \tag{2.50}$$

and the effective mixing angle in matter θ_m, given in Eq.(2.46), can also be expressed in the following way:

$$sin^2 2\theta_m = \frac{sin^2 2\theta}{\alpha^2} \tag{2.51}$$

where,

$$\alpha^2 = sin^2 2\theta + (\beta - cos2\theta)^2 \tag{2.52}$$

One notices the similarity between the expression for the MSW probability given in Eq.(2.50) and the vacuum oscillation probability. The vacuum mixing angle θ is replaced by the effective mixing angle θ_m which depends on the matter oscillation term $\sqrt{2} G_F N_e$ (through the parameter β). When a neutrino travels in vacuum, the electron density $N_e = 0$, and hence $\beta = 0$, so that $\alpha^2 = 1$. In this case the MSW probability reduces to the vacuum probability. However, when the neutrino travels through matter α^2 can become less than 1 due to the resonance effect. The oscillation probability increases with the resonance condition given by $\beta = cos2\theta$. At the resonance condition, $\alpha^2 = sin^2 2\theta$ and $sin^2 2\theta_m = 1$, and the oscillation probability reaches a maximum.

From Eq.(2.47) one sees that the resonance condition depends on the electron density of the matter through which the neutrino is traveling. The solar electron density varies as a function of the solar radius. It is largest at the center where nuclear fusion occurs and it decreases as the radius increases. For this range of solar densities, the value of the parameter β varies from a few tens near the core to a few hundredths near the surface of the sun. At some intermediate point it passes through a value of 1. Large values of β correspond to very small values of θ_m and hence damp out oscillations, whereas small values of β basically leave vacuum oscillations unchanged. For small θ, values of β near 1 give rise to the maximum enhancement of the oscillation probability. Now, given that the solar density varies as a function of the radius, a neutrino born with an energy larger than the critical energy E_{crit}, will always pass through a position in the sun where the resonance condition is satisfied. The critical energy is given by:

$$E_{crit} = \frac{\Delta m^2 cos2\theta}{2\sqrt{2}G_F N_{e,c}} = 6.6\, cos2\theta \left(\frac{\Delta m^2}{10^{-4} eV^2} \right) \;\; MeV \tag{2.53}$$

where, $N_{e,c}$ is the electron density at the center of the sun. Furthermore, the resonance condition must be satisfied for at least several oscillation lengths. The implication of this is that at resonance, the density must be slowly varying, and this is called the adiabatic condition. From the above equation one can now obtain the half width of the resonance ($sin^2 2\theta_m = \frac{1}{2}$) as:

$$|\delta A| = \Delta m^2 sin2\theta \tag{2.54}$$

therefore the resonance distance d $= |\delta N_e| \frac{dx}{dN_e}$ is given by:

$$d = \frac{dx}{dN_e} \frac{|\delta A|}{2\sqrt{2}G_F E} = \frac{N_e tan2\theta}{|dN_e/dx|} \tag{2.55}$$

From Eq.(2.49) the oscillation length at resonance is $L_m = 4\pi E/\Delta m^2 sin2\theta$. Therefore, applying the adiabatic condition $d \ll L_m$ we get the following:

$$\gamma \equiv \frac{\Delta m^2 sin2\theta tan2\theta}{2E|\frac{1}{N_e}\frac{dN_e}{dx}|_r} \ll 1, \tag{2.56}$$

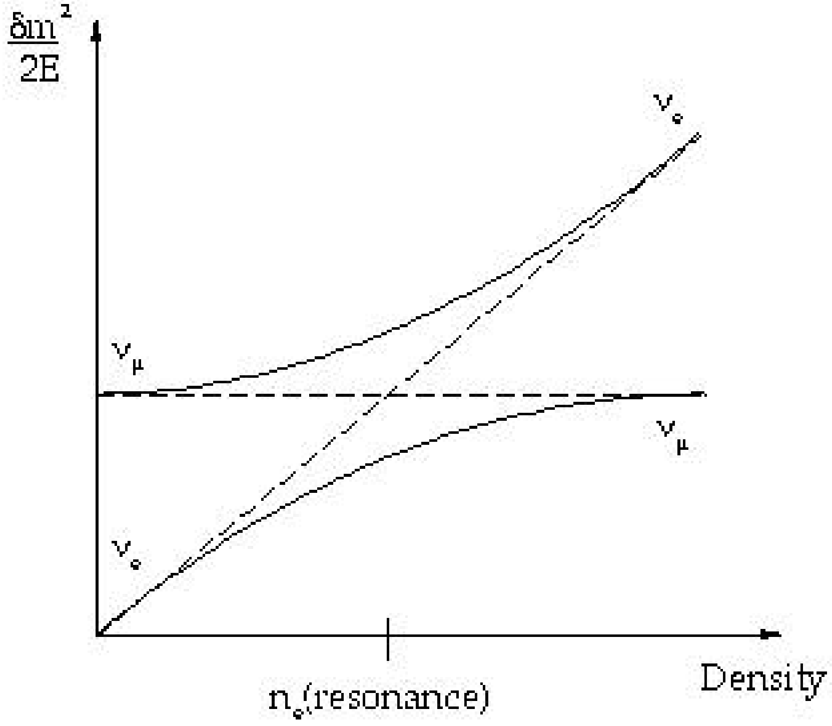

Figure 2.11: MSW Level Crossing Diagram.

where, γ is the adiabatic parameter. The mass eigenvalues of the two neutrino mass eigenstates in matter as a function of electron density is shown in Figure 2.11. If the energy of the neutrino is greater than E_{crit}, then $\theta_m \cong \pi/2$ and hence $|\nu_e\rangle$ is almost $|\nu_2\rangle$. Now, as the neutrino mass eigenstates propagate outward to the surface of the sun, the mass of the eigenstates will change as shown in Figure 2.11. When a neutrino passes the resonance region the mixing becomes maximal, i.e. at this point $\theta_m \cong \pi/4$. If the variation of the solar electron density obeys the adiabatic condition then the main component of flavor, for the mass eigenstate $|\nu_2\rangle$, changes from $|\nu_e\rangle$ to $|\nu_\mu\rangle$ if the vacuum mixing angle θ is small enough. Therefore under the adiabatic condition, a neutrino born as an electron neutrino transforms into a muon or tau neutrino by the time it reaches the solar surface (where the electron density is almost zero).

A formula for determining the survival probability with non-adiabatic corrections due to level crossing jumps between eigenstates has been provided by Parke [77]. If the adiabatic condition given in Eq.(2.55) is not satisfied then the eigenvalues are closer together at resonance. In this case the jump or tunneling probability becomes large and this is known as level crossing. The Parke formula is:

$$P(\nu_e \rightarrow \nu_e) = \frac{1}{2} + (1 - P_{jump}) cos2\theta cos2\theta_m \tag{2.57}$$

The tunneling probability was first calculated by Landau and Zener in atomic collisions for a linear density variation, where they obtained $P_{jump} = exp(-\frac{\pi}{2}\gamma)$ [61]. Similarly, the jump probability can be determined for other density functions, e.g. it can be calculated for the solar density function. The solar density can be well represented by an exponential radius and using this one can obtain the following jump probability:

$$P_{jump} = \frac{exp(-\frac{\pi}{2}\gamma F) - exp(-\frac{\pi}{2}\gamma(F/sin^2\theta))}{1 - exp(-\frac{\pi}{2}\gamma(F/sin^2\theta))} \tag{2.58}$$

where, $F = 1 - tan^2\theta$.

For a certain parameter range in Δm^2 and $sin^2 2\theta$, the MSW effect may convert a ν_e to a ν_μ on its way out of the sun. Similarly, due to the MSW effect it is possible, over a part of this parameter range, for the ν_μ to be converted back to ν_e when passing through the earth. A consequence of the MSW effect due to travel through the earth is an observed neutrino flux which is larger during the night than during the day, since the neutrinos detected during the night have to go through the earth whereas the day time neutrinos come directly from the sun to the earth. This is known as the “day-night” effect. Similar to the study of the seasonal variation of the neutrino flux, a study of the day-night effect requires high statistics and precision measurements of the neutrino flux. Currently none of the solar neutrino experiments have observed a significant day-night effect, which if observed would be an indication of neutrino oscillations.

2.6 Current Status and Future Prospects

Currently the most favored solution to the solar neutrino problem is the hypothesis of neutrino oscillation which implies that neutrinos are massive. Although solar neutrino experiments haven't yet been able to provide definite proof that neutrinos are indeed oscillating, there currently exits very strong experimental evidence of neutrino oscillation from the Super-Kamiokande atmospheric neutrino experiment [78, 79]. Atmospheric neutrinos are produced by collisions of cosmic rays with atoms in the earth's upper atmosphere. These collisions produce neutrinos with energies in the 0.1 GeV to 100 GeV range. Even though the calculations of the absolute flux of atmospheric neutrinos have a large uncertainty ($\sim 20\%$), the ratio of muon to electron neutrino is much better known ($\sim 5\%$), since it comes from the decay chain $\pi \rightarrow \mu\nu_\mu$, $\mu \rightarrow e\nu_\mu\nu_e$. The muon to electron flavor ratio is expected to be roughly 2 (one ν_e from muon decay for every two ν_μ). Experiments studying atmospheric neutrinos primarily measure the double ratio (R) of the observed to calculated ν_μ/ν_e ratios. Two experiments Frejus [80] and NUSEX [81] have measured a ratio of R = 1. Recently, experiments like Super-Kamiokande, IMB [82] and Soudan 2 [83] have reported a ratio of R $\sim$ 0.6 with a much higher level of significance than previous experiments.

Cosmic ray induced neutrinos are produced in the Earth's atmosphere and are detected by Super-Kamiokande since the attenuation of these high energy neutrinos is very small. The path length of the neutrinos vary from 15 km for neutrinos produced directly above the detector, to 13000 km for neutrinos produced directly below the detector. Therefore, by measuring the zenith angle, energy and flavor of the atmospheric neutrinos, one can test the neutrino oscillation hypothesis and determine the Δm^2 and $sin^2 2\theta$ parameters that best describe the data. In 1998, Super-Kamiokande published a paper [78] that provided strong evidence for neutrino oscillation. They found that the atmospheric neutrino data exhibited a zenith angle dependent deficit of muon neutrinos which is inconsistent with expectations based on calculations of the atmospheric neutrino flux. The experimental biases and uncertainties in the prediction of the neutrino fluxes and cross sections were unable to explain the data. However, upon a rigorous analysis of the data they found that their observation was consistent with two-flavor $\nu_\mu \leftrightarrow \nu_\tau$ oscillations where:

$$5 \times 10^{-4}\, eV^2 < \Delta m^2 < 6 \times 10^{-3}\, eV^2 \tag{2.59}$$

$$sin^2 2\theta > 0.82 \tag{2.60}$$

at the 90% confidence level. Since then, the Super-Kamiokande collaboration has collected more data and further analysis has found the preferred neutrino oscillation mechanism and the resultant oscillation parameters to be consistent with the above results.

The Liquid Scintillator Neutrino Detector (LSND) at the Los Alamos National Laboratory in New Mexico has also provided a yet unconfirmed hint of neutrino oscillations [84, 85, 86]. The experiment studying the $\overline{\nu_\mu}$ flux from μ^+ decay at rest has found evidence for the appearance of $\overline{\nu_e}$, which suggests the occurrence of the oscillation $\overline{\nu_\mu} \to \overline{\nu_e}$. They have also studied the ν_μ flux from the decay $\pi^+ \to \mu^+\nu_\mu$ of positive pions in flight and have found evidence for the appearance of ν_e, which suggests the occurrence of the oscillation $\nu_\mu \to \nu_e$. The neutrino oscillation interpretation of the data favors the following range of the oscillation parameters:

$$0.2\, eV^2 \leq \Delta m^2 \leq 10\, eV^2 \tag{2.61}$$

$$0.002 \leq sin^2 2\theta \leq 0.03 \tag{2.62}$$

However, there currently exists controversy regarding the LSND data since another experiment, namely KARMEN-2, which is sensitive to similar oscillation parameter region as LSND has been unable to confirm the LSND findings, in fact it has ruled out a good fraction of the LSND favored region. Therefore the LSND result cannot yet be ruled out. In order to verify the LSND finding, one needs an independent test of its result. A new experiment called MiniBoone is now being constructed at Fermilab in Batavia, Illinois, to further test the results of the LSND experiment. One hopes that the issue will be resolved soon as it has serious implications on the properties of the neutrino.

Presently the Sudbury Neutrino Observatory is playing a very important role in determining whether neutrinos oscillate while traveling from the Sun to the Earth. In the next chapter a description of this detector will be provided.

Chapter 3

The Sudbury Neutrino Observatory

3.1 Introduction

The Sudbury Neutrino Observatory (SNO) is a second generation real-time solar neutrino observatory that has been designed to help resolve the more than three decades old solar neutrino problem. The detector has been designed to not only provide further constraints to the possible SNP solutions but to also provide a model-independent proof of neutrino oscillations. The main objective of SNO is to independently measure the electron neutrino flux and the total neutrino flux (electron, muon and tau neutrinos). If electron neutrinos are experiencing flavor transitions into other states, then the observed electron neutrino flux would be lower than the total neutrino flux, and the neutrino oscillation hypotheses would be tested in a model-independent manner. That is the primary motivation of the Sudbury Neutrino Observatory. In the following sections the neutrino reactions, the SNO detector and detection mechanisms are described.

3.2 Neutrino Interactions at SNO

The SNO detector utilizes 1000 tonnes of 99.92% enriched D_2O to detect solar neutrinos via three distinct reactions. In the following discussion these reactions are described briefly.

3.2.1 The Charged Current Interaction

The charged-current (CC) reaction is given by the following:

$$\nu_e + d = p + p + e^-, \tag{3.1}$$

where, the energy threshold is given by Q = 1.44 MeV. When a deuteron (d) interacts with electron neutrinos through the charged-current exchange of a W^+ boson, the neutron transforms into a proton, and a relativistic electron is emitted. The nucleus that is created now contains two protons. These two repel each other and break the nucleus apart. The protons do not recoil with sufficient energy to create a signal in the detector, however the electron produces Cerenkov radiation which can be detected by the photo-multiplier tubes. The energy and direction of the electron neutrino can be extracted from the Cerenkov signal.

In all cases, in particular at high energies, most of the incoming solar neutrinos's momentum is imparted to the electron. Therefore, the CC reaction is ideal for the study of the electron neutrino energy spectrum. Another advantage of this reaction is the angular distribution of the recoil electrons, which is given approximately by the following equation[87]:

$$W(\theta_e) = 1 - \frac{1}{3} cos\theta_e \tag{3.2}$$

where, θ_e is the angle between the incoming neutrino and the recoil electron directions. This two-to-one backward-forward asymmetry with regards to the Suns' direction can be utilized to separate the CC signal from other signals and backgrounds.

3.2.2 The Neutral Current Interaction

The neutral-current (NC) reaction is given by the following:

$$\nu_x + d = n + p + \nu_x, \tag{3.3}$$

where, x = e or μ or τ. The threshold for this reaction is the deuteron binding energy, which is 2.225 MeV. The NC reaction causes the deuteron to disintegrate without any change of particle identity. An exchange of a Z^0 boson transfers energy into the deuteron, which breaks up into a proton and a neutron, as shown in the above equation. This reaction occurs with equal probability for any flavor of neutrino whose energy is above the 2.225 MeV deuteron binding energy.

This neutrino interaction is observed via the detection of the free neutron in Eq.3.2 and techniques for observing this neutron will be discussed later in this chapter. Since the detection of free neutrons generated by solar neutrinos is an essential measurement at SNO, it is paramount that one understands all forms of neutron backgrounds in the detector. In addition to other forms of neutron backgrounds, those that are generated by through-going muons contribute to the neutron background and will be carefully examined in chapters 5 and 6.

Finally, it is important to appreciate the fact that SNO will detect all neutrinos, regardless of flavor, and the electron neutrino in two independent measurements. A comparison of the two fluxes will therefore provide a definitive test of the neutrino oscillation hypothesis.

3.2.3 The Electron Scattering Interaction

The elastic scattering (ES) reaction is given by the following:

$$\nu_x + e^- = \nu_x + e^-, \tag{3.4}$$

where ν_x can be any flavor of neutrino. Since the interaction with ν_e's can be mediated by $W^{\pm}$ bosons in addition to the Z^0 boson, the cross-section for ν_e

interaction is six times higher than the interaction cross-section for ν_μ and ν_τ. The overall ES cross-section is much lower than the CC cross-section, and even though there are five times more target electrons than deuterons, the expected ES rates are one tenth that of the CC rates. But, in this reaction the scattered electron direction is highly correlated with the incoming solar neutrino direction and this information can be used to separate these events from other events.

3.3 Detector Description

The SNO detector is situated at the 6800 ft.level of INCO's Creighton mine near Sudbury, Canada [88]. This level was chosen because of its appreciable depth which helps to significantly reduce the cosmic ray background and because it is an actively mined level serviced by INCO. The rock overburden provides almost 6200 m.w.e. shielding against cosmic rays and as a result of the through-going muon flux at SNO is much smaller than the flux at the Super-Kamionkande detector. The through-going muon flux will be experimentally determined later in Chapter 5. The excavation of the detector cavity began in March 1990 and the acquisition of production data began in November 1999.

The barrel-shaped cavity that houses the detector is 33 m. high by 22 m. in diameter. The cavity is surrounded by a control room, a water storage and purification room, and various other utility rooms. The whole lab is maintained under clean room conditions and all construction materials were choosen for their radiopurity. The cavity is divided by a deck which is 27 meters above the cavity floor. The upper deck includes the SNO electronics, calibration hardware, and piping which feeds water from the water purification plant to the cavity. The entire cavity below the deck is lined with polyurethane which enables it to be filled with approximately 7800 tonnes of ultra-pure light water which is used to shield the D_2O from radioactive emissions emanating from the rock surrounding

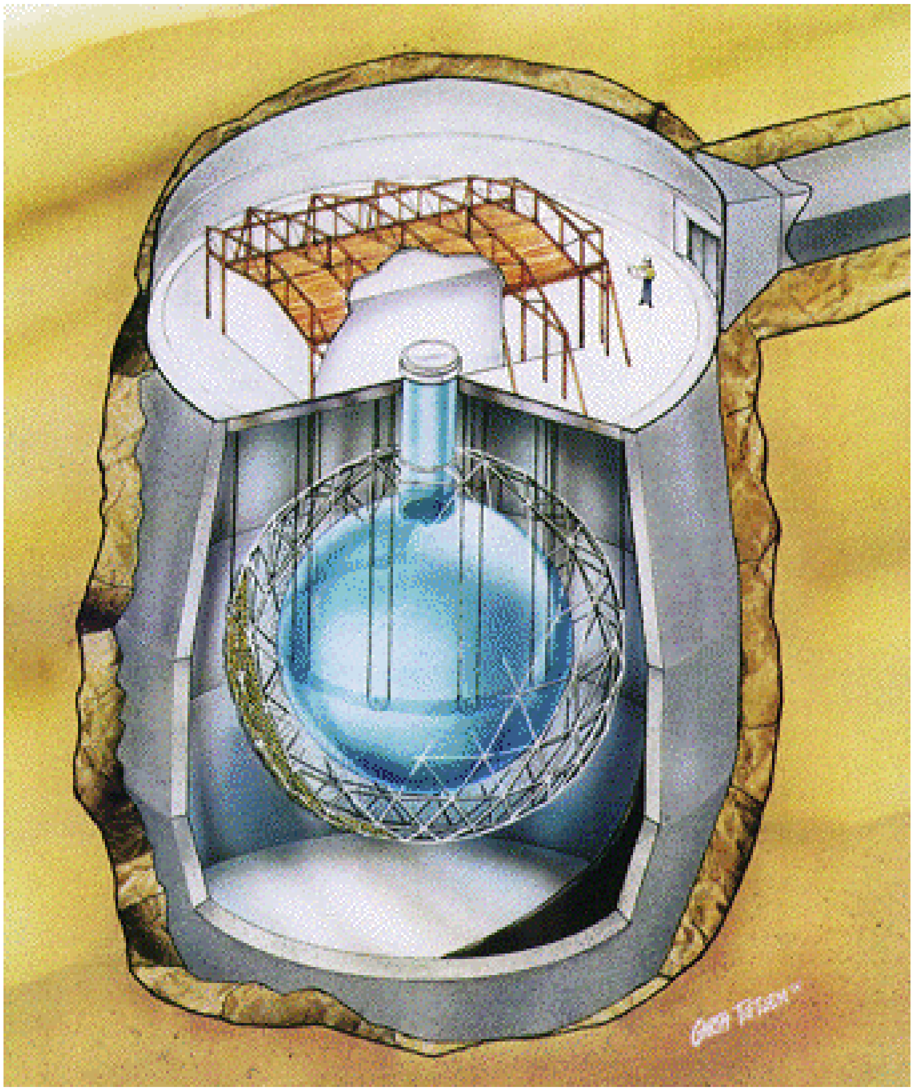

Figure 3.1: An artist's rendition of the SNO detector.

the detector while simultaneously providing mechanical support for the vessel that contains the D_2O.

In the center of the cavity is the 12 meter-diameter spherical acrylic vessel (AV) that contains the 1000 tonnes of D_2O, which has been provided to SNO on loan by AECL with the cooperation of Ontario Hydro. The AV was constructed of 122 panels, each approximately 5 centimeters thick, that were machined and thermoformed before they were assembled underground. The equatorial panels have an approximately 11.4 cm thickness and have grooves for support ropes connected to the deck above. The AV also has a 1.5 meter diameter, 8 meter high chimney made of 5 additional cylindrical segments. The chimney enables the insertion of calibration devices and the D_2O piping from the water utility room. The sphere is made of ultraviolet-transmitting (UVT) acrylic panel for maximum transmittance of light, and the neck of the ultraviolet absorbing (UVA) acrylic to prevent it from behaving like a light guide.

Surrounding the vessel are 9547 Hamamatsu model R1408 PMTs with 20.4-cm photocathode diameter. The requirements for the SNO PMTs are low noise, high efficiency for single photoelectron detection, and a small transit time spread for electrons produced at the photocathode. The energy resolution of the detector and its ability to perform event reconstruction of high accuracy are dependent on these requirements. In addition to these, the PMTs must be low in radioacitivity (K, U, and Th) and therefore the PMT envelopes were constructed of borosilicate and this provided the low radioactivity glass capable of withstanding long term submersion in water.

A geodesic frame, know as the PSUP (PMT Support Structure), anchoring the array of PMTs surrounds the AV. The PSUP has been designed to primarily optimize the overall geometrical efficiency. Furthermore, the PSUP serves as a partial barrier to enable H_2O flow from the inner H_2O volume between the AV and the PSUP to the outer cavity volume. A geodesic structure constructed out of 92 nodes and 270 struts made of a variety of stainless steel alloys make up the skeleton of the PSUP. Mounted on the geodesic structure are 751 hexagonal ABS plastic housings which hold between 7 and 21 PMTs each. The PMTs are placed on average about 2.5 meters away from the acrylic vessel. Horizontal coils are placed around the cavity to cancel out the vertical component of the Earth's magnetic field so as to improve the tube gain by about 10% on average.

3.4 Detection Mechanisms

The SNO detector employs several techniques to detect solar neutrinos. The measurement of neutrinos is carried out indirectly by measuring the various end-products of the neutrino reactions described earlier. Neutrinos are identified by either detecting the relativistic electrons in Eqs. 3.2 and 3.4 or by detecting the free neutron in Eq. 3.3. In the following sections two different detection techniques, Cerenkov light detection and direct neutron detection, are briefly described. In this thesis the detection of muon induced neutrons is carried out via the Cerenkov light detection technique.

3.4.1 Cerenkov Light Detection

In SNO neutrinos can be detected via Cerenkov photons that are radiated by electrons moving faster than the speed of light in the D_2O medium. The relativistic electrons produced in the CC and ES reactions given in Eqs. 3.2 and 3.4 generate Cerenkov light which is detected by the PMTs. For the NC reaction in Eq. 3.3, the Cerenkov light production is the result of Compton scattering of γ-rays subsequent to neutron capture. The free neutrons produced by the NC reaction can be captured on the deuterium nuclei resulting in the release of 6.25 MeV γ-rays. This technique has been used to detect the muon induced neutrons that have been analyzed in this thesis and will be discussed in detail in Chapter 6. The capture efficiency of neutrons in pure D_2O, as shown in Chapter 6, is 27.9%. One can increase the neutron capture efficiency in SNO by adding salt to the D_2O volume. In SNO a plan is in place to dissolve 2.5 tonnes of NaCl to the D_2O volume. The neutron will capture on ^{35}Cl resulting in a 8.6 Mev γ-ray with a 83% capture efficiency [88]. The Cerenkov light produced by relativistic electrons that are Compton scattered by these γ-rays are detected by the PMTs. However, since both the neutral- and charged-current interactions produce Cerenkov light, the two signals combine to produce the total Cerenkov signal in SNO. In other words, the two signals become backgrounds to each other. In order to disentangle the signals, the detector would have to operate first with and then without salt. A separation of the NC and CC signals can then be achieved by a subtraction of one data set from the other, which is a fairly complicated task. Therefore, it becomes evident that one also needs a direct way of distinguishing between NC and CC events in real-time that does not depend on the Cerenkov method. This method will be briefly described in the following section.

In the Cerenkov detection technique, the number of PMTs that are hit in an event, NHIT, is proportional to the number of Cerenkov photons produced and can therefore be used as an estimate of the deposited energy. Furthermore, the hit patterns of the PMTs and their relative timing can be used to reconstruct the event position and direction. The energy, position and direction can be used to separate neutrino induced events from background events. Currently the SNO experiment is operating as a pure D_2O Cerenkov detector and is therefore primarily sensitive to the CC spectrum.

3.4.2 Direct Neutron Detection with NCDs

The discrete Neutral-Current Detector (NCDs) is an array of ^{3}He proportional counters. Each counter is made up of a cylindrical tube filled with a gas mixture which contains ^{3}He. The detection of neutrons, which are thermalized in the D_2O, is achieved by the following reaction which has a cross-section of 5330 barns:

$$^3He + n = p +^3 H + 764\ keV. \tag{3.5}$$

The free neutrons easily penetrate the thin walled tube and are captured by ^{3}He to produce an energetic proton and triton, both of which lose energy by ionizing the gas molecules in the tube. A detailed description of the NCD array can be found in [89].

3.5 Detector Calibration

In order to extract neutrino flux and energy measurements from SNO it is crucial that one understands the optical and energy response of the detector. This involves energy and optical calibration of the detector as well as a determination of the neutron detection efficiency in SNO. The calibration procedure also involves a thorough calibration of the detector electronics. The various calibration sources that are deployed in SNO are done by utilizing the source manipulator, which is a system of ropes and pulleys attached to the inside of the AV allowing for placement of sources in three dimensions.

SNO utilizes a number of optical sources for electronics, timing, and optical calibration. The requirement is that these sources must have short time pulse widths, span the Cerenkov wavelengths of interest, be triggerable, and in general produce isotropic light at varying intensities. SNO uses a nitrogen/dye laser system [90] that uses the Laser Photonics Inc. LN203C laser, which generates pulsed radiation at 337.1 nm up to a 45 Hz pulse rate. The laser can be used to pump dye lasers with wavelengths ranging from 360 to 700 nm. This is the primary optical source at SNO. In addition to this, SNO has light-emitting diodes mounted at various locations on the PSUP which can be used for calibration purposes.

The energy calibration of the SNO detector is achieved by using β and γ sources. The sources are preferably triggered and mono-energetic and together need to span the solar neutrino energy range. These sources emit γ-rays with energies between 1.37 MeV and 19.8 MeV, and β particles with endpoints ranging from 4.3 MeV to 13.1 MeV. A beta spectrum source will be obtained from the decay of the ^{8}Li source which has a roughly 13 MeV endpoint. The decay of ^{16}N with a 7.13 second half-life is used to produce 6.13 MeV (66.2% branch) and 7.12 MeV (4.8% branch) γ-rays. An activated NaI detector is used for lower energy gamma source [91]. Higher energy gammas are produced by a miniature accelerator source that can be lowered into the detector volume [92]. This source produces 19.8 MeV gammas from the ^{3}H(p,γ)^{4}He reaction.

In order to determine the neutron capture efficiency a ^{252}Cf ($\tau_{1/2} = 2.64$ years) source will be used. The source will be encapsulated in an acrylic enclosure containing a plastic scintillator. A total of 4 neutrons and 20 gammas are emitted during the spontaneous fission of ^{252}Cf. The interaction of the γ-rays with the scintillator produces light that is detected by the PMTs and serves as a trigger for the reaction. By moving the source to various locations one can then determine the neutron detection efficiency. The decay of ^{17}N can also be used to produce neutrons where coincident beta can be used as a tag. In order to simulate radioactive background there are sources that include U and Th chain elements encased in acrylic, and a proportional counter source in which ^{228}Th is deposited on the anode wire [93].

3.6 Backgrounds

The energy thresholds for the CC and NC reaction are 1.422 MeV and 2.225 MeV respectively and is zero for the ES reaction. The effective detector threshold is determined by the backgrounds in SNO. In order to properly extract the neutrino signal it is crucial that one thoroughly understands the backgrounds in SNO.

The primary source of the background is due to the cosmic ray muons that are constantly streaming through the detector at a rate of approximately 3 per hour. The muons that penetrate the detector are easily distinguished and are eliminated from the data sample. However, these muons are responsible for producing various spallation products which are also easily eliminated from the final neutrino sample. A detailed discussion of through-going muons and muon induced spallation products can be found in Chapters 5 and 6.

The primary contribution to SNOs backgrounds are β-s and γ-s from the Th and U decay chains. These come from the surrounding rock and radioactive isotopes in the water and other detector materials. These can produce Cerenkov events in the solar neutrino energy range. It should be mentioned that the approximately 7800 tonnes of light water that surrounds the AV helps to minimize the γ-ray contribution from the rock-wall.

In addition to contributing to the Cerenkov background some radioactive isotopes are also responsible for contributing to the neutron background. Two of the daughters of Th and U, namely ^{214}Bi and ^{208}Tl, are problematic for SNO since both of these decay with one γ-ray with an energy that is greater than the binding energy of the deuteron. Therefore, these daughter nuclei contribute to the neutron background by producing free neutrons via the photodisintegration of deuterium. As a result limits had been placed on the Th and U content of SNO construction materials, with the most stringent limits placed on the materials in the D_2O.

In the following chapter a detailed description is provided of the SNO Electronics and Data Acquisition system.

Chapter 4

Data Acquisition System

4.1 Introduction

The electronics and data acquisition (DAQ) systems form an integral part of the SNO detector. The electronics system is ultimately responsible for capturing and recording digital representations of signals that occur within the detector. The primary responsibility of the data acquisition system is to provide the interface and tools to control the electronics and systematically and efficiently gather the captured data from the electronics system for physics analysis.

Once an event occurs in the SNO detector the electronics and data acquisition systems ensure that the event, as part of the data stream, is recorded appropriately for analysis. The DAQ system is additionally responsible for real-time monitoring of the health of the detector. Figure 4.1 depicts at a high level the data flow in the SNO detector. The electronics system acquires data in the form of signal and noise, the DAQ system reads the data from the electronics, builds the events and makes them available for monitoring and analysis.

The author was involved in the design, development, testing and debugging, and commissioning of the SNO DAQ system, which will be described in detail in

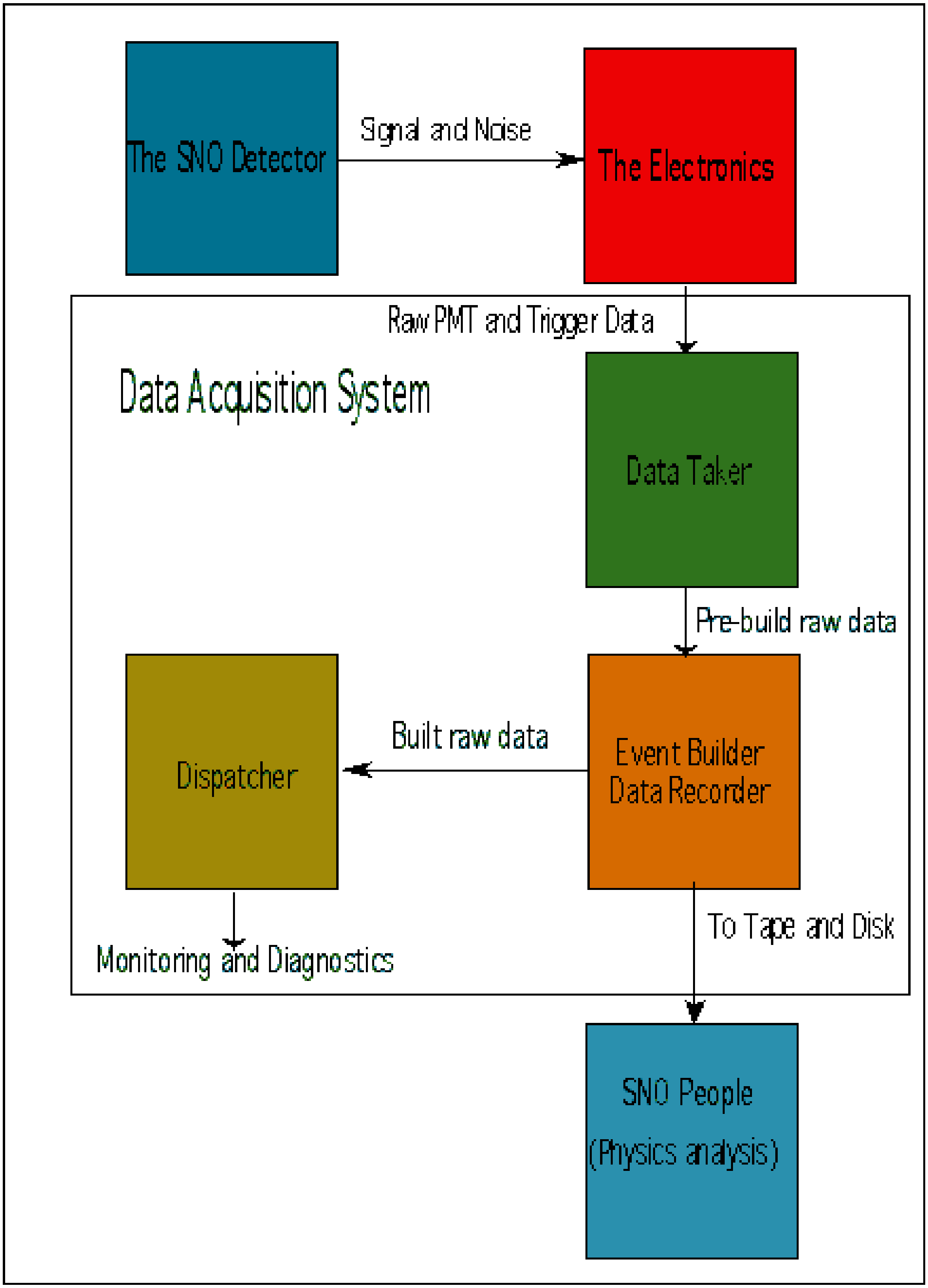

Figure 4.1: SNO Data Flow.

this chapter. To aide the reader the definition of all acronyms used in this chapter are provided in the following section.

4.2 Definition of Acronyms

Provided below are definition of acronyms used in this chapter. The function of the individual hardware and software components will be described in the following sections.

ADC	Analog to Digital Converter
ASIC	Application Specific Integrated Circuit
CPU	Central Processing Unit
CMOS[1]	Complimentary Metal-Oxide Semiconductor
CTC	Crate Trigger Card
eCPU	Embedded CPU
FEC	Front End Card
GPS	Global Positioning System
GT	Global Trigger
GTID	Global Trigger ID
GUI	Graphical User Interface
HV	High Voltage
MAC	Macintosh Computer
MDPM	MAC Dual Port Memory
MTC	Master Trigger Card

---

[1] In CMOS technology, both N-type and P-type transistors are used to realize logic functions. It is the dominant semiconductor technology for microprocessors, memories and ASICs.

PMTIC	PMT Interface Card
SDPM	SUN Dual Port Memory
SNOBUS	SNO Custom Electronics Backplane
TAC	Time to Amplitude Converter
VME[2]	Versa Modular Europa
XL1 & XL2	SNO Translator Cards

Since the DAQ system is tightly coupled to the electronics system, a brief overview of the electronics system is given in the following section.

4.3 SNO Electronics System

One of the primary neutrino detection mechanisms at SNO is the Cerenkov light detection mechanism via the photo-multiplier tubes (PMTs) [3]. The SNO electronics system has been designed and developed to provide sub-nanosecond time and wide-dynamic-range charge measurement for the PMT pulses. While the solar neutrino rate at SNO is very low, the electronics must be able to handle background rates greater then 1 kHz and burst rates from potential supernovae in excess of 1 MHz. The electronics system utilizes three custom application specific integrated circuits (ASICs), commercial Analog-to-Digital converters (ADCs), memory and logic. The analog signal processing and parts of the digital signal processing is carried out by these custom ASICs. The ASIC chip set includes a wide-dynamic-range integrator (SNOINT), a fast and sensitive discriminator/gating circuit (SNOD), and an analog/digital pipelined memory with a timing circuit (QUSN7). High-volume, large-scale-integration commercial com-

---

[2] VME Bus is a flexible open-ended bus system which makes use of the Eurocard standard. It was introduced in 1981 and is defined by the IEEE 1014-1987 standard.

[3] The electronics system for the Neutral Current Detectors (NCDs) will not be discussed in this chapter.

ponents, which include numerous field programmable gate arrays (FPGAs), are also used in the construction of the SNO electronics system. A detailed description of the electronics system can be found in [6].

A high-level overview of the SNO Electronics and DAQ system is provided in Figure 4.2[4]. As represented in Figure 4.2, the electronics system that processes the signals from the PMTs is organized into 19 custom built SNO crates. Each crate can handle signals from 512 PMTs. The signal and high voltage for each PMT are transmitted by a single cable and are connected in groups of 8 at the back of each crate to one of 16 PMT Interface Cards (PMTICs). Each PMTIC is connected to a Front End Card (FEC), which processes the signal using the on-board custom ASICs. The ASICs are situated on four daughter boards (DBs), each handling a total of 8 channels. Each DB consists of discriminator chips, time-to-amplitude converters (TAC), and channel and trigger logic for the detector.

A single FEC processes a total of 32 channels, digitizes the signals, and then stores the digitized data on 4 MB of on-board memory. The FECs are attached to a custom backplane ("SNOBUS") which is responsible for distributing the power and signals. In addition to the 16 FECs, the SNOBUS has attached to it a translator card (XL2) and a trigger-formation card called the Crate Trigger Card (CTC). The XL2 translator card communicates with a similar translator card (XL1), which resides in a separate DAQ VME crate.

The CTC on a SNO crate is responsible for the analog addition of the individual channel triggers and then sending this sum to the Master Trigger Card (MTC)[5]. The analog sum of PMT hits is used by the MTC as the primary event trigger. If the sum is above a programmable threshold, a global trigger (GT) is generated by the MTC. The nominal setting for the trigger time window is 100 ns, slightly longer than the transit time of light across the detector (66 ns).

---

[4] The DAQ Control, VME Crate and the role of the Sun Workstation will be explained in the following section.

[5] There is one MTC for the SNO detector.

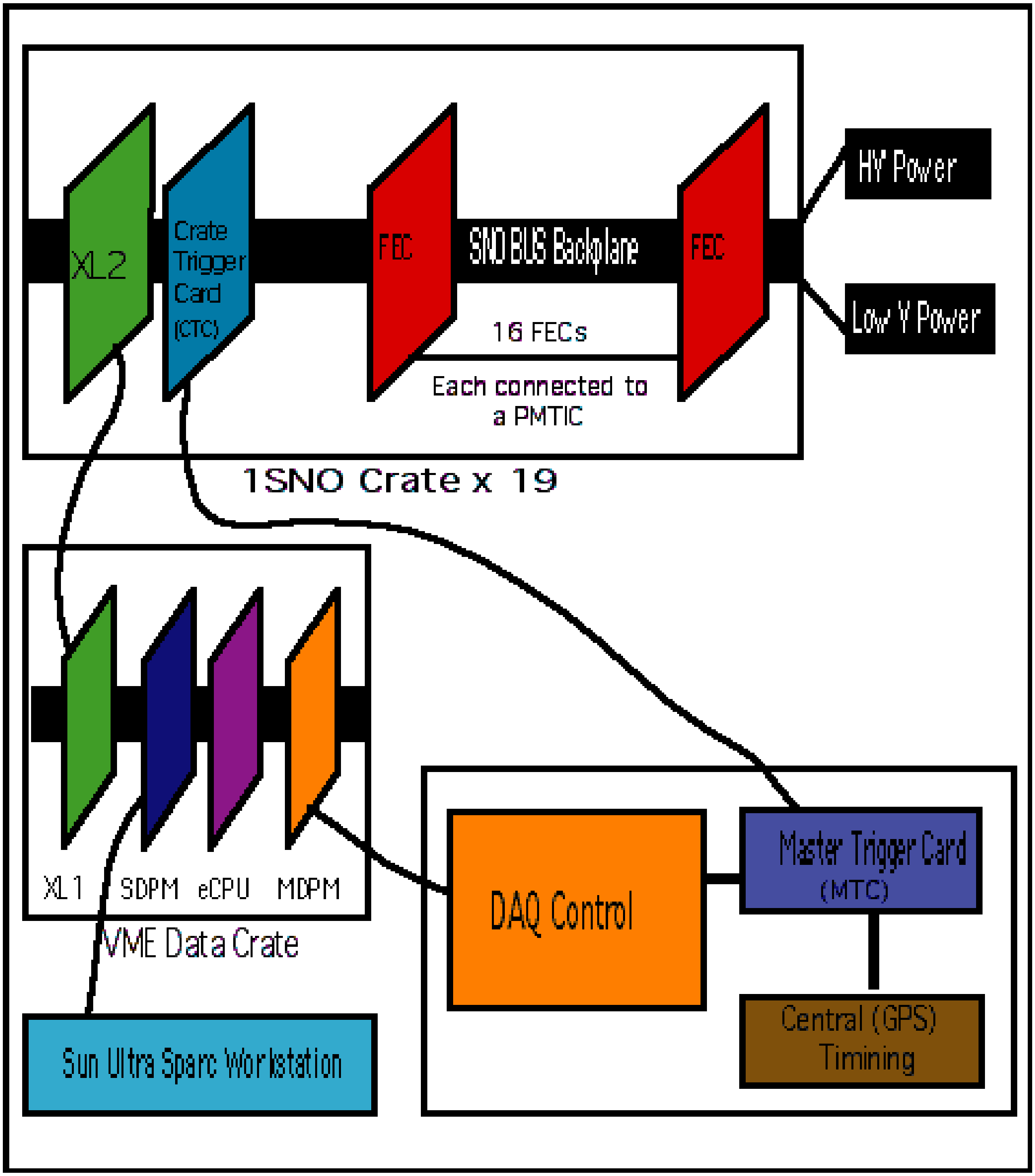

Figure 4.2: High-level overview of the Electronics and Data Acquisition System.

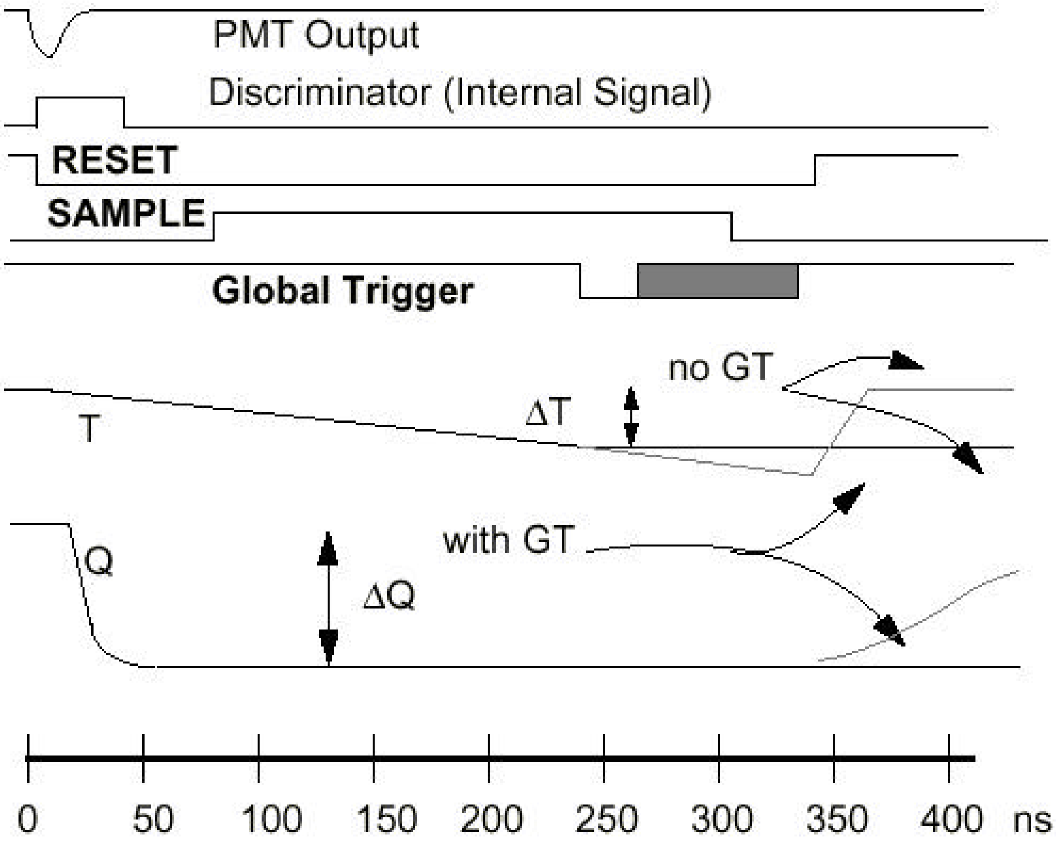

Figure 4.3: Timing cycle of a single channel. With no Global Trigger (GT) present, a channel resets automatically at the end of a timing cycle ($\sim$ 400 ns) [6].

A timing diagram for a single channel is shown in Figure 4.3. The TAC for a given PMT is initiated when the PMT fires and is stopped by the MTC generated GT signal or it is reset if no GT arrives after a programmable internal timeout period. If a GT arrives before the timeout period then four analog voltages (corresponding to one time and three of the four selectable charge measurements) are stored in one of 16 analog memory banks on the CMOS member of the SNO chip set (QUSN7). Additionally, an associated digital memory records the sequence number of the GT, which is used later on by the DAQ system for event building. The QUSN7 chip also has internal counters which are used to track PMT noise rates and count error conditions.

A data available flag from any QUSN7 chip initiates an external 32-channel readout sequencer. The sequencer is a clocked, synchronous state machine that is implemented in a standard FPGA. At the end of the sequencer's cycle, a 3-word, 12-byte, fixed format data structure is loaded into the 4 MB on-board memory of the FEC. This three word descriptor includes, among other things, the measured time and charge, the geographic channel number and the GT sequence number. The memory on the FEC is a standard SIMM DRAM under the control of a commercial dual port controller. The readout of the FEC on-board memory will be described in the following section.

In order to access the memory space of an individual FEC one needs to know the base memory address of that FEC. All 16 FECs that reside in a SNO Crate have associated with it a unique memory base address. This address can be programmed by setting hardware jumpers on the SNO Crate. An individual FEC in a SNO Crate is selected by setting a particular bit on a register (Select Register) on the XL2 translator card. This is achieved via a low level software control tool, which will be described in the following section. The FECs, in addition to memory, also have registers[6] that can be accessed to perform various operations. Similar to the memory space, all 16 FECs in a SNO crate have associated with it a unique register base address. The memory and register address map for the Electronics and DAQ system will be provided in the following section.

Two separate oscillators are utilized to keep a record of the absolute and relative time. The MTC is connected to a commercial Global Positioning System (GPS), which is used to synchronize a 10 MHz universal clock. This clock permits 100 ns time resolution and can be used to determine the absolute time of an event. It can also be used for correlating the observation of astrophysical events (i.e supernovae) with that from other experiments, such as Super-Kamiokande. Furthermore, a 50 MHz quartz oscillator is used to provide a finer resolution

---

[6] A FEC has a total of 64 registers.

(20 ns) for inter-event timing. The electronics system also provides a short time window (20 ns), a summed charge trigger (ESUM), and a programmable trigger (Pulse GT) along with special triggers for calibration devices.

Given the above overview of the SNO Electronics system, a description of the SNO DAQ system will now be provided.

4.4 SNO Data Acquisition System

The design, development and deployment of the SNO Data Acquisition system spanned a period of almost four years from 1995 to 1998. During that time the design and development of a proto-type system was first accomplished. The production DAQ system was based on the design considerations and lessons learned from this proto-type system. This phased approach to the development of the production DAQ system ensured that the end product would be thoroughly tested and understood, thus resulting in a time efficient deployment of a robust DAQ system into the SNO detector.

A single FEC of the electronics system, as described in the last section, consists of a total 32 channels. During the early stages of the development of the FEC a proto-type Front-End-Card (pFEC), consisting of only 8 channels, was designed and developed. The goal was to carefully study and understand this proto-type card before designing the production FEC. In order to perform operations on the pFEC, low-level drivers and a software graphical interface needed to be developed. This requirement resulted in a software tool that served as a proto-type for the eventual design and development of the production DAQ system. This proto-type system was used extensively to study the pFEC functionality, which provided valuable information for the design of the production electronics system. Furthermore, the proto-type DAQ system provided insight into the design considerations for developing an architecture for the production DAQ system. The author designed and developed the proto-type DAQ system.

The task of designing and developing a robust and reliable DAQ system required that the people in the DAQ group, the author in particular, responsible for delivering the system thoroughly understand the various components that make up the electronics system. With an understanding of the electronics the author developed low-level software algorithms that would provide capabilities to control all aspects of the electronics system. The production DAQ system was required to provide the capability to initialize the electronics system, to read-out the data, to build events from raw data, to package the data for distribution, and to monitor in real-time various aspects of the detector health and integrity[7]. These aspects of the DAQ system will be briefly discussed in the following sections.

The capability to initialize and control the electronics system is provided to the end-user via an intuitive and easy to use graphical interface called the "SNO Hardware and Real-Time Control" (SHaRC). An Object Oriented Programming (OOP) language [94], namely C++, was used in the design and development of SHaRC. A brief outline of the design considerations for SHaRC will be presented shortly.

The deployment of the DAQ system into the SNO detector took place in the fall and winter of 1997. The DAQ system was integrated with the complete electronics system (consisting of 9728 channels) and fully operational by the spring of 1998. The DAQ system has been successfully functioning since then and has not faced any major issues. It should be noted that production data taking commenced in November of 1999, at which point the DAQ system had already been thoroughly tested and certified by SNO.

---

[7] The DAQ system also includes the capability to carry out detector calibration. However, this aspect of the system will not be discussed in this chapter. The DAQ group also designed and developed the procedure and algorithms, known as the "TestStand", to test all production FECs and PMTICs prior to their deployment.

4.4.1 DAQ System Requirements

The SNO Data Acquisition system consists of hardware and software components. The hardware and software components had to be designed and selected carefully in order to meet the following requirements:

1) Front end electronics block transfer rate $>$ 2 Mb per sec.

2) Sustained data transfer rate to storage device $=$ 500 kb per ses.

3) System should be very stable.

4) System should require very little operator intervention with minimal downtime.

5) Capability to take SNO Crate off-line without halting data taking.

6) Sorted events written to tape.

7) Sorted events shipped to surface via dedicated ethernet link.

8) Some fraction of data sent to workstation for monitoring.

9) PC used for low-level control and expert monitoring of hardware.

4.4.2 Hardware Components

Provided below is the list of hardware components that are shown in Figure 4.2:

Controllers:

a) SBS BiT3 PCI : VME Bus to MAC PCI, 8 MB Memory (MDPM).
b) SBS BiT3 S-Bus : VME Bus to SUN S-Bus, 8 MB Memory (SDPM).

Single Board Computer:

a) MVME 167 : Motorola 68040 processor, 32 MB Memory (eCPU).

SNO Electronics:

a) XL1 and XL2 Translators : VME Bus to SNOBUS.

b) FEC : 32 Channels per Card, 16 Cards per SNO Crate.
c) CTC : 1 Card per SNO Crate.
d) MTC : 1 Card per detector.
e) PMTIC : 16 Cards per SNO Crate.

Crates:

a) VME Crate : 1 Data Crate and 1 MTC/D Crate.
b) SNO Crate : 19 SNO Crates, 512 Channels per SNO Crate.
c) MTC/A Crate : 1 Custom crate for MTC/A cards.

Power Supplies:

a) High Voltage : For the SNO PMTs.
b) Low Voltage : For the SNO Electronics and VME Crates.

Computers:

a) SUN Ultra Sparc 1/170 Workstation
b) Macintosh Power PC (DAQ Control)

The primary control and interface to the approximately 10,000 channels of electronics, provided by the software tool SHaRC, resides on a Macintosh Power PC[8] (DAQ Control), which has a clock speed of 250 MHz and operates under MAC OS 8.6. The BiT3[9] PCI controller (MDPM) allows the Macintosh to access the memory and register space of the VME Data Crate which contains the eCPU, SDPM and XL1 hardware components. Since SHaRC has access to the Data Crate it can control the FECs via the XL1/XL2 translators. Furthermore, since the eCPU resides on the Data Crate it too can access the FECs via the XL1/XL2 translators.

---

[8] Manufactured by Power Computing.

[9] The Bit3 Computer Corporation was acquired in 1996 by SBS Technologies, an established leader in the embedded computer market. Their web site can be found at http://www.sbs.com/.

The SUN workstation[10], primarily responsible for building and packaging events, accesses the memory of the SUN S-Bus controller (SDPM) to read the raw data that has been collected by the eCPU from the on-board memory of the FECs.

4.4.3 Memory and Register Address Map

In order to initialize, control, and perform read-out of the FECs and MTC, the memory and register space of these cards needs to be properly defined. In Section 4.3 the concept of the memory and register base addresses was introduced. The software tool, SHaRC, and the single board computer (eCPU) require access to the FECs and MTC to perform the various tasks of the DAQ system. These tools use the base addresses to access the memory and register space of the FECs and MTC. In the following, the memory and register address [11] map is provided. Since all FECs in a given SNO Crate have the same register base address and the same memory base address, the base addresses for the individual SNO crates are provided.

MTC Memory Base Address = 0x03800000L
MTC Register Base Address = 0x00007000L

FEC Memory Base Address:

SNO Crate 0 = 0x01400000L
SNO Crate 1 = 0x01B00000L
SNO Crate 2 = 0x01C00000L
SNO Crate 3 = 0x02000000L

---

[10] Manufactured by SUN Microsystems. Their web site can be found at http://www.sun.com/.

[11] The addresses are provided in hexa-decimal notation. The register address is given with respect to the Macintosh. From the eCPU perspective the register addresses are of the form 0xFFFFYYYY instead of the given 0x0000YYYY form.

SNO Crate 4 = 0x02400000L

SNO Crate 5 = 0x02B00000L

SNO Crate 6 = 0x02C00000L

SNO Crate 7 = 0x03000000L

SNO Crate 8 = 0x03400000L

SNO Crate 9 = 0x03C00000L

SNO Crate 10 = 0x04000000L

SNO Crate 11 = 0x04400000L

SNO Crate 12 = 0x04B00000L

SNO Crate 13 = 0x04C00000L

SNO Crate 14 = 0x05000000L

SNO Crate 15 = 0x05400000L

SNO Crate 16 = 0x05B00000L

SNO Crate 17 = 0x05C00000L

SNO Crate 18 = 0x06000000L

SNO Crate 19 = 0x06B00000L

FEC Register Base Address:

SNO Crate 0 = 0x00002B00L

SNO Crate 1 = 0x00003000L

SNO Crate 2 = 0x00003B00L

SNO Crate 3 = 0x00004000L

SNO Crate 4 = 0x00004B00L

SNO Crate 5 = 0x00005000L

SNO Crate 6 = 0x00005B00L

SNO Crate 7 = 0x00006000L

SNO Crate 8 = 0x00006B00L

SNO Crate 9 = 0x00007B00L

SNO Crate 10 = 0x00008000L

SNO Crate 11 = 0x00008B00L

SNO Crate 12 = 0x00009000L
SNO Crate 13 = 0x00009B00L
SNO Crate 14 = 0x0000A000L
SNO Crate 15 = 0x0000AB00L
SNO Crate 16 = 0x0000B000L
SNO Crate 17 = 0x0000BB00L
SNO Crate 18 = 0x0000C000L
SNO Crate 19 = 0x0000D000L

The dual port memory of the BiT3 controllers can be accessed via the following.

MDPM Dual Port Memory Base Address = 0x08000000L
SDPM Dual Port Memory Base Address = 0x00800000L

4.4.4 Software Components

During the design, development and deployment of the DAQ system a large number of software tools were developed to aide in the production of a robust and reliable system. Provided below is the list of software tools that have been developed by the DAQ group and are currently in use during the production data taking phase:

1) *Initialization, Control and Debugging* = SHaRC.
2) *FEC and MTC Event Readout by eCPU* = EVRead.
3) *Building and Packaging of Events by the SUN Workstation* = Builder.
4) *Dispatching events to client machines for monitoring* = Dispatcher.
5) *Real-time and Off-line Monitoring* = XSNOED and SNOSTREAM.

These tools are responsible for providing the core functionality of the DAQ system. The *SHaRC* software tool provides the low-level controls and the main graphical user interface (GUI) through which the user can perform all possible operations on the electronics system. Control and low-level monitoring information, e.g. user commands and eCPU status, are transferred between SHaRC and the eCPU via a set of small, predefined data blocks. SHaRC can initialize the hardware, can take individual hardware elements (channels, cards, crates) in and out of the readout, and can store the current hardware configuration (in terms of which components are present and which are being read out). The hardware configuration is stored in a control block in the MDPM during initialization. SHaRC also provides control to SNO's calibration sources through a manipulator computer that moves the sources inside the detector.

The *EVRead* algorithm has been written in straight C code, with the utilization of some assembly code, to perform the read-out of the FEC and MTC on-board memory. This code is downloaded to the eCPU via SHaRC. The eCPU uses the current configuration stored in the MDPM to perform the readout of the appropriate detector configuration. The readout is performed in a systematic manner by looping through the individual on-board memory blocks of the FECs and MTC. The eCPU will periodically check the configuration block for changes and will alter the readout loop if a change is detected. This mechanism enables one to remove individual cards or even entire SNO crates from the readout loop. The eCPU transfers the data from the FEC and MTC to a circular buffers in the SDPM.

The *Builder* algorithm resides on the SUN workstation and is responsible for reading data from the circular buffer in the dual port memory of the SDPM, then building the events and dispatching them to other processes. The SUN after reading FEC and MTC data from the SDPM, sorts through it and combines PMT hits with the associated MTC trigger information via the common GTID (Global Trigger ID). Once events have been built, they are passed to a FORTRAN process that translates data into ZEBRA format [95] and writes the resulting file to disk.

The *Dispatcher* [12], which resides on a separate SUN workstation, is responsible for sampling events in the data stream and dispatching them to client machines for monitoring. Since this broadcast of data is over the network, client machines can be located practically anywhere. Since the data are labeled, different clients can request data with different labels.

The *XSNOED* and *SNOSTREAM* software tools can run on any Unix or Linux box and can be used as a real-time monitoring and event veiwing tool by connecting as a client to a dispatcher process. The *XSNOED* tool can also be used off-line for viewing and analyzing events. In the following section an overview of SHaRC will be provided.

4.4.5 SNO Hardware and Real-Time Control

The SHaRC software tool provides capabilities for initialization, control and debugging of the electronics and calibration systems. SHaRC has been developed in C++ under the Metrowerks [13] Codewarrior development environment. SHaRC consists of two primary components, i.e. the low and high-level software algorithms that control and drive the electronics and the graphical user interface (GUI) that allows a detector operator to use the provided tools to control the electronics and DAQ system. The author was primarily responsible for designing, developing and testing the low and high-level software algorithms that control the hardware. The design and development of SHaRC was based on the work that was done previously by the author to develop software tools for testing and debugging the proto-type electronics system. The design and development cycle

---

[12] This is a CERN tool that has been integrated into the SNO DAQ system.

[13] Metrowerks develops, markets and supports Codewarrior development tools for the most widely used desktop and embedded operating systems and microprocessor targets. Codewarrior's cross-platform compilers support C, C++, Java and assembly programming languages.

consisted of carefully testing each unit component of the system before integrating the individual components into the larger system. This methodology was rigorously implemented and it resulted in a robust and reliable DAQ system that was easily integrated into the SNO detector.

4.4.6 Object-Oriented Programming (OOP)

An object oriented programming language was used to develop SHaRC. The architecture of the SNO electronics system was ideal for applying Object-Oriented (OO) Design to develop an architecture for the software interface to the electronics system.

Structured analysis, design and programming was used by the software community prior to the development of OO technology. With structured programming methods a large and complex project becomes very hard to manage, maintain and grasp in its totality. In order to solve this problem Object-Oriented Programming (OOP), in particular C++ [14], was developed. The purpose of C++ is to help the programmer comprehend and manage larger, more complex programs.

An object-oriented programming language by definition must provide objects, classes and inheritance. An object is a software entity that combines data and behavior. A class is a programming construct that defines the common data and behavior of a group of similar objects. Think of an object's data as a collection of variables whose values give the object's internal state, and think of an object's behavior as a set of operators that change the state. A class has a name and it describes the state (member data) and services (member function) provided by objects that are instances of that class. During runtime the system when required instantiates an object based on a class definition. Classes can be related

---

[14] C++ was invented by Bjarne Stroustrup in 1980, at Bell Laboratories in Murray Hill, New Jersey. He initially called the new language "C with Classes". In 1983 the name was changed to C++.

by inheritance, where inheritance is the process by which one class can acquire the properties of another class. A good introduction to C++ programming can be found in [96].

Now, let us see how OO technology was applied to the design of SHaRC. The SNO electronics system consists of approximately 9728 logically identical channels (as opposed to physically identical). Furthermore, a total of 32 channels constitute an FEC and there are approximately 304 logically identical FECs. Finally there are 19 logically identical SNO crates, each consisting of 16 FECs. This very modular architecture makes it ideal for the utilization of OO technology in the design and development of SHaRC. From a DAQ perspective the basic building blocks to creating a control interface to the electronics system are the register and memory read and write operations. Since the register and memory base addresses for a given SNO Crate are well defined one can construct two primary classes. One class will perform memory read/write operations and the other will perform register read/write operations, both using the respective base address as the input parameter. With these primary classes one can construct classes that encapsulate the functionality of an FEC, MTC, XL2 and a SNO Crate. In this manner by using OO technology the DAQ group [15] designed and developed the DAQ system from the ground up. This resulted in a software tool that is easily understood and maintained and can be quickly modified and extended if the need arises.

4.4.7 Brief Description of SHaRC

This chapter will now conclude with a brief tour of SHaRC. A detailed description of SHaRC and how it is used at SNO can be found in the "SHaRC Users Guide" [97]. In summary, SHaRC provides run control, configuration and initialization of all hardware components, and control and monitoring of the eCPU based event

---

[15] The author was the chief architect for the design and development of the low-level algorithms to control the FEC, MTC and XL2 components of the electronics system.

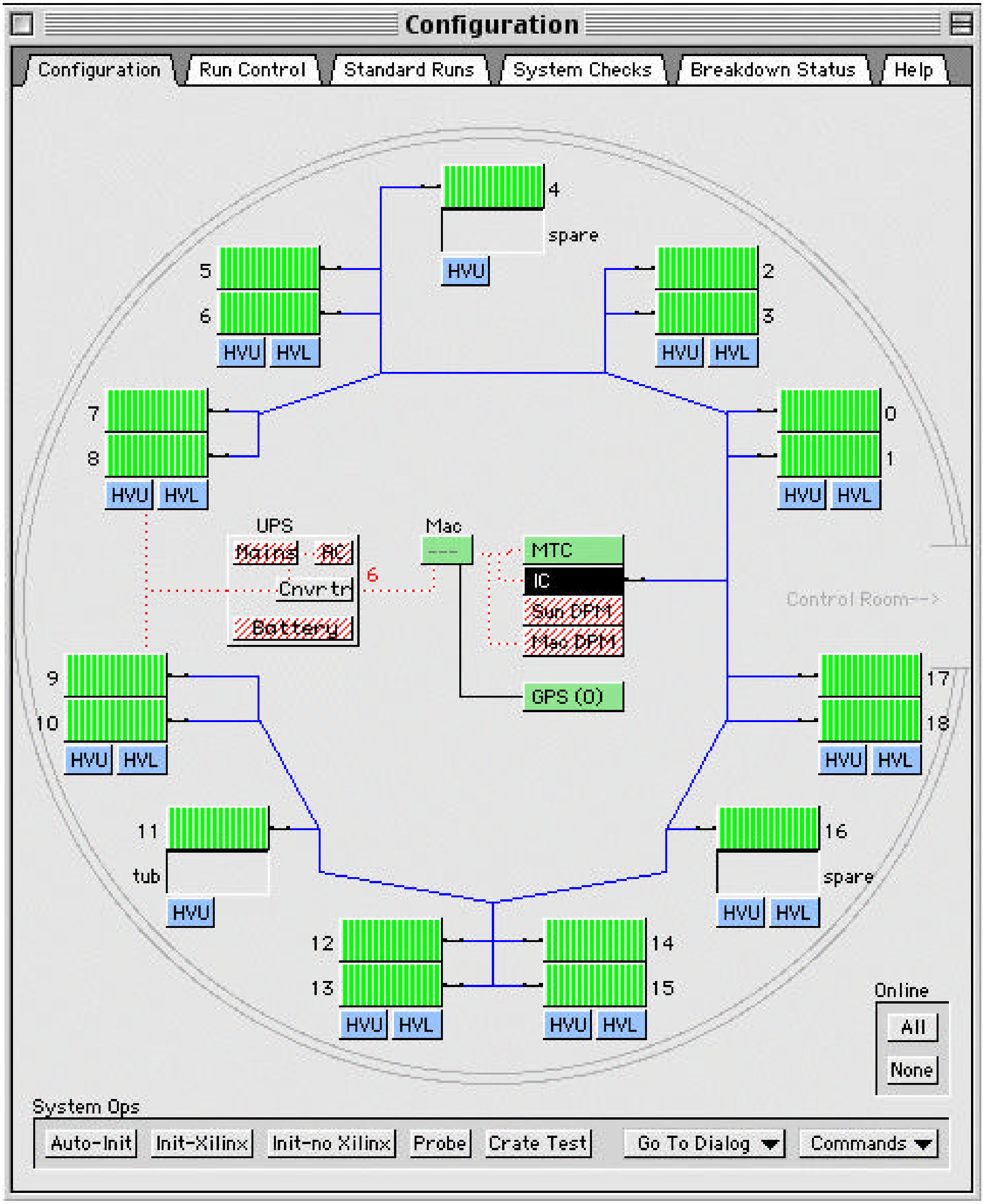

Figure 4.4: SHaRC Configuration Window.

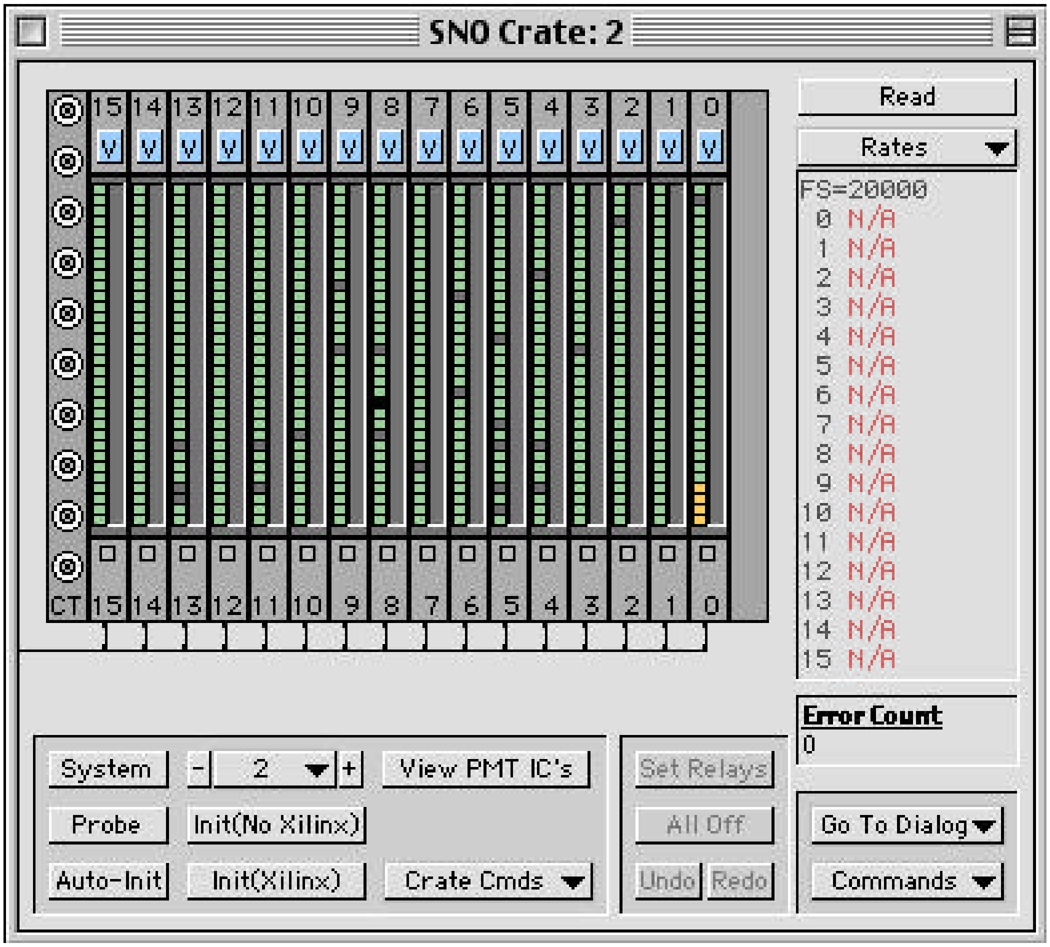

FS=20000
0 N/A
1 N/A
2 N/A
3 N/A
4 N/A
5 N/A
6 N/A
7 N/A
8 N/A
9 N/A
10 N/A
11 N/A
12 N/A
13 N/A
14 N/A
15 N/A

Error Count
0

Figure 4.5: SHaRC SNO Crate Control Window with FEC View.

read-out and the SUN based event builder processes. Furthermore, SHaRC provides the control to a separate PC based calibration computer which allows the insertion and movement of various calibration sources.

In Figures 4.4, 4.5 and 4.6 three screen shots of the SHaRC graphical user interface (GUI) are shown. It should be noted that there are many more windows in the SHaRC application. Detailed discussion of the different windows will not be presented in this chapter since they can be found in the "SHaRC Users Guide".

In Figure 4.4 the main SHaRC configuration window is displayed. The GUI was designed in such a way so that individual SNO Crates were displayed similar to their positions at SNO. In other words, the application was developed so that it would be user friendly and intuitive. As a result it became a fairly simple task to train new detector operators. In addition to the SNO Crates, the figure shows the physical connections between the various hardware components. Two SNO Crates are grouped together in a rack and each rack has two high voltage supplies, each controlling the HV for a particular crate. The voltage control software can be accessed from this window by clicking on the HVU (High Voltage Upper) or HVL (High Voltage Lower) boxes below the crates. The author was responsible for the initial design and testing of the HV control software. From the configuration in Figure 4.4, it can be seen that all crates are on-line.

The configuration of the system is determined by performing the “Probe” operation found on the bottom left-hand corner of Figure 4.4. The “Auto-Init” button automatically initializes the whole detector, i.e. it first performs a “probe” of the detector to determine the configuration and then goes through the predefined steps to initialize the individual SNO crates and MTC. Appropriate error messages are displayed if initialization fails in order to assist the operator in understanding the cause of the problem. The initialization routine is a perfect example of object-oriented programming. Given the modular architecture one can construct a class, call it $INIT\_CRATE$, that performs all the steps to initialize a single crate. Once that is defined the full initialization method would consist of instantiating an $INIT\_CRATE$ object within a loop that cycles through the different crates. In a similar fashion the initialization of a single crate would consist of instantiating an $INIT\_FEC$ object within a loop that cycles through the 16 individual FECs. Code reusability is one of the key values that OOP provides.

The initialization routine is a large and complex piece of algorithm that utilized many of the low-level algorithms that access and program the various components of the XL2, FEC and MTC hardware. The author was responsible for designing, testing and debugging all low-level tools that control the SNO electronics. Once these tools were developed and thoroughly tested the development of

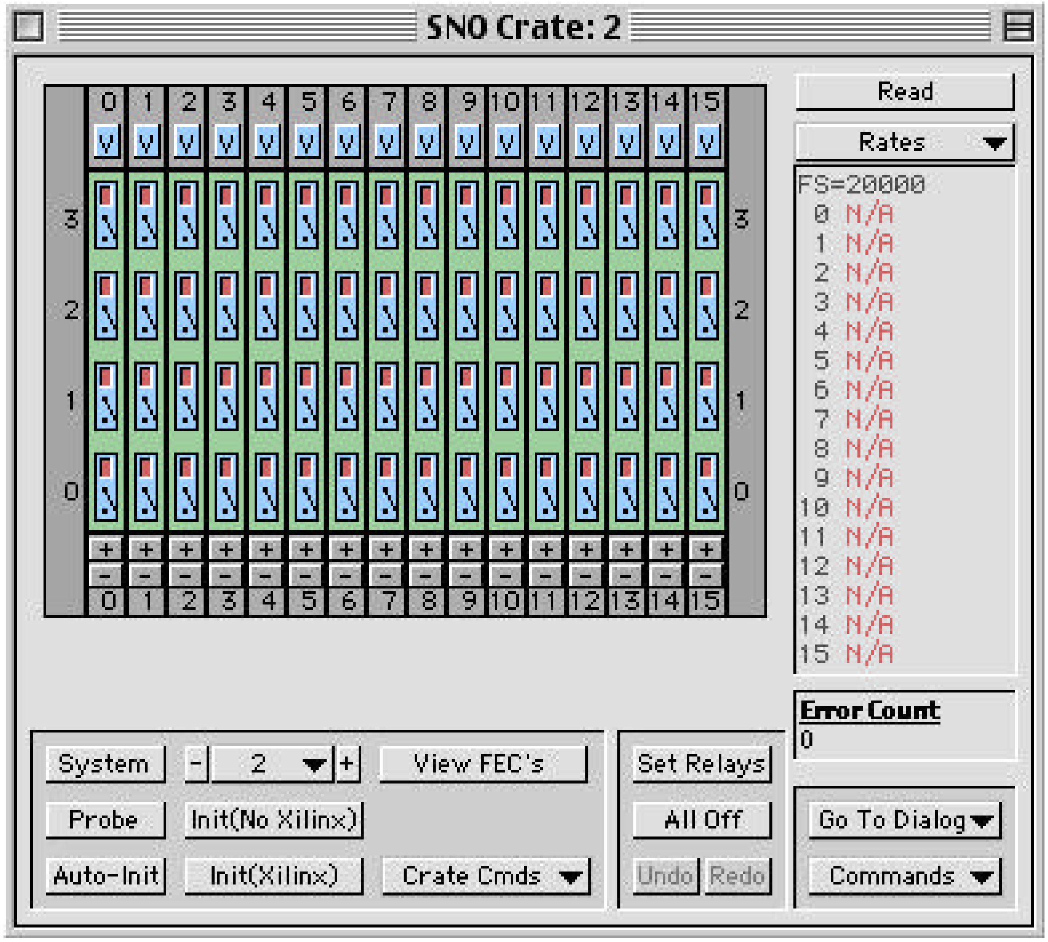

```
FS=20000
 0 N/A
 1 N/A
 2 N/A
 3 N/A
 4 N/A
 5 N/A
 6 N/A
 7 N/A
 8 N/A
 9 N/A
10 N/A
11 N/A
12 N/A
13 N/A
14 N/A
15 N/A
```

Error Count
0

Figure 4.6: SHaRC SNO Crate Control Window with PMTIC view.

the initialization routine was a fairly easy task. This was made possible by the object-oriented design of the software architecture which made the code easy to understand, manage and modify.

Figure 4.5 shows an individual SNO crate, i.e. SNO Crate 2. This window can be accessed from the configuration window by clicking on a particular crate. In this figure the FECs are shown. Figure 4.6 also provides a view of SNO Crate 2, but in this case the PMTICs are shown. In both of these pages diagnostics for this particular crate is provided on the right-hand side. At the bottom of the window one can perform various operations on the crate or from the bottom right-hand corner one can go to a different dialog box or perform other commands. The GUI for SHaRC was also developed in C++.

4.5 Conclusion

In this chapter the SNO Electronics system was briefly described, since an understanding of the DAQ system is contingent upon an understanding of the electronics. The goal of this chapter was to provide a high-level understanding of the DAQ system and to provide the motivation and design considerations that were taken into account in using OO technology for the development of the DAQ system.

Chapter 5

Muon Characteristics at SNO

5.1 Introduction

One of the primary goals of the SNO experiment is to measure the total ^{8}B solar neutrino flux. This task, as mentioned in Chapter 3, is accomplished by the detection of the following neutral-current[NC] reaction:

$$\nu_x + d = \nu_x + p + n \tag{5.1}$$

Since all flavors of neutrinos (ν_x) take part in this reaction, one can determine the total number of ^{8}B solar neutrinos impinging on the detector by counting the number of neutrons that are produced in the above reaction, assuming the absence of sterile neutrinos in the solar neutrino flux. In order to accurately determine the NC reaction rate, it is imperative that one properly accounts for the various forms of background events that can distort signal.

There are a number of background sources of neutrons in SNO. The sources of backgrounds to the neutral-current signal resulting from D_2O are shown in Table 5.1. The estimated neutron background numbers provided in this table are based on various measurements and calculations [8]. The estimated muon-induced neutron background is derived in Chapter 6.

Neutron Sources			Expected y^{-1}
Neutrons from NC Interaction (BBP98)			4610
Muon-induced Neutrons			3920
Other Neutron Sources	Rate	Unit	Expected y^{-1}
^{2}H(γ,n)^{1}H: ^{208}Tl [Th]	95	n μg^{-1} y^{-1}	1060
^{2}H(γ,n)^{1}H: ^{214}Bi [U]	8.9	n μg^{-1} y^{-1}	100
^{2}H(γ,n)^{1}H: ^{214}Bi [^{222}Rn]	8.9	n μg^{-1} U y^{-1}	445
Fission	0.43	n μg^{-1} U y^{-1}	5
^{2}H(α,αn)^{1}H [Th]	1.9	n μg^{-1} y^{-1}	21
^{2}H(α,αn)^{1}H [U]	0.80	n μg^{-1} y^{-1}	9
^{2}H(α,αn)^{1}H [^{222}Rn]	0.80	n μg^{-1} U y^{-1}	40
^{17}O(α,n)^{20}Ne [Th]	0.027	n μg^{-1} y^{-1}	0
^{17}O(α,n)^{20}Ne [U]	0.074	n μg^{-1} y^{-1}	1
^{17}O(α,n)^{20}Ne [^{222}Rn]	0.074	n μg^{-1} U y^{-1}	2
Total neutron background from other sources			1683

Table 5.1: NC signal and neutron backgrounds to the NC Signal [8]. The right hand column shows the expected number of neutrons produced within the heavy water volume. The calculation to determine the expected muon-induced neutrons per year can be found on page 149.

From Table 5.1 it can be seen that the largest source of background comes from neutrons produced by nuclear spallation of the ^{16}O and ^{2}H nuclei in heavy water by high energy atmospheric muons. Other sources arise from photodisintegration of deuterons by gammas, impurities in the heavy water and radiation emanating from the surrounding cavity rock. The analysis that will be presented in Chapter 5 will focus on understanding the properties of atmospheric muons with the goal of creating the framework from within which a detailed analysis of muon-induced background events can be performed. The primary objective is to understand the properties of muon-induced neutrons that serve as a background to the neutral-current signal.

In addition to producing neutrons, atmospheric muons can produce other radioactive nuclei which then decay by emitting electrons, positrons or γ-rays with energies ranging from a few MeV up to about 20 MeV. Since the energies of these events are similar to the energy signature of solar neutrino events, these "spallation" events become a source of background. In order to identify and efficiently eliminate muon-induced background events from the final neutrino sample one needs to first accurately identify and characterize the muons that are constantly streaming through the detector. Only by isolating the muons can an attempt be made to remove the background events that are produced by them.

In the current chapter the analysis results pertaining to the identification and characterization of muons will be presented. In this analysis, through-going muons have been identified via a combination of a software algorithm, called MuonID, and a careful hand-scanning method. The hand-scanning method demonstrated the MuonID algorithm to be an efficient tool at identifying through-going muons in SNO. The long term goal is to perform an analysis of through-going muons with a finely tuned MuonID algorithm. The ultimate objective of any future analysis will be to eliminate all biases that could possibly be introduced by the hand-scanning method in identifying through-going muons. Finally, in Chapters 6 and 7 the characteristics of muon-induced spallation products will be studied.

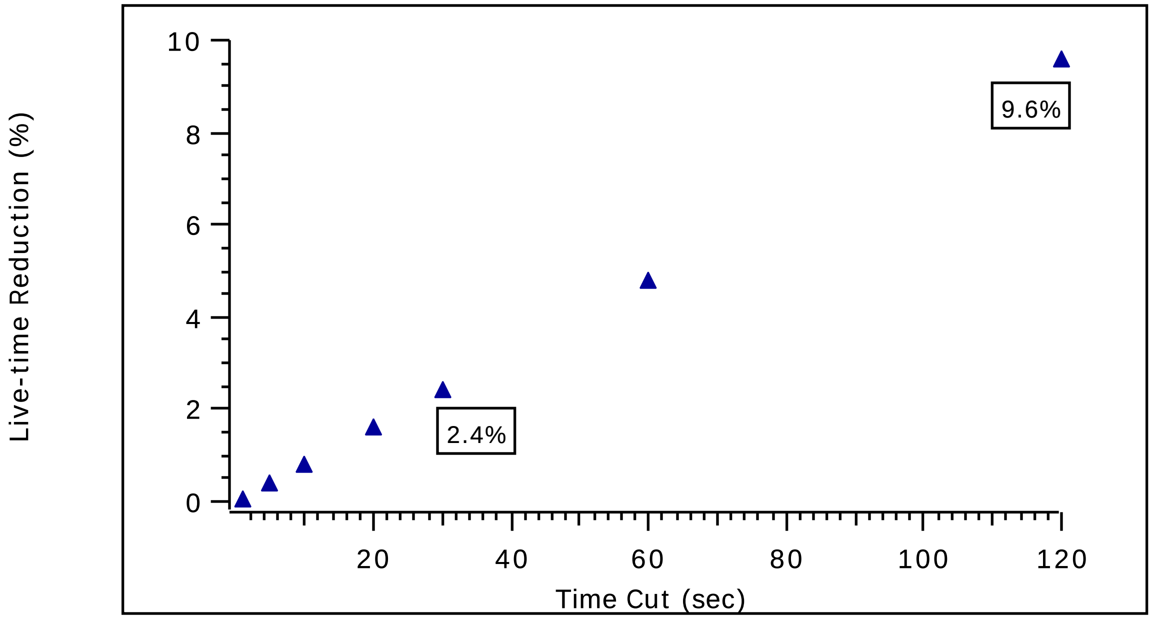

Figure 5.1: Live-time Reduction from Muon Time Cut.

Muon-Tagged Time Cut

Unlike other background events, muon-induced spallation events can be readily eliminated since these events are preceded by high energy muons. Therefore, if muons at SNO can be accurately identified then one can place a simple muon-tagged time cut on the data to significantly reduce the background events induced by muons. For example, after thermalization neutrons are captured by deuterium with a characteristic mean capture time of 40 ms and the longest lived radioactive isotope that could potentially be produced by muon spallation (^{11}Be) has a half-life of 13.8 seconds. Therefore, in order to significantly reduce the signal contamination due to muon spallation, one could very simply eliminate 30 seconds of data following a muon event.

At the SuperKamiokande[SuperK] detector the rate of muons is 2.2 Hz [98] and hence it is not at all feasible to employ such a conservative time cut at SuperK, since it appreciably compromises the detector live-time. However, the measured atmospheric muon rate at SNO is approximately 69 day^{-1} or 0.80 mHz. Given this low muon rate, one can utilize a fairly conservative muon-tagged time cut to eliminate muon induced background events with little effect on the detector live-time and performance. Given a muon rate of 0.80 mHz and assuming no muon overlap within the muon-tagged time cut window, Figure 5.1 shows the maximum percentage reduction in detector live-time as a function of the applied time cut. From this figure it can be seen, for example, that a muon-tagged time cut of 30 seconds would result in a 2.4% live-time reduction. Therefore, given a detector live-time of 365 days, a 30 second cut following each individual muon would reduce the live-time by a maximum of only 8.75 days. To first order this is a very reasonable time cut, but the ultimate goal is to sacrifice as little live-time as possible. This can only be done by a thorough and systematic study of all muon-induced spallation products.

Objective

The ultimate goal is to analyze muon-induced neutrons produced within the fiducial volume of the detector. Therefore, the study of muons is designed to provide a list of muons that could potentially produce neutrons within the D_2O. In this process the total muon rate at SNO, among other useful characteristics, will be determined. The muon rate will be used in Chapter 6 to determine the muon-induced neutron rate at SNO, which wlll be compared to results from past underground experiments.

Furthermore, in addition to determining the average number of neutrons produced by muons at the depth of SNO, it will be demonstrated that these neutrons can be utilized to perform an independent measurement of the SNO γ-ray energy calibration. The results from this type of γ-ray energy calibration will then be compared to calibration results obtained from the SNO ^{16}N γ-ray calibration source. Unlike deployable devices which need to be occasionally scheduled to perform energy calibration of the detector, muon-induced neutrons are being constantly produced at SNO at a steady rate and, therefore, one can use them for calibration purposes without any disruption to normal data taking.

5.2 Muons at SNO

5.2.1 Introduction

High energy atmospheric muons are generated continuously by the interaction of primary cosmic rays with the nuclei of the Earth's upper atmosphere. The primary cosmic ray particles impinge on the Earth's atmosphere at the rate of about 1000 $m^{-2}s^{-1}$. These particles consist of ionized nuclei, of which about 90% are protons, 9% are alphas and the rest are heavier nuclei [99]. Most cosmic ray particles are relativistic with energies typically a few GeV or slightly greater. A very small fraction of these have ultrarelativistic energies as large as 10^{20} eV. These energetic primary cosmic rays impinging upon the Earth's upper atmosphere produce copious amounts of pions and kaons which subsequently decay into neutrinos and muons. These reactions can be of the following form:

$$p +^{14} N \rightarrow \pi^+(K^+) + X \qquad \pi^+(K^+) \rightarrow \mu^+\nu_\mu \tag{5.2}$$

Relativistic muons are relatively long-lived particles with a small cross section for interaction and as a result they are extremely penetrating. The neutrinos and muons of the above reaction are thus the "penetrating components" of the cosmic rays. Underground detectors looking for low-energy neutrino events from the Sun and other astrophysical sources are continuously bombarded by these penetrating particles. The muons, being charged particles, are easy to identify, whereas the neutrinos are difficult to detect. In addition to the muons, the high energy neutrino component of the cosmic rays interacts with the rock surrounding the detector to produce energetic muons that can also penetrate the detector. In this study all muons that go through the detector, in particular those that go through the heavy-water, will be considered since they can be responsible for producing spallation events within the fiducial volume of the detector.

5.2.2 Muon Selection Procedure

Objective

The goal is to develop a procedure that will not only identify muons but will also determine whether a particular muon has gone through the AV or not. A description of the muon selection and categorization procedure will now be presented.

Muon Selection and Categorization Procedure

The muon selection and categorization procedure requires the use of certain basic tools and processes, which are provided and maintained by the SNO collaboration. Below are brief descriptions of the tools that were used to perform the analysis. A more detailed description of these tools and processes can be found in [6].

- SNOMAN : This is the official SNO Monte Carlo and Analysis software package. It is used for generation of SNO Monte Carlo data and for analysis of SNO data files. In this study Version 4.0081 was used for Monte Carlo and data analysis.

- SNODB : This is the official SNO database and it is based on the CERNLIB package HEPDB. SNODB contains ZEBRA banks that consist of all the information about calibrations and detector status, configuration, and performance which is needed to interpret SNO data. Version 3.07.03 was used for analysis.

- XSNOED : A SNO graphical event display package. Version 4.2.0 was used to aid in the analysis process.

The analysis procedure to identify and categorize muons consists of the following three parts:

- Data Selection : A total of 103 production runs between run number 10000[11/2/99] and run number 11431[3/15/00] were selected for analysis of muons and muon-induced spallation events. The total live-time for the selected runs corresponds to approximately 85.7 days. The run selection criteria are discussed in Appendix A. Furthermore, the list of selected runs used in this study, with live-time and number of muons identified within each individual run, can be found in Table A.1 of Appendix A.

- MuonID Algorithm : A custom SNOMAN algorithm called MuonID is applied to the selected data files as a first pass filter to identify and write candidate muons to Reduced Data Set[RDS] files. In addition to identifying possible muon events, the algorithm also provides an initial guess to the path length of the muons. Muons that go through the AV are called AV-going muons, whereas muons that do not are called non-AV going muons. Based on path length muons are categorized as AV-going or non-AV going muons. Muons that enter and exit the detector are called through-going muons. A detailed description of the MuonID algorithm can be found in Appendix B.1.

- Hand-scanning : The RDS files are hand-scanned by trained "scanners" to determine the efficiency of the MuonID algorithm. In this process true positives are identified and false positives are eliminated from the candidate muon sample. Furthermore, a subset of the selected runs are fully scanned so as to determine the percentage of muons missed by the MuonID algorithm. The hand-scanning procedure also determines the MuonID accuracy of the AV-going vs. non-AV going muon categorization. A detailed description of the hand-scanning procedure can be found in Appendix B.2.

The MuonID algorithm was not optimized to identify partially or fully contained events [PC or FC events]. These are categorized as non-AV going events. The PC events are primarily muons that enter the detector, then stop and are either captured by a nucleus or decay into an electron and (corresponding) neutrinos with a characteristic decay time of 2.2 μs. For this case the entering muon does not exit the detector. In most cases MuonID identifies PC events as through-going muons. However, during the hand-scanning procedure they are properly labeled as PC muons. A total of 27 runs were fully hand-scanned and a list of 22 PC events identified by this method is provided in Table A.3 of Appendix A. On the other hand, the FC events are not identified by the MuonID algorithm, since for these events the PMTs that are outward facing [OWL] do not fire and MuonID requires that at least 4 OWL tubes fire for a given event to be considered as a possible muon. However, these events can be identified by a full hand-scan of the raw data files. The FC events are created by neutrino-nucleon interaction within the detector. They can be either muons or electrons depending on the flavor of the incoming neutrino. The task of distinguishing fully contained muons from fully contained electrons was not part of this study. From the 27 fully scanned runs a total of 21 FC events were identified and a list of these events is provided in Table A.2 of Appendix A.

The muon selection process has analyzed a total of 129,239,415 events in 103 production runs with a detector live-time of 85.65 days. This corresponds to an average data rate of approximately 17.5 Hz. The muon selection process imposed an NHITS cut of 350 and this yielded a total of 102998 events [0.08%] before any other cuts were applied. Then a combination of cuts in the MuonID algorithm and hand-scanning yields a total of 5916 muons, i.e. approximately 5.7% of all events above an NHITS of 350 are muons. Figure 5.2 shows the NHITS distributions of all events [blue] and muons [red] above an NHITS of 350. The y-axis is logarithmic and the bin-width of the horizontal NHITS scale is 80. It can be seen from the plot that the majority of the background events are in the lower NHITS region.

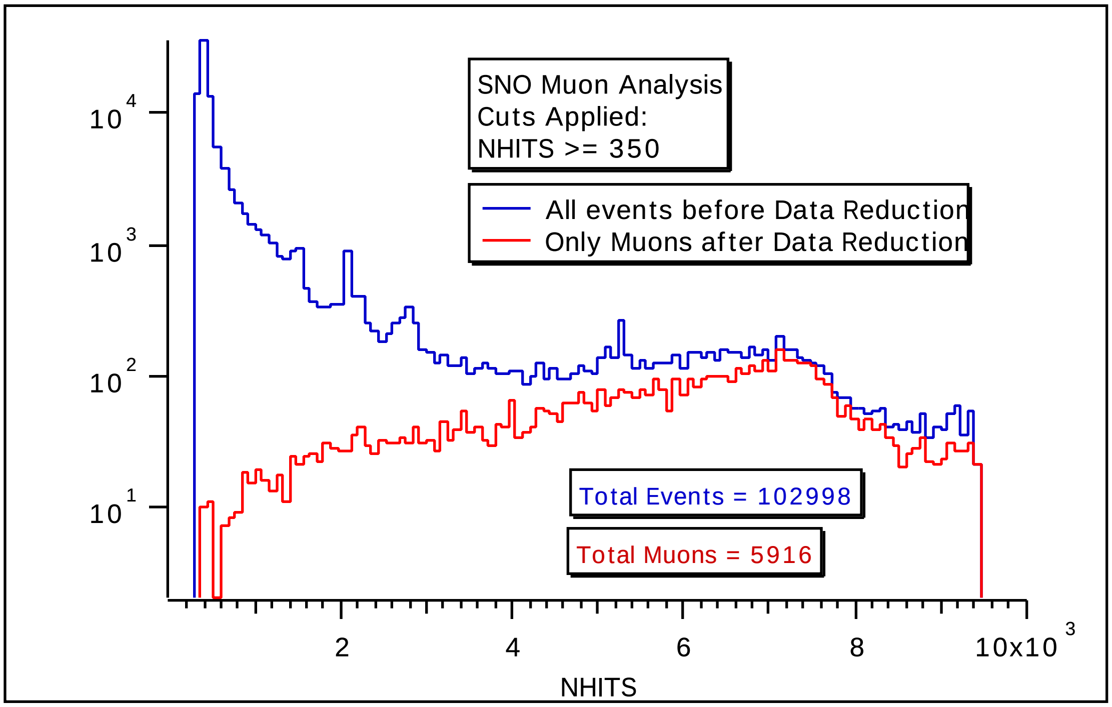

Figure 5.2: Muon Data Selection Results : NHITS Distribution

These events are mostly flashers and neck events[1].

In this study the hand-scanning procedure was utilized to demonstrate how well the MuonID identifies true muons, rejects false muons, and categorizes muons. Since the determination of the expected muon-induced neutron rate at SNO is dependent on the AV-going muon rate, account will be taken of the errors associated with the overall muon categorization procedure. In the next section the muon selection efficiencies of the MuonID algorithm will be presented.

---

[1] Flashers are events that are most likely produced by a breakdown in the dynode structure of the PMTs. These events can be easily identified by their characteristic light pattern and from the fact that in almost all cases the flashing PMT fires its adjacent channels. The neck events are produced in the neck region of the AV and are easily distinguished by their characteristic light patterns.

Total Runs Analyzed	103
Start Date	11/2/99
End Date	3/15/00
Start Run Number	10000
End Run Number	11431
Total Muons Identified	5897
Total Live-time	85.65 days

Table 5.2: Muon Selection via MuonID and Hand-Scanning.

Muon Selection Efficiencies

In Tables 5.2 and 5.3 the results of the muon selection process are summarized. From these tables it can be seen that the MuonID and hand-scanning procedure have identified a total of 5897 events as muons. These include 5842 through-going muons, 52 PC muons, and 3 FC muons with associated decay electrons. In addition to the 5897 muons, 19 FC events were identified without any subsequent decay electrons (these FC events could be either muons or electrons). So a grand total of $(5897+19) = 5916$ events were identified by a combination of the MuonID algorithm and hand-scanning procedure. Furthermore, according to the muon categorization procedure, 2704 events have been labeled as AV-going muons and a total of 3193 events have been labeled as non-AV going muons.

In order to determine the efficiencies of the MuonID algorithm only through-going muons are considered. The PC and FC events will not be considered in this calculation since the MuonID is not designed to identify these events. From Table 5.4 it can be seen that the MuonID does a very good job of rejecting false muon

AV-going Muons	2704
Non-AV going Muons	3193
Through-going Muons	5842
FC + PC Events	22 + 52 = 74
PC with decay e^-	31
PC without decay e^-	21
FC with decay e^-	3
FC without decay e^-	19

Table 5.3: Muon Categories from Selection Process.

Total Runs Analyzed	103
Total Muon Candidates	5846
Total False Positives	21 [0.4%]

Table 5.4: False Muon Rejection Efficiency.

Number of Runs	27
Live-time	27.92 days
Through-going Muons	1875
Muons Missed by MuonID	17 [0.9%]
FC + PC events	43
PC with decay e^-	10
PC without decay e^-	12
FC with decay e^-	3
FC without decay e^-	18

Table 5.5: Full Hand-scanning Results and Muon Identification Efficiency.

events. Of the 5846 events that the MuonID had identified as possible through-going muon events, only 21 were found to be false muons (via hand-scanning). So the MuonID can introduce a ∼0.4% contamination to the final muon sample. From Table 5.5 it can be seen that the MuonID also does a good job at identifying true muons. A complete hand-scan of 27 runs was performed and in this process a total of 1875 through-going muons were identified. The MuonID was then applied to these 27 runs and it was found that the algorithm missed 17 muons [0.9%]. Therefore, the MuonID is 99.1% efficient at identifying true muon events.

From Table 5.6 it can be seen that the MuonID algorithm miscategorizes muons 7.8% of the time. This is not surprising since the MuonID is not a true muon fitter and is not intended to accurately determine the muon path length or direction. Based on hand-scanning of the RDS files the MuonID categorization efficiencies were determined. With the assumption that the hand-scanning procedure is 100%

Total Through-going Muons	5842
Miscategorized Muons	459 [7.9%]
AV-going Muons	2704
False AV Muons	194 [7.4%]
Missed AV Muons	265 [9.8%]
non-AV going Muons	3138
False non-AV Muons	265 [8.3%]
Missed non-AV Muons	194 [6.2%]

Table 5.6: MuonID Categorization Summary for Through-going Muons.

efficient at determining whether a muon is AV or non-AV going, it is found that MuonID has erroneously categorized non-AV muons as AV muons 7.4% of the time [194 events], i.e. these events are false AV muons. Furthermore, it has erroneously categorized AV muons as non-AV muons 8.3% of the time [265 events], i.e these events are false non-AV muons. On the other hand, 9.8% of the time the MuonID algorithm failed to identify a true AV-going muon and 6.2% of the time it failed to identify a true non-AV going muon.

In the following section characteristic distributions of the muons that have been selected by the MuonID algorithm and hand-scanning procedure will be presented.

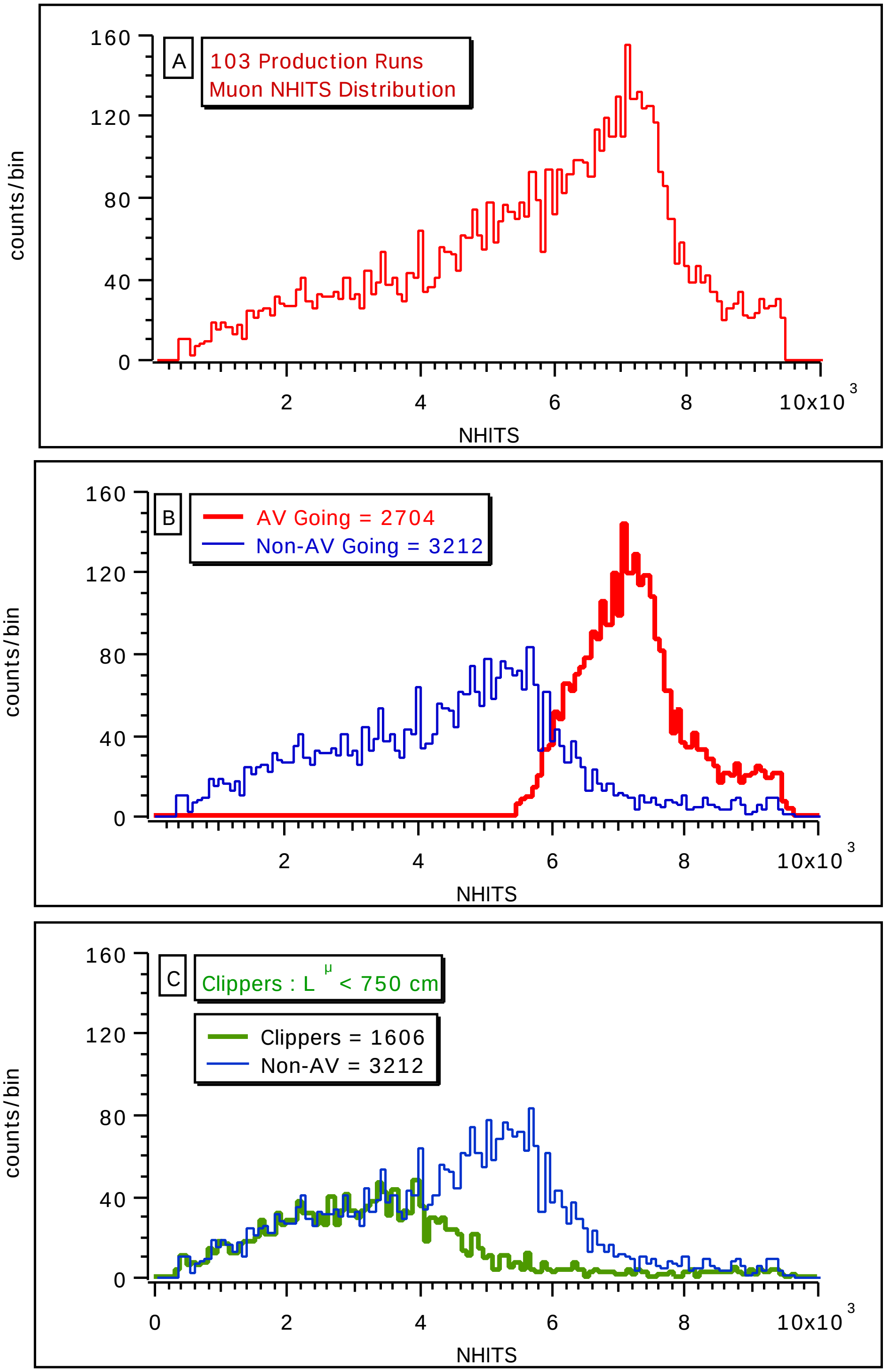

Figure 5.3: Muon NHITS Distributions.

5.2.3 Characteristic Distributions of Selected Muons

Muon NHITS Distributions

In Figure 5.3 the characteristic NHITS distributions of muons at SNO have been plotted. The NHITS distribution of all analyzed muons is shown in Figure 5.3.A. The first and second moments of the distribution are as follows:

$$All\ Muons\ :\ \overline{NHITS} = 5832\ \ and\ \ \sigma = 2015 \tag{5.3}$$

In Figure 5.3.B the NHITS distributions of the AV and non-AV going muons are shown. The non-AV going muon sample includes all PC and FC events. It can be seen from the distribution that the AV going muons, in general, have a much higher NHITS value than non-AV going muons. It should be remembered that a pre-defined cut of (NHITS $\geq$ 350) was applied to the data set. [Muons with NHITS below this value are extremely rare ($<$ 0.1%). This was determined by hand-scanning 27 runs with NHITS $\geq$ 150.] The first and second moments of the AV and non-AV muon NHITS distributions are as follows:

$$AV\ Muons\ :\ \overline{NHITS} = 7271\ \ and\ \ \sigma = 832 \tag{5.4}$$

$$non\ AV\ Muons\ :\ \overline{NHITS} = 4437\ \ and\ \ \sigma = 1796 \tag{5.5}$$

In Figure 5.3.C the NHITS Distribution of muons defined as “Clippers” have been plotted. Here is the definition of clipper muons:

- Clipper Muons : Muon Path Length $\equiv$ $L^{\mu} < 750$ cm

The first and second moments of the distribution are as follows:

$$Clipper\ Muons\ :\ \overline{NHITS} = 3338\ \ and\ \ \sigma = 1628 \tag{5.6}$$

It can be seen that on average the muons that clip or graze the PSUP illuminate fewer PMTs than AV-going muons. This is expected since the clippers in general have a shorter path length than AV muons. However, occasionally muons that clip the PSUP will deposit enough charge so as to trigger almost all the PMTs in the detector. This is evidenced from the long tail of the clippers NHITS distribution. A total 93 clipper muons out of 1606 clippers, i.e. 5.8% clippers, have (NHITS > 6000).

Muon Path Length Distributions

The plot in Figure 5.4.A shows the muon path length (L^{μ}) distribution, as determined by MuonID, for AV and non-AV muons. The MuonID algorithm provides an initial guess to the muon path length which is subsequently verified by the hand-scanning procedure. Miscategorized muons, as determined by hand-scanning, have been excluded from the plot. As shown in Appendix B.1, the AV muons have a path length greater than 1179 cm. The first and second moments of the AV and non-AV muon path length distributions are as follows:

$$All\ Muons\ :\ \overline{L^{\mu}_{A}} = 1058\ cm\ \ and\ \ \sigma = 485\ cm \tag{5.7}$$

$$AV\ Muons\ :\ \overline{L^{\mu}_{AV}} = 1491\ cm\ \ and\ \ \sigma = 168\ cm \tag{5.8}$$

$$non\ AV\ Muons\ :\ \overline{L^{\mu}_{nAV}} = 674\ cm\ \ and\ \ \sigma = 318\ cm \tag{5.9}$$

Muon Charge Distributions

The plot in Figure 5.4.B shows the distribution of the charge deposited by AV and non-AV going muons. The horizontal axis [NPH] is the total integrated charge [pedestal corrected QLX] normalized by the total number of PMTs in the event. The first and second moments of the distributions are as follows:

$$All\ Muons\ :\ \overline{NPH} = 233\ \ and\ \ \sigma = 154 \tag{5.10}$$

$$AV\ Muons\ :\ \overline{NPH} = 298\ \ and\ \ \sigma = 170 \tag{5.11}$$

$$non\ AV\ Muons\ :\ \overline{NPH} = 178\ \ and\ \ \sigma = 114 \tag{5.12}$$

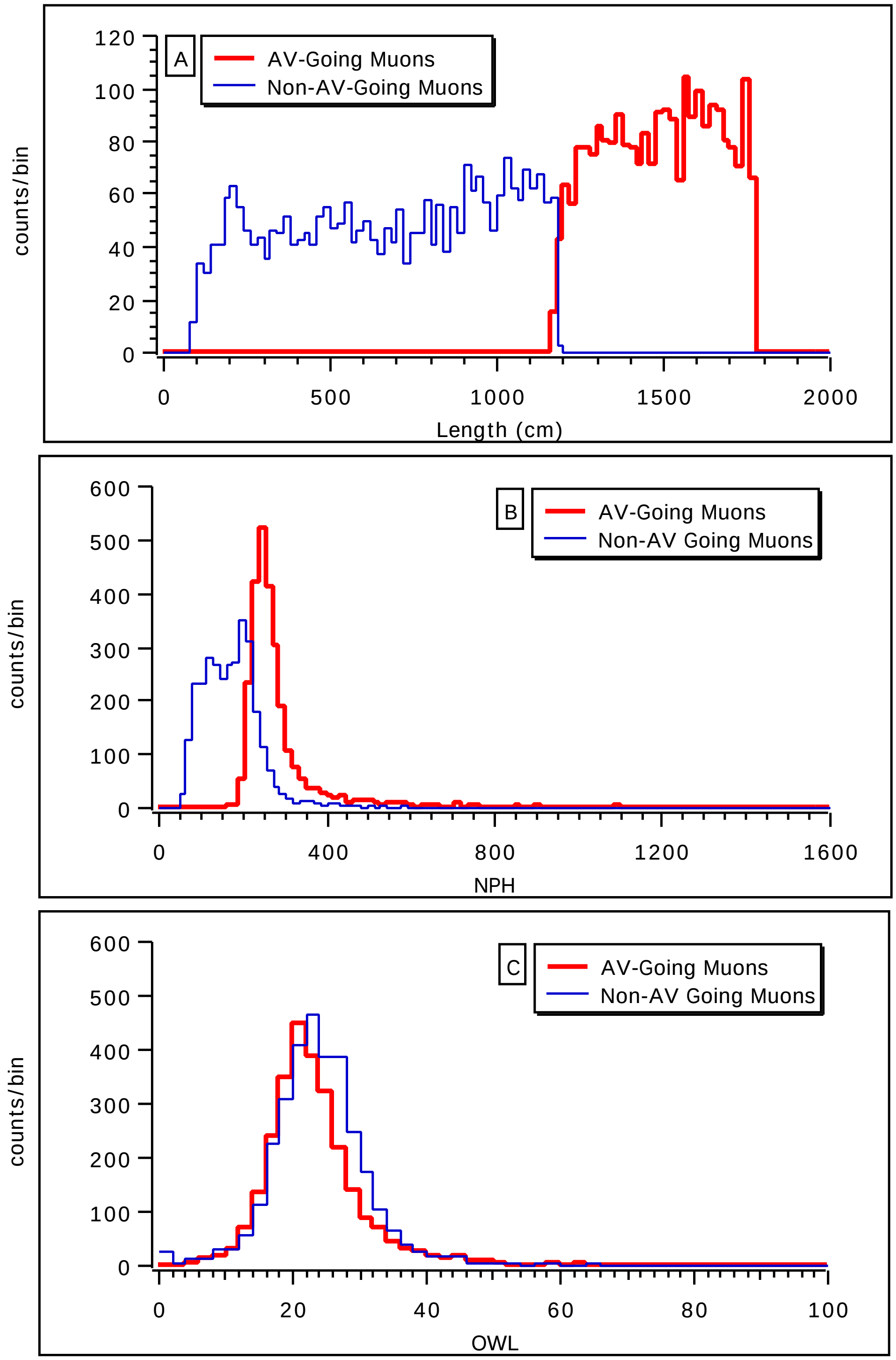

Figure 5.4: Muon Characteristic Distributions.

On average AV muons deposit more charge than the non-AV muons. This is because, on average, the path length of the AV muons is longer than the non-AV muons and the deposited charge is correlated with the muon path length.

Muon OWL Tube Distributions

The plot in Figure 5.4.C shows the distribution of the total number of OWL tubes that have fired for AV and non-AV going muons. The first and second moments of the AV and non-AV OWL tube distributions are as follows:

$$All\ Muons\ :\ \overline{OWL} = 23.2\ \ and\ \sigma = 7.3 \tag{5.13}$$

$$AV\ Muons\ :\ \overline{OWL} = 22.7\ \ and\ \sigma = 7.0 \tag{5.14}$$

$$non\ AV\ Muons\ :\ \overline{OWL} = 23.6\ \ and\ \sigma = 7.5 \tag{5.15}$$

The small peak at zero corresponds to the fully contained [FC] events, since OWL tubes did not fire for these events. MuonID does not consider events with less than 4 OWL tubes, therefore FC events that were identified were done so by hand-scanning of the raw data files.

Distinctive AV-going Events

In Table 5.7 the average values for the NHITS, OWL, NPH and TRMS[2] parameters of AV-going muons have been presented. During the muon selection procedure a total of five distinctive AV-going [DAGs] events were identified whose values for the above parameters are very different from the average values that are given in Table 5.7. Table 5.8 shows the values of these parameters for the five DAGs. From these two tables it is evident that the DAGs are not typical AV-going muons. In particular, these events have deposited a substantial amount of charge in the detector as compared to the charge deposited by typical AV-going muons. The

---

[2] Width of the PMT timing distribution for an event.

Parameter	Average Value	RMS
NHITS	7271	832
OWL	23	7
NPH	298	170
TRMS	29.6	5.4

Table 5.7: AV-going Muon Characteristics.

DAGs are most probably muons accompanied by an energetic electromagnetic shower.

5.2.4 Observed Muon Rate at SNO

The through-going muon rate at SNO can be determined by two different methods. In Method 1, the rate is obtained by dividing the total number of through-going muons by the total live-time of the muon counting period. In Method 2, the rate is determined by constructing an interval distribution from the time differences between consecutive through-going muons and then fitting it to an exponential to get the time constant, which then gives the muon rate. These two different methods will be employed to measure the muon rate at SNO. A comparison of the results obtained from these two methods will provide an important consistency check. In order to determine the rate, muons from the 27 runs that have been hand-scanned will be used.

	Run	GTID	NHITS	OWL	NPH	TRMS (ns)
1	10008	1697058	9518	70	3009	8.17
2	10549	3301460	9567	47	2704	14.24
3	10946	299141	9578	58	2928	15.36
4	11291	1015858	9491	24	2403	13.67
5	11347	92584	9572	47	2845	11.09

Table 5.8: Characteristics of the 5 Distinctive AV-going Events.

Method 1

From Table 5.5 it can be seen that a total, N^{μ}_{thru}, of 1875 through-going muons were identified from the 27 fully hand-scanned runs. The through-going muon sample does not include any partially contained or fully contained muons. The total live-time, L_{tot}, for these 27 runs was found to be 27.92 days. The live-time was determined by counting the total number of PGT triggers for those runs. The PGT is triggered at a 5 Hz rate during the course of a run and, therefore, should provide an accurate measure of the live-time. The following has been measured:

$$N^{\mu}_{thru} = 1875 \pm 43(stat.) \tag{5.16}$$

$$L_{tot} = 27.92 \pm 0.01(stat.) \text{ days} \tag{5.17}$$

Therefore, the through-going muon rate is given by the following:

$$R^{SNO}_{\mu} = \frac{N^{\mu}_{thru}}{L_{tot}} = 67.2 \pm 1.6(stat.) \text{ day}^{-1} \tag{5.18}$$

The total number of through-going muons identified by the MuonID algorithm and hand-scanning procedure from the 103 production runs can also be used to

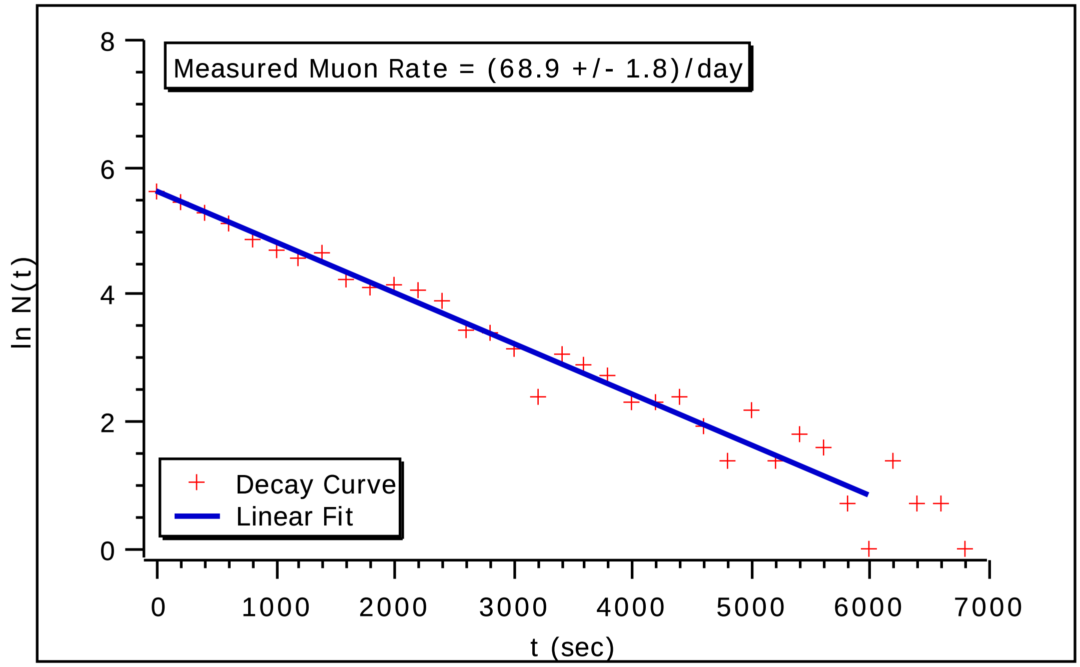

Figure 5.5: Observed Muon Rate at SNO.

determine the observed muon rate. In this case the muon identification efficiency of the MuonID algorithm will be used in order to determine the total number of muons. For the 103 runs the following is obtained:

$$N^{\mu}_{thru} = 5894 \pm 77(stat.) \tag{5.19}$$

$$L_{tot} = 85.65 \pm 0.07(stat.) \;\; \text{days} \tag{5.20}$$

Therefore, the measured through-going muon rate as determined from the 103 runs is found to be:

$$R^{SNO}_{\mu} = 68.8 \pm 0.9(stat.) \;\; \text{day}^{-1} \tag{5.21}$$

It can be seen that the through-going muon rates given by Eqs. 5.18 and 5.20 are consistent within errors.

Method 2

In this method the 1875 through-going muons have been used to construct an exponential curve by histogramming the time differences between consecutive muons. By using all inclusive verified muons from the fully scanned 27 runs, fitter effects on the rate have been eliminated by not discarding legitimate muons due to fitter inadequacies. The horizontal axis on Figure 5.5 is the time difference (in seconds) between verified consecutive muons. The vertical axis is the natural log of the number of muons per 200 second bin. A straight line fit has been performed to determine the observed through-going muon rate at SNO. The rate has been calculated to be:

$$R_\mu^{SNO} = 68.9 \pm 1.8(stat)\ \text{day}^{-1} \tag{5.22}$$

It can be seen that the through-going muon rates given by Eqs. 5.18 and 5.22 are consistent within errors.

In a recent paper titled "Initial Observation of Through-going Muons in the Sudbury Neutrino Observatory"[100] the reported rate of through-going muons within the entire active volume is roughly 3 per hour. The paper states that from an examination of downward muons it has been found that the intensity and angular distributions are consistent with measurements from past experiments.

AV-going Muon Rate at SNO

The MuonID algorithm and hand-scanning procedures have identified a total of 2704 AV-going muons. Therefore, 46% of the 5842 through-going muons were categorized to have gone through the D_2O volume. During the hand-scanning procedures it was found that approximately 4.5% of the through-going muons could not be unambiguously categorized as either AV-going or non-AV going muons. Based on this the total number of AV-going muons is:

$$N^\mu[SNO, AV] = 2704 \pm 52(stat.) \pm 132(sys.) \tag{5.23}$$

Now, using the above equation and Eq. 5.20 the following AV-going muon rate at SNO is obtained:

$$R^{\mu}[SNO, AV] = 31.6 \pm 0.6(stat.) \pm 1.5(sys.) \text{ day}^{-1} \text{ kt}^{-1} \tag{5.24}$$

5.3 Conclusion

One of the primary goals of this chapter has been to demonstrate that the MuonID algorithm and hand-scanning procedures are efficient at identifying and categorizing the atmospheric muons that traverse the SNO detector. Using the muon selection and categorization procedure a list has been constructed of through-going muons that can potentially generate spallation products, in particular neutrons, within the D_2O volume. This list of muons will be used to investigate the characteristics of muon-induced spallation products. In particular, the measured AV-going muon rate at SNO will be used in the following chapter to determine the muon-induced neutron rate at SNO.

Chapter 6

Muon Correlated Background

6.1 Objective

Muons are responsible for creating various radioactive nuclei and free neutrons in the SNO detector through the process of spallation. In this chapter the focus will primarily be on muon-induced neutrons produced within the D_2O at SNO. A measurement of the production rate of these neutrons will be compared to the rates determined by past underground experiments. In order to understand the properties of the detected muon-induced neutrons a comparison of the findings will be made to Monte Carlo results. In particular, the mean NHITs value of neutron capture on deuterium obtained from muon-induced neutron data and Monte Carlo will be compared and contrasted.

Muons provide a constant supply of spallation induced neutrons which can capture on deuterium to produce 6.25 MeV gamma rays. Therefore, these neutrons can be used to perform a measurement of the SNO detector's response to γ rays and as a consistency check this measurement can be compared to the SNO ^{16}N calibration results. Even though a thorough comparison of this type is beyond the scope of this study, the process and tools will be in place for such a study in the near future.

In this thesis the analyzed data[1], which has a total live-time of approximately 86 days, was gathered over a period of four and a half months since SNO started acquiring production data. During those early days of SNO data acquisition (between November 2, 1999 and March 15, 2000) many of the tools and inputs for data analysis were being developed and refined. In particular, during this analysis the reported ^{17}O abundance in D_2O at that time was used in the Monte Carlo study to understand neutron capture in D_2O. Since the results from the muon-induced neutron data are compared to the Monte Carlo results, a future adjustment to the ^{17}O abundance in D_2O can have consequences for the conclusions arrived at in this chapter. Furthermore, the NHITs value of a given event during data analysis was not corrected for missing channels[2], which could vary, albeit slightly, from run to run. An application of this correction could affect the resulting mean NHITs value of events where muon-induced neutrons are captured by deuterium. Therefore, the analysis procedure should incorporate this correction when it becomes available.

6.2 Introduction

Deep underground detectors searching for low-energy neutrino events from the Sun and other astrophysical sources must contend with atmospheric muon-induced background events. Muons streaming through the detector can produce electromagnetic nuclear reactions via inelastic scattering :

$$\mu + \mathrm{A} \rightarrow \mu' + \mathrm{A}^* \tag{6.1}$$

$$\mathrm{A}^* \rightarrow \mathrm{B} + \mathrm{X} \tag{6.2}$$

where, A is the target nucleus, A^* is the excited nucleus, μ is the incoming muon and μ' is the outgoing muon. The A^* excited nucleus can then decay and produce

---

[1] The analysis of muons and muon-induced spallation data was concluded in August of 2000.

[2] This correction mechanism did not exist at the time the analysis was concluded.

a radioactive daughter isotope, B, and a stable daughter, X.

This process in which a muon or some other high energy particle inelastically scatters and breaks the target nucleus into smaller fragments is called nuclear spallation. When the A^* excited nucleus decays it can generate a signal in the detector fiducial volume that can be mistaken for a neutrino event with the same energy. As mentioned in the last chapter, if the decay time of A^* and all its daughter products are short, $t_{1/2} < 1$ sec, then the muon-induced spallation events can be eliminated from the final data sample through a time coincidence with the signal produced by the muon as it traverses the detector. On the other hand, if the decay times of A^* or any of its daughter products B is long, $t_{1/2} > 1$ sec, then the signal associated with the decay of A^* or B is less easily eliminated and could be confused with a neutrino event.

In SNO, high-energy atmospheric muons are responsible for spallation on ^{16}O and ^{2}H nuclei in water. As a result, free neutrons and other radioactive nuclei are created in the fiducial volume of the detector. The purity of the solar neutrino sample depends on identifying and removing these muon-induced background events. During the process of solar neutrino analysis all events within 1 minute of a parent muon are tagged and, therefore, one could eliminate these followers from the data. However, as seen in Figure 5.1, this results in a $\sim 5\%$ reduction in live-time, which is undesirable. So one needs to devise intelligent methods of eliminating the spallation products without sacrificing any significant detector live-time. In order to accurately eliminate these background events one needs to understand their properties and production mechanisms in detail, which is the subject matter of the next section.

6.3 Muon Induced Spallation

Introduction

Spallation products are generated in SNO by energetic atmospheric muons passing through the detector via the following primary electromagnetic nuclear reactions:

$$\mu + {}^{16}\mathrm{O} \rightarrow \mu' + {}^{16}\mathrm{O}^* \tag{6.3}$$

$$\mu + {}^{2}\mathrm{H} \rightarrow \mu' + \mathrm{n} + \mathrm{p} \tag{6.4}$$

When an energetic muon of energy E passes a nucleus it is accompanied by a flux of virtual photons whose energy spectrum is given by[101] :

$$N_\mu(E,\omega) = \frac{\alpha}{\pi\omega}\left[(1+\epsilon^2)ln\frac{2\epsilon E^2}{m_\mu \omega} - 2\epsilon\right], \tag{6.5}$$

where, ω is the energy of the virtual photon, $\epsilon = (E-\omega)/E$, $\alpha = \frac{1}{137}$, and m_μ is the mass of the muon(106 MeV). These virtual photons can be absorbed by the target nucleus to produce spallation products as shown in equations 6.3 and 6.4.

The deuterium in the heavy water can produce free neutrons within the AV through the process of photodisintegration initiated by the virtual photons. In addition, the spallation of ^{16}O can produce a number of radioactive isotopes which then decay and generate free neutrons, βs and/or γs. Spallation of ^{16}O also produces stable nuclei, but these are inconsequential and will not be considered in this study, since the primary interest is in the unstable nuclei that are produced by muon-induced spallation.

In order to accurately predict the expected number of unstable nuclei that are produced in the SNO detector, a knowledge of the cross sections for the specific reactions that produce those spallation products is required. Unfortunately, very little information is available on spallation cross sections for producing unstable nuclei from oxygen. As a result it is prudent to consider all unstable nuclei that could be produced in this process. This includes all unstable nuclei that produce neutrons, βs and/or γs as decay products.

Since the trigger threshold of the detector is approximately 2 MeV, spallation products that produce βs and γs with energies greater than 2 MeV will be considered. Using the *Table of Isotopes* [102] a list has been compiled, as given in Table 6.1, of potential muon-induced ^{16}O spallation products with their associated half-lives, decay modes, branching ratios and maximum total energies of the emitted particles. The spallation products generated from ^{16}O have a maximum atomic mass number of 16, i.e. $A \leq 16$. From the table it can be seen that the longest lived ^{16}O spallation product that produces a neutron is ^{9}Li, which has a half-life of 0.178 sec.

There are also trace amounts of ^{17}O and ^{18}O isotopes in the heavy water. Therefore, it is possible to get spallation products with $A \leq 18$ and these are also listed in Table 6.1. The longest lived of these isotopes that produce a neutron is ^{17}N, which has a half-life of 4.173 sec. This possible spallation product decays 95% of the time by emitting a neutron and a beta which has a maximum energy of 3.7 MeV. The analysis threshold used in this study is approximately 4 MeV. Therefore, if ^{17}N is produced via muon spallation then the beta from ^{17}N will not contribute to the muon-induced spallation sample.

Muon Induced Neutron and Radioactive Nuclei Production

Muons that dissociate deuterium to generate free neutrons, will produce a signal in the detector within many milli-seconds. Therefore, to first order it would be a relatively easy task to eliminate muon-induced spallation neutrons from the data sample by cutting events within a few seconds of a muon without sacrificing any significant detector live-time. The spallation products that generate neutrons will be denoted by μ_n^{sp}. The neutrons, after production, random walk about the detector before capture and detection. Since there is a weak correlation between the neutron capture location and the muon track, it will be difficult to associate the neutron with the parent muon by considering only the distance between the

Isotope	$\tau_{\frac{1}{2}}(sec)$	Mode	Br. Ratio	Max. Energy(MeV)
^{6}He	0.807	β^-	100%	3.51
^{7}He	4×10^{-21}	n	100%	-
^{8}He	0.119	$\beta^-\gamma$	84%	$10.66(\beta)+0.99(\gamma)$
		β^-n	11%	$7.44(\beta)$
^{8}Li	0.838	β^-	100%	16.0
^{8}B	0.770	β^+	100%	18.0
^{9}He	1×10^{-21}	n	100%	-
^{9}Li	0.178	$\beta^-\gamma$	50.5%	$11.0(\beta)+2.5(\gamma)$
		β^-n	49.5%	11.2
^{9}C	0.127	β^+p	100%	16.5
^{10}Li	5.2×10^{-22}	n	100%	-
^{11}Li	0.0085	β^-n	85%	16.0
		β^-	15%	20.6
^{11}Be	13.8	β^-	55%	11.5
		$\beta^-\gamma$	42%	$9.4(\beta)+8.0(\gamma)$
^{12}Be	0.0236	β^-	100%	11.7

Table 6.1: Possible Muon-Induced Spallation Products at SNO.

Isotope	$\tau_{\frac{1}{2}}(sec)$	Mode	Br. Ratio	Max. Energy(MeV)
^{12}B	0.0203	β^-	97%	13.3
^{12}N	0.011	β^+	95%	17.3
^{13}B	0.0174	β^-	92%	13.4
		$\beta^-\gamma$	8%	9.7(β)+3.6(γ)
^{13}O	0.0086	β^+	90%	17.8
		$\beta^+\gamma$	10%	14.3(β)+3.5(γ)
^{14}Be	0.0044	β^-n	81%	10.0
		β^-	15%	16.2
^{14}B	0.0138	$\beta^-\gamma$	95%	25.0(β)+6.7(γ)
		β^-	5%	20.6
^{14}O	70.6	β^+	0.61%	5.1
^{15}B	0.0105	β^-	100%	19.1
^{15}C	2.449	$\beta^-\gamma$	63%	2.5(β)+5.3(γ)
		β^-	37%	9.8
^{16}C	0.748	β^-n	100%	4.6
^{16}N	7.134	$\beta^-\gamma$	66%	4.27(β)+6.13(γ)
		β^-	28%	10.44

Table 6.1: Possible Muon-Induced Spallation Products at SNO[cont].

Isotope	$\tau_{\frac{1}{2}}(sec)$	Mode	Br. Ratio	Max. Energy(MeV)
^{17}N	4.173	$\beta^- n$	95%	3.7
^{18}N	0.063	β^-	100%	9.4

Table 6.1: Possible Muon-Induced Spallation Products at SNO[cont].

neutron detection point to the track of the muon. The Cerenkov light patterns, generated by neutrons from neutrino induced neutral-current reaction are identical to those which are generated by muon-induced neutrons. However, in the latter case the neutron is temporally associated with the muon whereas a neutrino-induced neutron is not, except for extremely rare coincidences ($\sim 3 \times 10^{-14}$ Hz).

From Table 6.1 it can be seen that for nuclei that do not emit neutrons the longest lived spallation induced nuclei are ^{16}N and ^{11}Be with half-lives of 7.13 secs and 13.8 secs respectively. Spallation products that generate βs and/or γs will be denoted by $\mu^{sp}_{\beta\gamma}$. These decay products can produce signals in the detector that will be impossible to distinguish from the signals of neutrino events. However, based on the half-lives of the decay products these events could be eliminated by simply discarding all events within many seconds of a muon. It has been shown earlier that a muon tagged time cut of 30 seconds will result in a live-time reduction of 2.4%. However, unlike neutrons which random walk after production, the β-γ emission should in general be spatially correlated with the muon track since these spallation products will not recoil significantly from the muon track along which it was produced. Therefore, instead of using a simple muon tagged time cut one could shorten the reduction in live-time by imposing a spatial cut around the reconstructed muon track within a specified time window. A procedure similar to this was employed by the Kamiokande and Super-Kamiokande detectors. However, this is not necessary at SNO since the muon rate (roughly 3 muons/hour) is much lower than the muon rate at SuperK (roughly 7920 muons/hour), and therefore a simple muon tagged time cut could be applied at SNO.

Muon Induced ^{16}N Production

From Table 6.1, it can be seen that ^{16}N has been listed as a possible spallation product. The most likely method of producing this isotope is not spallation but the following muon capture reaction:

$$\mu^- + {}^{16}\mathrm{O} \rightarrow {}^{16}\mathrm{N} + \nu_\mu \tag{6.6}$$

Negative muons that slow down in the detector and stop can be captured by the Coulomb field of a nucleus into a Bohr orbit forming a muonic atom. The muon then rapidly ($\sim 10^{-11}$ sec) cascades down to the atomic 1s level from which it decays via the reaction:

$$\mu^- \rightarrow e^- + \overline{\nu}_e + \nu_\mu \tag{6.7}$$

or is captured by a proton of the nucleus (Z,A) via the reaction:

$$\mu^- + {}^{A}_{Z}\mathrm{X} \rightarrow {}^{A}_{Z-1}\mathrm{X}^* + \nu_\mu \tag{6.8}$$

The capture rate (Λ_c) of muons that stop in the SNO detector can be determined by the following [103]:

$$\Lambda_t = \Lambda_c + \mathrm{Q}\Lambda_d \tag{6.9}$$

where

$$\Lambda_t = 1/\tau_{\mu^-} \tag{6.10}$$

and

$$\Lambda_d = 1/\tau_{\mu^+} \tag{6.11}$$

In the above equations t, d and c denote “total”, “decay” and “capture” respectively. Q is the Huff factor which accounts for the fact that the normal muon decay rate is reduced since the energy available in the decay is slightly reduced by the binding of the μ^- to the atom. An experiment by Suzuki et al. [103] measured the lifetime of negative muons (τ_{μ^-}) in 50 elements and 8 isotopes. Using the results from this experiment, the negative muon capture rate in ^{16}O can be determined. For the ^{16}O target Suzuki et al. measured a value of (1795.4 ± 2.0) ns for τ_{μ^-}. Using their reported value of (2197.03 ± 0.04) ns and 0.998 for τ_{μ^+} and Q respectively, one gets for the ^{16}O target a total μ^- capture rate of $(102.6 \pm 0.6 \times 10^3)$ sec^{-1}. Therefore, 18.4% of the negative muons that stop in the SNO detector will be captured by the oxygen nuclei.

For capture on ^{16}O the isotope produced is ^{16}N, which then decays and generates betas and gammas with energies above the operating threshold of the detector. The dominant decay channel(68%) of ^{16}N produces a 6.13 MeV γ ray. As mentioned earlier, a ^{16}N source is used to perform energy calibration of the SNO detector. Therefore, the muon-induced ^{16}N isotopes could be used to perform an independent energy calibration of the detector. Unlike the calibration source which is localized in space within a calibration chamber, the muon-induced ^{16}N isotopes are distributed across the D_2O volume. So with muon-induced ^{16}N isotopes, the possible systematic effects due to source localization could be eliminated from the calibration procedure. Furthermore, during the source calibration procedure the interaction of the γs with the ^{16}N chamber can affect the energy output. Systematic effects on the energy calibration will need to be carefully understood. Therefore, by utilizing muon-induced ^{16}N isotopes, the inherent complexities that are involved with a source can be removed from the calibration process. This may provide an understanding of the various systematic effects that are involved with the ^{16}N source calibration procedure.

In order to use the muon-induced ^{16}N isotopes to perform γ ray energy calibration, muons that stop in the detector and are not accompanied by a subsequent decay electron need to be identified via an analysis of the data. Muons that fall under this category are prime candidates for producing ^{16}N isotopes. From the last chapter it was found that a full hand-scan of the 27 runs identified a total of 12 PC muons without an associated decay electron. In identifying these muons we found distinct entrance points and no exit points. Furthermore, 18 FC events were found without an associated decay electron. These events could be either muons or electrons depending on the type of neutrino-nucleon interaction. The live-time for the 27 runs is (27.92 ± 0.01) days. Therefore, if we now assume that the FC events are all muons then the upper limit to muon-induced ^{16}N production rate per 1 kt D_2O is:

$$\mathrm{R}^{\mu}_{^{16}\mathrm{N}} \leq 1.1 \pm 0.2 \text{ day}^{-1} \text{ kt}^{-1} \tag{6.12}$$

In order to determine the muon-induced ^{16}N production rate one needs to be able to distinguish FC muons and electrons. This is beyond the scope of this study.

In addition to the muons that are captured by the ^{16}O nucleus to produce ^{16}N isotopes, there are muons that stop in the detector and then decay to produce Michel electrons and corresponding neutrinos. The energy of the μ decay electron events ($\sim$37 MeV) is much higher than that of solar neutrino events and hence these events are not very useful for an absolute energy calibration for the study of solar neutrinos. However, one could use these events to investigate the systematic difference in the absolute energy scale between data and Monte Carlo simulations.

The hand-scanning procedure that identifies muons which stop and decay to produce electrons (with a characteristic decay lifetime) is fairly robust. From the 27 runs a total of 13 PC and FC muons were found to be accompanied by a decay electron. Therefore, the measured rate of muons producing decay electrons within the 1 kt D_2O volume is:

$$\mathrm{R}^{\mu}_{dcye} = 0.5 \pm 0.1 \text{ day}^{-1} \text{ kt}^{-1} \tag{6.13}$$

At Super-Kamiokande the rate is [98] a factor of $\sim$350 times larger:

$$\mathrm{R}^{\mu}_{dcye}[\mathrm{SuperK}] \sim 178 \text{ day}^{-1} \text{ kt}^{-1} \tag{6.14}$$

Now, the muon charge ratio is: $\frac{\mathrm{N}(\mu^+)}{\mathrm{N}(\mu^-)} = 1.25$ [99]. Given that 18.4% of the stopping muons are captured by ^{16}O, if a total of 13 muons decay then one would expect $(4 \pm 2) \times 10^{-2}$ day^{-1} kt^{-1} muons to have been captured by ^{16}O to produce

^{16}N. This is consistent with the upper limit of the muon-induced ^{16}N production rate given in Eq. 6.12.

6.3.1 Predicted Rate of Spallation Products

It has been shown that muons, through the process of spallation, primarily generate two types of spallation products within the detector, neutrons (μ_n^{sp}) and radioactive isotopes ($\mu_{\beta\gamma}^{sp}$). Here the results of two different experiments will be used to determine an estimate for the expected production rates of these muon-induced spallation products at SNO.

Expected μ_n^{sp} Production Rate

The results of an experiment by Bezrukov et al. [104] are used to provide an estimate of the expected muon-induced neutron production rate at SNO. The experiment was performed at two depths underground, 25 m.w.e. in a gypsum mine and 316 m.w.e. in a salt mine, in order to determine the rate of production of neutrons generated by atmospheric muons as a function of depth. The average energy of muons coming from all directions at depths of 25 m.w.e. and 316 m.w.e. is 16.7 and 86.0 GeV respectively. It was found that the number of neutrons produced per muon increased with increasing average muon energy and that this dependence agreed with the theoretically calculated curve when the process of nuclear-cascade development was taken into account.

The detector consisted of three rows of scintillation counters. The upper and lower rows registered charged particles and the center row was sensitive both to charged particles and to neutrons. Neutron detection was accomplished by dissolving gadolinium salt in the scintillation material of this counter. The detector was triggered if a muon passed through it and if within 200 μsec of the muon trigger the central counter registered a γ ray, which is emitted after a neutron is captured by a gadolinium nucleus. At both depths the detector was placed flush against the ceiling. Therefore, muon-induced neutrons were predominantly produced within the surrounding cavity walls of the detector. A detailed description of the experimental setup can be found in [105].

In their experiment it was found that a given muon could produce multiple neutrons, i.e. the neutron multiplicity per event can be written as $\mathrm{N}_{mult} \geq 1$. At a depth of 25 m.w.e. the experiment registered a total of 1520 neutrons in 25 hours, which included events with $\mathrm{N}_{mult} \geq 1$. This implies the following measured average neutron production yield:

$$\overline{\mathrm{N}}_{25\,m.w.e.} = (4.7 \pm 0.5) \times 10^{-5}\ \mathrm{gm}^{-1}\ \mathrm{cm}^{2}\ \mathrm{muon}^{-1} \tag{6.15}$$

Furthermore, the average number of neutrons measured at a depth of 316 m.w.e. was found to be:

$$\overline{\mathrm{N}}_{316\,m.w.e.} = (12.1 \pm 0.12) \times 10^{-5}\ \mathrm{gm}^{-1}\ \mathrm{cm}^{2}\ \mathrm{muon}^{-1} \tag{6.16}$$

The absolute difference in the neutron production rate given in Eqs. 6.15 and 6.16 is $(7.4 \pm 0.5) \times 10^{-5}$. This corresponds to a relative difference of 1.3 as determined from the neutron production yield curve given by Bezrukov et al. in [104]. Based on this curve, the relative difference between the neutron production rate at a depth of 25 m.w.e. and at SNO's depth of 6150 m.w.e. is found to be 6.0. Therefore, the estimated average number of muon-induced neutrons produced at SNO is:

$$\overline{\mathrm{N}}_{6150\,m.w.e.} = \left(\frac{6.0 \times 7.4}{1.3} + 4.7\right) \times 10^{-5} = (39.0 \pm 3.0) \times 10^{-5}\ \mathrm{gm}^{-1}\ \mathrm{cm}^{2}\ \mathrm{muon}^{-1} \tag{6.17}$$

For through-going muons penetrating the 1 kt of heavy water in the AV, the target thickness at SNO is approximately:

$$\mathrm{A}_{SNO} = \frac{10^{9}}{\pi \times 600^{2}} = 884\ \mathrm{gm}\ \mathrm{cm}^{2} \tag{6.18}$$

Therefore, from Eqs. 6.17 and 6.18 one gets the following expected number of neutrons produced within the AV:

$$\mathrm{N}^{\mu_n^{sp}}[\mathrm{SNO,\ AV}]_{exp.} = (0.34 \pm 0.03)\ \mathrm{kt}^{-1}\ \mathrm{muon}^{-1} \tag{6.19}$$

In Chapter 5 the measured AV-going muon rate at SNO was found to be $(31.6 \pm 0.5(stat.) \pm 1.5(sys.))$ day^{-1} kt^{-1} [Eq. 5.24]. The largest uncertainty in this rate is the ~5% systematic error associated with the procedure that categorizes muons as AV-going or non-AV going. Now, combining Eqs. 5.24 and 6.19 one gets the following expected muon-induced neutron production rate per day at SNO:

$$\mathrm{R}^{\mu_n^{sp}}[\mathrm{SNO,\ AV}]_{exp.} = (10.74 \pm 1.11)\ \mathrm{day}^{-1}\ \mathrm{kt}^{-1} \tag{6.20}$$

This corresponds to approximately (3920 ± 405) neutrons produced per year by atmospheric muons within a fiducial volume of 1-kt of heavy water. The error estimate given in Eq. 6.20 can be reduced by improving the muon categorization procedure.

A recent experiment by Chen et al. [106] measured the muon-induced neutron production yield in an organic liquid scintillator. The detector was filled with 190 liters of a 0.09% gadolinium scintillator and installed in the Stanford Underground Facility at a depth of approximately 20 m.w.e. The apparatus used in this experiment served as both the target and the detection material. The experimental measurement found the following single-neutron yield:

$$\overline{\mathrm{N}}_{20\,m.w.e.}[N_{mult} = 1] = (4.3 \pm 0.3 \pm 0.5) \times 10^{-5}\ \mathrm{g}^{-1}\ \mathrm{cm}^2\ \mathrm{muon}^{-1} \tag{6.21}$$

The double-neutron production yield was measured to be:

$$\overline{\mathrm{N}}_{20\,m.w.e.}[N_{mult} = 2] = (1.6 \pm 0.2 \pm 0.5) \times 10^{-5}\ \mathrm{g}^{-1}\ \mathrm{cm}^2\ \mathrm{muon}^{-1} \tag{6.22}$$

Based on the neutron production yield curve derived by Bezrukov et al., one finds that as the average muon energy increases with depth so does the muon-induced neutron production yield. Given this depth dependence and the fact that the Bezrukov result of Eq. 6.15 considers events with $N_{mult} \geq 1$, one can compare the result in Eq. 6.21 with that given in Eq. 6.15. One finds that the results obtained by these two experiments follow a general trend of neutron production yield versus underground depth.

One of the goals of this thesis is to measure the muon-induced neutron production rate at SNO. The rate will then be compared to the predicted rate as determined by the Bezrukov experiment. It should be kept in mind that the SNO and Bezrukov experiments are at two different depths and use two different targets. The Bezrukov experiment uses CH_2 as its target, whereas SNO uses D_2O.

Expected $\mu^{sp}_{\beta\gamma}$ Production Rate

The results of the $\mu^{sp}_{\beta\gamma}$ production rate at SuperK is used to provide an estimate of the expected $\mu^{sp}_{\beta\gamma}$ production rate at SNO. At SuperK it has been found that, given a Low Energy(L.E.) trigger threshold of 4 MeV, approximately 600 spallation products are generated per day in the 22.5 kt fiducial volume [107]. All spallation products with A$\leq$ 16, except for ^{6}He, as listed in Table 6.1 produce β-γ events with a maximum energy greater than 4 MeV. Therefore these products can be detected at SuperK above the L.E. trigger threshold. On the other hand, muon-induced neutrons produced at SuperK are promptly captured by hydrogen in the light water of the detector to produce a 2.2-MeV γ, which is below the threshold and therefore goes undetected. From an analysis of 300 days of data, the SuperK collaboration was able to fit the decay curve of the $\mu^{sp}_{\beta\gamma}$ spallation products by including the half-lives of the radioactive isotopes: ^{8}Li, ^{9}Li, ^{11}Be, ^{12}B, ^{15}C, ^{12}N and ^{16}N. The half-lives, in seconds, of these isotopes are: 0.84, 0.178, 13.8, 0.0203, 2.449, 0.011 and 7.134 respectively. The fit yielded the following result [108]:

$$\begin{aligned} \mathrm{N}(\Delta t) &= 1254 \times 2^{\frac{-\Delta t}{0.84}} + 338.6 \times 2^{\frac{-\Delta t}{0.178}} + 7.791 \times 2^{\frac{-\Delta t}{13.8}} \\ &\quad +120100 \times 2^{\frac{-\Delta t}{0.0203}} + 134.7 \times 2^{\frac{-\Delta t}{2.449}} + 33900 \times 2^{\frac{-\Delta t}{0.011}} \\ &\quad +676.1 \times 2^{\frac{-\Delta t}{7.134}} \end{aligned}$$

where, Δt is the time difference between the parent muon and the spallation event and the denominators in the exponents are the respective half-lives of the spallation products listed above. As can be seen from the above result the dominant component was found to be ^{12}B with a half-life of 20.3 ms.

Since the primary interest of this study is in muon-induced neutrons it is necessary to take into account the possible spallation products that could provide a background for the muon-induced neutron signal. In the next section it is shown from Monte Carlo that free neutrons in the D_2O volume are typically captured by deuterium within 500 ms of their generation, in which a 6.25 MeV γ ray is produced. Therefore, spallation products with decay times greater than 500 ms, in general, will not interfere with muon-induced neutron signals. From Table 6.1 it can be seen that of the seven spallation products identified by the SuperK analysis, only ^{9}Li, ^{12}B and ^{12}N have half-lives less than 500 ms. These spallation products, based on the above fit coefficients, contribute 98.7% to the total spallation product intensity in SuperK. However, these radioactive isotopes have a β end-point energy which is appreciably larger than 6.25 MeV. In the following, the expected $\mu^{sp}_{\beta\gamma}$ production rate at SNO will be determined.

Given the SuperK measured $\mu^{sp}_{\beta\gamma}$ production rate, an estimate can be provided for the expected $\mu^{sp}_{\beta\gamma}$ production rate per muon at SNO by the following:

$$\mathrm{R}^{\mu^{sp}_{\beta\gamma}}[SNO]_{exp.} = \alpha_d \times \mathrm{R}^{\mu^{sp}_{\beta\gamma}}[\mathrm{SK}]_{meas.}, \quad (\mathrm{E}_{th} = 4\,\mathrm{MeV}) \tag{6.23}$$

where, E_{th} is the energy threshold and α_d is the scaling factor that provides the correction resulting from the difference in the muon energies at the two detectors. Since SNO is situated much deeper than SuperK, the minimum energy required by muons to reach SNO is larger than the minimum energy of muons at SuperK. From the muon-induced neutron production yield curve, as derived by Bezrukov et al., it is found that as the average muon energy increases with depth so does the neutron production rate. In a similar manner the production of $\mu^{sp}_{\beta\gamma}$ will also depend on depth. In Eq. 6.23, $\alpha_d \geq 1$, since SNO is situated deeper than SuperK. As mentioned earlier, in this study the primary interest is in muon-induced neutrons and the task of determining the value of α_d will not be addressed here. It should be remembered that the target element responsible for producing $\mu^{sp}_{\beta\gamma}$ is the same for both SuperK and SNO, i.e. in both cases it is ^{16}O.

The following measurements [107] from SuperK are used to determine the $\mu^{sp}_{\beta\gamma}$ production rate at SNO:

$$\text{SuperK Muon Rate} \equiv R^{\mu}[SK] = 8448.0 \pm 92.0(stat.)\ \text{day}^{-1}\ \text{kt}^{-1} \tag{6.24}$$

$$\text{SuperK } \mu^{sp}_{\beta\gamma} \text{ Rate} = 600.0 \pm 24.5(stat.)\ \text{day}^{-1} \tag{6.25}$$

The analysis presented here uses a 4-MeV energy threshold for both SuperK and SNO. The SuperK fiducial volume is 22.5 kt. Therefore, the measured production rate of $\mu^{sp}_{\beta\gamma}$ at SuperK per muon per 1-kt volume is:

$$\text{R}^{\mu^{sp}_{\beta\gamma}}[\text{SK}]_{meas.} = (3.2 \pm 0.1) \times 10^{-3}\ \text{day}^{-1}\ \text{kt}^{-1}\ \text{muon}^{-1} \tag{6.26}$$

If it is now assumed that the $\mu^{sp}_{\beta\gamma}$ production rate at SNO scales in a similar fashion to the μ^{sp}_{n} production rate, then from the Bezrukov neutron production yield curve one finds that $\alpha_d = 1.4$. This is a reasonable assumption since the target element is the same for both SuperK and SNO. Based on this and Eq. 6.23, an estimate for the production rate of $\mu^{sp}_{\beta\gamma}$ at SNO per muon, per 1 kt volume is found to be:

$$\text{R}^{\mu^{sp}_{\beta\gamma}}[\text{SNO, AV}]_{exp.} = (4.5 \pm 0.1) \times 10^{-3}\ \text{day}^{-1}\ \text{kt}^{-1}\ \text{muon}^{-1} \tag{6.27}$$

In Chapter 5 the measured AV-going muon rate at SNO was found to be (31.6 ± 1.7) day^{-1} kt^{-1} [Eq. 5.24]. So, the expected $\mu^{sp}_{\beta\gamma}$ production rate above a threshold of 4-MeV within 1 kt of heavy water at SNO is:

$$\text{R}^{\mu^{sp}_{\beta\gamma}}[\text{SNO, AV}]_{exp.} = (14.2 \pm 0.6) \times 10^{-2}\ \text{day}^{-1}\ \text{kt}^{-1},\ \ (\text{E}_{th} = 4\,\text{MeV}) \tag{6.28}$$

If one considers only spallation products with $\tau_{\frac{1}{2}} \leq 500\,ms$, then using the SuperK result one will get the following expected $\mu^{sp}_{\beta\gamma}$ production rate:

$$\text{R}^{\mu^{sp}_{\beta\gamma}}[\text{SNO, AV}]'_{exp.} = (14.0 \pm 0.6) \times 10^{-2}\ \text{day}^{-1}\ \text{kt}^{-1},\ \ (\text{E}_{th} = 4\,\text{MeV}) \tag{6.29}$$

Therefore, based on the SuperK data one would expect ∼14 $\mu^{sp}_{\beta\gamma}$ products per 100 days within the AV at SNO, given an energy threshold of 4-MeV. Comparing Eqs. 6.20 and 6.29 one sees that ∼1% of the spallation products generated within 500 ms of through-going muons are $\mu^{sp}_{\beta\gamma}$. However, by applying an energy cut to isolate the 6.25 MeV γ ray signal, one could reduce the contribution of the $\mu^{sp}_{\beta\gamma}$ background events.

6.4 Muon Induced Spallation Neutrons

6.4.1 Monte Carlo Study and Discussion

It has been found that atmospheric muons, through the process of spallation, can produce free neutrons in the SNO detector. These muon-induced neutrons after production are moderated within nano-seconds to thermal energies by the heavy water. Once thermalized, these free neutrons randomly walk before being captured by the various nuclei in the detector. Monte Carlo simulations with SNOMAN were performed to determine the mean capture time and the capture percentage of neutrons by the various isotopes. Furthermore, the mean random walk distance from neutron generation to capture position was determined. Since these parameters are sensitive to the isotopic abundances in heavy water, the most recently measured values in SNO for the abundances [6] were used in the Monte Carlo simulations. These values are shown in Table 6.2.

Neutrons produced within the detector can capture via the following two main reactions:

$$\mathrm{n} + \mathrm{d} \rightarrow \mathrm{t} + \gamma + 6.25\,\mathrm{MeV},\ \ \sigma_\gamma = 0.519(7)\,\mathrm{mb} \tag{6.30}$$

$$\mathrm{n} + \mathrm{p} \rightarrow \mathrm{d} + \gamma + 2.22\,\mathrm{MeV},\ \ \sigma_\gamma = 0.3326(7)\,\mathrm{b} \tag{6.31}$$

In the above reactions the γ energies and the neutron capture cross-sections are given. The reaction in 6.30 occurs only within the heavy water, in which a neutron

Isotope	Abundance		Isotope	Abundance
^2H	99.917(5)%		^{17}O	0.17(2)%
^3H	0.097(10) μCi/kg		^{18}O	0.71(7)%
^1H	0.082(5)%		^{16}O	99.11(1)%

Table 6.2: Isotopic Composition of SNO Heavy Water[6].

Medium	Capture Percentage
D_2O	58.9
• H in D_2O	15.0
• D in D_2O	27.9
• ^{16}O(n,γ) in D_2O	4.8
• ^{17}O(n,α) in D_2O	11.2
Acrylic and Exterior(H_2O)	41.1

Table 6.3: Monte Carlo Results for Neutron of Capture Probabilities by Isotope.

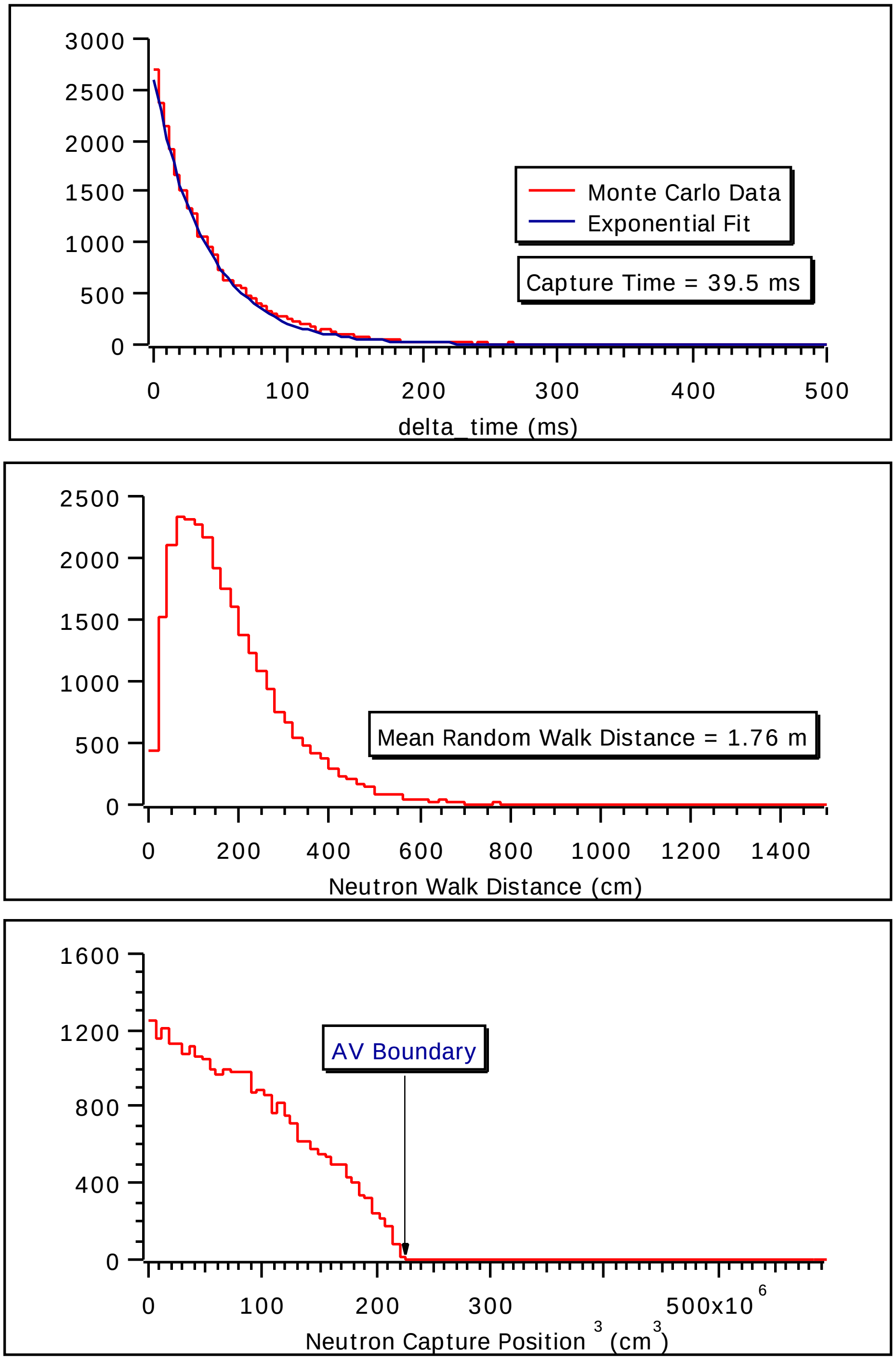

Figure 6.1: Monte Carlo Results of Neutron Capture on Deuterium.

capture on deuterium produces a 6.25 MeV gamma. Neutrons can also capture within the heavy water via reaction 6.31, where capture on trace amounts of hydrogen produces a 2.22-MeV γ ray. In addition, neutrons can also capture via the following two reactions:

$$\mathrm{n} + {}^{16}\mathrm{O} \rightarrow {}^{17}\mathrm{O} + \gamma, \quad \sigma_\gamma = 0.190(19)\,\mathrm{mb} \tag{6.32}$$

$$\mathrm{n} + {}^{17}\mathrm{O} \rightarrow {}^{14}\mathrm{C} + \alpha, \ \sigma_\alpha = 0.235(10)\,\mathrm{b} \tag{6.33}$$

Since ^{14}C is a long-lived isotope, the reaction given by Eq. 6.33 does not produce any observable signal in the detector. The cross-section for reaction 6.32 is small compared to the others and the maximum γ energy of 3.27 MeV comes from the transition to the 0.87-MeV state (18%). This is a negligible effect and will be ignored in this study.

In addition to being present in the heavy-water, hydrogen nuclei exist in the AV material and in the light water outside the AV. Therefore, neutrons that manage to random walk to the AV will probably be captured by the hydrogen in the AV, or if they escape the vessel then they will capture on the light water. A consequence of the AV barrier is that as one approaches the AV from the center of the vessel one will see a decrease in neutron capture on deuterium. This is because the neutron capture cross-section of hydrogen is much larger than that of deuterium and, therefore, the probability of neutron capture on hydrogen rises as one gets closer to the AV boundary. This can be seen in the third plot of Figure 6.1. Tables 6.3 and 6.4 present the results of the neutron capture Monte Carlo simulations. The Monte Carlo simulations were performed with the measured isotopic abundances as given in Table 6.2, where 100,000 neutrons with 1 keV kinetic energy were uniformly generated within the AV volume. The plots in Figure 6.1 were generated by considering only neutron captures on deuterium, i.e. no other analysis cuts were imposed during the process. As seen in Table 6.3, 58.9% of all neutrons capture within the heavy water while the remaining 41.1% of them capture in the AV material and the light water outside the AV. The capture percentage of

Parameters	${}^{17}_{8}O = 0.172\%$	${}^{17}_{8}O = 0.344\%$
Capture Time (ms)	39.5	34.3
Walk Distance (m)	1.76	1.64

Table 6.4: Monte Carlo Results for Neutron Capture in D_2O.

neutrons by deuterium within the AV is 27.9%.

For the measured levels of isotopic abundances in the heavy water, the mean neutron capture time by deuterium is 39.5 msec and the mean neutron random walk distance before capture is 1.76 meters. All neutrons are captured within 500 ms of being generated. The capture efficiency is dependent on the presence of ^{17}O in the heavy water. As seen in Table 6.4, for twice the value of the measured ^{17}O abundance, the neutron capture time is reduced to 34.3 ms and the mean neutron random walk distance is reduced to 1.64 meters. By repeating the Monte Carlo with different neutron kinetic energies, e.g. at 10 keV, 100 keV and 1 MeV, it has been found that the capture time and walk distance parameters are insensitive to the initial neutron kinetic energies.

In the Monte Carlo procedure described above, analysis cuts were not applied to the Monte Carlo data and as a result one cannot quite compare those results to the results obtained from an analysis of muon induced spallation data from SNO. In the above scenario, unlike the real experiment, neutrons that captured only on deuterium were considered, information which is readily available from the Monte Carlo process. However, in SNO, the specific type of neutron capture information is not available and in order to determine the capture time of neutrons on deuterium one has to place various cuts to reduce the contributions from background and other competing neutron capture processes. Therefore, in order to make proper comparisons between data and simulation, Monte Carlo analy-

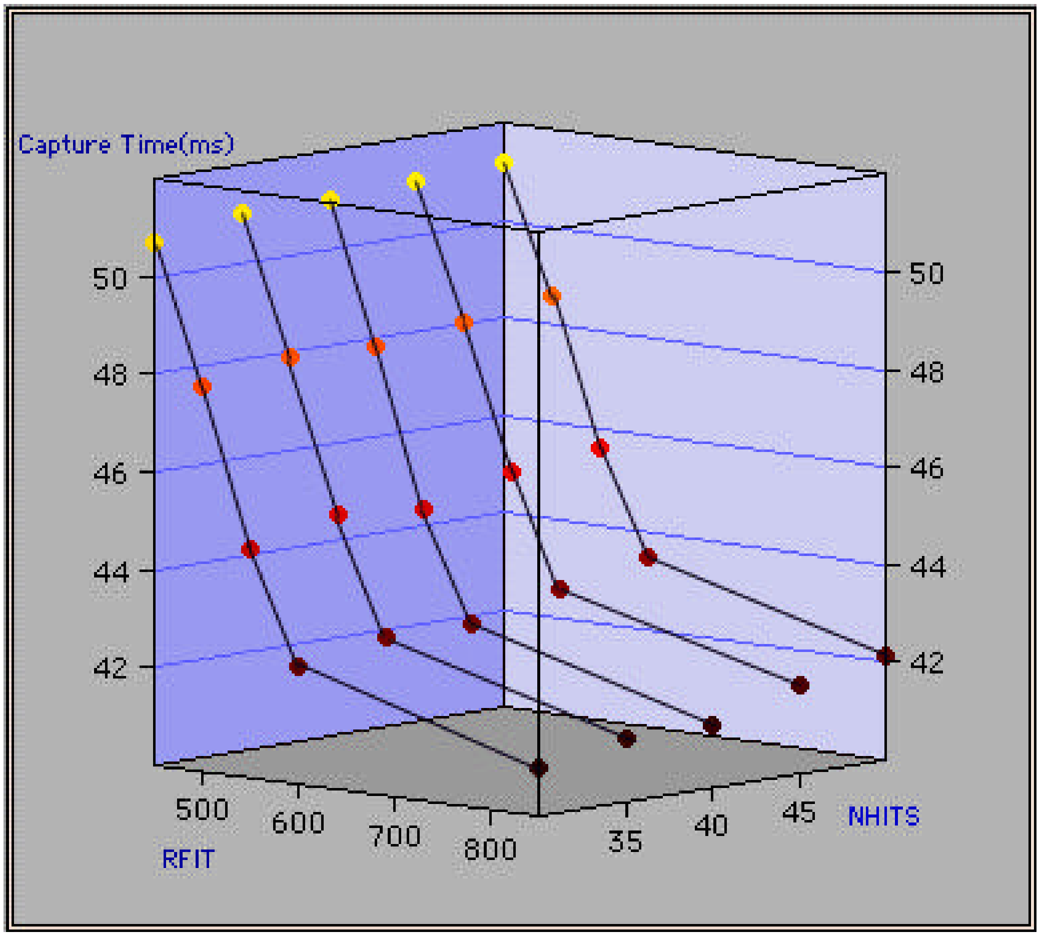

Figure 6.2: Neutron Capture Time Dependencies

NHITS Cut	Neutron Capture Time(ms)
30	44.7 ± 0.1
35	45.1 ± 0.1
40	45.0 ± 0.1
45	45.4 ± 0.2
50	45.6 ± 0.2

Table 6.5: Neutron Capture Time Dependence on NHITS with RFIT = 550 cm.

sis was performed in which the Monte Carlo data was processed in an identical manner to SNO data.

There are primarily three factors that impact the resulting capture time of neutrons by deuterium. The effect of the isotopic abundances in heavy water on the capture time has already been discussed. In addition to this, it has been found that during the data analysis process the capture time determination is weakly sensitive to an NHITS cut and strongly sensitive to an RFIT cut. It is important to understand these dependencies since during the muon-induced neutron analysis procedure NHITS and RFIT cuts will be placed on the data. Assuming that only muon induced neutrons have been isolated from the data, the capture time determined from these neutrons will be compared to the Monte Carlo capture time generated by imposing cuts similar to the ones placed on real data.

In Tables 6.5 and 6.6, results of the Monte Carlo processes are presented in which various combinations of the NHITS and RFIT cuts were applied. In this procedure, with the measured isotopic abundances, 233,000 1-keV neutrons were uniformly generated within the heavy water region. During the analysis of these

RFIT Cut(cm)	Neutron Capture Time(ms)
850	41.3 ± 0.1
600	42.7 ± 0.1
550	45.1 ± 0.1
500	48.2 ± 0.1
450	51.0 ± 0.2

Table 6.6: Neutron Capture Time Dependence on RFIT with NHITS = 35.

Monte Carlo data all neutron interactions within the detector were considered in order to determine the neutron capture times as a function of the imposed NHITS and RFIT cuts. The RFIT or the vertex position with respect to the center of the detector was determined by the standard SNOMAN Time Fitter. The results of the neutron capture Monte Carlo analysis is graphically displayed in Figure 6.2. The vertical axis of the 3-D plot is the mean neutron capture time determined from an analysis of the Monte Carlo data. The statistical errors for all indvidual points on the plot are less than 0.3% and have not been shown.

In Table 6.5, it can be seen that for a nominal RFIT cut of 550 cm the maximum change in capture time over an NHITS range of (30 → 50) is 2.0%. On the other hand, for a nominal NHITS cut of 35, the capture time gradually increases as RFIT decreases from 600 cm to 450 cm and the maximum change in capture time is 19.5%. Since the majority of the neutrons are captured within the D_2O and within AV material, the capture time changes by a very small amount [3.4%] when going from an RFIT cut of 850 cm to 600 cm. Given an NHITS cut of 35, Table 6.6 shows the capture times as a function of RFIT cut. NHITS cuts of 30, 35, 40, 45 and 50 were used during the analysis. The RFIT cuts used were 450 cm, 500 cm, 550 cm, 600 cm and 850 cm. The Monte Carlo results will be compared to the results obtained from an analysis of muon-induced neutrons at SNO.

6.5 Data Analysis and Results

6.5.1 Procedure

The study of muon-induced spallation events utillized a total of 103 production runs, listed in Table A.1, to identify muons and the spallation products that muons created as they traversed the detector. As mentioned in the previous section, the majority of the spallation products produced within the D_2O are neutrons, i.e. μ_n^{sp} events, and in this section the primary concentration will be on measuring the flux of muon-induced spallation neutrons at SNO. These neutrons will also be used to provide an independent method of performing γ-ray energy calibration of the SNO detector. An example of a muon-induced spallation event is shown in the XSNOED display of Figure 6.3, where the associated Run Number, GTID and NHIT of the event is given. This particular event occurred 29.09 ms (Δt) after an AV-going muon went through the detector and it was reconstructed to have occurred within the D_2O volume, 173 cm from the center of the vessel. The dots in the figure are the individual PMTs that fired in the event. One notices the very nice Cerenkov ring pattern. Given the measured NHITS and Δt values, this event is a likely candidate for a 6.25-MeV γ-ray from neutron capture on deuterium. It should be noted, however, that most Cerenkov events of interest don't exhibit such nice ring patterns. An outline with brief descriptions of the steps involved in the analysis procedure will now be provided:

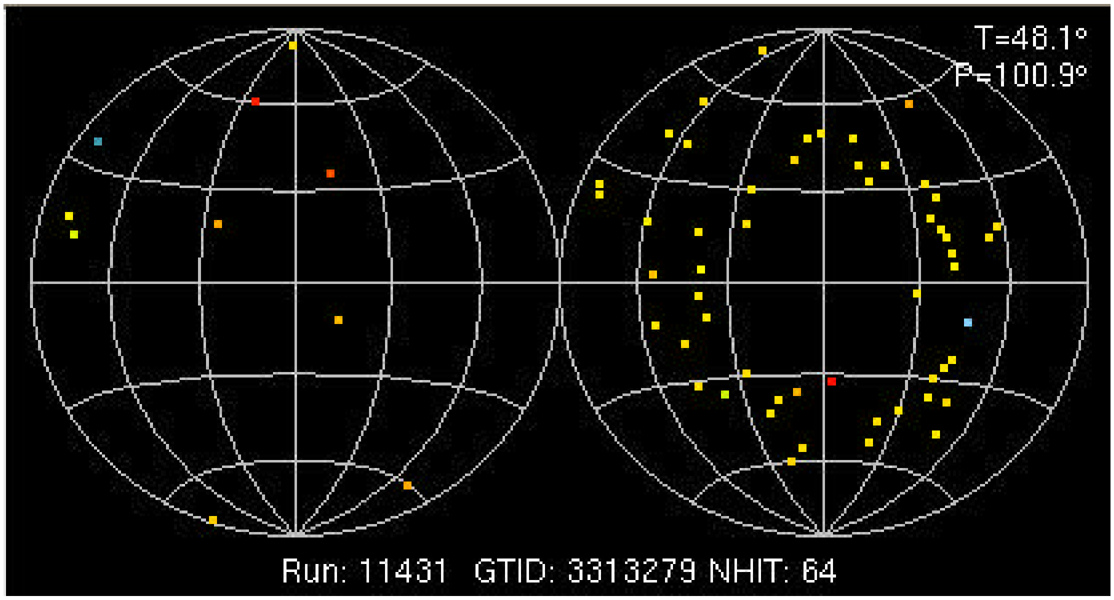

Figure 6.3: A Muon Follower Example.

- STEP 1 : MuonID and hand-scanning were used to identify a total of 5916 events that could produce muon-induced spallation events within the detector. It should be noted that the primary purpose of the hand-scanning procedure was to estimate the efficiency of the MuonID algorithm. In the future only the algorithm will be used to identify muons in order to maintain a blind analysis procedure.

- STEP 2 : Once a list of verified muons was constructed, it was used to process the runs in order to collect follower events given a muon event in the list. In this step a total of 103 Reduced Data Set [RDS] files were written to disk. Each file contained, for a particular run, muons and subsequent followers within 20 seconds of a muon. No analysis cuts except for this 20 second time cut were applied to the data.

	Muon Follower Parameters
1	Run Number
2	Parent Muon GTID
3	GTID
4	NHITS
5	Δt (ms)
6	Reconstructed Vertex Position {x,y,z} (cm)
7	$\hat{u}.\hat{r}$ ($\vec{u}$=direction vector, $\vec{r}$=radial vector)
8	ΔL_μ, Distance from Muon Track (cm)

Table 6.7: Muon Follower Information.

- STEP 3 : The 103 RDS files were then processed to produce a list of possible muon-induced spallation events. In this step the official SNO data cleaning cuts, known as DAMN cuts (described in Appendix B), were applied to remove instrumental background events or non-physics events from the final muon follower data sample. The "standard" neutrino DAMN cuts were not applied since those cuts would have eliminated most of the muon-induced spallation events. At this point various pieces of information, as described in Table 6.7, were gathered for each muon follower.

- STEP 4 : In this analysis step the muon-induced neutron production rate within the AV volume is determined. As mentioned earlier, the majority of the muon-induced spallation events that are created within the D_2O by AV-going muons are neutrons. From a Monte Carlo study in section 6.4.1 it was found that neutrons produced within the AV capture on deuterium with a capture time that does not extend beyond 500 ms. Therefore, in order to reduce the background from the muon-induced neutron sample only followers within 500 ms of a muon were considered. An NHITS cut of 35 was also applied to further reduce the background. Moreover, an NHITS cut of 35 corresponds to a $\sim$ 4-MeV energy threshold. Previously in Section 6.3.1 a 4-MeV threshold was used to derive the expected $\mu^{sp}_{\beta\gamma}$ production rate at SNO based on a SuperK result. Therefore, with a 4-MeV threshold the expected $\mu^{sp}_{\beta\gamma}$ production rate can be used to determine the expected μ^{sp}_{n} production rate at SNO within the AV volume, denoted by the symbol $R^{\mu^{sp}_{n}}[SNO, AV]_{measured}$. In order to do this, the efficiency of detecting neutrons above an NHITS cut of 35 will need to be calculated.

	Cuts
1	NHITS > 35
2	$\Delta t \leq 500$ ms
3	RFIT ≤ 600 cm

Table 6.8: Analysis Cuts.

- STEP 5 : The muon-induced neutron sample determined in the previous step is used to perform γ-ray energy calibration of the SNO detector. Neutrons produced within the D_2O are captured by deuterium and in the process generate 6.25-MeV γ rays. Given the NHITS distribution of the muon-induced neutron sample one can determine the NHITS to MeV conversion factor. This can then be compared to the γ-ray energy calibration result obtained from the ^{16}N calibration procedure.

In the following Section results from STEP 4 and STEP 5 are presented.

6.5.2 Results and Discussion

In order to reduce the background events to the muon-induced neutron sample, muon followers which satisfy the cuts defined in Table 6.8 have been used in the analysis. The time difference between the detection of the follower and the detection of its parent muon is denoted by Δt. It was shown in Section 6.3.1 that the production rate of $\mu^{sp}_{\beta\gamma}$ events is significantly smaller than the production rate of μ^{sp}_{n} events at SNO. The cuts defined in Table 6.8 further help to reduce the contribution of $\mu^{sp}_{\beta\gamma}$ to the muon-induced neutron signal. Therefore, the muon followers satisfying the above cuts are predominantly neutrons. By ignoring possible $\mu^{sp}_{\beta\gamma}$ contamination to the muon-induced neutron sample, one is truly determining the upper limit of the μ_n^{sp} production rate at SNO. However, since the contribution of $\mu_{\beta\gamma}^{sp}$ is very small, the measured upper limit of the μ_n^{sp} production rate would be very close to the true μ_n^{sp} production rate.

Neutron Multiplicity

A given muon can produce single or multiple neutrons within the D_2O, so the neutron multiplicity for a muon can be:

$$N_{mult} \geq 0 \tag{6.34}$$

After processing the runs a total of 656 events were found to satisfy the analysis cuts given in Table 6.8. These events consist of followers with $N_{mult} \geq 1$. Given that the neutron detection efficiency at SNO is not 100%, the N_{mult} parameter should be interpreted as the measured neutron multiplicity. In other words, if the true neutron multiplicity is N_{mult}^t, then $N_{mult} = N_{mult}^t \times \epsilon_{tot}$. Here, ϵ_{tot} is the total efficiency for detecting neutrons. A breakdown of the measured muon-induced neutron multiplicities is given in Table 6.9, where the second column gives the number of events that generated N_{mult} number of neutrons. The five events responsible for producing followers with $N_{mult} > 14$ are rare events ($\sim$ 0.1% of all detected through-going muons) and have been identified as distinctive AV-going events [DAGs] in Section 5.2.2. These DAGs are clearly distinguished from the typical muons that traverse the detector and, therefore, these events and their followers will be analyzed separately. The measurements of the muon-induced neutron production rate will be carried out for ($1 \leq N_{mult} \leq 14$) and ($N_{mult} > 14$). From Table 6.9 it can be seen that only 169 muons [3%] out of 5916 events generated neutrons that were detected. A total of 127 muons generated single neutrons and 42 muons generated multiple neutrons with $N_{mult} \geq 2$.

N_{mult}	Number of Events	Total Followers
0	5747	0
1	127	127
2	20	40
3	8	24
4	4	16
5	1	5
6	3	18
14	1	14
17	1	17
37	1	37
46	1	46
117	1	117
195	1	195

Table 6.9: Muon-induced Neutron Multiplicity.

Muon-induced Neutron Production Rate

In order to derive the upper limit on μ_n^{sp}, the production of $\mu_{\beta\gamma}^{sp}$ at SNO will be ignored. The following steps are involved in this process:

- STEP 1 : Determine the measured total number of neutrons and correlated accidental background counts, $\mathrm{N}_{measured}^{sp}$ and $\overline{\mathrm{B}}_{acc.}$ respectively, satisfying the DAMN cuts and the cuts given in Table 6.8.

- STEP 2 : In this step the background corrected muon-induced neutron count, $\mathrm{N}_{corr.}^{sp}$, is determined.

- STEP 3 : Determine the total neutron detection efficiency, $\epsilon_{tot.}$, which is a combination of the neutron capture efficiency, ϵ_c, within the D_2O volume and the efficiency due to the NHITS cut, ϵ_n. The individual efficiencies are derived from Monte Carlo.

- STEP 4 : Using the results from the above steps and given the total live-time, $\mathrm{L}_{tot.}$, for the analyzed runs the measured muon-induced neutron rate within the AV volume at SNO, $\mathrm{R}^{\mu_n^{sp}}[\mathrm{SNO, AV}]_{measured}$, is determined in this step.

- STEP 5 : Determine the production rates based on different values for the neutron multiplicities N_{mult}. Since followers with $\mathrm{N}_{mult} > 14$ are produced by the rare DAGs, rates are measured for $(1 \leq \mathrm{N}_{mult} \leq 14)$ and $(\mathrm{N}_{mult} > 14)$.

Given a valid muon trigger, followers within 20 seconds of the parent muon were collected. The events were required to pass the necessary cuts described in STEP 1. The data was then divided into 40 time segments where each segment is 500 ms wide. As mentioned earlier the first 500 ms segment contains the muon-induced neutron events. From this the total number of measured neutrons is found to be:

$$\mathrm{N}_{measured}^{sp} = 656.0 \pm 25.6(stat.) \tag{6.35}$$

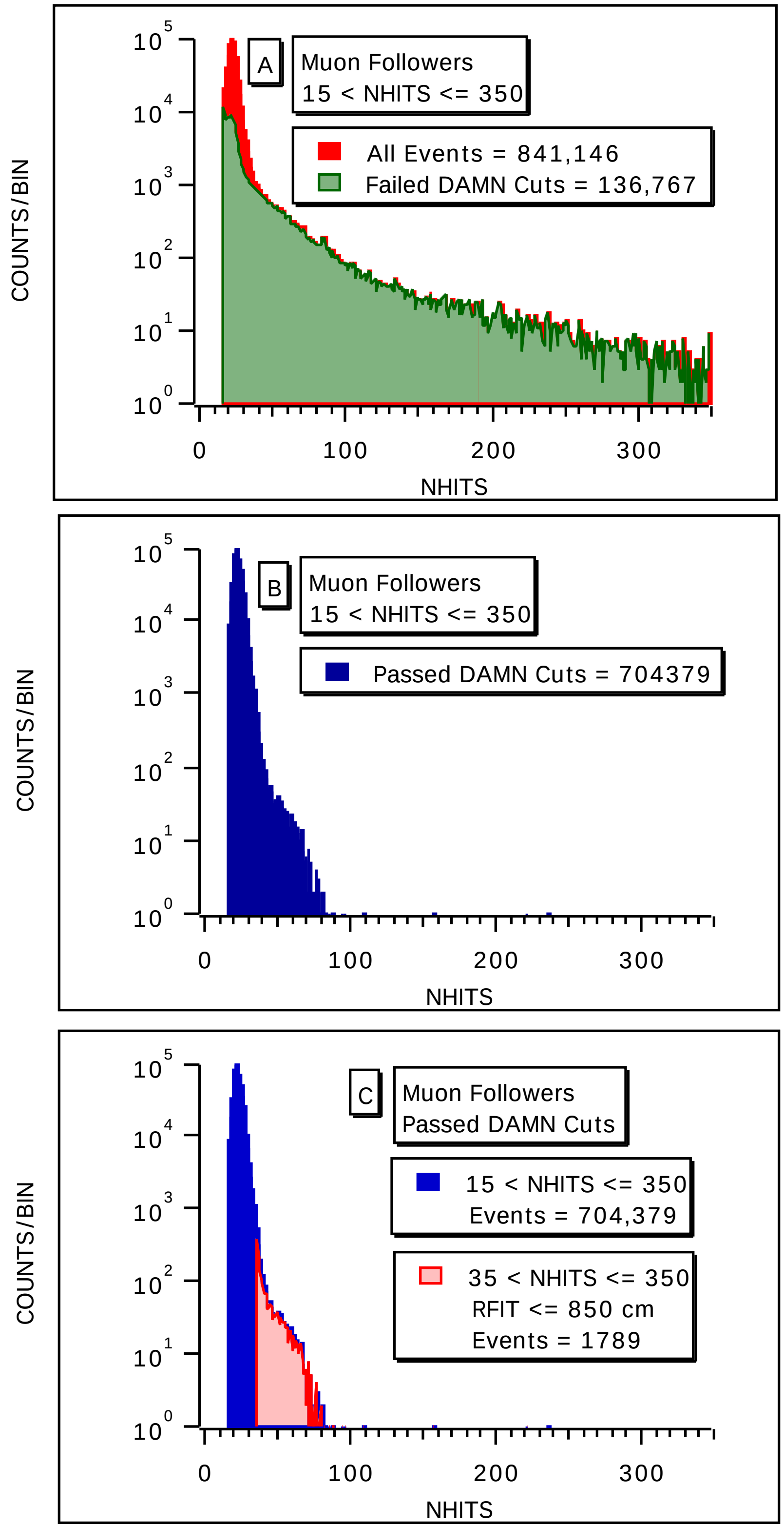

Figure 6.4: Spallation Data Collection Steps.

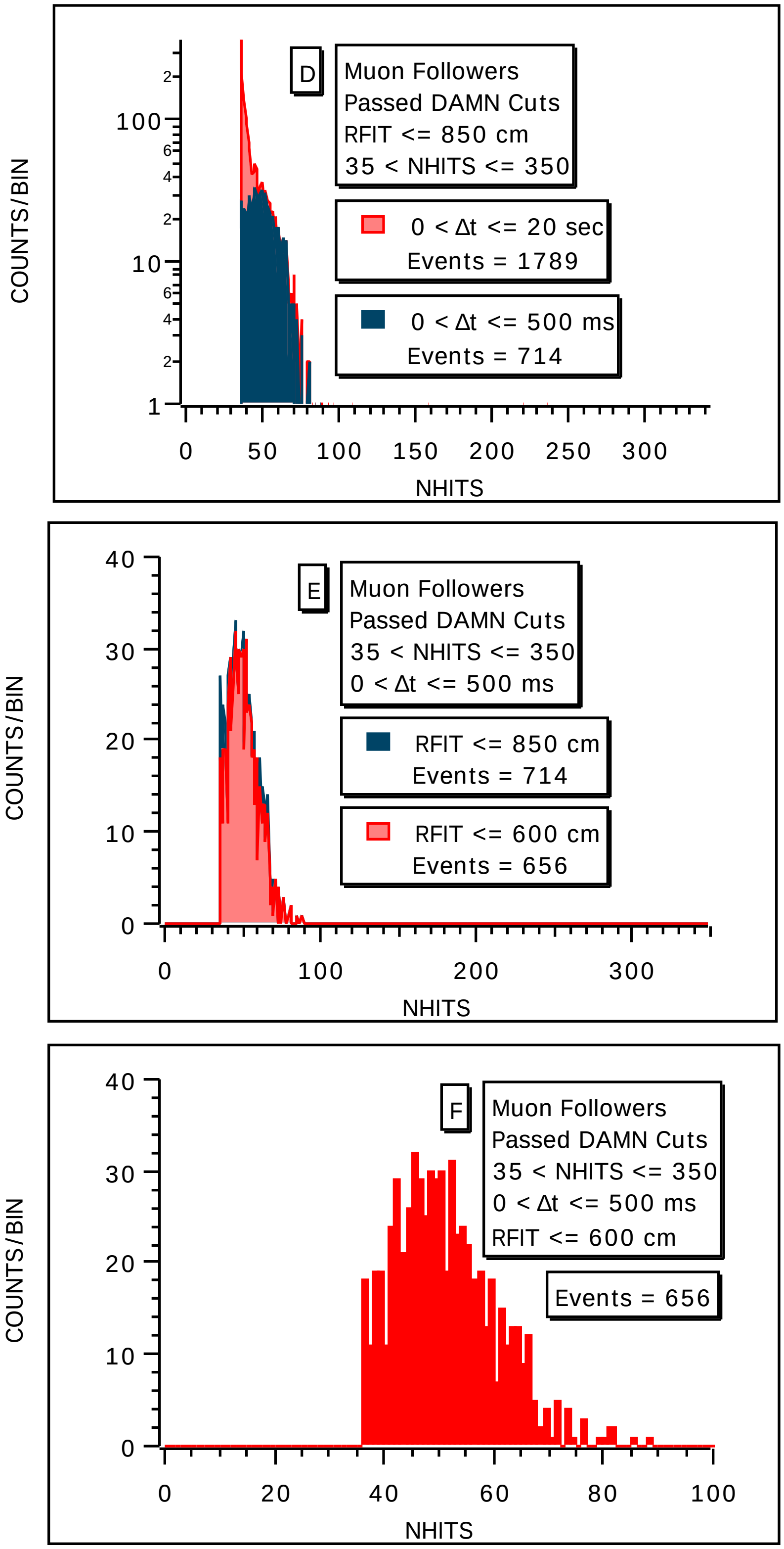

Figure 6.4: Spallation Data Collection Steps[cont].

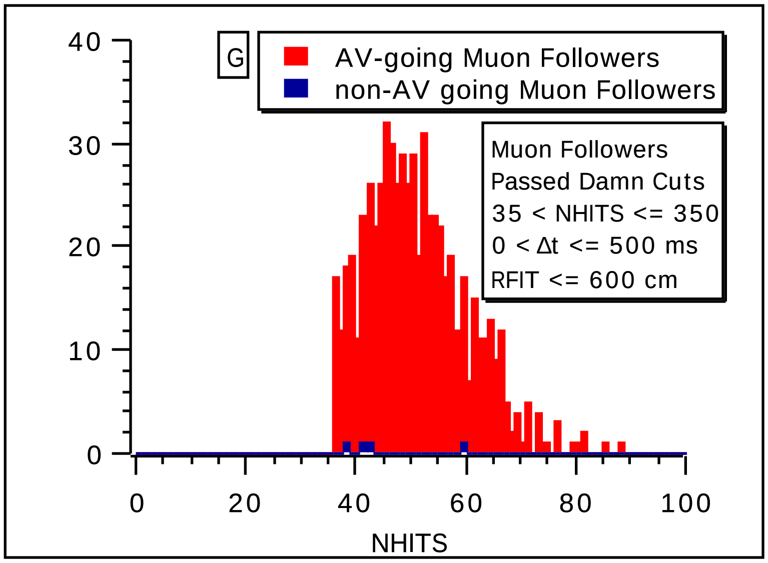

Figure 6.4: Spallation Data Collection Steps[cont].

Figure 6.4 presents seven plots which show the step by step data selection procedure involved in collecting the 656 spallation events. It was found that a total of 841,146 events fall within 20 seconds of the 5916 muons. These events satisfy the initial cut given by $(15 < \text{NHITS} \leq 350)^3$ as shown in Figure 6.4.A. Of these, a total of 136,767 events (16%) failed and the remaining 704,379 events (84%) passed the DAMN cuts (Figure 6.4.B). If it is now demanded that the events that pass the DAMN cuts also reconstruct within the detector and satisfy the NHITS cut given in Table 6.8 then only 1789 events (0.2%) survive (Figure 6.4.C). Now, a total of 714 events out of 1789 events satisfy the Δt cut given in Table 6.8, i.e. these events fall within 500 ms of the parent muons (Figure 6.4.D). By demanding that these events reconstruct within the heavy water region one gets from an initial sample of 841,146 events only 656 events (0.08%) to fall into the final spallation data sample. This is shown in Figures 6.4.E and 6.4.F. Furthermore,

---

[3] The hardware NHITS trigger threshold is set at 18. The Low NHITS trigger threshold, used mainly to sample the low NHITS background, is set at 11. During data taking this trigger is scaled by a factor of 1000.

in Figure 6.4.G the followers from AV and non-AV going muons are shown. It can be seen from this plot that the muons that go through the AV generate, as expected, the majority of the followers within the D_2O.

Figure 6.5 shows all muon correlated followers that were collected within 20 seconds of each individual muon and then passed the applied analysis cuts as defined in STEP 1. From the first plot one sees an excess counts in the first bin which is significantly larger than the relatively flat background. There are a total of 656 events in this bin and they are predominantly muon-induced neutrons. The second plot excludes the first bin to show the characteristics of the accidental background.

In order to determine the possible correlated backgrounds to the muon-induced neutron signal, accidental background spectra within 20 seconds of a Pulsed Global Trigger (PGT) event were acquired. The PGT signal is generated by the SNO electronics at a rate of 5 Hz so as to acquire background data during the life time of a particular run. An event that is initiated by a PGT is called a PGT event and the events following them are called PGT followers. For the purpose of this study PGT events and followers are ideal and they have been utilized to determine the accidental background counts to the muon-induced neutron signal. The PGT followers were taken across all 103 runs so as to provide an unbiased background sample. These events were processed in a similar fashion to the muon-induced follower events, i.e. the cuts described in STEP 1 were also applied to the PGT followers. Therefore, only PGT followers that reconstructed within the D_2O volume and had NHITS > 35 were used. The muon trigger has been used to provide a measure of the accidental background by acquiring background data quasi-simultaneously to the muon signal. But the drawback to this is that we only have 5916 muon triggers and this limitation results in a larger error estimate for $\overline{B}_{acc.}$. Furthermore, one cannot guarantee that there will not be any contamination of the background signal due to spallation events. However, the background distributions determined by muon trigger and PGT will be compared

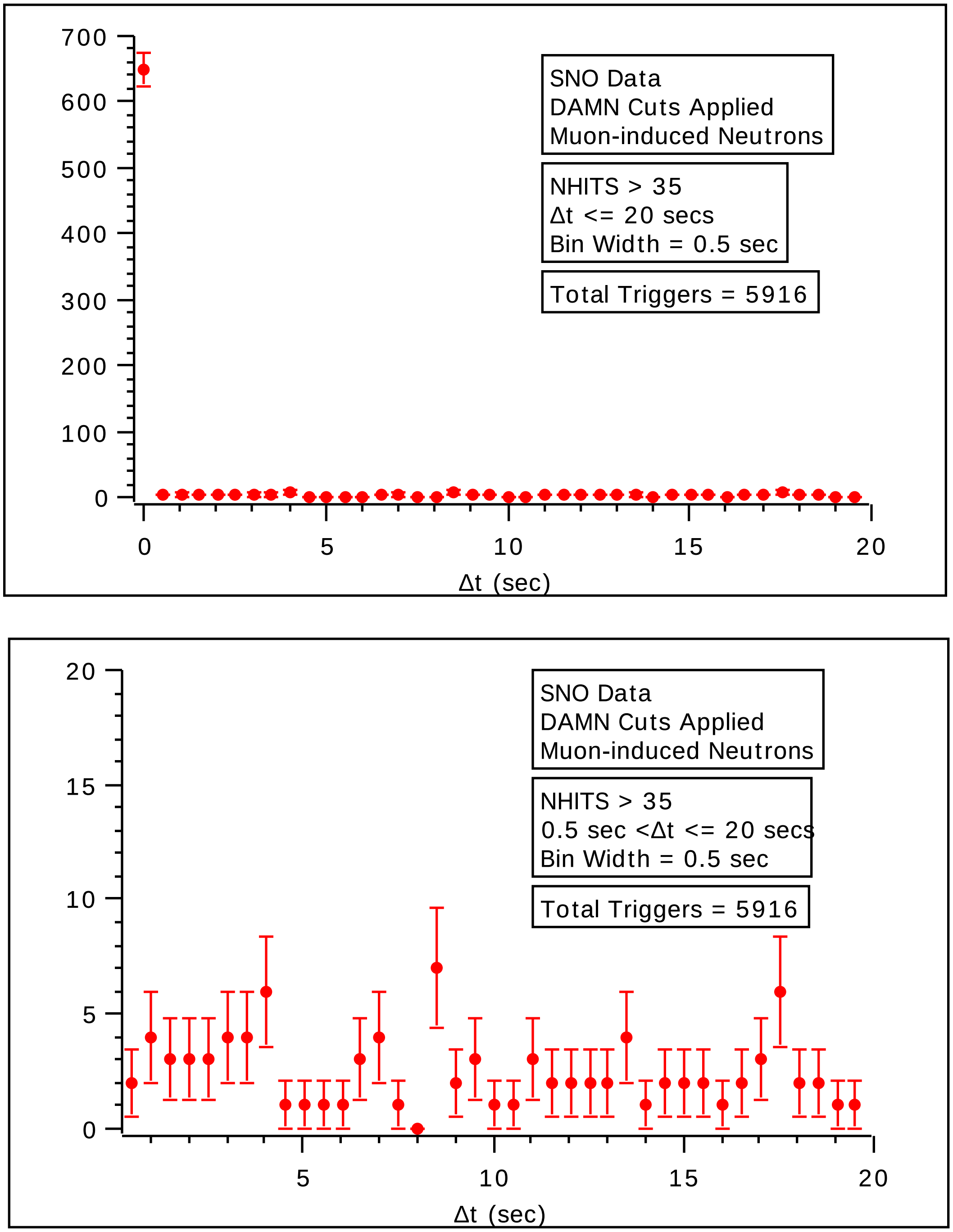

Figure 6.5: Muon Correlated Followers.

so as to perform a consistency check.

A total of 30,303 PGT events were sampled in this process and PGT followers within 20 seconds of each of these PGT events were collected. The total number of PGT followers satisfying applied cuts is:

$$\mathrm{N}^{PGT}_{measured} = 433 \pm 21(stat.) \tag{6.36}$$

The total time sampled during this process is:

$$\mathrm{T}^{PGT}_{tot.} = 168.48 \text{ hrs} \tag{6.37}$$

Now, for the 5916 muon triggers the total sampled time during the collection of muon follower events is:

$$\mathrm{T}^{\mu}_{tot.} = 32.87 \text{ hrs} \tag{6.38}$$

Therefore, by using Eqs. 6.37 and 6.38 one can appropriately scale the result given in Eq. 6.36 to determine the accidental background to the muon-induced neutron sample within a 500 ms time window:

$$\overline{\mathrm{B}}_{acc} = \frac{\mathrm{N}^{PGT}_{measured} \times \mathrm{T}^{\mu}_{tot.}}{\mathrm{T}^{PGT}_{tot.} \times 40} = 2.11 \pm 0.11 \tag{6.39}$$

For a consistency check we counted the number of muon-induced followers which satisfy 10 sec $< \Delta$t $\leq$ 20 sec, since 10 seconds after a muon the contamination due to muon-induced spallation events is insignificant. The measured number is found to be:

$$\mathrm{N}^{\mu}_{bckgnd}[\text{measured}] = 42.0 \pm 6.5 \tag{6.40}$$

Eq. 6.39 is used to determine the expected muon trigger correlated background count within a 10 second time window:

$$\mathrm{N}^{\mu}_{bckgnd}[\text{expected}] = 42.2 \pm 2.2 \tag{6.41}$$

Therefore, from Eqs. 6.40 and 6.41 one finds that the accidental background count determined by sampling PGT followers correctly predicts the accidental

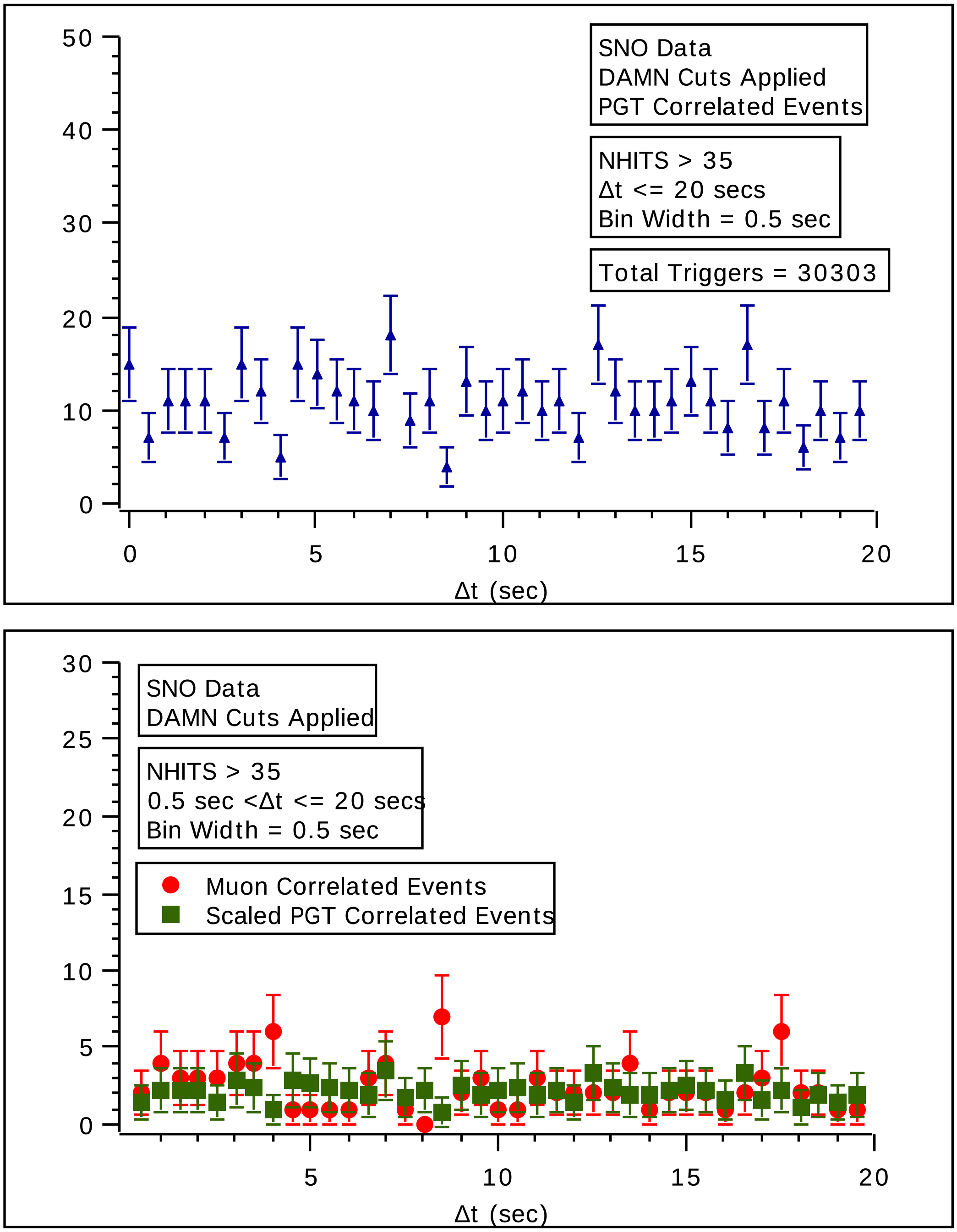

Figure 6.6: PGT and Muon Correlated Background.

background that is collected quasi-simultaneously to the muon trigger. This consistency check also demonstrates that beyond 10 seconds after a muon the background count is independent of the muon trigger. The 433 PGT correlated background events are shown in the first plot of Figure 6.6. The bin width for the two plots in this figure is 500 ms. The second plot shows the superposition of the muon and PGT correlated background events, where the PGT correlated background has been scaled appropriately to the muon sampling time. The first 500 ms bin, which includes the 656 muon-induced spallation events, has been excluded from this plot so as to zoom in on the remaining bins.

Using Eqs. 6.35 and 6.39 the background corrected muon-induced neutron count is determined:

$$\mathrm{N}^{sp}_{corr.} = \mathrm{N}^{sp}_{measured} - \overline{\mathrm{B}}_{acc.} = 653.9 \pm 25.6 \tag{6.42}$$

The measured muon-induced neutron rate within the AV is given by the following:

$$\mathrm{R}^{\mu_n^{sp}}[SNO, AV]_{measured} = \frac{\mathrm{N}^{sp}_{tot}}{\mathrm{L}_{tot}} \tag{6.43}$$

where, N^{sp}_{tot} is the total number of spallation neutrons generated within the AV and L_{tot} is the total live time of the 103 production runs used in this study. The data sample analyzed has a total live-time of:

$$\mathrm{L}_{tot} = (85.65 \pm 0.07) \text{ days} \tag{6.44}$$

The total number of muon-induced neutron events within the AV is given by the following equation:

$$\mathrm{N}^{sp}_{tot} = \frac{\mathrm{N}^{sp}_{corr.}}{\epsilon_n \times \epsilon_c} \tag{6.45}$$

where, ϵ_n is the neutron detection efficiency due to the NHITS cut and ϵ_c is the neutron capture efficiency in $\mathrm{D_2O}$. Previously in Table 6.3 the following was found:

$$\epsilon_c = 0.279 \tag{6.46}$$

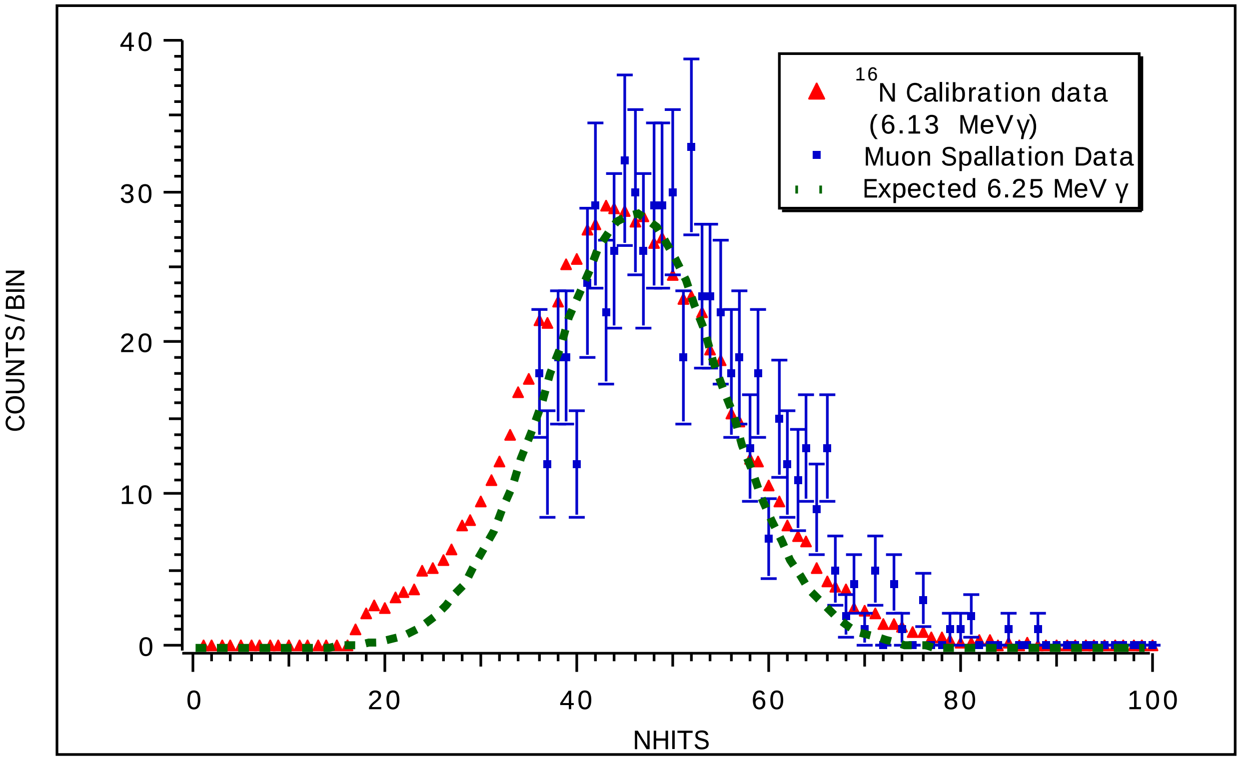

Figure 6.7: NHITS Distributions of ^{16}N and Spallation Data. The error bars for the ^{16}N and expected 6.25 MeV γ distributions are not displayed since they are smaller than the data points.

In order to determine the value of ϵ_n, one will have to rely on Monte Carlo to provide the expected mean value, $\overline{\mathrm{N}}^{6.25\gamma}_{expected}$, and width, $\sigma^{6.25\gamma}_{expected}$, of the 6.25-MeV γ-ray NHITS distribution generated by neutron capture on deuterium. From pg.158 of Andre Hamer's Ph.D. thesis one finds [109]:

$$S_\epsilon \equiv \frac{\overline{\mathrm{N}}_{measured}}{\overline{\mathrm{N}}_{MC}} = 1.047 \tag{6.47}$$

where, S_ϵ is the scaling factor obtained from the ratio of NHITS means from the experimental and Monte Carlo generated ^{16}N 6.13-MeV γ-ray. In Monte Carlo 233,000 neutrons were uniformly distributed within the D_2O of which 27.9% captured on deuterium. From the 6.25-MeV γ generated by this capture, the following was obtained:

$$\overline{\mathrm{N}}^{6.25\gamma}_{MC} = 43.37 \tag{6.48}$$

In Figure 6.7 the NHITS distribution of a ^{16}N calibration run at SNO is shown. Superimposed on it are the expected NHITS distribution of 6.25-MeV γs and the NHITS distribution of the muon-induced spallation data. The distributions have been vertically scaled to the NHITS distribution of the 656 spallation events. Now, using Eq. 6.47 one gets:

$$\overline{\mathrm{N}}^{6.25\gamma}_{expected} = 43.37 \times 1.047 = 45.41 \tag{6.49}$$

Furthermore, from the Monte Carlo simulation one finds an expected width of:

$$\sigma^{6.25\gamma}_{expected} = 9.55 \tag{6.50}$$

Since neutron capture on deuterium produces a monoenergetic 6.25-MeV γ-ray, both experimental and Monte Carlo NHITS distributions of 6.25-MeV γ-rays can be approximated by a Gaussian distribution. Therefore, given a Gaussian distribution $P_G(x : \mu, \sigma)$, where $\mu = 45.41$ and $\sigma = 9.55$, one can calculate ϵ_n by integrating the Gaussian distribution with $x > 35$. The following result from the integration was obtained:

$$\epsilon_n = 0.88094 \tag{6.51}$$

Therefore, the following is obtained:

$$\epsilon_{tot} = \epsilon_n \times \epsilon_c = 0.8809 \times 0.2790 = 0.2458 \tag{6.52}$$

Combining Eqs. 6.42, 6.45 and 6.52 one gets the following:

$$\mathrm{N}_{tot}^{sp} = 2604 \pm 104 \tag{6.53}$$

Utilizing Eqs. 6.43, 6.44 and 6.53, the measured muon-induced neutron rate within the AV at SNO is determined to be:

$$\mathrm{R}^{\mu_n^{sp}}[\mathrm{N}_{mult} \geq 1][\mathrm{SNO,\ AV}]_{measured} = (30.40 \pm 1.21)\ \mathrm{day}^{-1}\ \mathrm{kt}^{-1} \tag{6.54}$$

Ignoring the followers generated by the rare DAGs, i.e. by only considering events with ($1\leq N_{mult} \leq 14$) one gets the following result:

$$\mathrm{R}^{\mu_n^{sp}}[1 \leq \mathrm{N}_{mult} \leq 14][\mathrm{SNO,\ AV}]_{measured} = (11.49 \pm 0.74)\ \mathrm{day}^{-1}\ \mathrm{kt}^{-1} \tag{6.55}$$

From Eq. 6.20 the predicted muon-induced neutron rate within the AV was found to be (10.74 ± 1.11) day^{-1} kt^{-1}. It can be seen that the results given by Eqs. 6.20 and 6.55 are consistent within errors. Therefore, the production rate of muon-induced neutrons at the depth of SNO is independent of the target materials used in these two experiments (CH_2 and D_2O respectively). However, if one includes the followers of the DAGs into the muon-induced neutron sample then the measured rate is ~ 3 times larger than that predicted by Bezrukov. Furthermore, excluding the DAGs one finds that the measured neutron multiplicities are larger at SNO $\mathrm{N}_{mult} \leq 14$ than at the Bezrukov experiment $\mathrm{N}_{mult} \leq 5$. This is expected since the muons in general are more energetic at SNO than at the Bezrukov experiment.

6.6 A Closer Look at SNO Spallation Products

From an analysis of the data it has been determined that if one considers only muon-induced spallation products that are generated within 500 ms of a through-going muon and reconstruct within the D_2O, then given a multiplicity of $N_{mult} \leq 14$ (i.e. excluding followers of the DAGs), the measured rate of production of the spallation products is consistent with the predicted rate of production of muon-induced neutrons within the D_2O volume at SNO. A closer look at the properties of the muon-induced spallation products will now be conducted in order to further demonstrate that these products are neutrons which have been generated by through-going muons. Since the background is only 0.3% of the signal and since it cannot be separated from the signal on an event by event basis, the data sample will be analyzed inclusive of the background events. The properties of the spallation products will be investigated by dividing the data sample into the following four categories:

- 1. $N_{mult} \geq 1$: Includes all 656 spallation products.

- 2. $N_{mult} = 1$: Includes 127 spallation products.

- 3. $1 \leq N_{mult} \leq 14$: Includes 244 spallation products. The followers from the five DAGs are excluded.

- 4. $N_{mult} > 14$: Includes the 412 spallation products that were generated by the five DAGs.

In the next section the characteristics of the muons that were responsible for generating the 656 spallation products will be presented.

6.6.1 Muon Characteristics

From the data sample it was found that a total of 5916 events (from 103 production runs) can potentially produce spallation products in the SNO detector. However, the primary interest is in spallation products that are generated within

Multiplicity	Number of Muons	Total Spallation Products
$N_{mult} = 0$	5747	0
$N_{mult} \geq 1$	169	656
$N_{mult} = 1$	127	127
$1 < N_{mult} \leq 14$	37	117
$N_{mult} > 14$	5	412

Table 6.10: Number of muons producing N_{mult} spallation products.

	Run	GTID	Spallation Products
1	10008	1697058	46
2	10549	3301460	17
3	10946	299141	195
4	11291	1015858	117
5	11347	92584	37

Table 6.11: Spallation product multiplicity of the 5 Distinctive AV-going Events.

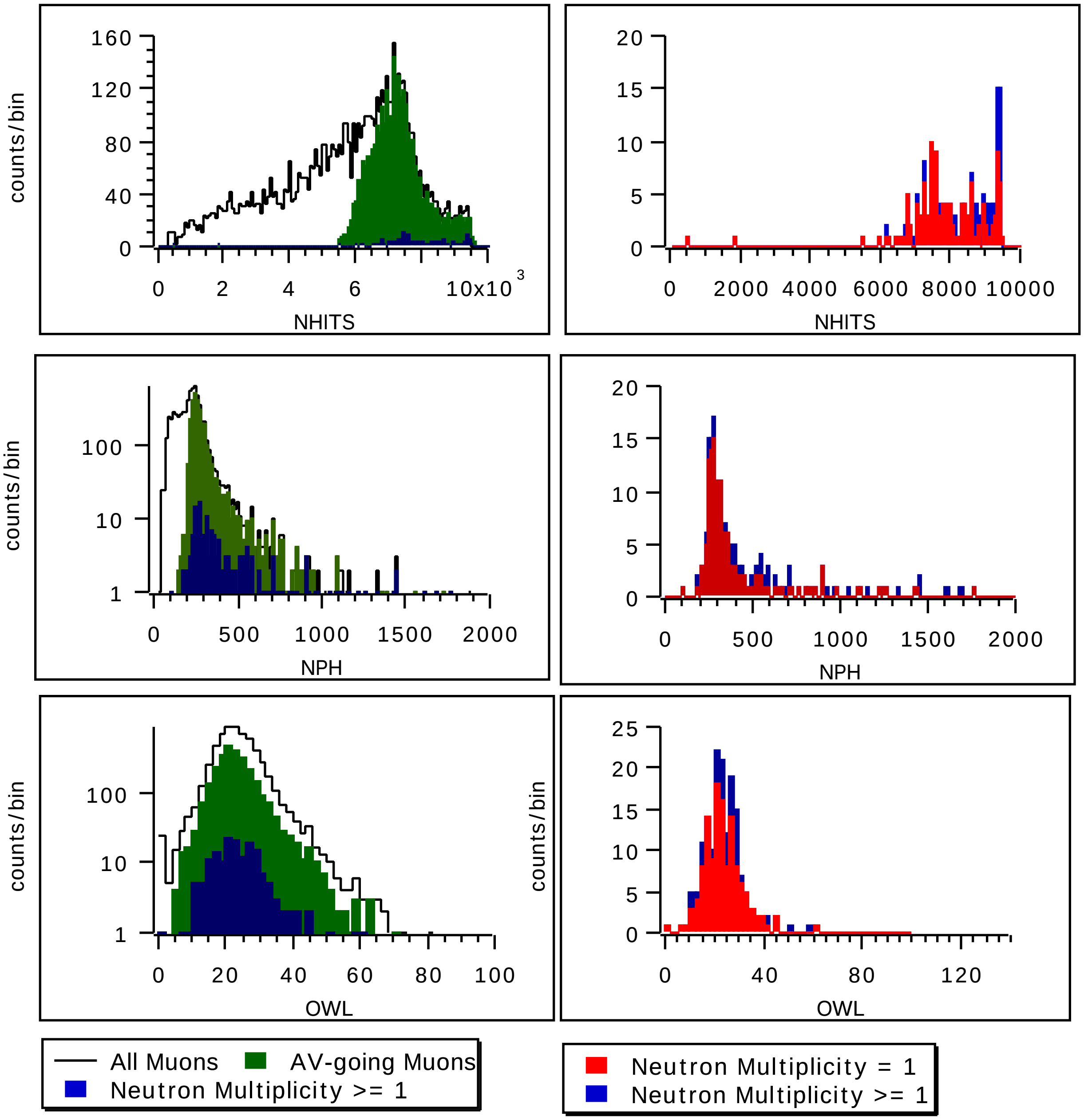

Figure 6.8: Characteristic Distributions of Neutron Generating Muons.

the D_2O and only muons that go through the AV can produce such spallation products. From Table 6.10 it can be seen that only 169 muons [3%] were responsible for producing these spallation products. Of these, 127 muons [75%] produced single followers and 37 muons [22%] produced followers with ($1 < N_{mult} \leq 14$). The remaining 5 events [3%] have produced followers with $N_{mult} > 14$, resulting in a total of 412 followers, i.e. they were responsible for generating 63% of all followers in the data sample. As shown in Section 5.2.3, five of these high-multiplicity spallation product generating events are not typical AV-going muons. These DAGs are most probably high energy muons accompanied by an energetic electromagnetic shower. Therefore, the spallation products associated with these events need to be considered separately from the spallation products associated with typical AV-going muons. The multiplicities of the DAG generated spallation products are given in Table 6.11. In the following section the NHITS and Δt distribution of the spallation products associated with these rare DAGs will be looked at in order to determine whether they are consistent with the distributions obtained from neutron capture on deuterium.

In Figure 6.8 the NHITS, NPH and OWL distributions of the neutron generating muons are presented. From the plots in the first column it can be seen that these distributions, as expected, are a subset of the AV-going muon distributions. In the second column the plots show the same distributions for muons producing spallation neutrons with $N_{mult} \geq 1$ and $N_{mult} = 1$. The peak at the end of the NHITS distribution is due to the five DAGs producing spallation products with $N_{mult} > 14$.

6.6.2 Spallation Product Characteristics

In this section the NHITS, Δt, R^3_{fit} distributions of the spallation products, as defined in Table 6.7, will be presented. The objective is to determine whether these distributions are consistent with the distributions that would be expected

	Category	Events	$\overline{\mathrm{N}}_{data}$	σ^N_{data}	τ_{data}
1	$\mathrm{N}_{mult} \geq 1$	656	48.4 ± 1.2	9.7 ± 0.5	40.3 ± 1.1 ms
2	$\mathrm{N}_{mult} = 1$	127	45.6 ± 1.8	14.2 ± 3.0	45.3 ± 2.9 ms
3	$1 \leq \mathrm{N}_{mult} \leq 14$	244	46.1 ± 0.8	11.4 ± 1.5	43.7 ± 2.1 ms
4	$\mathrm{N}_{mult} > 14$	412	49.3 ± 1.1	8.8 ± 0.4	38.8 ± 1.2 ms
5	Monte Carlo	65,007	45.41 ± 0.05	9.55 ± 0.08	42.7 ± 0.1 ms

Table 6.12: Spallation Product Characteristics.

from neutron capture on deuterium. As mentioned earlier, these distributions will be constructed for different categories, where each category corresponds to a different value of N_{mult}. For all categories the NHITS distribution will be fit to a truncated Gaussian with (NHITS > 35), and from that the mean NHITS value, $\overline{\mathrm{N}}_{data}$, its uncertainty, and the width of the distribution, σ^N_{data}, will be determined. Furthermore, the Δt distribution will be fit to an exponential in order to determine the mean capture time, τ_{data}, of the spallation products.

Results

The NHITS, Δt and R^3_{fit} plots for the four different N_{mult} categories are presented in Figures 6.9 $\rightarrow$ 6.12.The results of fitting the NHITS and Δt distributions are given in Table 6.13. Also shown in this table are the expected mean and width of the 6.25-MeV γ-ray NHITS distribution and the expected neutron capture time on deuterium. All results have been derived for cuts defined in Table 6.8.

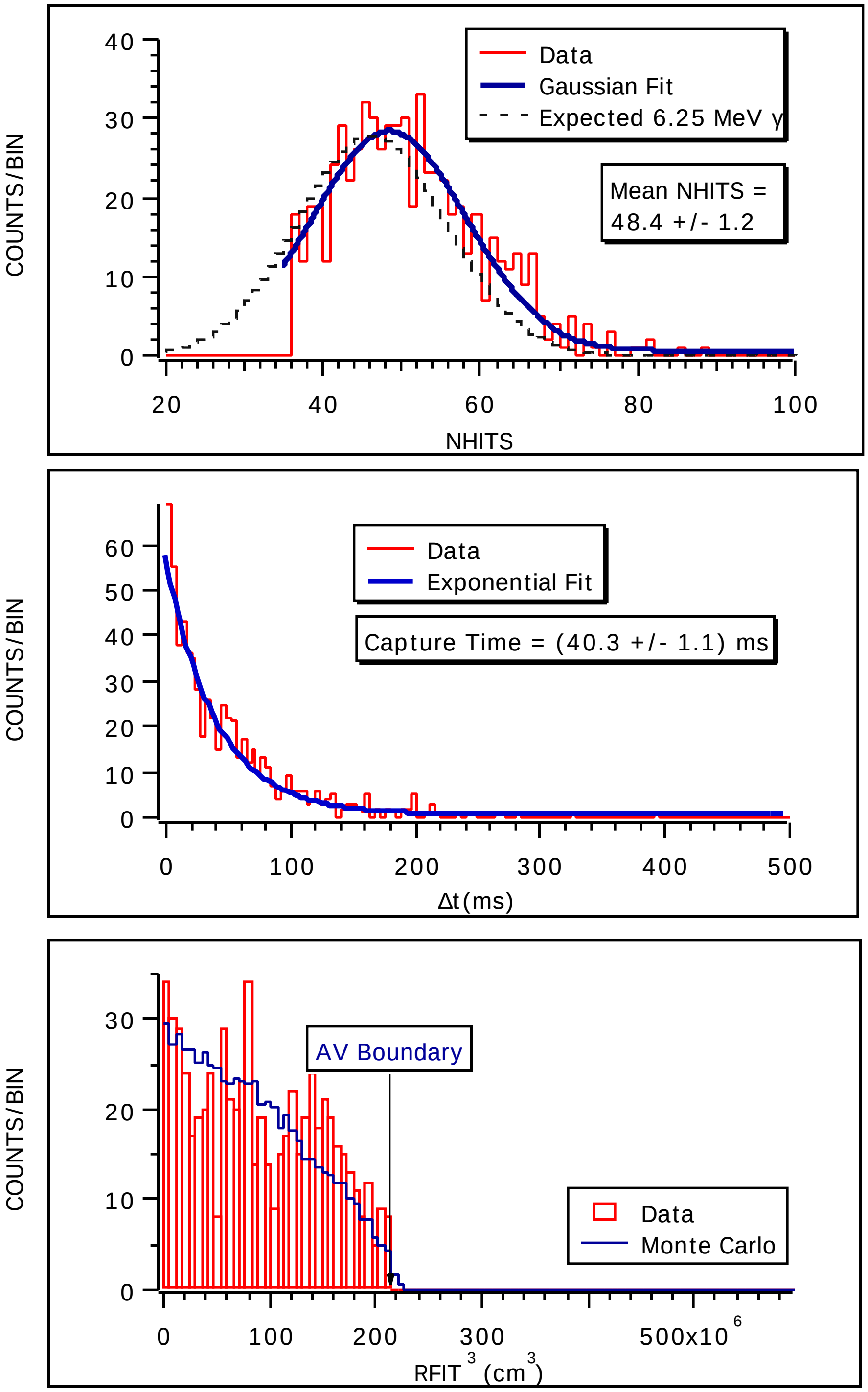

Figure 6.9: Spallation Data Characteristics : $N_{mult} \geq 1$. Events = 656.

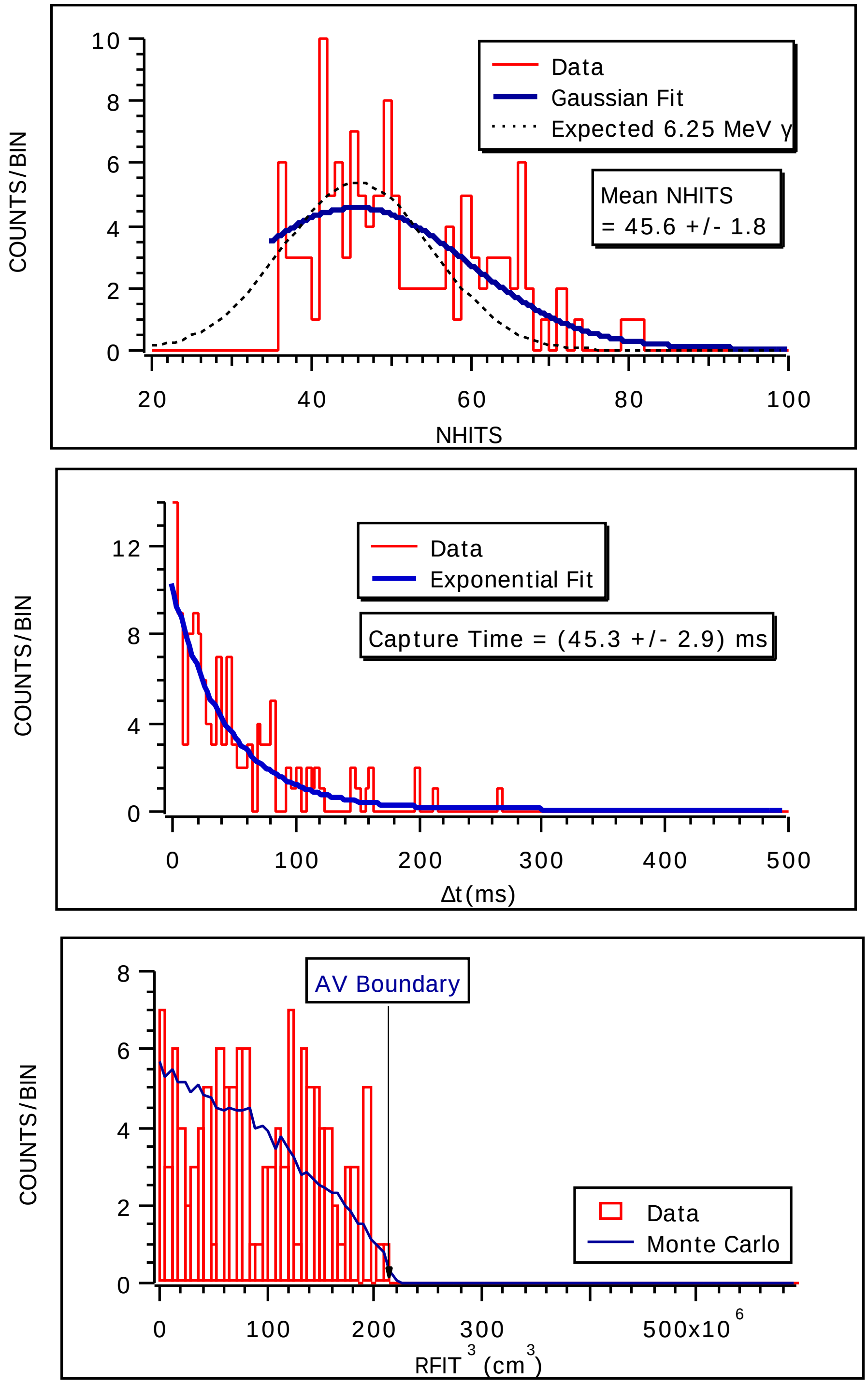

Figure 6.10: Spallation Data Characteristics : $N_{mult} = 1$. Events = 127.

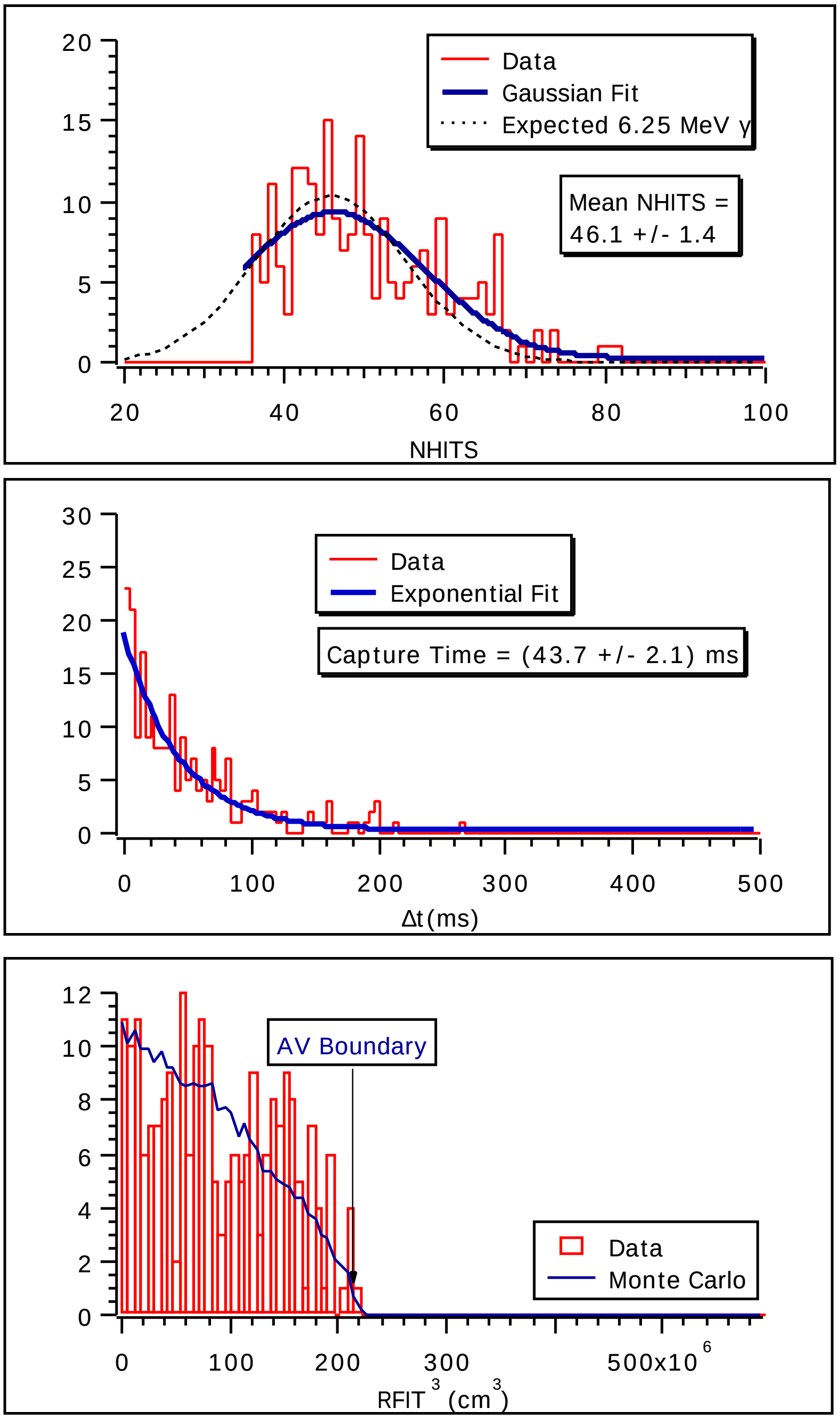

Figure 6.11: Spallation Data Characteristics : $N_{mult} \leq 14$. Events = 244.

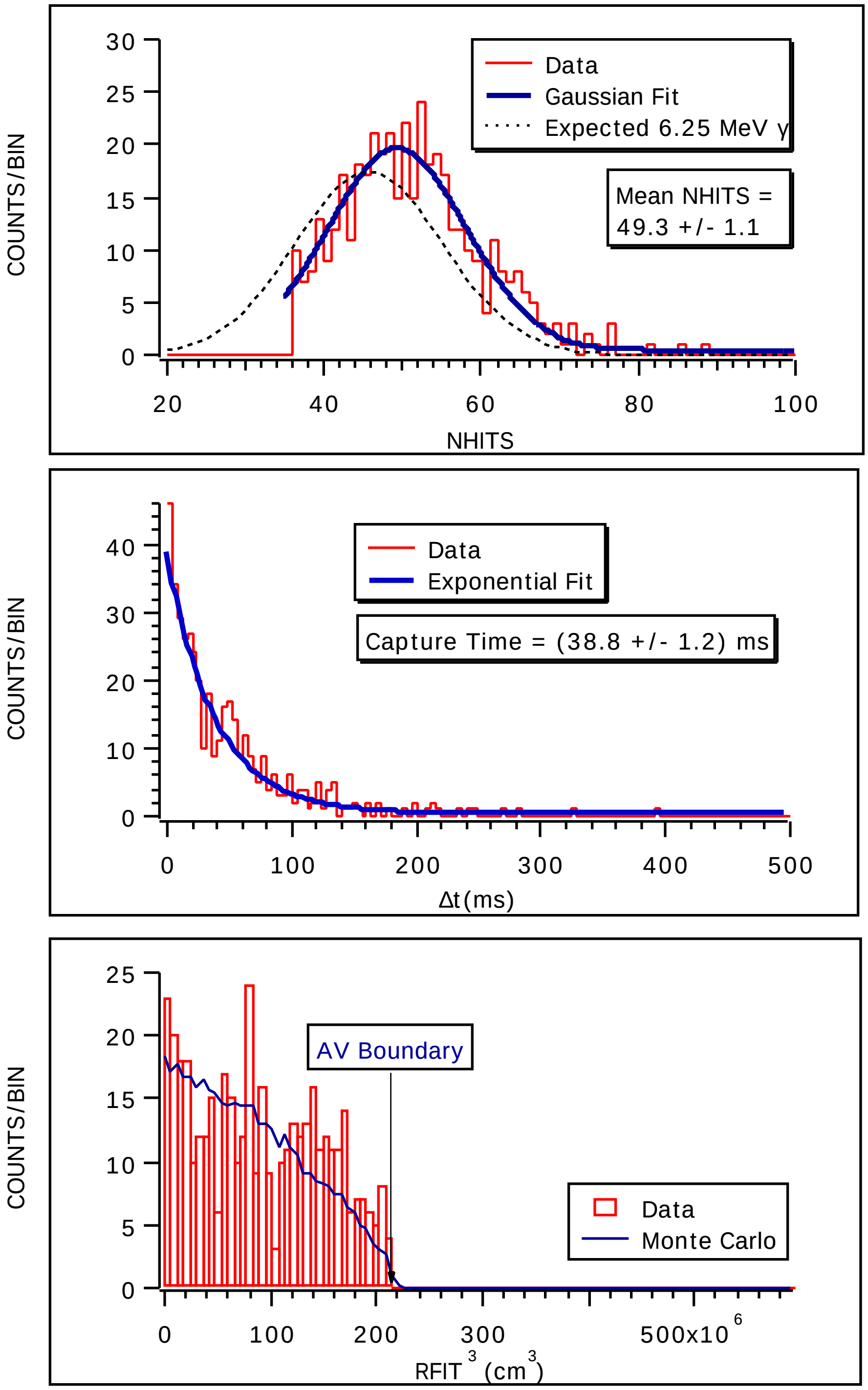

Figure 6.12: Spallation Data Characteristics : $N_{mult} > 14$. Events = 412.

Measured R^3_{fit} Distribution for Spallation Products

The density or R^3_{fit} distributions of the spallation product capture positions for all scenarios show that, as one goes from the center of the vessel and approaches the AV boundary the distribution gradually drops off, which as discussed earlier is the expected behavior for the capture of neutrons uniformly distributed within the D_2O (Figure 6.1).

Discussion

By comparing the measured $\overline{\mathrm{N}}_{data}$ and τ_{data} values for the different categories to the Monte Carlo values for neutron capture on deuterium, one can determine whether the muon-induced spallation events exhibit the characteristics of neutrons that are generated within the D_2O.

In the first plot of Figure 6.13 the measured $\overline{\mathrm{N}}_{data}$ values for the four different categories along with the expected mean NHITS value, $\overline{\mathrm{N}}^{6.25\gamma}_{expected}$, are shown. The bars in the figure represent 1σ error and the straight line represents the Monte Carlo determined expected mean NHITS. From the figure, it can be seen that the measured $\overline{N}_{data}$ values for the categories ($N_{mult} = 1$) and ($1 \leq N_{mult} \leq 14$) include the expected mean NHITS value within the 1σ error bar. This is a good indication that the spallation products created by muons, where spallation products created by DAGs are excluded, produce an NHITS spectrum at SNO that is consistent with the NHITS spectrum that is generated by 6.25-MeV γ-rays from neutron capture on deuterium. Therefore, these spallation products are most likely neutrons produced by through-going muons. On the other hand, spallation products that are generated by DAGs do not produce an NHITS spectrum that is consistent with the NHITS spectrum from neutron capture on deuterium(the deviation from the expected mean is greater than 5σ). In this case the spallation products most probably contain a combination of muon-induced neutrons and muon-induced radioactive isotopes. Therefore, in order to utilize muon-induced

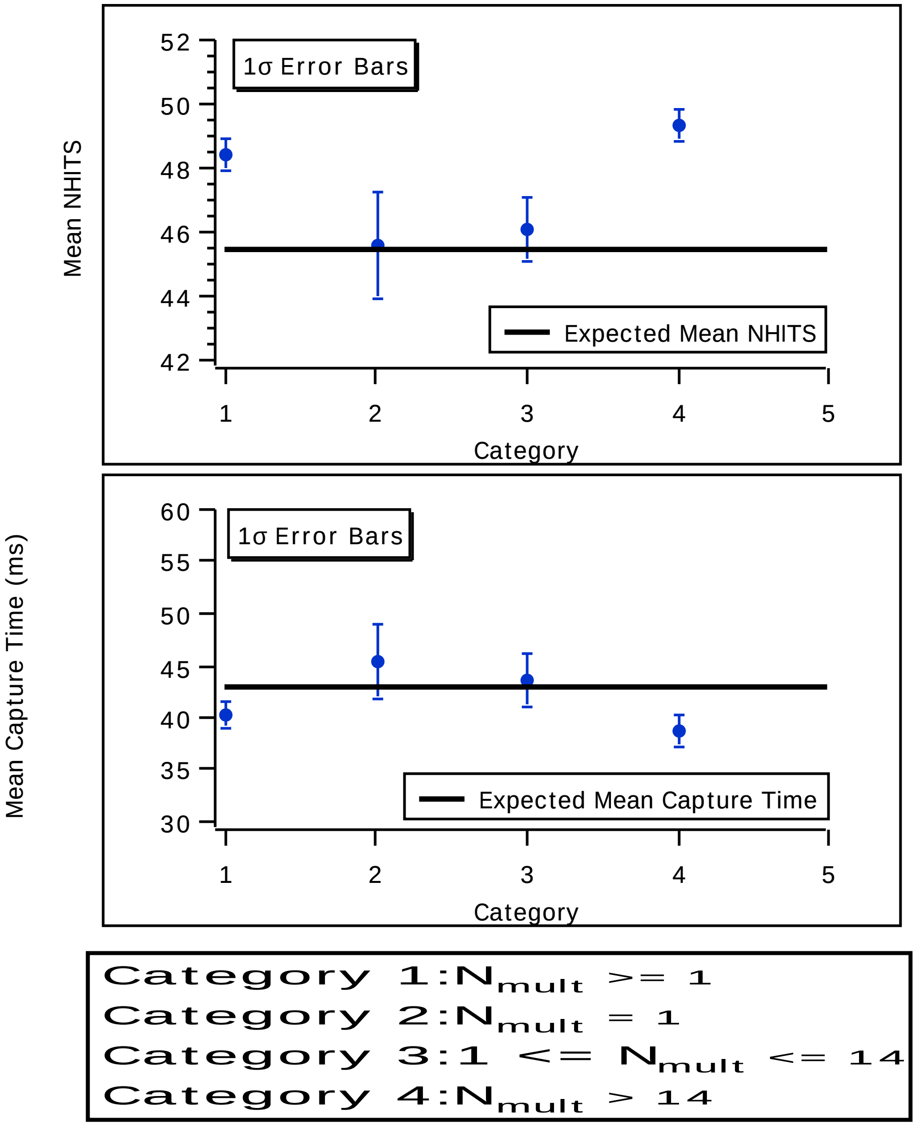

Figure 6.13: Spallation Data vs. Monte Carlo.

	Category	Capture Time (ms)
1	$\mathrm{N}_{mult} \geq 1$	40.3±1.1
2	$\mathrm{N}_{mult} = 1$	45.3±2.9
3	$1 \leq \mathrm{N}_{mult} \leq 14$	43.7±2.1
4	$\mathrm{N}_{mult} > 14$	38.8±1.2
5	Monte Carlo	42.7±0.1

Table 6.13: Spallation Product Capture Time. NHITS = 35, RFIT = 600 cm.

neutrons to perform an independent γ-ray energy calibration of the SNO detector, one will need to select only those spallation products that are not produced by DAG like events. In the present study this corresponds to selecting spallation products with ($1 \leq N_{mult} \leq 14$).

In Table 6.13 and 6.14 the measured τ_{data} value for the 4 different N_{mult} categories in addition to the Monte Carlo results are shown. Table 6.13 was generated for (RFIT$\leq 600\,cm$) and Table 6.14 was generated for (RFIT$\leq 550\,cm$). From both of these tables it can be seen that the capture times derived from the spallation products with ($\mathrm{N}_{mult} = 1$) and ($1 \leq \mathrm{N}_{mult} \leq 14$) are consistent with the mean neutron capture time on deuterium. The spallation products generated by the DAGs, i.e. spallation products with ($\mathrm{N}_{mult} > 14$), have a lower capture time than expected. The results in Table 6.13 are shown graphically in the second plot of Figure 6.13. The bars in the figure represent 1σ error and the straight line represents the Monte Carlo determined expected mean capture time. From the figure, it can be seen that the measured τ_{data} values for the categories ($\mathrm{N}_{mult} = 1$) and ($1 \leq \mathrm{N}_{mult} \leq 14$) include the expected mean capture time value within the 1σ error bar. This again is indication that the sample consisting of spallation prod-

	Category	Capture Time (ms)
1	$N_{mult} \geq 1$	41.9±1.1
2	$N_{mult} = 1$	48.4±3.3
3	$1 \leq N_{mult} \leq 14$	46.9±2.5
4	$N_{mult} > 14$	40.3±1.5
5	Monte Carlo	45.1±0.1

Table 6.14: Spallation Product Capture Time. NHITS = 35, RFIT = 550 cm.

ucts generated by AV-going muons, and excluding the spallation products from DAGs, are most likely neutrons. Since for the ($N_{mult} > 14$) category the τ_{data} is smaller than expected, the capture time for the possible spallation products, other than neutrons, is smaller than the neutron capture time on deuterium.

An investigation to determine the characteristics of the DAG-induced spallation products will not be performed in this study.

Chapter 7

Conclusions

The primary goal of this dissertation has been to describe the detector development work, research and data analysis that I have conducted over the course of almost six years during my tenure as a graduate student on the Sudbury Neutrino Observatory (SNO). In order to provide the foundation and motivation for this research the field of neutrino physics, the people and events that were responsible for the discovery of the neutrino, the solar neutrino problem, and results from past and current solar neutrino experiments were presented in Chapters 1 and 2. With the motivation for this research being established, a description of the SNO detector was provided in Chapter 3.

I joined the SNO project as a member of the SNO Data Acquisition (DAQ) group. The first four years were devoted to the design, development, debugging and deployment of the Electronics and DAQ system. The system was successfully deployed on site at Sudbury in late 1997 and acquisition of production data commenced in November of 1999. Although there have been minor changes to the DAQ system over the course of time, the system has been operating successfully since production data taking began in 1999. The SNO Electronics and Data Acquisition system has been described in Chapter 4.

In addition to making contributions to the development and deployment of an integral system of the SNO detector, I had the opportunity to perform analysis of the first 135 days of SNO production data. The main focus of the data analysis was on through-going muon-induced spallation neutrons that provide a background for the neutrino-induced neutron signal at SNO. Since the measurement of the neutron signal is critical to the success of SNO, it is imperative that one thoroughly understands the various backgrounds to the neutron signal. If due to fitter inefficiencies through-going muons escape detection, then an understanding of the production rate of muon-induced neutrons would allow the necessary correction factor to the calculated neutral current signal. In Chapters 5 and 6 the study of through-going muons and muon-induced spallation products, in particular neutrons, has been described in detail. In the following section, a brief summary of the results from Chapters 5 and 6 will be presented, after which guidance will be given for possible future improvements to the analysis procedure. Given that the tools and inputs for SNO data analysis are being continuously developed, modified and improved upon, it is important to identify areas of this research that will be impacted by the development of new correction factors or by the adjustment of input parameters to data analysis.

7.1 Summary of Analysis

In this study the first 135 days of SNO production data [$\sim$ 86 days live-time] was analyzed with the objective of providing measurements that would characterize muons and muon-induced spallation products at SNO.

For the purpose of this study a software algorithm, called MuonID, was developed to identify muons from the SNO production data set. Through the process of hand-scanning, all muon candidates in the data sample were verified and from that it was estimated that the contamination of the muon sample due to false positives is 0.4%. These were then removed from the final muon sample. Furthermore, it was demonstrated that the MuonID algorithm is better than 99.1% at identifying muons. The muons that were missed by MuonID were mostly non-AV going low NHITS muons. The few AV-going muons that were missed by MuonID came from a few runs in which the OWL tubes were not operating optimally. As a result these muons failed the OWL tube cut which requires that at least 3 OWL tubes fire for an event to be considered as a muon. Unlike the official SNO muon fitter algorithm [FTM], the MuonID algorithm isn't a true fitter and, therefore, cannot provide accurate measurements for the muon track and direction. A combination of the two algorithms would therefore enhance the capabilities for muon identification and muon track reconstruction.

The MuonID algorithm and hand-scanning procedure were utilized in the measurement of the through-going muon rate at SNO. The following daily muon rate was found:

$$\mathrm{R}_{\mu}^{SNO} = 68.9 \pm 1.8(stat)\ \ \mathrm{day}^{-1}$$

The list of verified muons derived from the SNO data set was used to perform the search and collection procedure for muon-induced spallation events. In this process a total of 656 spallation events that occurred within 500 ms of a muon and reconstructed within the $\mathrm{D_2O}$ were collected. A total of 169 AV-going muons [3%] out of 5916 total muons were responsible for generating these spallation products. It was found that muons can produce spallation products with a measured multiplicity of $\mathrm{N}_{mult} \geq 1$. Assuming these spallation products to be muon-induced neutrons, the following was determined to be the muon-induced neutron rate within the AV at SNO:

$$\mathrm{R}^{\mu_n^{sp}}[\mathrm{SNO,\ AV}]_{measured} = (30.40 \pm 1.21)\ \mathrm{day}^{-1}\ \mathrm{kt}^{-1}$$

Ignoring the spallation products generated by the rare distinctive AV-going events [DAGs], i.e. considering events with ($1 \leq \mathrm{N}_{mult} \leq 14$), the following rate was obtained:

$$\mathrm{R}^{\mu_n^{sp}}[1 \leq \mathrm{N}_{mult} \leq 14][SNO, AV]_{measured} = (11.49 \pm 0.74)\ \mathrm{day}^{-1}\ \mathrm{kt}^{-1}$$

In Section 6.3.1 it was found that the predicted muon-induced neutron rate, as determined from the Bezrukov et al. experiment, within the AV at SNO is:

$$\mathrm{R}^{\mu_n^{sp}}[\mathrm{SNO,\ AV}]_{expected} = (10.74 \pm 1.11)\ \mathrm{day}^{-1}\ \mathrm{kt}^{-1}$$

Therefore, the production rate of muon-induced neutrons, as predicted by Bezrukov et al., is consistent with the production rate of neutrons at the depth of SNO, i.e. the rate is independent of the target materials used in these two experiments (CH_2 and D_2O respectively). However, if the followers from the DAGs are included into the muon-induced neutron sample then the measured rate is ~ 3 times larger than that predicted by Bezrukov.

Recently the ^{17}O and ^{18}O abundance values in heavy water have been revised. The most recent official SNO value for the ^{17}O abundance in heavy water is 0.0487% and for ^{17}O the value is 0.32%. The abundance values used in this thesis were the official values reported at that time and were 0.172% and 0.344% respectively. Since the neutron capture efficiency and the detection efficiency due to the NHITS cut is sensitive to the ^{17}O and ^{18}O abundance values in heavy water, these efficiencies have been recalculated to be 0.3089 and 0.9115 respectively[1]. Using these efficiencies we get the following muon-induced neutron rate within the AV at SNO:

$$\mathrm{R}^{\mu_n^{sp}}[\mathrm{SNO,\ AV}]_{measured} = (27.13 \pm 1.06)\ \mathrm{day}^{-1}\ \mathrm{kt}^{-1}$$

Ignoring the spallation products generated by the rare distinctive AV-going events [DAGs], i.e. considering events with ($1 \leq \mathrm{N}_{mult} \leq 14$), the following rate was obtained:

$$\mathrm{R}^{\mu_n^{sp}}[1 \leq \mathrm{N}_{mult} \leq 14][SNO, AV]_{measured} = (10.03 \pm 0.64)\ \mathrm{day}^{-1}\ \mathrm{kt}^{-1}$$

---

[1] Correspondence with John Orrell at the Center for Experimental Nuclear Physics and Astrophysics, University of Washington, Seattle. He is a member of the SNO collaboration.

An investigation of the properties of the muon-induced spallation products revealed that the spallation products that satisfy ($1 \leq \mathrm{N}_{mult} \leq 14$), produce an NHITS spectrum that is consistent with the NHITS spectrum generated by the 6.25-MeV γ-rays from neutron capture on deuterium. Furthermore, the measured capture time of these products is also consistent with the neutron capture time on deuterium. The following presents the measured mean NHITS and mean capture time values:

$$\overline{\mathrm{N}}_{data} = 46.1 \pm 1.4$$

$$\tau_{data} = (43.7 \pm 2.1)\,\mathrm{ms}$$

These are consistent with the following expected mean NHITS and mean capture time values derived from a Monte Carlo of neutron capture on deuterium:

$$\overline{\mathrm{N}}^{6.25\gamma}_{expected} = 45.41 \pm 0.05$$

$$\tau_{expected} = (42.7 \pm 0.1)\,\mathrm{ms}$$

Furthermore, it has been shown that the radial dependence of these spallation products is consistent with neutrons produced isotropically within the heavy water. Therefore, based on the above results it can be seen that the spallation products that satisfy ($1 \leq \mathrm{N}_{mult} \leq 14$) exhibit characteristics that are consistent with that which is expected from muon-induced neutrons. Therefore, these spallation products are most likely neutrons and can be used, among other things, for an independent calibration of the SNO detector's response to γ-rays.

7.2 Future Guidance for Analysis

In the following two sections guidance and suggestions are provided for next steps and possible improvements to the MuonID algorithm and the muon-induced neutron analysis procedure that has been presented in this thesis.

7.2.1 MuonID Algorithm

It has been mentioned that the MuonID algorithm has been developed to identify, with high efficiency, through-going muons in SNO. The algorithm is not a robust muon fitter and as a result cannot be used to determine, with high accuracy, the path length or direction of the muon. However, once muons are identified by MuonID one can feed these muons to a muon fitter, e.g. the SNO muon Fitter [FTM], for path reconstruction. Therefore, it is recommended that one use MuonID as a first pass filter to a muon fitter in order to increase the efficiency and accuracy of the muon path reconstruction procedure.

The MuonID algorithm has been developed by a single individual and therefore it is essential that the algorithm be thoroughly understood and tested by others. It should be noted that the primary goal of the algorithm to identify through-going muons has been achieved since the high efficiency of the algorithm has been determined by a careful hand-scanning procedure. It is also recommended that the efficiency of the algorithm be determined whenever there are any changes to the detector operating parameters.

7.2.2 Muon-induced Neutron Analysis

In this dissertation the muon-induced neutron rate at SNO was compared to a rate that was determined at a shallow depth by a detector utilizing a different target material than SNO. As a next step one needs to perform a theoretical calculation to estimate the muon-induced neutron rate at SNO. Figure 7.1 shows a diagram for the photonuclear process that can take place when an energetic muon, with energy E_μ, interacts with a nucleon. In this Feynman diagram P_μ and P'_μ are the four-momenta of the muon before and after the interaction respectively. In this figure, $q = P_\mu - P'_\mu$ is the four-momentum transferred to the nucleon by the virtual photon and P and X are the four-momenta of the nucleon before interaction (assumed to

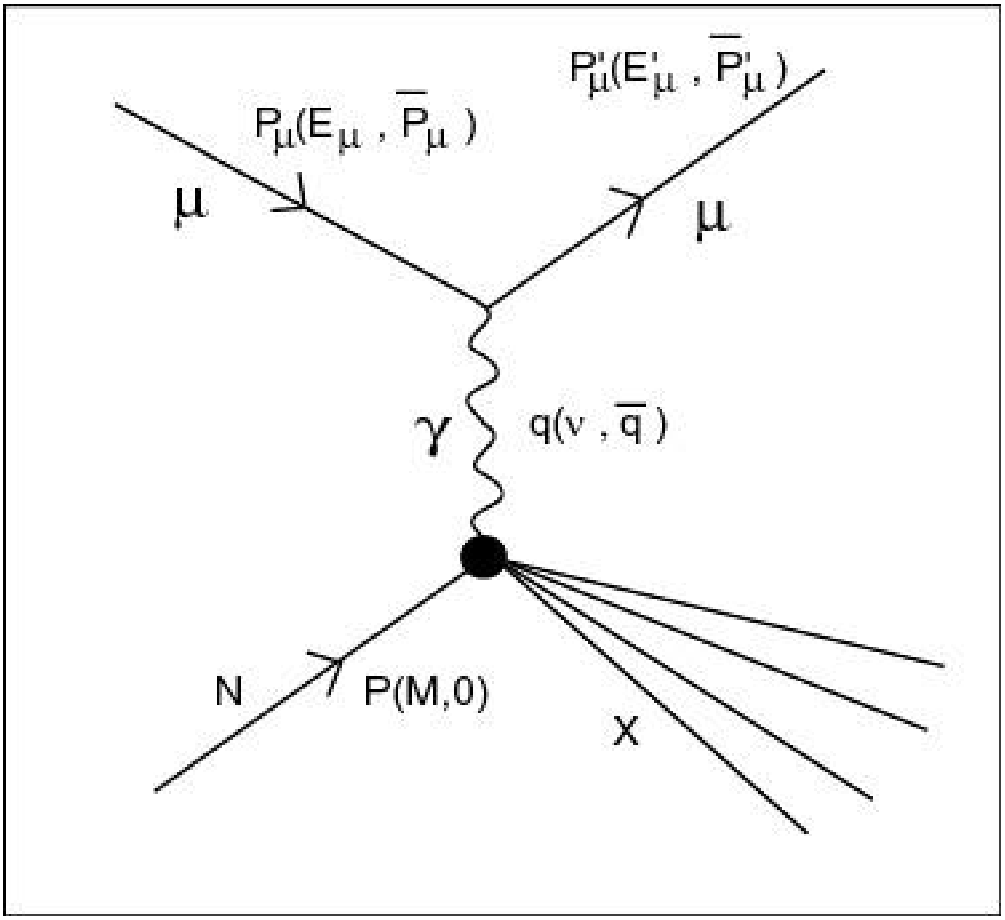

Figure 7.1: Muon-induced Spallation Process.

be at rest) and of the final state hadronic system. The nuclear spallation process can be described by the exchange of a virtual photon between the muon and the nucleon. This process is often referred to as photonuclear interaction of muons.

In Chapter 6 we provided Eq. 6.5 that gives the energy spectrum, $\mathrm{N}_\mu(E, \omega)$, of virtual photons that is generated when an energetic muon of a particular energy passes a nucleus. If the cross-section for real photon absorption on a nucleus leading to a particular daughter nucleus is $\sigma_\gamma(\omega)$, then the cross-section for virtual photon absorption is given by:

$$\sigma_\mu(E) = \int_{S_n}^{E-m_\mu} N_\mu(E, \omega)\sigma_\gamma(\omega)d\omega, \tag{7.1}$$

where, ω is the energy of the virtual photon and S_n is the neutron separation energy. If the photo-neutron cross-section, $\sigma_\gamma(\omega)$, for a given target is known from past experiments then the equation can be solved to provide the cross-section for virtual photon absorption. For example, the photo-neutron cross-section for ^{2}H at 2.80 MeV is 1.45 mb[110] and in this case $S_n = 2.225 MeV$. Now, with a knowledge of the energy spectrum of through-going muons at SNO one could use the above to determine the expected neutron flux from the spallation of ^{2}H and ^{16}O by through-going muons. The systematic error on the determination of an expected muon-induced neutron rate will most probably be dominated by the uncertainties of the muon energy spectrum.

The calculation of the muon-induced neutron rate should take into account all possible systematic errors. There are two primary systematic errors that need to be considered. First of all, it has been reasonably assumed in this study that within 500 ms of a muon trigger most of the spallation products generated are neutrons. It has been argued that approximately 1% of the spallation products come from β-γ events and hence this contribution to the muon-induced neutron rate has been omitted. Secondly we have not taken into account the inefficiencies of the time fitter (FTT) as it pertains to the determination of the neutron capture position. Even though the time fitter is very efficient at position reconstruction given an analysis threshold of $\sim$ MeV, one needs to determine the systematic error that would give rise due to fitter inefficiencies.

The run selection was custom developed by the author. This was done during the early days of SNO production data taking when the tools, algorithms and input parameters for data analysis were being developed and refined and as a result the official SNO tools were not readily available. The runs that were used in the analysis were conservatively selected. It should be noted that these runs are included in the official SNO run list. However, some runs were excluded from the analysis given the conservative selection procedure. It is therefore recommended that runs in the SNO run list be used in any future muon-induced neutron analysis.

The analysis in this thesis was concluded in August 2000. Since then the ^{17}O abundance in D_2O has been adjusted. The neutron capture time and efficiency in D_2O is sensitive to the ^{17}O abundance. Therefore, one needs to take into account the new ^{17}O abundance in the Monte Carlo simulation that generates the neutron capture time and efficiency in D_2O. The ultimate effect of this will be on the muon-induced neutron rate in SNO. However, the SNO muon rate determined in Chapter 5 will not be affected by the new ^{17}O abundance value.

In Chapter 6 the mean of the NHITS distribution, generated by the capture of muon-induced neutrons by deuterium, was calculated. Since not all PMT channels are active for a given run, one needs to correct for the missing PMTs from run to run when determining the effective NHITS for a particular event. With this correction it would be appropriate to compare the NHITS of events from different runs. This correction mechanism was not utilized during the analysis in this thesis. The correction will affect, albeit slightly, the determination of the mean of the NHITS distributions. It is therefore recommended that one takes into account this correction factor during future analysis of muon-induced neutrons.

In this thesis a thorough study of spallation products produced by Distinctive AV-going Events (DAGs) was not conducted. These DAGs are most probably high energy muons accompanied by an energetic electromagnetic shower. Any future analysis should take a closer look at these events and their spallation products.

The muon-induced neutrons in the SNO detector can be utilized to provide an independent calibration of the detector's response to γ-rays. Furthermore, one can use these neutrons to investigate and study the possible drift of the detector energy scale over time. The utilization of muon-induced neutrons for these purposes was not carried out in this thesis but definitely needs to be investigated in the near future since it will provide valuable information in understanding the detector.

Appendix A

Muon Run List

For the purpose of this study a simple selection process was implemented to identify runs that would be used in the analysis of muons and muon-induced spallation products. In this thesis the analyzed data[1], which has a total live-time of approximately 86 days, was gathered over a period of four and a half months since SNO started acquiring production data. During those early days of SNO data acquisition many of the tools, e.g. run selection and live-time calculation tools, for data analysis were being developed and refined. As a result, the SNO run selection tool was not utilized for the purpose of data analysis in this thesis and a conservative approach was taken to select runs for data analysis. It should be noted that all runs selected by this process are included in the official SNO run list, but in this case due to the conservative nature of the selection process some good runs from the official run list were discarded for data analysis. In the future these omitted runs should be utilized during the analysis of muons and muon-induced spallation products.

Only "production" runs were considered for selection, i.e. runs with run numbers greater than or equal to 10,000. The selection process that was used to

---

[1] The data was collected between November 2, 1999 and March 15, 2000. The analysis of the muon-induced spallation data was concluded in August of 2000.

generate the list of SNO production runs included only stable “neutrino type” runs with live-times at least 3 hours long. A minimum conservative value of 3 hours for individual run live-times was chosen so as to ensure detector stability during that run period, since long live-times are in general an indication of stable conditions during the course of a particular run. In addition to the 3 hour time constraint, it was verified that no anomalous activities, e.g. rock bursts in the mine, took place during the run. This was accomplished by reading in detail the Log Files that were associated with each run. The following Table A.1 presents the list of selected runs which were used in this study. It includes, for each run, the associated run number, the live-time and the number of muons identified by the MuonId and Hand-scanning procedure.

Table A.2 and A.3 presents the 21 fully contained[FC] events and the 22 partially contained[PC] events that have been identified from the 27 fully hand-scanned runs.

	Run	Live-time (hrs)	Muons			Run	Live-time (hrs)	Muons
1	10003	7.02800	21		19	10197	7.29233	22
2	10008	14.50928	28		20	10221	5.22433	10
3	10031	815256	26		21	10224	7.46733	15
4	10034	8.47428	22		22	10237	59.03650	186
5	10038	28.22133	87		23	10534	6.09483	17
6	10040	35.26044	98		24	10536	8.74267	23
7	10125	14.66611	37		25	10549	10.30150	35
8	10133	21.91433	60		26	10551	30.60994	81
9	10141	6.68050	14		27	10554	10.27533	42
10	10142	16.17106	51		28	10555	6.65783	22
11	10149	11.72094	39		29	10611	6.59006	18
12	10162	7.87794	28		30	10649	13.62150	37
13	10169	19.23317	66		31	10655	32.34289	79
14	10172	16.52511	50		32	10659	33.96422	96
15	10174	46.34478	135		33	10677	4.19617	15
16	10177	21.46917	59		34	10680	10.12206	23
17	10189	16.11039	55		35	10686	19.14706	43
18	10196	10.49339	35		36	10687	22.98072	72

Table A.1: SNO Muon Run List

	Run	Live-time (hrs)	Muons			Run	Live-time (hrs)	Muons
37	10700	18.95922	59		55	10797	20.27372	58
38	10705	36.00817	87		56	10801	24.69511	80
39	10706	30.47417	86		57	10803	36.00028	101
40	10709	35.75911	86		58	10811	10.54622	32
41	10714	5.11906	13		59	10815	18.92756	59
42	10735	35.90961	114		60	10821	18.01150	42
43	10738	35.91939	99		61	10826	20.80828	44
44	10739	35.82433	98		62	10843	12.66267	39
45	10748	35.99972	108		63	10871	13.99350	31
46	10749	7.96783	25		64	10879	16.01267	52
47	10756	10.69087	33		65	10884	6.25306	17
48	10762	20.78589	63		66	10885	18.09933	46
49	10772	35.99722	110		67	10886	13.74944	45
50	10775	21.04250	64		68	10887	33.96194	95
51	10779	20.80433	66		69	10894	13.22728	48
52	10781	23.98128	71		70	10922	16.22467	51
53	10783	5.20317	7		71	10927	8.21050	16
54	10784	15.28228	48		72	10938	7.57944	25

Table A.1: SNO Muon Run List[cont.]

	Run	Live-time (hrs)	Muons			Run	Live-time (hrs)	Muons
73	10946	17.27106	50		91	11366	25.82511	63
74	10948	35.81967	104		92	11368	21.28728	74
75	10955	5.59083	23		93	11384	29.00478	86
76	10956	16.40300	44		94	11389	15.93722	48
77	10961	29.06183	81		95	11393	24.18861	71
78	10963	13.33022	25		96	11397	6.98206	18
79	10970	9.98639	36		97	11399	95.89028	261
80	10972	10.42839	26		98	11400	20.44944	46
81	10975	35.99722	124		99	11402	14.28278	51
82	10976	30.12767	84		100	11407	20.50261	62
83	11269	18.22239	59		101	11415	18.99722	46
84	11289	15.44250	39		102	11429	27.26339	78
85	11291	19.13467	62		103	11431	42.76328	100
86	11303	16.85939	40					
87	11310	20.23917	53					
88	11312	18.68367	84					
89	11313	13.22439	36					
90	11347	9.73539	37					

Table A.1: SNO Muon Run List[cont.]

No.	Run	GTID	NHITS	No.	Run	GTID	NHITS
1	10174	2374112	438	12	10709	7274707	1845
2	10174	2700633	1465	13	10735	889732	895
3	10174	2937873	836	14	10735	1645272	975
4	10174	4189230	1107	15	10735	2413567	1144
5	10237	738767	4175	16	10922	620872	2027
6	10237	2010195	1531	17	10922	763984	1362
7	10237	3484174	1598	18	11399	2371389	872
8	10551	4855513	1107	19	11399	6141889	1564
9	10659	744215	515	20	11399	6534396	1564
10	10687	2005970	2322	21	10174	3574030	1662
11	10687	2647717	2658				

Table A.2: FC Events from 27 Fully Hand-scanned Runs.

No.	Run	GTID	NHITS	No.	Run	GTID	NHITS
1	10174	2668894	5925	12	10687	3150544	5405
2	10174	2761489	6019	13	10709	6091391	5195
3	10237	1681607	3191	14	10735	1172602	3832
4	10237	1772186	2203	15	10739	5329941	2490
5	10551	5013926	5302	16	10748	725324	5468
6	10659	135661	5070	17	10756	651366	3893
7	10659	764950	2170	18	10887	4273850	3907
8	10659	1016917	7143	19	10887	4867453	2467
9	10659	1626688	4345	20	11399	4143000	2553
10	10659	1783084	2306	21	11399	5186696	6340
11	10687	1709082	1201	22	11399	6372272	5182

Table A.3: PC Events from 27 Fully Hand-scanned Runs.

Appendix B

MuonID and Hand-Scanning Procedure

B.1 MuonID Algorithm

The process of creating a list of candidate muons is initiated after run selection by running the SNOMAN process called *MuonID* on the selected SNO data files. It should be made clear that MuonID is not intended to accurately determine the muon path length (L^{μ}) or the muon direction with respect to the zenith ($cos\theta^{\mu}$). It is a first pass filter which creates a list of possible muons and provides an initial estimate for the path length of that event, which is used to categorize the prospective muons into AV and non-AV going events.

The MuonID algorithm uses a number of predefined cuts to eliminate non-muon events from the final muon candidate sample. An event is regarded as a muon candidate if the event passes all these cuts. A complete list of these cuts is provided below:

- NHITS Cut : $NHITS \geq 350$, where NHITS is the number of PMTs that have triggered for a given event. It has been found that muons with NHITS below a value of 350 are rare. From a hand-scan of 27 runs only two muons out of 1872 muons had $NHITS < 350$. Muons with very low NHITS are ones that barely clip the PSUP. As a result the study of muon induced backgrounds within the AV will not be compromised if such rare, clipping muons are eliminated from the data sample.

- NHIT Trigger Cut : This cut demands that at least one of the NHIT trigger bits is set for the event. The NHIT trigger bits are : NHIT100H, NHIT100M, NHIT100L, NHIT20, NHIT20LB, PRESCALE. This cut eliminates some of the non-physics events, e.g. some flashers are discarded by this cut.

- OWL Tube Cut : Number of OWL Tubes ≥ 4, i.e. the cut demands that at least 4 out of the 91 outward looking tubes have fired for the event. The OWL tubes are triggered by through-going muons when they enter the detector. It has been found that if the OWL tubes are operating optimally then all through-going muons will fire at least 4 OWL tubes. The OWL tube distribution for muons is given in Figure 5.4. The mean of the distribution is 23.2. Only fully contained muons will not fire any OWL tubes since they are created within the volume of the PSUP.

- Neck Tube Cut : Number of Neck Tubes ≤ 2. There are a total of 4 PMTs, called NECK Tubes, that are located in the neck area of the detector. These were inserted in order to eliminate non-physics events, called NECK events, that are generated occasionally in the neck region. Without this cut the muon sample can be contaminated by NECK events.

- Flasher Cut : A custom flasher cut algorithm is used to eliminate large flashers that otherwise would contaminate the muon sample.

- Integrated Charge Cut : $NPH/NHITS \geq 61.0$, where NPH is the total integrated charge for the event. For a given event, the integrated charge or NPH is calculated by summing together the pedestal corrected QLX values for all PMTs that were properly calibrated. Since muons in general deposit a large amount of charge in the detector this cut can eliminate many types of non-muon events that do not deposit enough charge. Flashers, Neck events, bubblers, breakdown events, and other electronics pick-up events can be eliminated by this cut. The $NPH/NHITS$ distribution for all verified muons can be found in Figure 5.4.

- TRMS Cut : TRMS $\leq$ 36.0 ns. This cut uses the width of the calibrated PMT timing distribution to eliminate non-physics events, e.g. some flashers, bubblers, and breakdown events are discarded by this cut, since for these events the timing distribution is in general much broader than the timing distribution for muon events.

- Path Length(L^{μ}) Cut : $L^{\mu} > 0.0$, i.e. this cut demands that the entrance and exit points of the prospective through-going muon event have been properly determined. If that isn't the case then $L^{\mu} = 0.0$. It has been found that many non-physics events, in particular bubblers, are eliminated by this method from the final muon sample.

- Bad PMT Calibration Cut : If more than 20% of the PMTs for a given event fail to be calibrated then that event is discarded. It has been found that this cut eliminates some non-physics events, e.g. some breakdown events are discarded by this cut.

Once the algorithm has identified a particular event as a potential muon event it uses a simple method to determine the entrance and exit positions of the event. Since MuonID is primarily looking for through-going muons it assumes that all potential muon events have an entrance and exit point.

- Entrance and Exit Points : The best guess for the muon entrance position is determined by the PSUP location of the PMT that has fired the earliest. To avoid selecting a PMT that is uncorrelated with the event it is demanded that the two earliest tubes are in close proximity in physical space. Then the earliest of these two tubes is taken to be the best guess for the entrance position of the event. The center of mass of the location of the 10 tubes that have registered the highest charge is taken to be the exit position.

Once the algorithm selects an event as a candidate muon event it is then categorized as an AV or non-AV going muon based on the path length of that event. The following describes how this is done:

- Muon Categorization : The path length is the distance between the entrance and exit positions. It is safe to assume that the muon will travel in a straight line trajectory between the entrance and exit positions. Assuming a perfectly spherical PSUP and AV with radii 841 cm and 600 cm respectively, a muon that grazes the AV or is tangential to it will have a path length equivalent to approximately 1179 cm.

$$AV\ Grazing\ Muon\ Path\ Length \equiv L^{\mu}_{AV} = 1179\, cm \tag{B.1}$$

$$If\ L^{\mu} > L^{\mu}_{AV}\ , then\ Muon = AV\ Muon \tag{B.2}$$

$$If\ L^{\mu} \leq L^{\mu}_{AV}\ , then\ Muon = non\ AV\ Muon \tag{B.3}$$

Therefore, any muon with a path length greater than 1179 cm will have gone through the AV. The primary interest is in AV going muons that produce spallation events within the AV, therefore, it is important to determine whether the muon penetrated the AV or not. The MuonID algorithm does a modest job at categorizing muons as AV and non-AV going. However, the hand-scanning procedure is responsible for creating the final sample of AV and non-AV muon categories.

B.2 Hand-Scanning Procedure

The final step in the muon selection procedure involves the human verification of all muon candidates as selected by the MuonID algorithm. The verification is done by viewing the candidate events with XSNOED, a SNO event display software package. The people that were involved in carrying out the hand-scanning procedure are listed below:

- Ryuta Hazama
- Miles Smith
- Tom Steiger
- Rushdy Ahmad : Head Scanner

The main goal of the hand-scanning procedure is to determine the efficiency of the MuonID selection process. With a knowledge of the efficiency MuonID can be used in the future without resorting to an extensive and involved hand-scanning procedure. Given a specific guideline, every single muon in the candidate sample was verified and the occasional, albeit rare, false muons were discarded from the final sample. The MuonID categorization of muons into AV-going and non-AV going events is also verified by this procedure. The various steps involved in the hand-scanning process are described below:

1) Generate RDS Files: The generation of the Reduced Data Set files is done by the MuonID algorithm. RDS files were created for each individual run. A total of 103 RDS files were generated.

2) Train Human Scanners: Representative RDS files were selected for training the people responsible for performing the hand-scanning procedure. It is important for all scanners to be consistent with one another in identifying muons, rejecting false muons and categorizing muons into AV and non-AV categories. Training on the same representative data set was an attempt to ensure the quality of the verification process. The head scanner, someone with the most experience in

hand-scanning, was responsible for resolving conflicts between the hand-scanning and MuonID results.

3) Perform hand-scanning: Once the training was successfully completed each scanner was assigned a set of RDS files for production hand-scanning. The five figures B.1 → B.5 will be used to illustrate the techniques employed to identify and categorize the muons.

a) Muon Identification: Muons, in general, are the most energetic physics events that occur in SNO at a rate of about 3 per hour. These events on the average trigger more than 5000 PMTs and their Cerenkov patterns as viewed with XSNOED can be easily distinguished from other non-physics events that can sometimes confuse the MuonID algorithm. For example, events like flashers, bubblers, NECK events and breakdown events have a very different event topology than muons when viewing the PMT timing map of these events with XSNOED.

b) Muon Categorization: In Figure B.1 the two types of event display windows that are used to identify and categorize a muon are shown. By definition through-going muons enter and exit the PSUP. Therefore, in order to categorize a muon one first needs to determine the entrance and exit points of the muon. In Plot A representative tracks of AV and non-AV going muons are shown. The muons that clip the PSUP are called “clippers” and these can be easily distinguished with XSNOED. These are the obvious non-AV going muons. The MuonID and hand-scanning are very good at identifying these types of non-AV going muons.

Plot B of Figure B.1 is a flat map window which is used to visually locate the entrance and exit points of the muon. On the flat map the boundaries of the 9 AV panels are clearly marked. It has been found that, in general, AV going muons have a difference of 4 AV panels between the entrance and exit points. In the case of muons that are borderline between AV and non-AV one uses the Full Event Display to visually reconstruct the muon track and by rotating the sphere in the display one is able to determine the category of the muon. For muons that are

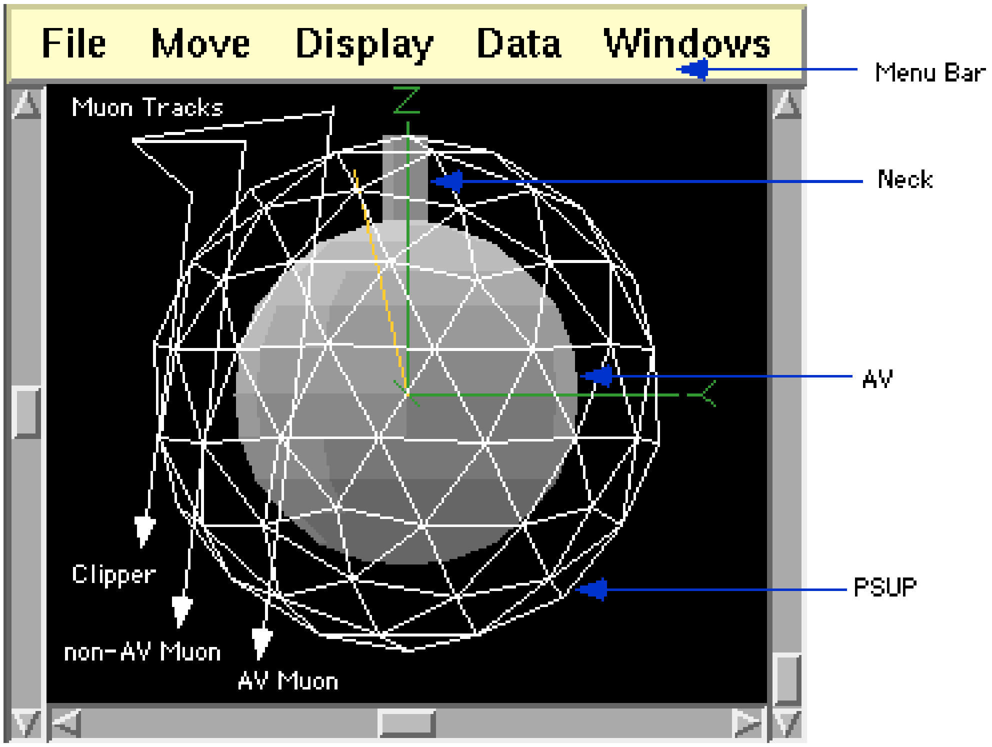

A) Full Event Display

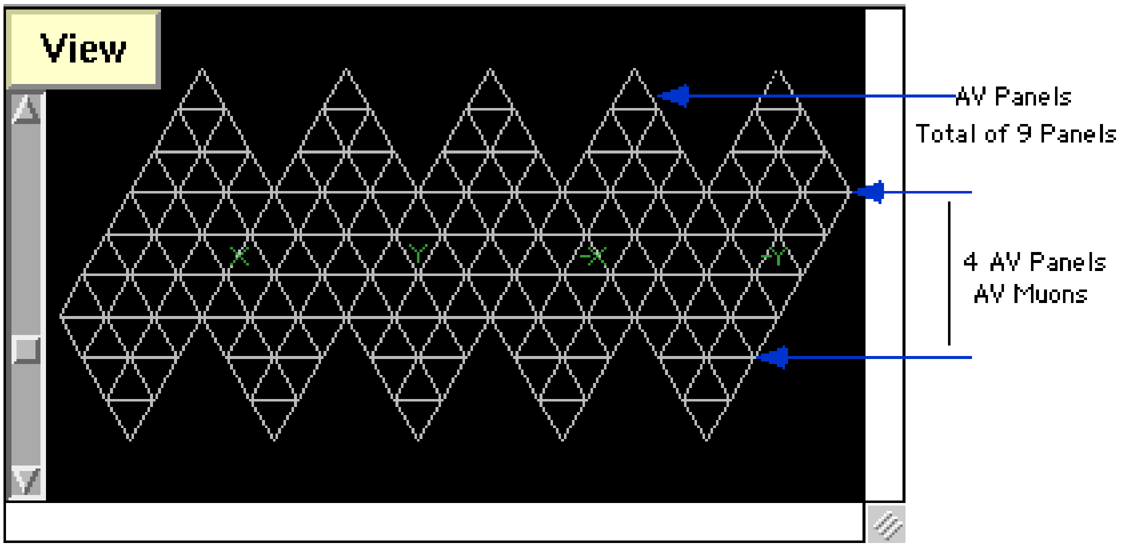

B) Flat Map Display

Figure B.1: XSNOED Event Display

still visually borderline between the two categories, the MuonID categorization is accepted since MuonID, in general, does a better job than hand-scanning at locating the entrance and exit points.

Figures B.2 and B.3 are representative TAC [timing] and QLX [charge] histograms of typical AV and non-AV muons respectively. Both the TAC and QLX spectra have been generated after calibrating the data. On the TAC spectrum the early time is on the left hand of the spectrum. On the QLX spectrum the higher charge is on the right hand side of the spectrum. It can be seen from these plots that the AV going muons in general deposit more charge in the detector than non-AV going muons. This is expected since AV muons have a longer track length and therefore deposit more charge. Another distinguishing feature of AV muons is the distinct 2nd minor peak in the TAC spectrum. This is due to the reflected light from the AV. The non-AV muons don't have a distinct 2nd peak. One also uses this feature of the TAC spectrum to categorize the muons.

Figures B.4 and B.5 can be used to illustrate the technique of determining the entrance and exit points. Figure B.4 is a flat map display of a typical AV muon. Plot A is the PMT charge distribution of the event. Plot B is the PMT timing distribution of the event. The entrance point is located by the PMTs that have triggered the earliest and this has been marked in Plot B. The exit point is located by the PMTs that have registered the highest charge. The exit point is otherwise known as the exit wound of the muon and this can be seen in Plot A. The difference between these two points is shown in Plot A and it is greater than 4 AV panels. Therefore, this particular muon has been categorized as an AV-going muon. Figure B.5 is a flat map display of a typical non-AV going muon. In this particular case the muon is a clipper. In Plot C) and D) the entrance and exit points of the muon can be seen. The difference between the two points is definitely less than 4 AV panels. Therefore, this muon was categorized as a non-AV going muon.

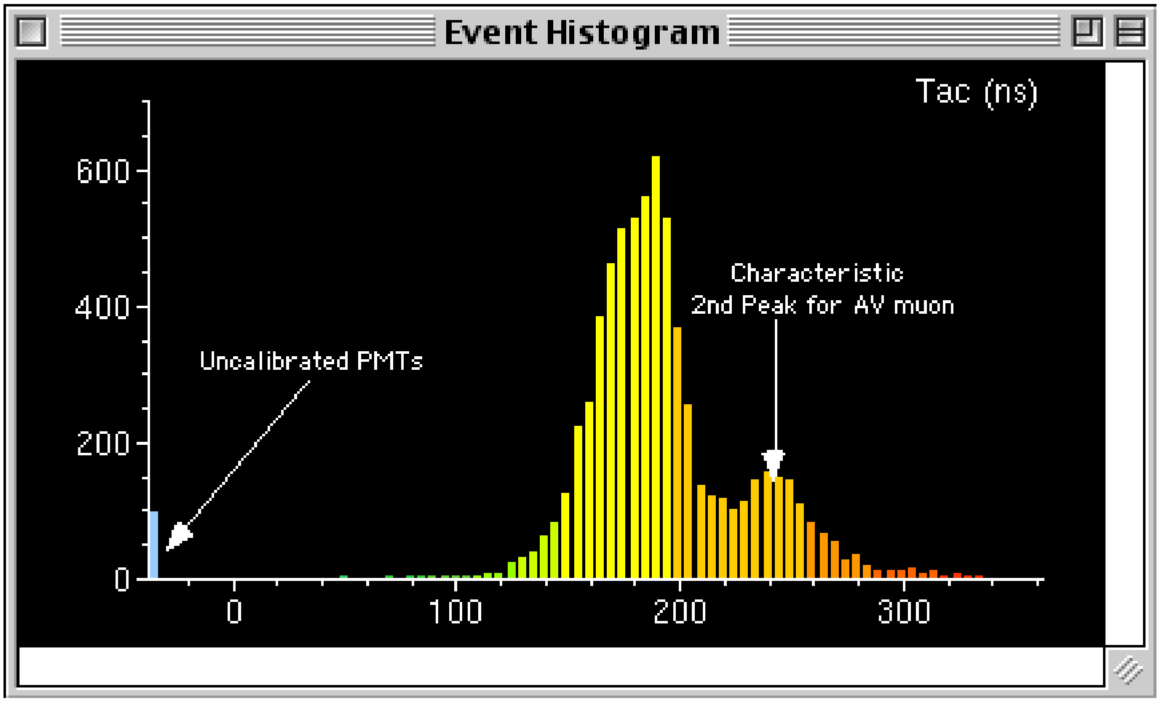

C) PMT Timing Distribution for a typical AV Muon

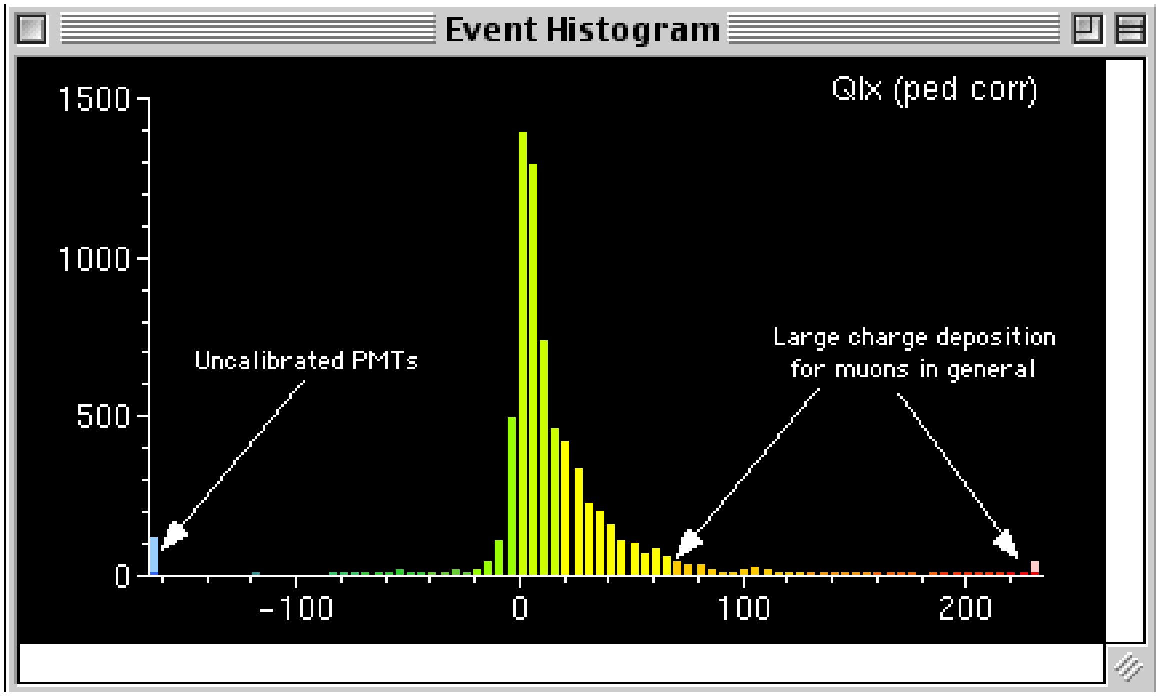

D) PMT Charge Distribution for a typical AV Muon

Figure B.2: PMT Timing and Charge Distributions of AV-going Muons.

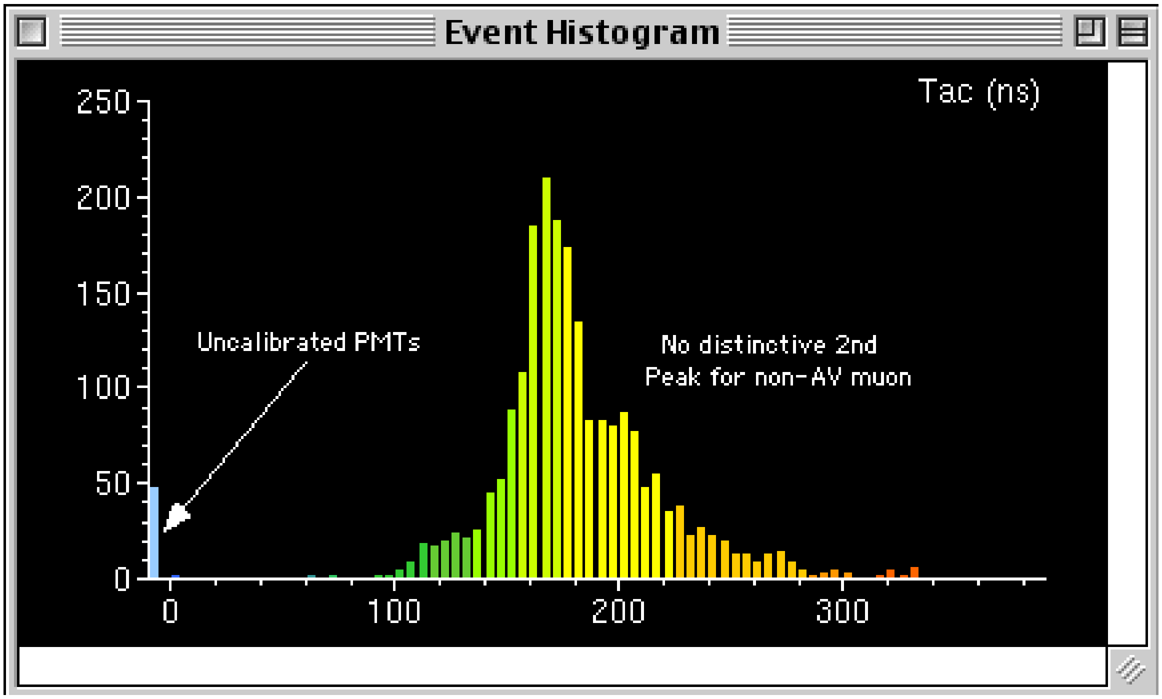

E) PMT Timing Distribution for a typical non-AV Muon

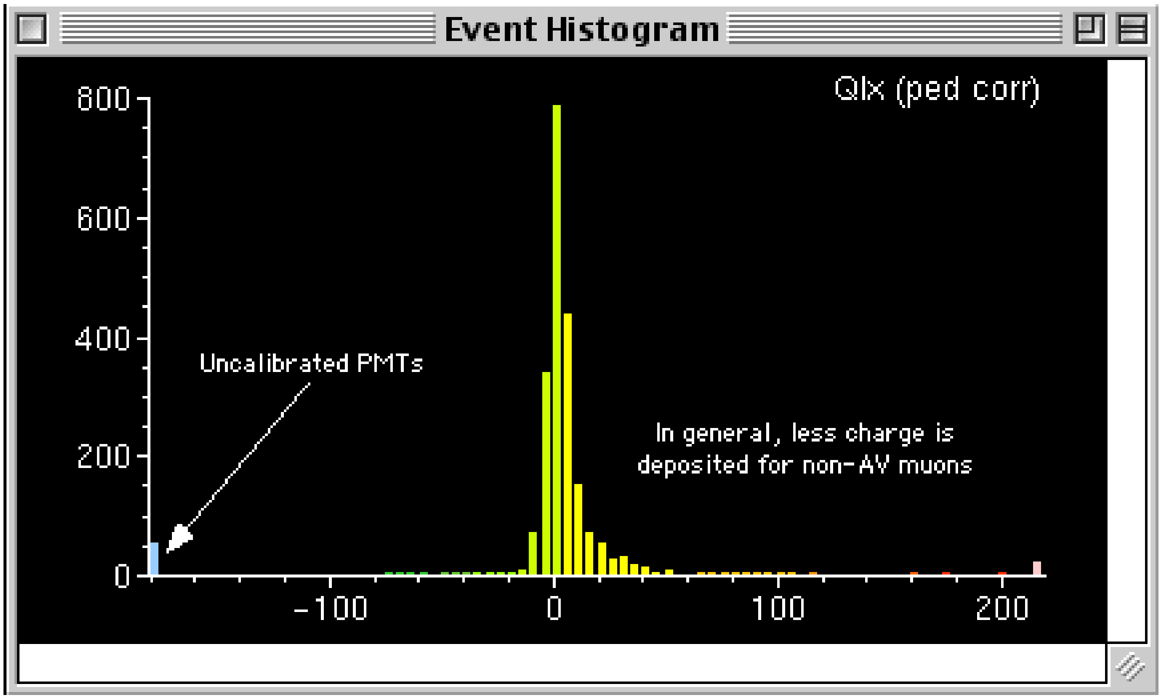

F) PMT Charge Distribution for a typical non-AV Muon

Figure B.3: PMT Timing and Charge Distributions of non-AV going Muons.

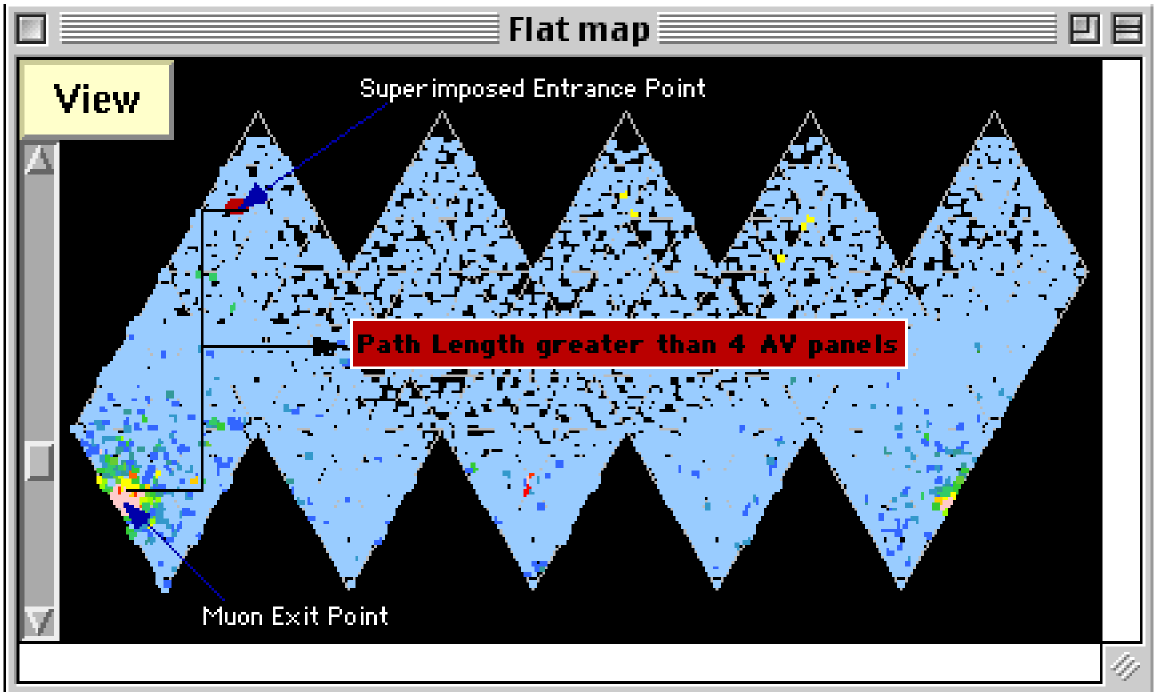

A) PMT Charge Map for a typical AV Muon

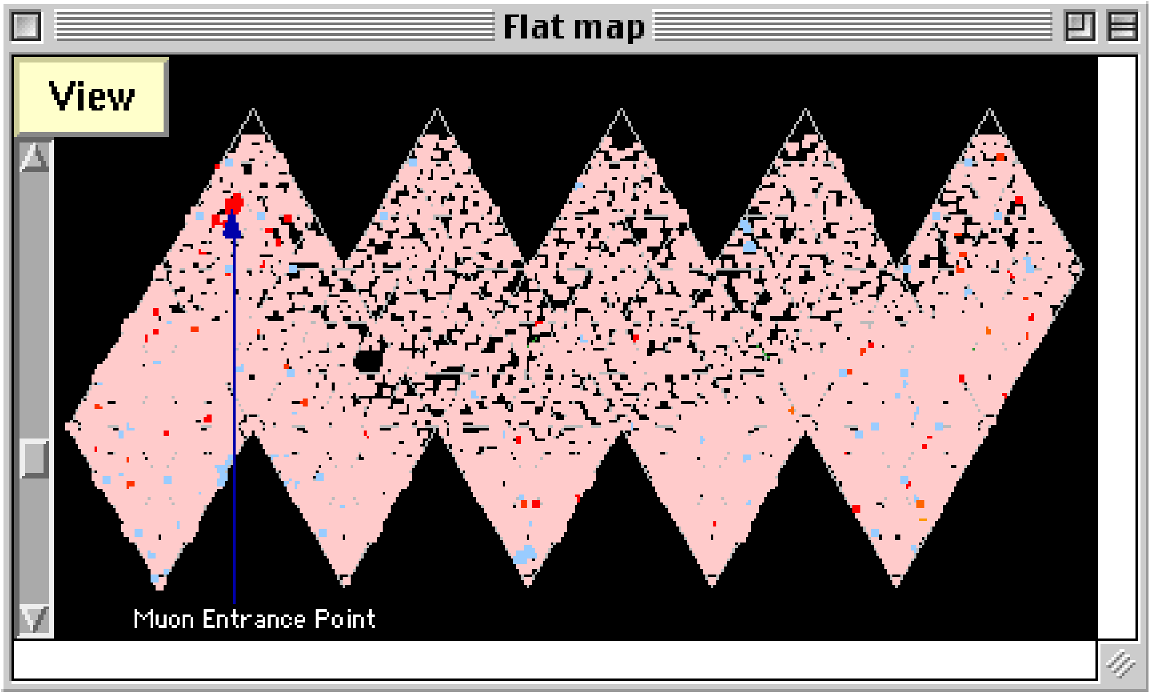

B) PMT Timing Map for a typical AV Muon

Figure B.4: AV-going Muon Categorization.

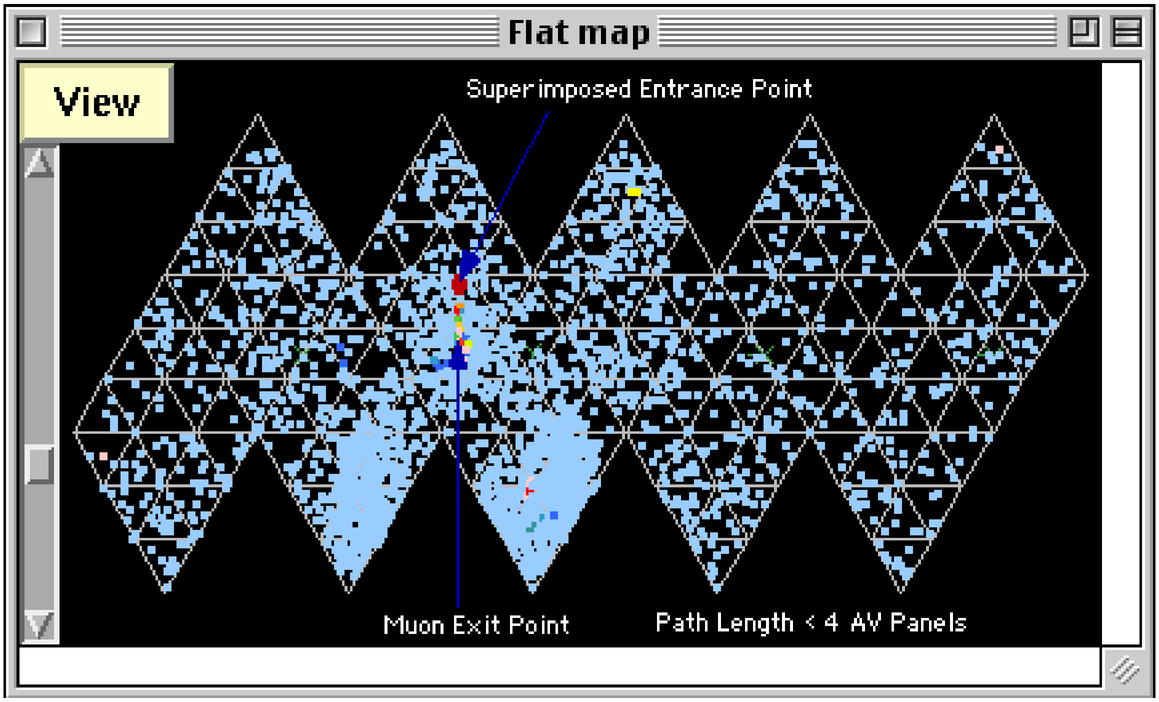

C) PMT Charge Map for a typical non-AV Muon

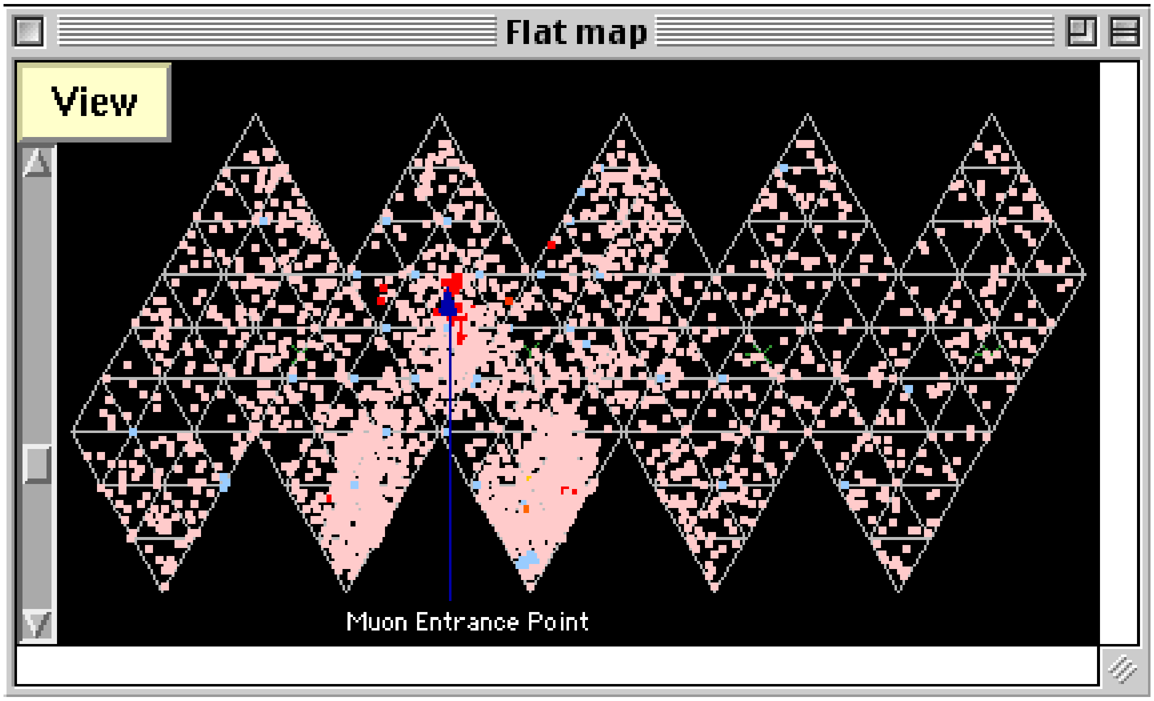

D) PMT Timing Map for a typical non-AV Muon

Figure B.5: Non-AV going Muon Categorization.

In addition to the above mentioned distinguishing features of AV and non-AV going muons one also needs to keep in mind the NHITS of the muons. In general, AV going muons have an NHITS greater than 5000.

4) Final Verification: After hand-scanning RDS files the discrepancies between the hand-scanning and MuonID results are resolved by the head scanner.

Appendix C

DAMN Cuts

The muon follower data selection was performed by applying the official SNO data cleaning cuts, known as DAMN cuts, to the 103 production runs that were used in this study. These cuts have been carefully constructed by the SNO collaboration to eliminate of non-physics events from the data sample. After a particular run has been written to tape the DAMN cuts are applied to every event in the run in an off-line analysis procedure. At the end of this process each event gets assigned a DAMN mask, which is a 25 bit number. Each bit in this mask corresponds to a particular DAMN cut. If an event fails a particular DAMN cut then its corresponding bit in the DAMN mask is set to 1, otherwise it is set to zero. The DAMN masks for all events are stored in the SNO database so that they can be accessed by members of the collaboration. The DAMN cuts and the corresponding bit numbers are given in Table 5.18. For physics analysis bits 1, 3, 4, 12 and 15 are not used.

For this study events were discareded from the muon follower sample when one or more of the following bits were set : Retrigger, QvT, Q/NHITS, Crate Isotropy, AMB, FTS, OWL, Junk, Neck, ESUM, QCluster, ITC, FGC and OWL Trigger. The BURST and NHIT Burst cuts are not used since these cuts could remove muon-induced spallation events. The combination of cuts used in this

Bit Number	DAMN Cut Name		Bit Number	DAMN Cut Name
0	Retrigger		12	ROF
1	First Event		13	NECK
2	Burst		14	ESUM
3	Charge		15	HIB
4	Cluster		16	QCluster
5	QvT		17	Muon
6	Q/NHITS		18	Muon Follower Short
7	Crate Isotropy		19	Muon Follower Long
8	AMB		20	ITC
9	FTS		21	FGC
10	OWL		22	NHIT Burst
11	Junk		23	OWL Trigger

Table C.1: SNO DAMN Cuts and Associated Bit Number study corresponds to a DAMN mask of 11628513 (decimal).

As examples provided below, from the *SNOMAN User's Manual*, are brief descriptions of some of the DAMN cuts that are applied during muon follower data selection:

- QvT : The QvT cut is used to mainly cut out flashers, in particular those with low charges in the flashing tubes. This tags events where: (The highest charge tube in QHL is more than 1000 pedestal subtracted counts above the events average QHL charge OR the highest charge tube in QLL is more than 80 pedestal subtracted counts above the events average QLL charge) AND (The high charge tube is between 60 and 250 ns before the median tube time in the events).

- Crate Isotropy : This cut eliminates events that exhibit distinct anisotropy in crate, card and channel space. This tags events where more than 70% of the hits occur on one crate and more that 80% of those hits occur on two adjacent cards.

- FTS : The Fitterless Time Spread Cut is based on the time spread of hit PMTs within an event. Events due to Cerenkov light have a relatively narrow time distribution compared to non-physics events, e.g. flashers. The absolute time differences of all pairs of hit tubes in close proximity to each other in the detector are calculated and the median time difference in the event is used as a cut statistic.

- OWL : This cut will remove events where there is a large amount of activity in the outer tubes which included the OWL and the BUTT tubes. Events where the number of OWLs + BUTTs is 3 or more will be eliminated by this cut.

- NECK : This cut is designed to eliminate a special type of instrumental background event known as a NECK event. This cut looks for firing of the neck tubes in an event and then uses an algorithm to determine whether it is a true NECK event.

- ESUM : This cut removes any event that has the ESUMLO and ESUMHI trigger bits set and none of the following trigger bits set: NHIT100LO, NHIT100MED, NHIT100HI, NHIT20, NHIT20LB, OWLN, OWLELO, OWLEHI, PULSE_GT, PRESCALE, MISS.

- FGC : The Flasher Geometry Cut identifies a flasher by first searching a cluster of hits in the event and then calculating the average distance between other hits and the cluster. If the average distance is larger than a pre-defined value then the event is identified as a flasher.

The DAMN cuts have been designed so that the sacrifice of physics events from the data sample due to these cuts is minimal. In this study, in addition to using the DAMN cuts, custom data cleaning cuts were used to produce a muon follower sample. It was found that both these methods generated similar muon follower samples. Furthermore, all muon followers above an NHITS cut of 30 and within 500 ms of a muon have been carfully hand-scanned and from that it was determined that the data cleaning cuts did not sacrifice any physics events, in particular all possible muon-induced neutron events were added to the data sample for analysis.

Appendix D

List of Acronyms

AV	Acrylic Vessel
CC	Charged-Current
DAG	Distinctive AV-going Event
DAMN	Official SNO Data Cleaning Cuts
ES	Neutrino-electron Elastic Scattering
ESUM	Energy Sum(total integrated charge in an event
FC	Fully Contained
FTT	Time Fitter
GTID	Global Trigger Identification
INCO	The International Nickel Company
NC	Neutral-Current
NCD	Neutral Current Detector (^{3}He-filled proportional counter)
NHITS	Number of PMTs with anode signal above threshold
NPH	Total integrated charge per PMT in an event
OWL	Outward-looking PMTs

PC	Partially Contained
PGT	Pulsed Global Trigger
PMT	Photomultiplier Tube
PSUP	PMT support structure
RDS	Reduced Data Set
SNO	The Sudbury Neutrino Observatory
SNOMAN	SNO Monte Carlo and Analysis Code
SNU	Solar Neutrino Unit (10^{-36} interactions per target per second)
SSM	Standard Solar Model
TAC	Time-to-Analog Converter
TG	Through-going
TRMS	Width of the PMT timing distribution for an event

Bibliography

[1] John N.Bahcall. *Neutrino Astrophysics*. Cambridge University Press, 1989.

[2] J.N.Bahcall, E.Lisi, D.E.Alburger, L.D.Braeckeleer, S.Freedman, and J.Napolitano. *Phys.Rev.C*, 54:411, 1996.

[3] John N.Bahcall, S.Basu, and M.H.Pinsonneault. *Phys.Lett.B*, 433:1, 1998.

[4] John N.Bahcall, P.I.Krastev, and A.Yu.Smirnov. Where do we stand with solar neutrino oscillations? *Phys.Rev.D*, 58:096016, 1998.

[5] M.B.Smy. Solar Neutrinos with Super-Kamiokande. *hep-ex/9903034*, 1999.

[6] J.Boger et al. The Sudbury Neutrino Observatory. *Nucl.Instrum.Meth.*, A449:172, 2000.

[7] K.S.Hirata et al. *Rev.Mod.Phys.*, 44:8, 1991.

[8] J. Dunmore and H. Robertson. Background Neutron Sources to the Neutral-Current Signal in Sno. *SNO-STR-98-025*, 1998.

[9] C.Caso et al. Review of particle physics. *The European Physics Journal C*, 3, 2000.

[10] S.S.M.Wong. *Introductory Nuclear Physics*, page 3. John Wiley and Sons, 1998.

[11] T.D.Lee and C.N.Yang. *Phys.Rev.*, 104:254, 1956.

[12] C.S.Wu et al. *Phys.Rev.*, 105:1413, 1957.

[13] T.D.Lee and C.N.Yang. *Phys.Rev.*, 105:1671, 1957.

[14] E.Majorana. *Nuo.Cim.*, 5:171, 1937.

[15] Christine Sutton. *Spaceship Neutrino.*, page 13. Cambridge University Press, 1992.

[16] Christine Sutton. *Spaceship Neutrino.*, page 21. Cambridge University Press, 1992.

[17] E.Fermi. *Z.Phys.*, 88:161, 1934.

[18] C. E. Lane and R. I. Steinberg. *Franklin Symposium Proceedings, Discovery of the Neutrino.*, page 154. World Scientific Publishing Co. Pte. Ltd., 1993.

[19] Necia Grant Cooper. *Celebrating the Neutrino.*, page 4. Los Alamos Science, 1997.

[20] Christine Sutton. *Spaceship Neutrino.*, page 79. Cambridge University Press, 1992.

[21] C. E. Lane and R. I. Steinberg. *Franklin Symposium Proceedings, Discovery of the Neutrino.*, page 158. World Scientific Publishing Co. Pte. Ltd., 1993.

[22] C. E. Lane and R. I. Steinberg. *Franklin Symposium Proceedings, Discovery of the Neutrino.*, page 166. World Scientific Publishing Co. Pte. Ltd., 1993.

[23] H.A.Bethe and C.L.Critchfield. *Phys.Rev.*, 54:248, 1938.

[24] C.F Von Weizsacker. *Physik.Zeits*, 38:176, 1937.

[25] S. Turck-Chièze and I.Lopes. *Astrophys.J.*, 426:347, 1993.

[26] Castellani, V.S.Degl'Innocenti, G.Fiorentini, L.M.Lissia, and B.Ricci. *Phys.Lett.B*, 324:425, 1994.

[27] A. Követz and G. Shaviv. *Astrophys.J.*, 426:787, 1994.

[28] J Christensen-Dalsgaard. *Europhysics News*, 25:71, 1994.

[29] X. Shi, D.N.Schramm, and D.S.P.Dearborn. *Phys.Rev.D*, 50:2414, 1994.

[30] H.A.Bethe. *Phys.Rev.*, 55:434, 1939.

[31] E.G.Adelberger et al. *Rev.Mod.Phys.*, 123:45, 1998.

[32] B.Filipone, A.Elwyn, and D.Koetke. *Phys.Rev.C*, 28:2222, 1983.

[33] S. Fukuda et al. Solar ^{8}/B/ and hep Neutrino Measurements from 1258 Days of Super-Kamiokande Data. *hep-ex/0103032*, 2000.

[34] Christine Sutton. *Spaceship Neutrino.*, page 151. Cambridge University Press, 1992.

[35] R.Davis. *Phys.Rev.Lett*, 12:303, 1964.

[36] R.Davis. *Prog.Part.Nucl.Phys.*, 32:13, 1994.

[37] B.T.Cleveland et al. *Nucl.Phys.(Proc.Suppl.)*, 38:47, 1995.

[38] B.T.Cleveland et al. *Astrophys.J.*, 496:505, 1998.

[39] Y.Fukuda et al. *Phys.Rev.Lett.*, 77:1683, 1996.

[40] Y.Fukuda et al. *Phys.Lett.B*, 433:9, 1998.

[41] M.Nakahata et al. *Nucl.Instr.Meth.Phys.Res.A*, 421:113, 1999.

[42] Y.Fukuda et al. *Phys.Rev.Lett.*, 82(12):2430, 1998.

[43] Y.Fukuda et al. *Phys.Rev.Lett.*, 81(6):1158, 1998.

[44] Christine Sutton. *Spaceship Neutrino.*, page 168. Cambridge University Press, 1992.

[45] P.Anselmann et al. *Phys.Lett.B*, 285:376, 1992.

[46] W.Hampel et al. *Phys.Lett.B*, 447:127, 1999.

[47] J.N.Abdurashitov et al. *Phys.Lett.B*, 328:234, 1994.

[48] J.N.Abdurashitov et al. *Phys.Rev.C*, 60:055801, 1999.

[49] T. A. Kirsten. Gallex solar neutrino results and status of Gno. *Nuclear Physics B*, 77:26, 1999.

[50] D.Vignaud et al. *Phys.Lett.B*, 388:384, 1996.

[51] J.N.Abdurashitov et al. *Phys.Rev.Lett.*, 77:4708, 1996.

[52] J.N.Abdurashitov et al. *Phys.Rev.C*, 59:2246, 1999.

[53] W.C.Haxton and B.R.Holstein. Neutrino Physics. *hep-ph/9905257*, 1999.

[54] John N.Bahcall and R.N.Ulrich. *Rev.Mod.Phys.*, 60:297, 1988.

[55] A.Cumming and W.C.Haxton. *Phys.Rev.Lett.*, 77:4296, 1996.

[56] N.Hata and P.Langacker. *Phys.Rev.D*, 49:420, 1995.

[57] K.H.Heeger and R.G.H.Robertson. *Phys.Rev.Lett.*, 77:3270, 1996.

[58] John N.Bahcall and H.A.Bethe. *Phys.Rev.Lett.*, 65:2233, 1990.

[59] W.Kwong and S.P.Rosen. *Phys.Rev.Lett.*, 73:369, 1994.

[60] A.Acker and S.Pakvasa. Solar Neutrino Decay. *Phys.Lett.B*, page 320, 1994.

[61] M.Fukugita and A.Suzuki. *Physics and Astrophysics of Neutrinos*. Springer-Verlag, 1994.

[62] L.D.Landau. *Nucl.Phys.*, 3:127, 1957.

[63] A.Salam. *Nuovo Cimento*, 5:299, 1957.

[64] B.Pontecorvo. *J.Exptl.Theoret.Phys.*, 33:549, 1957.

[65] G. Danby et al. Observation of high energy neutrino reactions and the existence of two kinds of neutrinos. *Phys.Rev.Lett.*, 9:36, 1962.

[66] B.Pontecorvo. *J.Exptl.Theoret.Phys.*, 53:36, 1967.

[67] M. Gell-Mann, P.Ramond, and R.Slansky. *Supergravity*, page 315. North Holland, Amsterdam, 1979.

[68] T.Yanagida. In O.Sawada and A.Sugamoto, editors, *Proceedings of the Workshop on Unified Theory and Baryon Number in the Universe*, KEK, Tsukuba, Japan, 1979.

[69] R.N.Mohapatra and G.Senjanovic. *Phys.Rev.Lett.*, 44:912, 1980.

[70] B.Kayser. On the Quantum Mechanics of Neutrino Oscillation. *Phys.Rev.D*, 24(1):110, 1981.

[71] C.L.Fogli. *Phys.Rev.D*, 56:4365, 1997.

[72] J.N.Bahcall and S.C.Frautschi. *Phys.Lett.B*, 29:263, 1969.

[73] S.L.Glashow and L.M.Krauss. *Phys.Lett.B*, 190:199, 1988.

[74] L.Wolfenstein. Neutrino Oscillations in Matter. *Phys.Rev.D*, 27:2369, 1978.

[75] S.P.Mikheyev and A.Yu.Smirnov. *Sov.J.Nucl.Phys.*, 42:913, 1986.

[76] S.P.Mikheyev and A.Yu.Smirnov. *Sov.J.Nucl.Phys.*, 64:4, 1986.

[77] S.J.Parke. *Phys.Lett.*, 57:1275, 1986.

[78] Y.Fukuda et al. *Phys.Rev.Lett.*, 81:1562, 1998.

[79] Y.Fukuda et al. *Phys.Rev.Lett.*, 82:2644, 1999.

[80] K.Daum et al. *Z.Phys.C*, 66:117, 1995.

[81] M.Aglietta et al. *Europhys.Lett.*, 8:611, 1989.

[82] R.Becker-Szendy et al. *Phys.Rev.D*, 46:3720, 1992.

[83] W.W.M.Allison et al. *Phys.Lett.B*, 391:491, 1997.

[84] C.Athanassopoulos et al. *Phys.Rev.C*, 54:2685, 1996.

[85] C.Athanassopoulos et al. *Phys.Rev.Lett.*, 77:3082, 1996.

[86] C.Athanassopoulos et al. *Phys.Rev.Lett.*, 81:1774, 1998.

[87] Yu. S. Kopysov and V. A. Kuz'min. *Yad. Fiz.*, 4:1031, 1966.

[88] G. T. Ewan et al. Sudbury Neutrino Observatory Proposal. *SNO-STR-87-12*, 1987.

[89] P. J. Doe et al. Construction of an Array of Neutral-Current Detectors for the Sudbury Neutrino Observatory. *SNO-STR-95-023*, 1995.

[90] R. J. Ford. Sno Nitrogen/Dye Laser and Fibre Optic Diffuser Ball System Manual. *SNO-STR-96-056*, 1996.

[91] M. R. Dragowski. Sudbury Neutrino Observatory Energy Calibration using Gamma-Ray Sources. *Ph.D Thesis, Oregon State University.*, 1999.

[92] A. W. P. Poon. Energy Calibration of the Sudbury Neutrino Observatory. *Ph.D Thesis, University of British Columbia.*, 1998.

[93] F. Dalnoki-Veress. Investigation of the Triggered Source for the Calibration of Sno. *M.Sc. Thesis, Carleton University.*, 1996.

[94] G. Lomow M. Cline and M. Girou. *C++ FAQs.*, page 65. Addison Wesley, 1999.

[95] Zebra. *CERN Program Library Long Writeup Q100/101, CERN, Geneva, Switzerland.*

[96] H. Schildt. *C++ from the ground up.* McGraw Hill, 1994.

[97] M. Howe et al. Sharc Users Guide. 1998.

[98] Makoto Takahata. Study of Neutrino Oscillation using Upward Through-going Muons in Super-Kamiokande. *Ph.D. Thesis*, page 30, 1999.

[99] Thomas K. Gaisser. *Cosmic Rays and Particle Physics.*, page 74. Cambridge University Press, 1990.

[100] Q.R.Ahmad et al. Initial Observation of Through-Going Muons in the Sudbury Neutrino Observatory. *To Be Submitted*, 2001.

[101] R.H. Dalitz and D.R. Yennie. *Phys.Rev.*, 105:1598, 1957.

[102] Firestone et al. *Table of Isotopes.* John Wiley and Sons, New York, Eighth edition, 1996.

[103] D.F. Measday T. Suzuki and J.P.Roalsvig. Total nuclear capture rates for negative muons. *Phys.Rev.C*, 35:2212, 1987.

[104] L.B.Berzukov et al. *Sov.J.Nucl.Phys.*, 17:51, 1973.

[105] L.B.Berzukov et al. *Sov.J.Nucl.Phys.*, 15:176, 1972.

[106] M.Chen et al. *Phys.Rev.C*, 52:3449, 1995.

[107] Hirokazu Ishino. Measurement of the Solar Neutrino Energy Spectrum at Super-Kamiokande. *Ph.D. Thesis*, page 165, 1999.

[108] Yusuke Koshio. Study of Solar Neutrinos at Super-Kamiokande. *Ph.D. Thesis*, page 157, 1998.

[109] Andre Hamer. Energy Calibration of SNO for the measurement of the Charged-Current Neutrino Reaction. *Ph.D. Thesis*, page 158, 1999.

[110] Jewell et al. *Phys.Rev.*, 139:71, 1965.